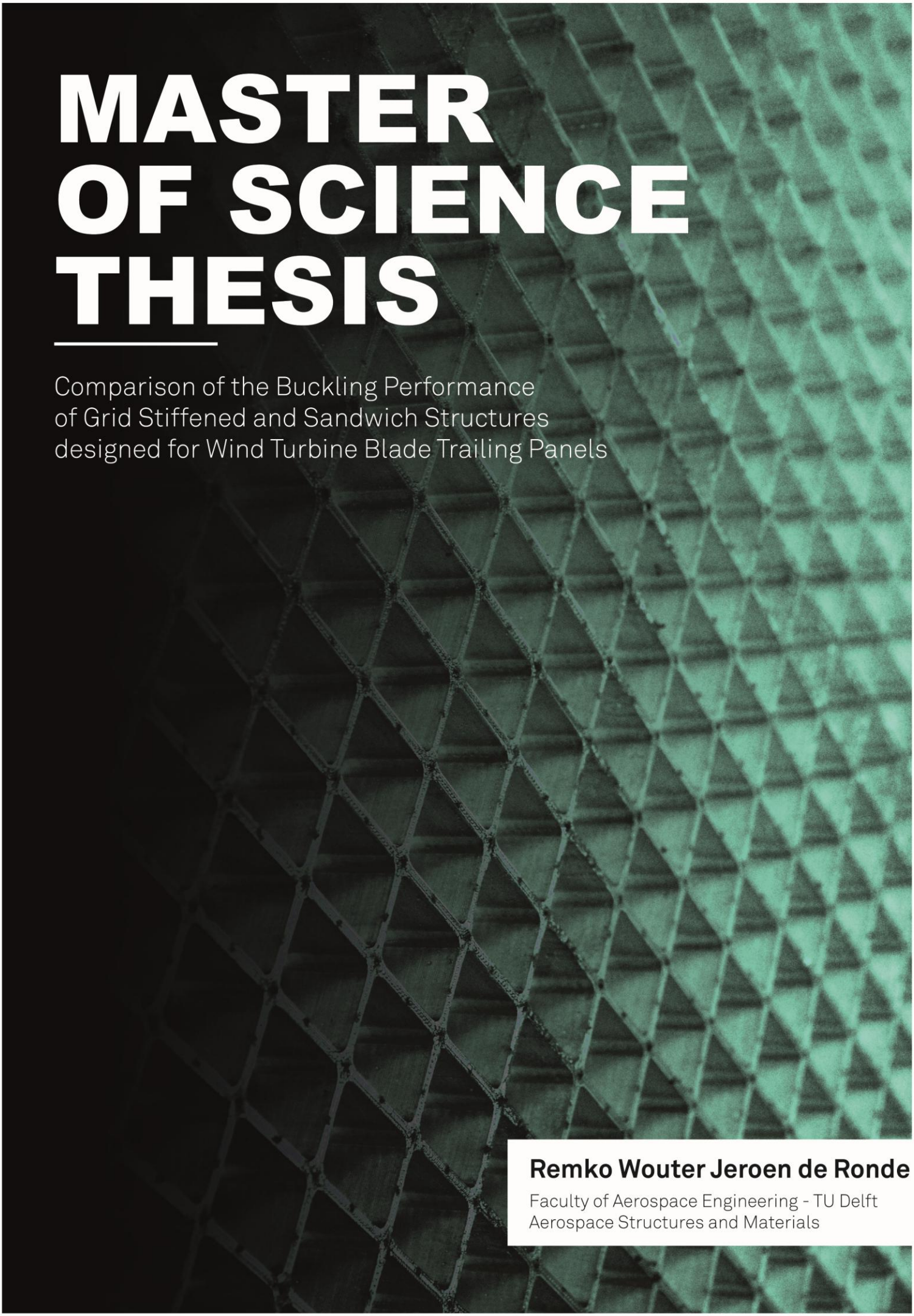

MASTER OF SCIENCE THESIS

Comparison of the Buckling Performance of Grid Stiffened and Sandwich Structures designed for Wind Turbine Blade Trailing Panels

Remko Wouter Jeroen de Ronde

Faculty of Aerospace Engineering - TU Delft
Aerospace Structures and Materials

MASTER OF SCIENCE THESIS

Comparison of the Buckling Performance
of Grid Stiffened and Sandwich Structures
designed for Wind Turbine Blade Trailing Panels

Remko Wouter Jeroen de Ronde

Faculty of Aerospace Engineering - TU Delft
Aerospace Structures and Materials

Comparison of the Buckling Performance of Grid Stiffened and Sandwich Structures designed for Wind Turbine Blade Trailing Panels

by

Remko Wouter Jeroen de Ronde

in partial fulfilment of the requirements for the degree of

Master of Science

in Aerospace Engineering at the Delft University of Technology

To be defended on February 23rd, 2018.

Supervisors:	dr.ir. S. Shroff	TU Delft
	dr.ir. J.M.J.F van Campen	TU Delft
	dr.ir. F. Lahuerta Calahorra	WMC
Thesis committee:	dr.ir. R. De Breuker	TU Delft
	dr.ir. J.J.E. Teuwen	TU Delft

TU Delft Knowledge Centre WMC INNWIND.EU

PREFACE

As a master student Aerospace Engineering at the Technical University of Delft, I have written this thesis report as one of the final steps to fulfil the requirements of graduation. The thesis report was written with two main purposes. The first was to give as much insight to the topic as possible, resulting in the addition of a lot of data and the intention to add new ideas on the studied subject. The second purpose was to present the findings in a clear and understandable way for the reader. Both purposes should help future researchers getting familiar with the topic in an efficient way.

During the full period of this master thesis project, new insight was gained on the buckling performance of grid stiffened structures, which can be considered a promising opponent for highly loaded sandwich structures. Based on the performed buckling analysis, weight reductions up to approximately 30% were found, which could possibly be further improved by introducing more design variables to the analysed structure.
A sneak preview of the manufactured grid stiffened panel is already shown on the cover, which was performed by a complex vacuum infusion process. The process is clearly explained with nice footage of all the different steps.
Compressions tests were also performed, where a new test set-up is designed in an attempt to model simply supported boundary conditions at the unloaded edges. The compression tests contributed to an improved understanding of the numerically performed analysis on the different structures.

All the described information in this project has taken a total of 10 months to be finished. This included a full literature study, designing and analysing different structural designs, manufacturing, testing and reporting on all of these steps.

I hope you enjoy reading the thesis as much as I enjoyed working on the topic and writing about it!

R.W.J. de Ronde
Delft, January 2018

ACKNOWLEDGEMENTS

As this report can be considered as the final step of my study Aerospace Engineering at the technical university of Delft, I first want to give the faculty with all its students and staff my gratitude in helping and motivating me to develop the skills I have obtained until today. The aim of the program is very high, but it helped me pushing myself to become more enthusiastic and driven to learn as much as possible on all different kinds of complex technical subjects.
I would also like to give a personal thanks to the people who helped, motivated, listened, encouraged or inspired me during my time I studied for my masters degree. In random order,

All of my colleagues at WMC, who made me feel welcome at their facility and gave me inspiration to learn a lot of new things about wind turbines. In particular, the advice and help of Koen, Frank and Luuk on the manufacturing and testing of the specimens had been of great help and the short discussions helped in improving both processes. My colleagues from “hokje 5”, Citty, Iuri and Sibrand for the Monday morning conversations about the weekends, the random small talks and off course the discussions on new ideas related to the project gave a glance to the work atmosphere. I am also thankful to Ben for the opportunity to present part of my work at the INNWIND.EU meeting at Politecnico di Milano, half way during the project, which is an experience I will never forget. My personal gratitude also goes to my supervisor Francisco, who has guided and challenged me throughout the full project, which definitely helped me in becoming a better engineer.

From the technical university of Delft, my gratitude goes to my supervisors Sonell and Julien. The knowledge, enthusiasm and valuable feedback about grid stiffened structures and the project in general which Sonell had inspired me with, have been motivating me after every Skype meeting we had. In addition, I am thankful to Julien, who supported me during the final two months of the thesis work and gave me the right feedback to further improve the content and readability of this thesis report.

I also spend loads of time at the gym Westerkoogsport, which is why I want to mention sensei Hans, who helped me training my physical and mental strength and to never give up to reach my goals.

My friends, Jamie, Tuan, Robert, Dax, Quincy and Jens, with who I could get my mind on different things in life. The holidays, the festivals, the road trips and all other activities were and still are a pleasure to share with you.

My brother for all the good conversations and the adventurous trips we experienced together, of which more will probably come in the future. My sister in law for her kindness and her support and advise on making the layout for this thesis. In addition I should not forget my niece, who gave me loads of big smiles or cries in the last 12 months!

Last but not least, I want to thank both of my parents, who were always interestedly listening to what I have learned, but most importantly were always available to give their endless support and encouragements when it was required the most.

The author acknowledges and is thankful for the contribution of the EU 7th framework programme INNWIND.EU (under Grant Agreement No.308974) to fund this research.

SUMMARY

The increasing rotor blade radius on wind turbine blades, requires the introduction of lower weight solutions to prevent the trailing edge of the blade from buckling under its own weight. Under the framework programme FP7 of the European Commission, part of the INNWIND.EU project focuses on the development of these light-weight structures. A particular case is studying the possibility to replace the sandwich trailing panels by lighter weight grid stiffened panels. Initial numerical analysis has estimated a weight reduction of approximately 30% on the trailing panel section of the blade.

A literature study gives an overview of the state-of-the-art on wind turbine trailing panels and grid stiffened structures in particular. Design and analysis is the first step of this project, on which numerous studies are performed on global and local failure modes. The limitation is mainly the expensive and complex manufacturing process involved, which is why the applications are mainly found in the aerospace industry. With the advancement of automated fibre layup, the costs of the manufacturing process can be drastically reduced in the future. A low number of publications were found on testing of grid stiffened structures, but the ones found were overall in relatively good agreement with the numerical analysis performed. Since bending moments on the trailing panels on a wind turbine blade are the driving factor behind the failure of the blade, this typical load case will be studied. This is simplified to a uniform compression load in order to enable a relatively simple test set-up. The main research question stated at the end of the literature study is:

“Is it possible to create a lighter weight trailing edge panel design by using an orthogrid stiffened panel, with remaining strength and stiffness properties at equal or lower cost?”

The performed research starts with a comparison between sandwich and orthogrid stiffened structures, where different failure modes for both types of structure are analysed. Verification between analytical and numerical models is performed for the sandwich panel, which showed relatively good agreement. A parametric study for the orthogrid panel shows good agreement between numerical and analytical models for the global buckling failure mode. The study also gave valuable insight in the influence of the different design variables of grid stiffened structures on specific local and global failure modes.
For a range of design loads, low-weight designs are found for sandwich and orthogrid structure. While comparing the weights of the panels along the different load cases, the sandwich and orthogrid panel relatively have the same structural performance. However, when the loading conditions increase to higher compressive loads, the orthogrid obtains a better specific stiffness than the sandwich panel. Weigh reductions are found between 20% and 30% for the higher design loads, of which the related sandwich designs are typically found on conventional wind turbine blades.

In an attempt to validate these results, manufacturing and testing of both types of structures is performed. The manufacturing of a sandwich panel is a rather straight forward vacuum infusion process. The orthogrid manufacturing process has first been tested with smaller sample panels. When relatively good quality products were obtained from the designed vacuum infusion set-up, a larger orthogrid panel was also manufactured for validation of the earlier obtained results.
All the manufactured panels have been tested in a compression machine, where simply supported conditions around the panel were tried to be introduced during the test. An aluminium test frame on the unloaded edges was designed to prevent out-of-plane displacement of these edges when panel buckling initiates. The test set-up was improved after the two sample orthogrid panels have been tested, since a better connection was required between the front and aft aluminium frame. A discussion on the manufacturing and testing process is written about the found limitations and opportunities for further improvements.

The data obtained from the performed compression tests are evaluated. The applied load is plotted along with the machine displacement and the measurements from the attached strain gauges. For each of the panels, a comparison with their corresponding numerical model is made. In order to obtain similar results between the experiment and the numerical model, different improvements were introduced. These improvements were based on the performed quality analysis, but boundary conditions have been adjusted as well to be in better agreement with the test set-up.

A list of conclusions can be drawn, based on the performed study. These conclusions are summarized for each chapter, where after the main research question is answered. Based on the study, a clear answer cannot be given yet, since the loading conditions addressed in this study are more complex in reality. Designing and analysing the structure under more complex loading conditions is therefore recommended for future research. Lower weight designs can also still be found by introducing more design variables in the analysis. Another limitation is the manufacturing process, which needs to be improved on the introduction of more design variables. Automation of the process is also necessary to enable the manufacturing of larger structures. Future research on wind turbine trailing edge panels also requires new test set-ups, which can validate the structures on sub-component level. The test set-up used during this project could therefore be further developed. Finally, other topics which are outside the scope of this project are stated as potential research questions, which would result in a stronger conclusion on the stated main research question in this project.

LIST OF SYMBOLS

Greek Symbols

ε_0	Mid-plane strain in a plate [-]
κ	Curvature of a panel [mm^{-1}]
σ_1	Normal stress in the 1-direction [N/mm]
σ_2	Normal stress in the 2-direction [N/mm]
τ_{12}	Shear stress in the 12-plane [N/mm]

Latin Symbols

a	Length of panel along x [mm]
a_0	Length of a unit cell of a grid stiffened structure along x [mm]
$A_{11,f}$	Membrane stiffness term in the 11-direction sandwich face sheet [N/mm]
$A_{12,f}$	Membrane shear stiffness term in the 12-plane sandwich face sheet [N/mm]
$A_{22,f}$	Membrane stiffness term in the 22-direction sandwich face sheet [N/mm]
b	Width of panel along y [mm]
b_0	Width of a unit cell of a grid stiffened structure along y [mm]
dx_{st}	Transverse stiffener spacing of grid stiffened panel [mm]
dy_{st}	Longitudinal stiffener spacing of grid stiffened panel [mm]
D_{11}	Bending stiffness of a structure in 11-direction [Nmm]
D_{12}	Bending/bending coupling of a structure between 1- and 2-direction [Nmm]
D_{22}	Bending stiffness in 22-direction [Nmm]
D_{66}	Torsional stiffness of a plate [Nmm]
D_{16}	Bending/torsion coupling of a structure between 1- and 6- direction [Nmm]
D_{26}	Bending/torsion coupling of a structure between 2- and 6- direction [Nmm]
E_c	Out-of-plane core stiffness [N/mm^2]
E_F	In-plane stiffness of the sandwich face sheet [N/mm^2]
G_c	Transverse shear stiffness of the sandwich core material [N/mm^2]
G_{xz}	Core shear stiffness in the xz-plane [N/mm^2]
h_{st}	Height of grid stiffened panel stiffener [mm]
h_{z0}	Distance between the neutral axis and the mid-plane of the skin [mm]
$N_{x,aswr}$	Sandwich antisymmetric wrinkling load [N/mm]
$N_{x,cc}$	Sandwich core crimping load [N/mm]
$N_{x,fpf}$	First ply failure load [N/mm]
$N_{x,gb}$	Global buckling load [N/mm]

$N_{x,gb,ts}$	Global buckling load, including transverse shear [N/mm]
$N_{x,ic,cc}$	Intracellular buckling load with clamped boundary conditions [N/mm]
$N_{x,ic,ss}$	Intracellular buckling load with simply supported boundary conditions [N/mm]
$N_{x,sc}$	Stiffener crippling load [N/mm]
$N_{x,swr}$	Sandwich symmetric wrinkling load [N/mm]
S	Shear strength [N/mm^2]
t_c	Thickness of sandwich panel core [mm]
t_f	Thickness of sandwich panel face sheet [mm]
t_{sk}	Thickness of grid stiffened panel skin [mm]
t_{st}	Thickness of grid stiffened panel stiffener [mm]
X^c	Compression strength in x-direction [N/mm^2]
X^t	Tensile strength in x-direction [N/mm^2]
Y^c	Compression strength in y-direction [N/mm^2]
Y^t	Tensile strength in y-direction [N/mm^2]

TABLE OF CONTENTS

1.Introduction

Under the framework programme FP7 of the European Commission, the INNWIND.EU project is focussed on the development of beyond-state-of-the-art 10-20 MW off shore wind turbines [28]. Part of this objective is the design and analysis of a light weight rotor blade, allowing further increase of rotor blade radius. The increased blade length leads to a larger rotor swept area, resulting in higher blade operation loads. This finally results in more rotational power and enabling higher energy production of the wind turbine. A potential weight reduction could be found by introducing a grid stiffened structure, shown in figure 1.1, into the rotor blade design, as a replacement of the conventional sandwich structure shown in figure 1.2. The background and motivation of this study is described in section 1.1. The general goals for this project are addressed in section 1.2. The roadmap which was followed to reach the formulated goals are explained in section 1.3, where the structure of the report is schematically drawn in a flow chart.

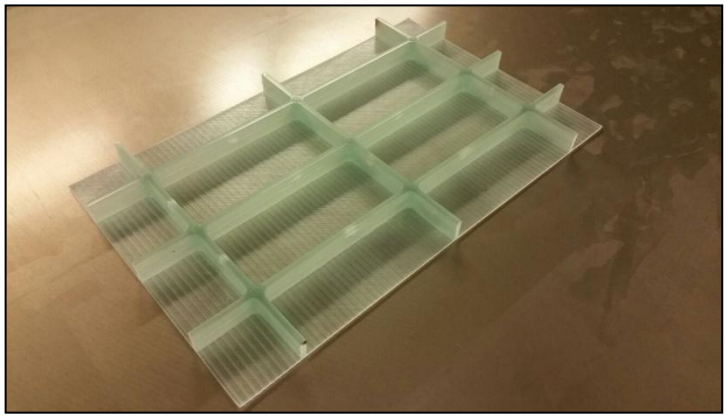

Figure 1.1: Grid stiffened structure

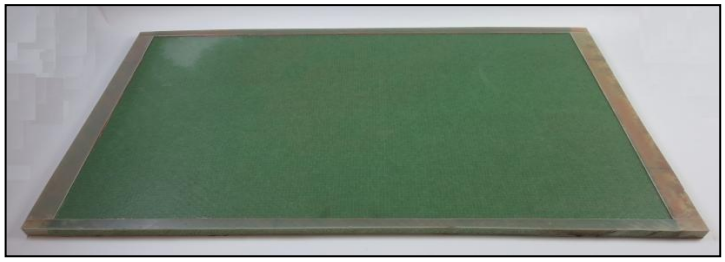

Figure 1.2: Sandwich structure

1.1 Background and motivation

Wang [1] performed a numerical analysis and optimization on the introduction of a grid stiffened structure on the trailing edge of a rotor blade. Comparing the optimized grid stiffened structural design with a conventional benchmark design, resulted in a potential weight reduction of more than 30%. The obtained blade design was numerically studied for its buckling performance, tip deflection and natural frequencies, which were all found within the design limits. As an additional conclusion, improved designs can still be found by introducing more design variables or using different optimization routines.

Shroff [2] manufactured a section of the designed blade as a demonstrator, which resulted in some conclusions regarding the complexity of the manufacturing process. One of the addressed problems with respect to upscaling the manufacturing process is found in the varying grid dimensions along the blade length. The introduction of fibre build-up or ply-drops on the stiffened grid should therefore be investigated and suitable manufacturing techniques should be developed. Another conclusion can be drawn with respect to the mould which was used to produce the grid. Each grid design requires a unique mould, resulting in multiple moulds to be produced to manufacture different grid designs. Finally, the demonstrator shown in figure 1.3 was manufactured by secondary bonding of a separate skin and grid. A suitable method to manufacture a grid stiffened skin as an integral structure without the need of bonding is expected to give the best result with respect to early separation of grid and skin.

The above described conclusions and recommendations drawn by Wang and Shroff will be taken into account in formulating the goal of the project in the next section.

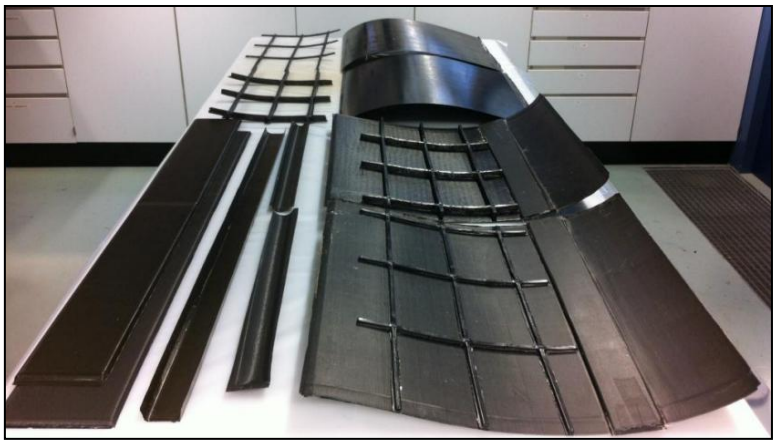

Figure 1.3: Demonstrator of a section of the blade design using the grid stiffened concept [2]

1.2 Goal of the project

Based on the background information, it can be concluded that validating test results are missing with respect to the performed numerical analysis.
The general goal of the project is therefore stated as follows:

- Validate the buckling performance and weight of a sandwich structure compared to a grid stiffened structure on the trailing edge of a wind turbine blade.

This goal should be reached by setting the following subgoals:

- Obtain a high quality product, which is suitable for testing. The aim is thereby to obtain an integral structure, without the need of secondary bonding grid and skin.
- Develop a suitable test method to validate the numerically studied designs and the high quality structures.

With the above goals in mind, the literature study will focus on the state-of-the art, from which the research questions for this project are set-up. The duration of a master thesis is thereby taken into account.

1.3 Structure

The project is divided in eight chapters, as shown in figure 1.4. Sufficient background information is obtained in chapter 2, where a detailed description on the state-of-the-art is given in a literature study, resulting in the research questions for this project.
Part I of the project is based on verification of results of analytical and numerical models and describes the theoretical foundation of the sandwich and grid stiffened structure. Chapter 3 and chapter 4 will focus on the design and analysis of a sandwich and orthogrid structure respectively. Chapter 5 will evaluate and compare both structures.
The last section of chapter 5 will describe the different designs to be manufactured and tested in order to validate the results. These given designs are addressed in the second part of the project, where chapter 6 gives insight in manufacturing and testing of the different designs. After obtaining results from the quality of manufacturing and the results of the experimental work, evaluation and improvements on the numerical models will be performed in chapter 7.
In chapter 8, conclusions with respect to the obtained results are made and a recommendation is given for future studies on the implementation of grid stiffened panels on a wind turbine rotor blade.

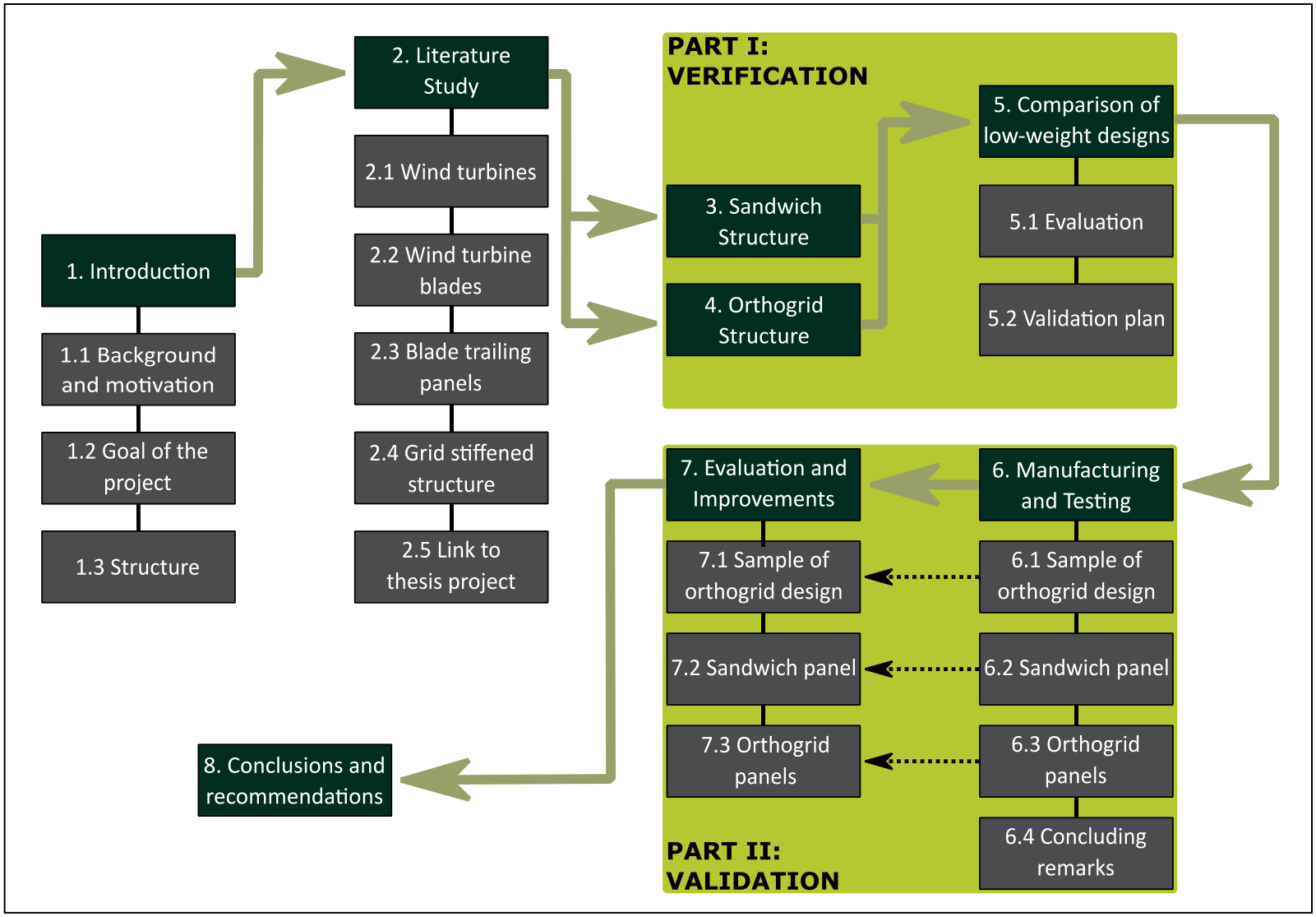

Figure 1.4: Flow chart thesis report

2.Literature Study

Wind turbines have grown significantly in size in the past decades. This increased size of wind turbines is necessary to accommodate the increasing demand of power and to lower the production costs per kilowatt hour electricity. One of the major limitations of further increasing the size of wind turbines is the mass of the blade. Gravitational forces become very high, resulting in buckling of the blade. New structural designs should therefore be analysed, which can potentially result in lower weight designs and the ability to increase the wind turbine size further.
From an earlier study carried out by Wang and Shroff under the FP7 European project INNWIND.EU [1, 2], a grid stiffened structure was proposed as a replacement of the sandwich trailing edge panels, in which a weight reduction of more than 30% was found with respect to the analysed section of the benchmark blade. To verify and validate these results, a buckling analysis should be performed, where a grid stiffened panel is compared to a benchmark sandwich panel.
This literature study is performed to obtain sufficient knowledge about all important aspects involved in wind turbine blade design. This knowledge can then be used in designing and analysing a grid stiffened panel, which could be used as a replacement of the sandwich trailing edge panels. Section 2.1 briefly describes the wind turbine in general and it gives information about aspects related to the blade design. The study narrows down to the wind turbine blades in section 2.2 and this information is used to describe the conventional wind turbine blade trailing edge design panels in section 2.3. Literature related to design, analysis, manufacturing and testing of a grid stiffened panel is given in section 2.4. The literature studied so far will be analysed in section 2.5, where it will result in the research questions being investigated in this thesis project.

2.1 Wind turbines

Wind turbines exist in different forms, but the main type of design seen in practice nowadays is a three bladed horizontal axis wind turbine. Such a wind turbine can be split into four main components, which are indicated in figure 2.1.

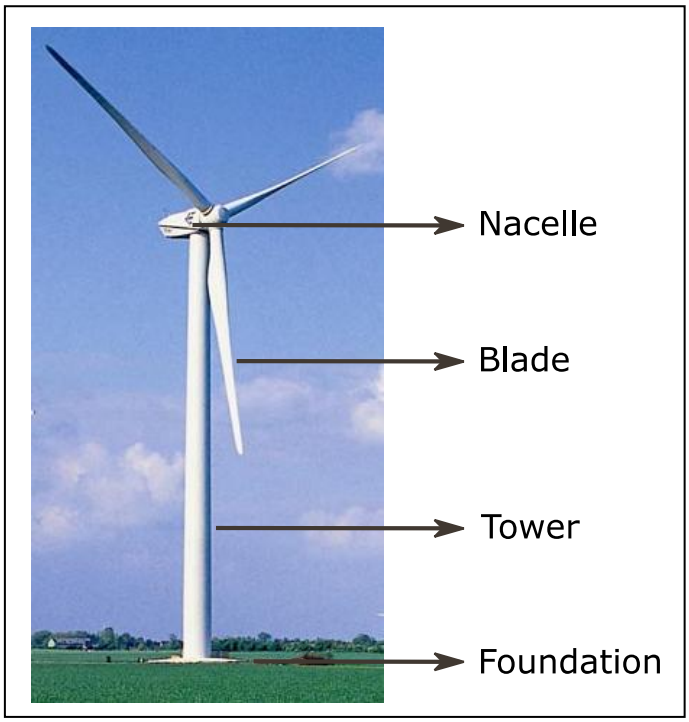

Figure 2.1: Main components of a horizontal axis wind turbine

The foundation connects the wind turbine to the ground and distributes the gravitational and aerodynamic loads over a large surface area. The type of foundation depends on local soil conditions, which could roughly be divided in on- and offshore wind turbines.
The tower is positioned on top of the foundation and should withstand the gravitation loads from the weight of the nacelle and the blades. Dynamic loads from the rotation of the blades and wind gusts should also be taken into account for the tower design. The tower is most of the times assembled from multiple tubular steel sections, which are joined by bolted flanges. On the inside, one can find thick copper cables to transfer the generated energy to the grid. A ladder is typically available to be able to reach the nacelle for maintenance purposes.
The blades of the wind turbine are the actual part that extract energy from the wind. Horizontal axis wind turbines are mainly seen with three blades. In comparison with two or four bladed designs, this is mostly found to be the most cost-effective design. The next section will give more details about the wind turbine blade.
The fourth and final component is the nacelle, which connects the tower and the rotor blades. Inside the nacelle, the rotational energy of the blades is converted to electrical energy. A gearbox is present to increase the slow rotational speed of the rotor blades. The obtained high rotational speed is used to drive the generator, from which the electrical energy is obtained. More smaller components could be found to control the wind turbine as efficient as possible, but since they are outside the scope of this project, these other components will not be discussed. Further reading could be found in books related to wind turbine engineering [3, 4].

2.2 Wind turbine blades

The study will now narrow down to the wind turbine blade, since the particular structure to be investigated is found here. The blade design could be divided in two main functionalities. First, the aerodynamics of the blade should be designed in such a way that as much energy as possible can be extracted from the wind. The second functionality a blade should posses is the structural strength to withstand all the loads applied to the blade, without the occurrence of material or structural failure, which is the main topic of this report.
The aerodynamic functionality is driven by the shape of the outer surface of the rotor blade. Chord length, thickness and camber of an airfoil should be optimized together with the twist along the length of the blade. The twist along the radius of the blade is applied, since the tips move a lot faster through the air than the rotor near the root of the blade. This results in a changing relative wind vector acting along the length of the blade, demanding for the twist giving an optimum angle of attack.
From the latter, it could be imagined that the requirements for the structural functionality become more complex, caused by the preferred aerodynamic shape of the rotor blade. The structure and materials selected for the blade should therefore not only cope with the ultimate loads, fatigue loads and stiffness requirements against low cost and weight, but should also be able to obtain the desired aerodynamic shape.
Figure 2.2 shows an example of a cross-section of a wind turbine rotor blade. Depending on the size and location along the length of the blade, the airfoil mostly contains one or two shear webs. The spar caps on top and bottom of the shear web are present to improve the bending stiffness of the blade. The leading edge has a lot of curvature, where the trailing edge has a relatively flat design. During most of the assemblies, four parts have to be joined. The shear webs are two separate parts, which are joined to the top and bottom blade panels and spar caps with an adhesive bond. Adhesive bonds are also present at the leading and the trailing edge of a typical wind turbine blade. Each part could be assigned a certain load case to counteract, which is further explained later in this section. The part of the blade indicated with “trailing panels” is analysed in this project.
To obtain the desired structural functionality of the blade, glass and carbon fibre reinforced polymers are mainly found in conventional rotor blade designs. However, since carbon fibre is much more expensive than glass fibre, the majority of the blade consists of glass fibre reinforced polymers.

Carbon fibre is sometimes chosen at the spar caps, where they are laid down as a unidirectional tape along the length of the blade.

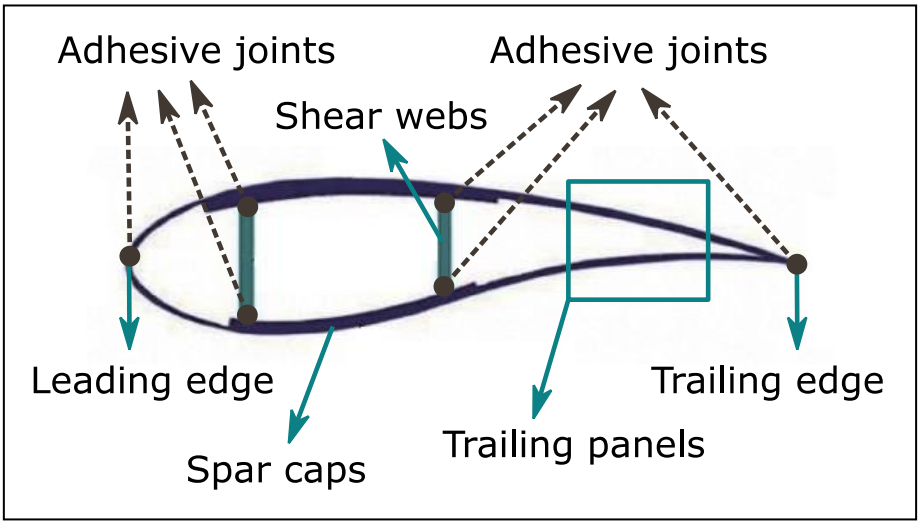

Figure 2.2: Example cross-section of a wind turbine rotor blade

The buckling resistance of the leading and trailing edge, consisting of glass fibre is improved by applying a lightweight core between the glass fabrics, resulting in a sandwich design. The relatively flat trailing sandwich panels will be assessed more specifically in section 2.3.

The loads applied to the rotor blade are an important aspect for structural design. The forces applied to the rotor blade are caused by the aerodynamic forces from the wind, inertial forces and gravitational forces from the weight of the rotor blades. These forces result in the three main contributors of force to the rotor blade as shown in figure 2.3.
The tangential force causes the rotation of the blades and causes a moment around the chord-wise (or edge-wise) direction. The thrust force causes a flap-wise moment. Both moments result in a torsional moment around the axis along the blade, since the shear resultants are not applied at the shear centre of the cross section.
The latter is a rather straight forward and simplified explanation of the applied forces. In reality, the aerodynamic forces could be divided in steady and unsteady loads. Steady loads occur if a uniform wind speed across the area of the rotor blade is present. Unsteady loads are more likely in practice and are caused by vertical wind shear, cross winds or wind turbulence across the rotor diameter. These differences in aerodynamic forces, cause periodic loads on the blades on each rotation.
These periodic loads are also caused by the gravity loads applied on the blade. At different angles of the blade with respect to its starting position, the weight of the rotor blade tensions and compresses the blade periodically. The inertial loads are thereby also present and are a result of the centrifugal force of the blades. All these load conditions could add up to worst load cases, which should be counteracted by the blades structural strength. In case of pitching and jawing of the blade, small loads are also introduced on the blade.
In order to simplify the complex loading scenario given above, the chord-wise (edge-wise) and flap-wise moments are assumed to be mainly determining the structural design.
Referring back to figure 2.2, the spar caps mainly counteract the flap-wise bending moment and the shear web is present to cope with the shear force resulting from the flap-wise moment.
The edge-wise moment is carried by the leading and trailing edge of the wind turbine rotor blade, where it should be taken into account that a shear force is also present as a result of the edge-wise moment.

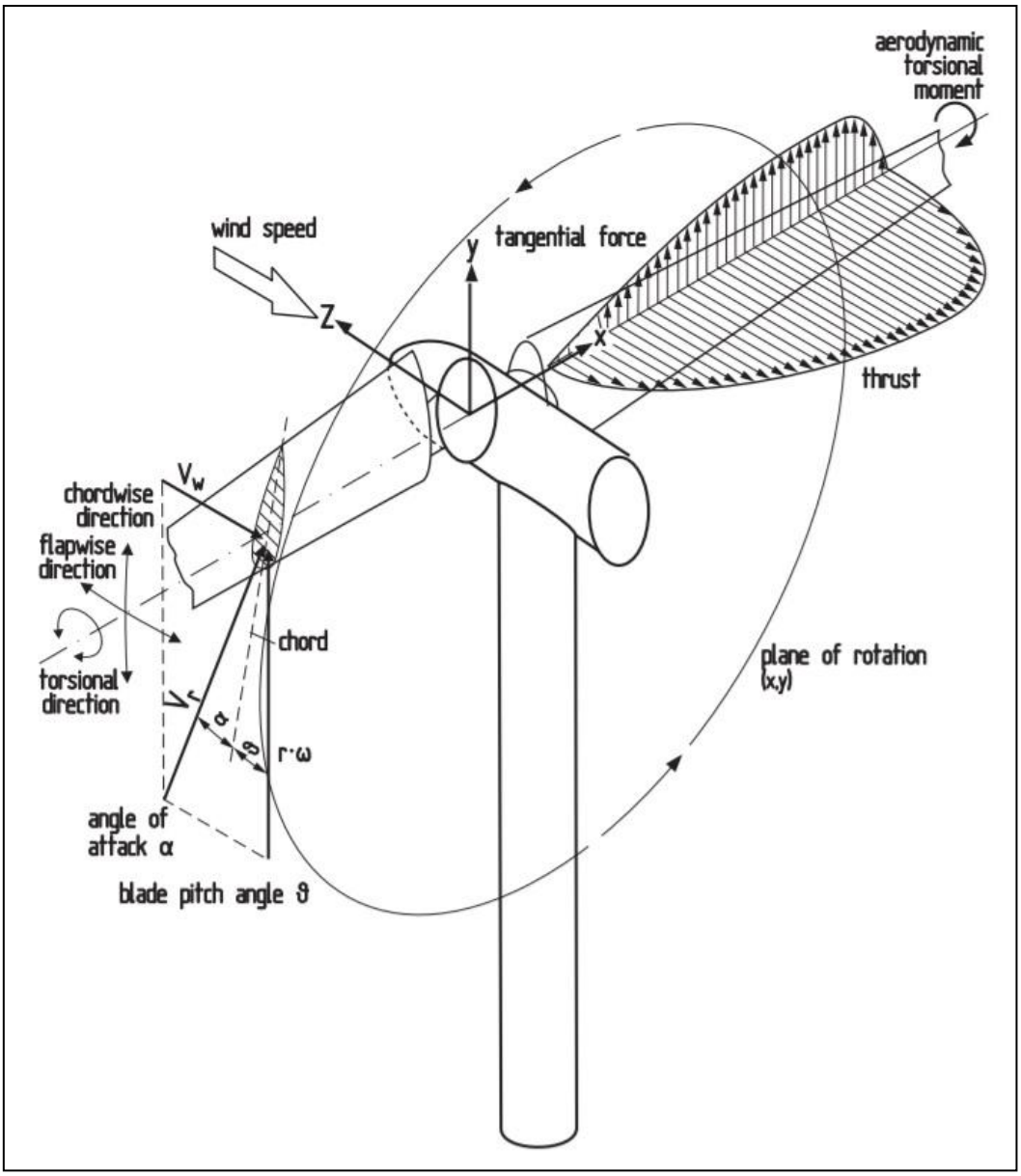

Figure 2.3: Loads on a wind turbine rotor blade [4]

2.3 Blade trailing panels

Due to the edge-wise moment on the rotor blade, the lightweight sandwich trailing panels require enough stiffness to resist panel buckling under the compressive loads it is subjected to. The highest compressive loads in the trailing panels occur during the upward movement of the blade every single rotation of the wind turbine. A simplified sketch of a wind turbine blade moving in upward direction is shown in figure 2.4.a. The load F_y is the sum of the aerodynamic loads and the gravitational loads. Since the gravitational loads pointing in the negative y direction are larger than the aerodynamic loads in the positive y direction, a resulting negative force in y is drawn. The load resultant acts along the length of the blade where in this case the cross-sectional area along the length is constant to simplify the explanation. The free body diagram in figure 2.4.b shows the moment M_z and the shear force V_y on the fixed end of the blade. Taking a small section of this free body diagram in figure 2.4.c, the gravitational loads could be assumed to impose a bending moment along the length. From bending theory, the stresses acting on the cross-section of the blade are shown in figure 2.4.d. It can be seen that during the upward movement of the blade, a varying compressive stress is acting on the trailing edge of the cross-section. To simplify the analysis during this project, a uniform compression

will be assumed to compare the buckling performance of a sandwich panel with that of a grid stiffened panel.
Kassapoglou [14] described analytical methods to determine the critical load of different failure modes of sandwich panels. Vadakke & Carlsson [29] studied compression of sandwich specimens and compared predicted failure loads with experimental results. The described methods, along with finite element models will be further addressed and used in chapter 3 and 4.

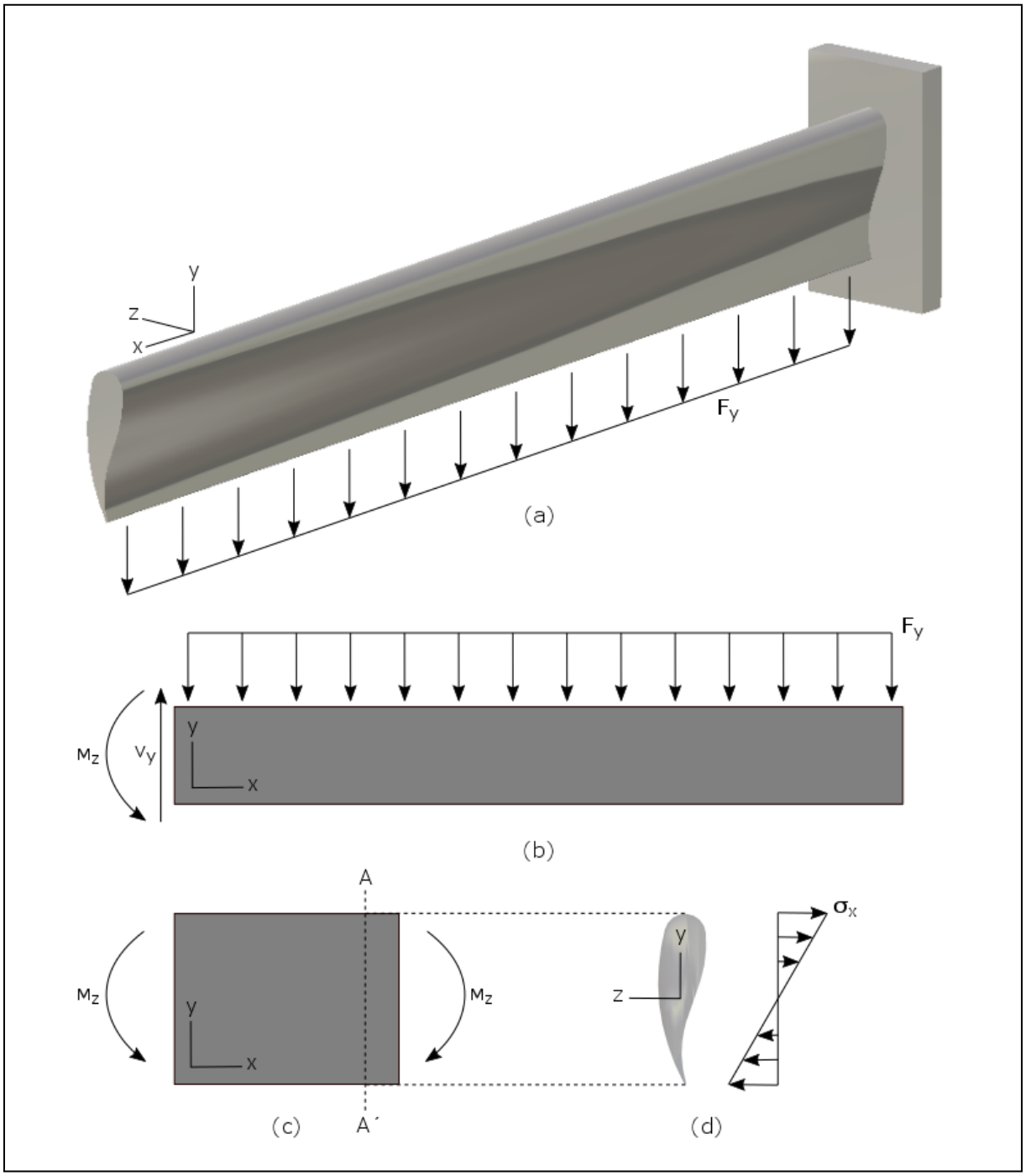

Figure 2.4: Simplified rotor blade with one end fixed (a); Simplified free body diagram of gravitational loads on a wind turbine blade (b); Enlarged section of the free body diagram drawn in b (c); Compressive and tensile stresses acting on the cross-section as a result of the bending moment (d)

2.4 Grid stiffened structure

Literature related to compression of grid stiffened panels could be divided in design and analysis, manufacturing and testing. Subsection 2.4.1 is focussed on different methods used for the design and analysis part. State-of-the-art manufacturing methods are discussed in subsection 2.4.2 and literature found on testing of grid stiffened structures is outlined in subsection 2.4.3.

2.4.1. Design and analysis

Since the main objective of the trailing panels is resisting of buckling, the study will focus on compressive loading on a grid stiffened structure.
The main failure modes of a grid stiffened structure under compression are attributed to global panel buckling as shown in figure 2.5, crippling of the stiffener as shown in figure 2.6, intracellular buckling as shown in figure 2.7, material failure and skin-stiffener separation. The two latter are expected to be post buckling failure modes and will therefore only be briefly assessed during this project.

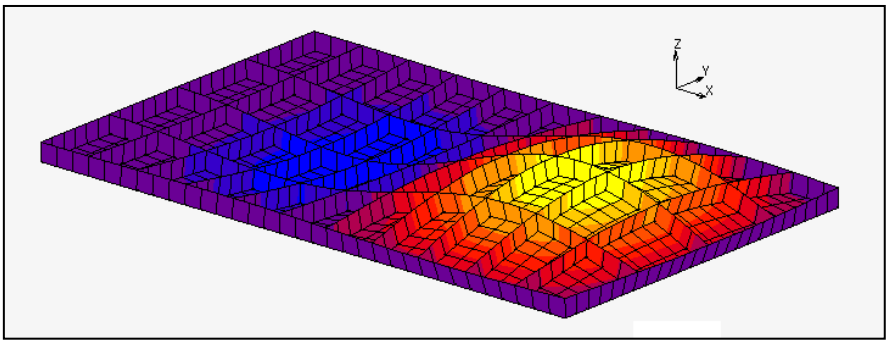

Figure 2.5: Global buckling of a grid stiffened structure

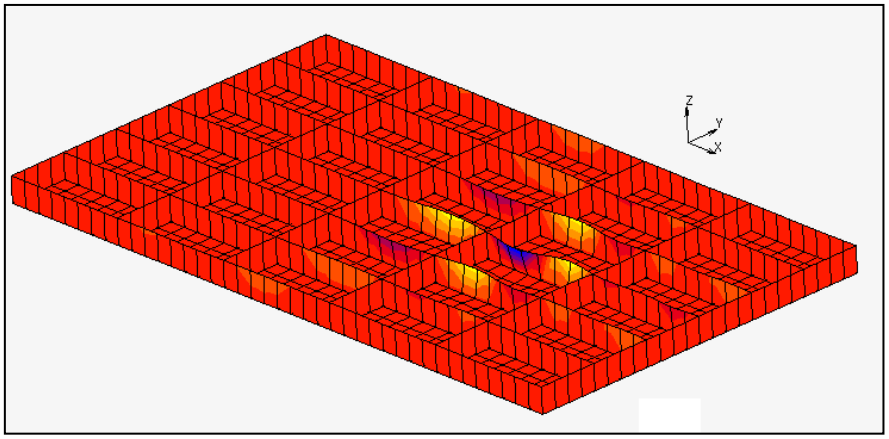

Figure 2.6: Stiffener crippling of a grid stiffened structure

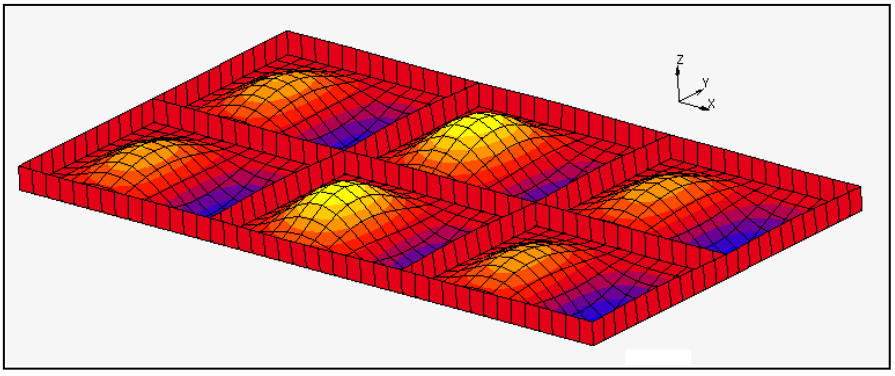

Figure 2.7: Intracellular buckling of a grid stiffened structure

Global buckling is considered when the complete skin and stiffener show large out of plane deflections as an integral structure. Many literature has been found to determine this type of failure mode for grid stiffened cylinders as well as for grid stiffened panels. In most cases, smeared stiffener models are used to determine the global buckling load analytically. Jaunky et al. [5] describe an improved theory for the calculation of the global buckling load. The approach in this paper calculates a shift of the neutral axis, by using the method of minimum potential energy. The results are compared to finite element models, which show good agreement with the described method. Another theory is described by Xu et al. [6], where the neutral axis for the stiffened grid is determined by introducing only the portion of the skin attached to the stiffener. The average neutral surface for the skin is then determined by smearing the stiffened grid along its own neutral axis. By superimposing the stiffness contribution obtained from the skin and the stiffener, the equivalent stiffness matrix is obtained. The bending stiffness is then used to determine the global buckling load of the grid stiffened panel. The results showed good agreement with finite element analysis performed on different grid stiffened structures. Different other studies have been performed on global buckling analysis of a grid stiffened panels or cylinders [7, 8, 9, 10, 11, 12].
The case of stiffener crippling was shown in figure 2.6. An exact method is obtained by Meink et al. [13]. Applying an approximate function for the out-of-plane displacement, which was in agreement with test results, in combination with a minimization of total potential energy resulted in an exact solution. The method is extended to different cross-sections of a stiffener. Stiffeners with linear varying thickness along the height are analysed, where different ratios are used. The procedure is then also applied to an hourglass type of cross-section. When the analytical results are compared to finite element models for some particular cases, it was found that obtained results were accurate for a certain range of dimensions. Since the results of the analytical solution described is limited to certain dimensions of the stiffener, stiffener crippling will be difficult to analyse and taken into account during an optimization. Future research should give more insight in the behaviour of the stiffeners under compressive loading.
To determine the intracellular buckling load, shown in figure 2.7, the skin of an orthogrid between the stiffeners could be modelled as a plate with four simply supported or clamped edges [14]. This method could be used to obtain a rough estimated value for the intracellular buckling load, where the real buckling failure load is expected to lie between the two results obtained from simply supported and clamped boundary conditions. However, any verification of the method has not been found in literature at the moment. Skin buckling has also been addressed by Weber and Middendorf [15], where for different types of panels the buckling coefficient is determined. The effect of angles, panel curvature and material orthotropy is outlined.
For each of the failure modes, a suitable model will be chosen and further explained and used in chapter 3 and 4.

2.4.2. Manufacturing

Next to the analysis of the different types of failure mode, manufacturing is another important aspect to take into account as a result of the complex geometry of a grid stiffened structure. In order to validate analytically or numerically determined behaviour of a structure, a good quality product should be manufactured and tested.
To obtain a high quality product, including continuous fibres at the stiffener crossings (nodes), Sorrentino et al. [16] have performed a numerical and experimental study on a cylindrical design with a stiffened grid on the inside of the cylinder. Producing the mould for the cylindrical structure was the first step prior to manufacturing. One of the requirements is to be able to easily remove the mould after the product is produced. Second, the ribs should obtain enough compaction from the mould, which means a compatible mould material should be used. The third requirement is to have sufficient space at the nodes, where the fibres cross and build up if the mould is not properly designed. Surface treatments were also performed to improve the mould and product separation after the manufacturing process. Once the mould was designed, a curing temperature simulation was

performed numerically to check for high temperature gradients at the nodes, where the material has the largest thickness. The manufacturing was performed by placing the mould in a fixture, which could rotate. Impregnated carbon fibres were wound through the channels of the mould by hand and on top of the filled channels, the prepreg skin was placed around the mould. The results from an axial compression test, were in good agreement with the numerically predicted stress.
As a follow-up on this experiment, Sorrentino et al. [17] manufactured the same specimen, but used a robotic filament winding process. This automated process was introduced for several reasons. In comparison with filament winding by hand, a robot could perform the process faster and it is able to reproduce the same quality every time. A robotic process is also capable of applying a continuous fibre tension during the layup process. The obtained product from the automated process was compared on geometrical and quality aspects with the handmade cylinder. It was shown that the robotic filament wound structure resulted in a better product on all aspects. A 20% higher failure load was also obtained.
As was mentioned before, the design and production of the mould of a grid stiffened panel is an important part for obtaining a high-quality product. Huybrechts et al. [18] have therefore formulated two effective manufacturing techniques and describe the theory behind the mould design. Both techniques focus on compaction of the ribs, by using the coefficient of thermal expansion of the mould material. The methods are validated by comparing the calculated geometry with the exact geometry measured after manufacturing.
Filament winding and state of the art fibre placement are described by Shroff [19, 20]. The filament winding process could be performed by winding dry or wet fibres around a mould. The main drawbacks are found in limitations of the shape of the product and the ability to steer the fibres in any direction. This drawback of filament winding is not found for automated fibre placement, which has the ability to steer fibres by directing a robot arm along the surface of a mould. The drawback here is that the robot has to apply pressure, when applying a layer of material. The pressure applied on a thin uncured stiffener could then be too high, making these complex shapes impossible to produce with this method. A solution to this problem could be found by using dry fibres, impregnated with a binding material. Upon heating and placement of the fibres, a dry preform of the grid stiffened panel is obtained, which can be infused with resin afterwards. The mentioned automated methods described, were however not used for manufacturing during Shroff's analysis. The actual test specimens were produced by a combination of hand layup, using a winding table, and a vacuum infusion process.

2.4.3. Testing

So far found in literature, test results are mainly found for compression of cylindrical structures [16, 17]. In chapter 6 of the Isogrid Design Handbook [21], some basic input is provided regarding models, sub-scale and full-scale tests.
Kim [22, 23] has performed compression tests on both a cylinder and a flat panel, which were both of an isogrid type of structure. From the compression test on the cylindrical structure, it was found that the design consists of good damage tolerance. Rib crippling was found to be the initial failure mode, but the load was redistributed over the other stiffeners. By increasing the load further, different stiffeners failed in crippling, but the load did not show a significant drop. Bending deformation of stiffener and skin was obtained from back-to-back placement of strain gauges. Transverse and longitudinal strains on the specimen were measured by rosette gauges.
The flat panel manufactured by Kim [23] using prepreg tows and plies and an autoclave was being tested in compression. A total of 18 strain gauges were applied, from which one on the back of the panel to capture plate bending. The load was introduced to the specimen uniformly by applying a thick rubber strip on top and bottom of the panel. Since no stiffeners were placed at the sides, two free edges were present during the test, probably causing a lower stability of the panel.
From almost all tests described so far, pinging sounds are heard prior to failure from instability of skin, stiffener or the whole structure. Researchers attribute these sounds to matrix or fibre failure.

2.5 Link to thesis project

From the previous work performed work during the FP7 European project INNWIND.EU, a lower weight design was found with respect to a reference wind turbine rotor blade. A demonstrator of a section of the blade was also produced. However, validation of the numerical results has not been done yet and regarding the manufacturing of the design, different complications were addressed.
Combining the previous work performed by Wang [1] and Shroff [2] with the present literature study, the next step of this research topic and the additional research questions can be set up. Three main aspects related to the project could be stated as follows:

1. Comparison of the compressive strength of low weight sandwich structures against low weight grid stiffened structure, for a range of design loads (Part I)
2. Manufacturing of a high quality grid stiffened structure, suitable for testing (Part II)
3. Validate numerical results for a grid stiffened panel (Part II)

To accommodate for the above three aspects within the given timeframe of a master thesis project, the comparison of a sandwich structure and grid stiffened structure is simplified to flat panels under compressive loading, also noted in figure 2.4. As an addition to the mentioned simplification of flat panel analysis, only the orthogrid structure will be compared to a sandwich panel, since this grid set-up was also used in the optimized design of Wang.
Analyzing these flat panels, the main research question of this project is stated as follows:

“Is it possible to create a lighter weight trailing edge panel design by using an orthogrid stiffened panel, with remaining strength and stiffness properties at equal or lower cost?”

To obtain a strong conclusion and recommendation with respect to the above main research question, the three earlier mentioned aspects should be analyzed. The first aspect evaluated in part I of the project, results in the following sub questions:

1. Which analytical or numerical methods could be used to determine the strength of a sandwich or orthogrid structure?
2. Are analytical and numerical models in sufficient agreement to be used for finding optimum results?
3. Which design constraints should be imposed during the analysis, as such that manufacturing and minimum structural requirements are met?

The second aspect evaluated in part II of the project, related to manufacturing of a high quality orthogrid stiffened structure results in the following sub questions:

1. Which manufacturing technique is suitable for obtaining the obtained designs from the performed analysis?
2. What tolerances occur on the different design variables during manufacturing and what influence do they have on the quality of the product?

The third aspect also evaluated in part II of the project, related to the validation of obtained results, should give an answer to the following sub question:

1. Are the test results of the manufactured and tested panels in agreement with the numerical models?
2. Is the testing method suitable for validation of the models or should the method of testing be improved?

2.5 Link to thesis project

According to conclusions drawn earlier, there are more aspects involved in designing a wind turbine rotor blade trailing edge. The following questions should be studied in the future as well prior to actual implementation, but are for now outside the scope of the project.

1. How is maintenance and repair minimized for grid stiffened structures?
2. How would load be introduced into grid stiffened structures?
3. How are top and bottom trailing edge panels adhered in case of a grid stiffened panel?
4. How would a grid stiffened panel behave under fatigue loading obtained from the periodic rotations of the blade?
5. Is it possible to repair small sections of the grid stiffened structure in case of small defects after manufacturing or in case damage occurs during operation?
6. Non-uniformity of the design variables of the grid stiffened structure along the rotor blade length should be studied and in what way this non-uniformity influences the structural properties and the manufacturing process.

PART I: VERIFICATION

Before any validation of the sandwich and orthogrid panels can be performed, analytical and numerical models should be evaluated in order to obtain a comparison on low-weight designs for a range of compressive loading conditions. The design and analysis of a low-weight sandwich and grid stiffened structure is outlined in chapter 3 and chapter 4 respectively. The comparison between the two structures will be made on the obtained results in chapter 5, where a plan for validation is also set up.

3.Sandwich Structure

As can be observed from figure 3.1, this chapter will describe the design variables of a sandwich structure first in section 3.1. The panel will be analysed for a compressive load by analytical methods in section 3.2, where local and global failure modes are taken into account. The global buckling load is numerically determined by using a finite element method in section 3.3, where three different element strategies are analysed. Verification of results is performed in section 3.4, where global buckling predictions by analytical and numerical models are compared. Section 3.5 is devoted to finding low-weight design solutions for a sandwich panel.

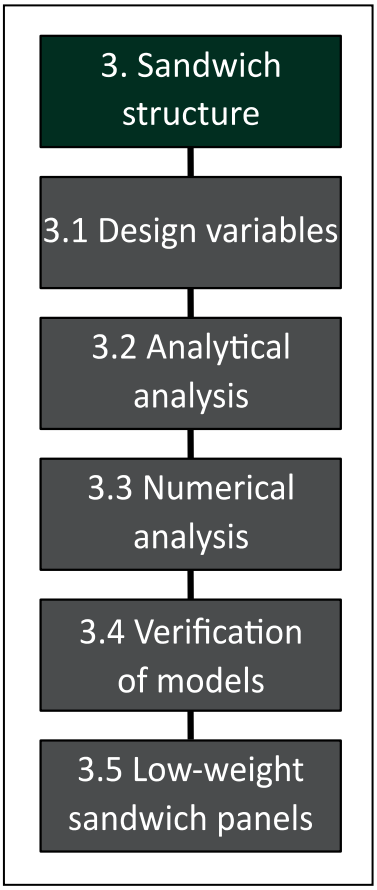

Figure 3.1: Flow chart chapter 3

3.1 Design variables

A sandwich panel design is mainly chosen for its high bending stiffness, obtained by applying an offset to the stiff face sheets with respect to the neutral axis. This offset is obtained by placing a light

weight core between the two face sheets. In wind turbine blades, a light weight foam or balsawood is normally used as core material.
Figure 3.2 shows the different design variables for the sandwich panel, which is analysed in this project as a benchmark design. Length a and width b describe the global panel dimensions. The core thickness is described by t_c and the face sheet thickness, depending on the number of stacked plies, is given by t_f. These geometric variables are used in the following subsections. The panel size has a fixed length a of 866 mm and a fixed width b of 500 mm during this project.

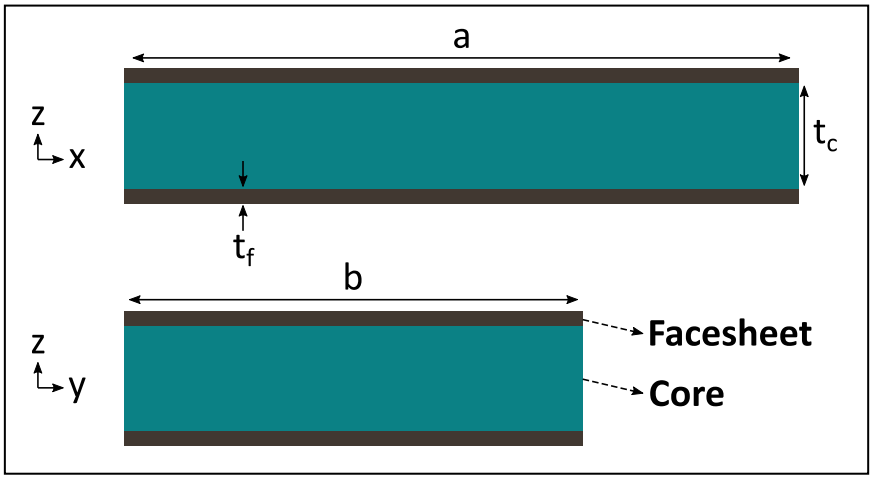

Figure 3.2: Design variables of a sandwich structure

In the trailing panels of the wind turbine blade, mainly biaxial [+/-45] degree plies or triaxial [60/0/-60] degree plies are found in the face sheets. The main fibre material used for the face sheet layups is glass-fibre. Since Knowledge Centre WMC has a Saertex-812g biaxial glass-fibre on stock at the facility, a stacking of biaxial plies will be used in finding low weight benchmark designs in section 3.5. The material properties of this biaxial glass-fibre fabric as well as the material properties of the foam core used in this project to analyse the sandwich panel are given in appendix A.

3.2 Analytical analysis

A flat sandwich panel under compression has different modes of failure, which will be outlined in this section. Global panel buckling is analysed and described in subsection 3.2.1. Wrinkling of the sandwich face sheets should also be considered and is treated in subsection 3.2.2. The core of the sandwich panel can also fail under compression, which is described as core crimping. The analytical method is described in subsection 3.2.3. To be sure that the material used in the face sheets has sufficient strength, a first ply failure analysis will also be performed in subsection 3.2.4. The main reference used for the analytical methods described in the following subsections are written by Kassapoglou in chapter 10 of [14] and Vadakke & Carlsson [29]. More information, which could be used to understand the described methods could also be found in chapters 15 till 17 of the book written by Vinson [24].

3.2.1. Global buckling

When a sandwich panel is subjected to a compressive loading, it could fail by buckling of the complete panel, also described as global buckling. The shape of the failure mode under compression is shown in figure 3.3.
Kassapoglou [14] described the global buckling load under unidirectional compressive loading and could be determined by equation (3.1), where the bending stiffness terms D_{11}, D_{12}, D_{22} and D_{66} are higher due to the light weight foam core in between the face sheets. For a particular length a and width b of a panel, the minimum buckling load could be found by calculating the failure load for a range of buckling modes, given by the number of half waves m.

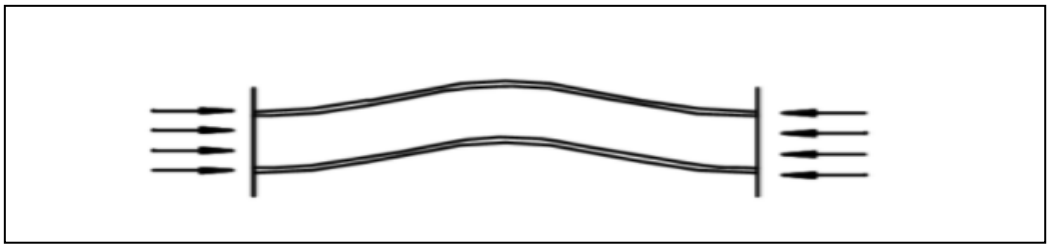

Figure 3.3: Example of global buckling of a sandwich panel under compressive loading

$$N_{x,gb} = \frac{\pi^2}{a^2}\left[D_{11}m^2 + 2(D_{12} + 2D_{66})\left(\frac{a}{b}\right)^2 + D_{22}\frac{\left(\frac{a}{b}\right)^4}{m^2}\right] \tag{3.1}$$

In the formulation given above, transverse shear effects are not taken into account, which makes it good for preliminary designs with relatively low thickness, but far from accurate when more detailed behaviour needs to be predicted for thicker sandwich designs. Therefore, a penalty on the buckling load is introduced based on the core thickness and shear stiffness. The final formulation [14], including transverse shear effect is given in equation (3.2).

$$N_{x,gb,ts} = \frac{N_{x,gb}}{1 + \frac{N_{x,gb}}{t_c G_c}} \tag{3.2}$$

In which the buckling load without including transverse shear effect was formulated in equation (3.1) and the thickness and the transverse shear stiffness of the core material are:

$$t_c: \text{core thickness}$$

$$G_c: \text{transverse shear stiffness of the core material alligned with the loading direction}$$

Equation (3.2) will be verified with a numerical model in section 3.4.

3.2.2. Facesheet wrinkling

The face sheets of a sandwich panel could also fail under a local failure mode called wrinkling. The failure mode could be considered as buckling of a small portion of the face sheet. Two particular types of wrinkling, symmetric and asymmetric wrinkling, are described in this subsection. Kassapoglou [14] has described the full derivations of the described methods.

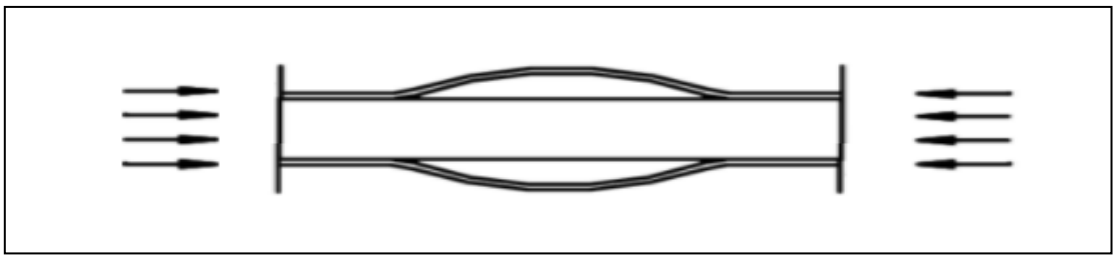

Figure 3.4: Example of symmetric wrinkling of a sandwich panel under compressive loading

Symmetric wrinkling considers the case where both face sheets of a sandwich panel locally buckle into or out of the core as is shown in figure 3.4. Asymmetric wrinkling considers the case where the face sheets both buckle in the same direction with respect to each other.

3.2 Analytical analysis

Symmetric wrinkling

A derivation of symmetric wrinkling is based on energy minimization, where the energy is obtained from bending of the face sheets and extension of the core. The work done is obtained from the applied force on the face sheet. The final resulting wrinkling load is dependent on the following condition:

$$t_c < 1.817 t_f \left(\frac{E_f E_c}{G_{xz}^2} \right)^{\frac{1}{3}} \tag{3.3}$$

Where:

$$E_f = \frac{1}{t_f} \left(A_{11,f} - \frac{A_{12,f}^2}{A_{22,f}} \right)$$

$$E_c: \text{out} - \text{of} - \text{plane core stiffness}$$

$$G_{xz}: \text{core shear stiffness}$$

If the condition given in (3.3) is true, the core is relatively thin and completely deforms trough the thickness and the symmetric wrinkling load is given by equation (3.4).

$$N_{x,swr} = 0.816 \sqrt{\frac{E_f E_c t_f^3}{t_c}} + G_{xz} \frac{t_c}{6} \tag{3.4}$$

Else, a part of the core deforms through the thickness and the failure load is given by equation (3.5).

$$N_{x,swr} = 0.91 t_f \left(E_f E_c G_{xz} \right)^{\frac{1}{3}} \tag{3.5}$$

It should be taken into account that from the resulting equations (3.4) and (3.5), waviness of the face sheet is not taken into account. This waviness is normally present when the core and sheet material are co-cured, which is a typical manufacturing method in wind turbine blades. This will affect the performance of the panel against wrinkling and other methods have been proposed using knockdown factors. By using the above formulation, it should therefore be taken into account that results could be unconservative.
For the symmetric wrinkling, a more conservative results is therefore formulated by equation (3.6), which has been found in [14] and takes waviness of the face sheet into account. This more conservative formulation will replace equation (3.5) in the analysis of the sandwich panel in the next chapter.

$$N_{x,swr} = 0.43 t_f \left(E_f E_c G_{xz} \right)^{\frac{1}{3}} \tag{3.6}$$

Asymmetric wrinkling

The same approach, but using a different approximated displacement function to satisfy the boundary conditions is used to obtain the wrinkling load of asymmetric wrinkling. The following condition provides the critical load for wrinkling:

$$t_c < 3 t_f \left(\frac{E_f E_c}{G_{xz}^2} \right)^{\frac{1}{3}} \tag{3.7}$$

If the condition stated in equation (3.7) is true, the core deforms completely through the thickness and the asymmetric wrinkling load follows from equation (3.8).

$$N_{x,aswr} = 0.59 t_f^{\frac{3}{2}} \sqrt{\frac{E_f E_c}{t_c}} + 0.378 G_{xz} t_c \tag{3.8}$$

Or else, the core only deforms partially and the wrinkling load is given by equation (3.9).

$$N_{x,aswr} = 0.51 t_f \left(E_f E_c G_{xz}\right)^{\frac{1}{3}} + \frac{G_{xz} t_c}{3} \tag{3.9}$$

As well as for symmetric wrinkling, waviness of the face sheets along the surface of the core is not taken into account in the formulation of equation (3.8) and (3.9). However, since there are many analytical methods proposed in determining the wrinkling load, the decision is made to evaluate the low-weight sandwich benchmark design by using equations (3.4), (3.6), (3.8) and (3.9) in section 3.5.

3.2.3. Sandwich core crimping

Core crimping of a sandwich panel mainly occurs when the shear stiffness of the core is low. Kassapoglou [14] describes the method for this failure mode in chapter 10 of his book. The failure mode could be compared to buckling of the panel with zero wavelength and is schematically shown in figure 3.5.

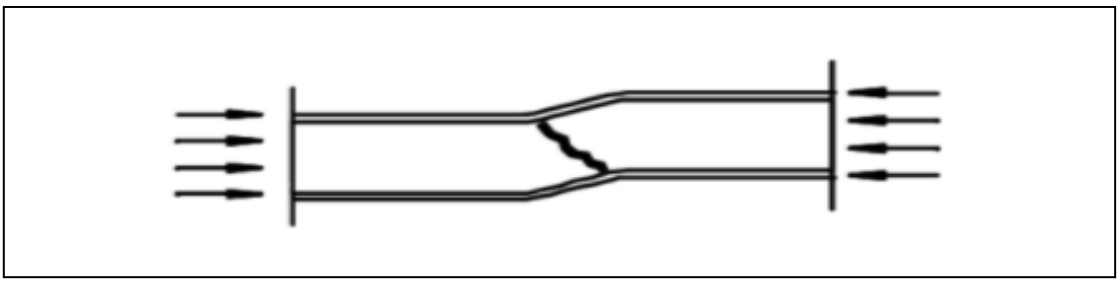

Figure 3.5: Example of core crimping of a sandwich panel under compressive loading

Considering the zero wavelength, equation (3.2) could be analysed by setting the length a of the panel to zero. In this case, it should be noted that $N_{x,gb}$ given by equation (3.1) goes to infinity and results in:

$$N_{x,cc} = \frac{\infty}{1 + \frac{\infty}{t_c G_c}} \tag{3.10}$$

Applying l'Hopital's rule to equation (3.10), the critical core crimping load is given by equation (3.11).

$$N_{x,cc} = \frac{1}{\frac{1}{t_c G_c}} = t_c G_c \tag{3.11}$$

Where t_c and G_c are mentioned in section 3.2.1. It can be noted from the formulation that a higher core crimping failure load is found by introducing a higher thickness of the core or by introducing a core material with higher shear stiffness. This increase of shear stiffness is however found to have an almost linear relationship with increase in density [24] and thereby resulting in increased weight of the structure.

3.2.4. First ply failure

When applying a compressive load to the sandwich panel, a Tsai-Wu [31] and a Tsai-Hill [32] failure criterion are used to see if material failure is not critical for the design. The procedure of the failure

analysis is described in appendix B. Both criteria are repeated here for convenience, where the Tsai-Hill criterion is given by:

$$\frac{\sigma_1^2}{X^2} - \frac{\sigma_1\sigma_2}{X^2} + \frac{\sigma_2^2}{Y^2} + \frac{\tau_{12}^2}{S^2} = 1 \tag{3.12}$$

And the Tsai-Wu criterion by:

$$\frac{\sigma_1^2}{X^t X^c} + \frac{\sigma_2^2}{Y^t Y^c} - \sqrt{\frac{1}{X^t X^c Y^t Y^c}}\sigma_1\sigma_2 + \left(\frac{1}{X^t} - \frac{1}{X^c}\right)\sigma_1 + \left(\frac{1}{Y^t} - \frac{1}{Y^c}\right)\sigma_2 + \frac{\tau_{12}^2}{S^2} = 1 \tag{3.13}$$

3.3 Numerical analysis

This section describes the numerical analysis of a sandwich panel by finite element models, using Marc Mentat software. The goal of this section is to find the mesh density for the sandwich panel, where convergence of results is reached. This convergence will be found for different types of element strategies, where the following design variables are used as an example sandwich panel in this whole section:

- Face sheet layup: $[+/-45]_2$
- Core thickness: 19 [mm]
- Length a: 866 [mm]
- Width b: 500 [mm]

The boundary conditions are modelled with simply supported conditions all around the panel, which are schematically drawn in figure 3.6. The out-of-plane displacements w are zero all around the panel. On the left-edge, displacements in x and y direction are also zero. The load is applied to the right edge, where the displacement in y direction is also set to zero.

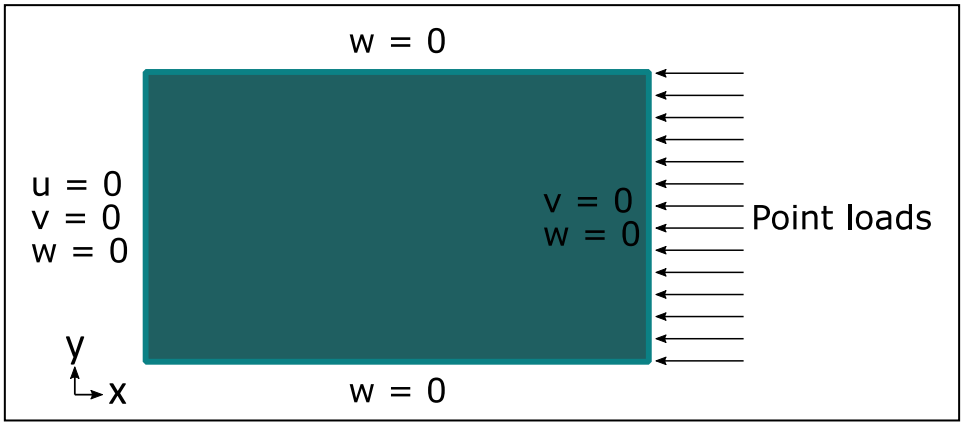

Figure 3.6: Boundary conditions of the sandwich numerical model

An eigenvalue buckling analysis is performed with three different modelling strategies to find the lowest failure load and its mode of failure. Subsection 3.3.1 described a 2D model for the layup of face sheets and foam core in one shell element. In subsection 3.3.2, the foam core is modelled by 3D solid elements and the face sheets by compatible shell elements. The third model, described in subsection 3.3.3 uses higher order elements and also uses 3D solid elements for the foam core and shell elements for the face sheets. A comparison of the three different models is made regarding computational cost, convergence rate and accuracy in subsection 3.3.4.
Heder [27] studied sandwich panel buckling with numerical models using different boundary conditions, which contributed to the study performed in this section.

3.3.1. Element Type 75 (Shell)

One of the simplest ways of modelling the sandwich panel is by using a quadrilateral shell element, which is referred to as a type 75 element in Marc Mentat. The element is shown in figure 3.7, where every one of the four nodes has 3 translational and 3 rotational degrees of freedom.

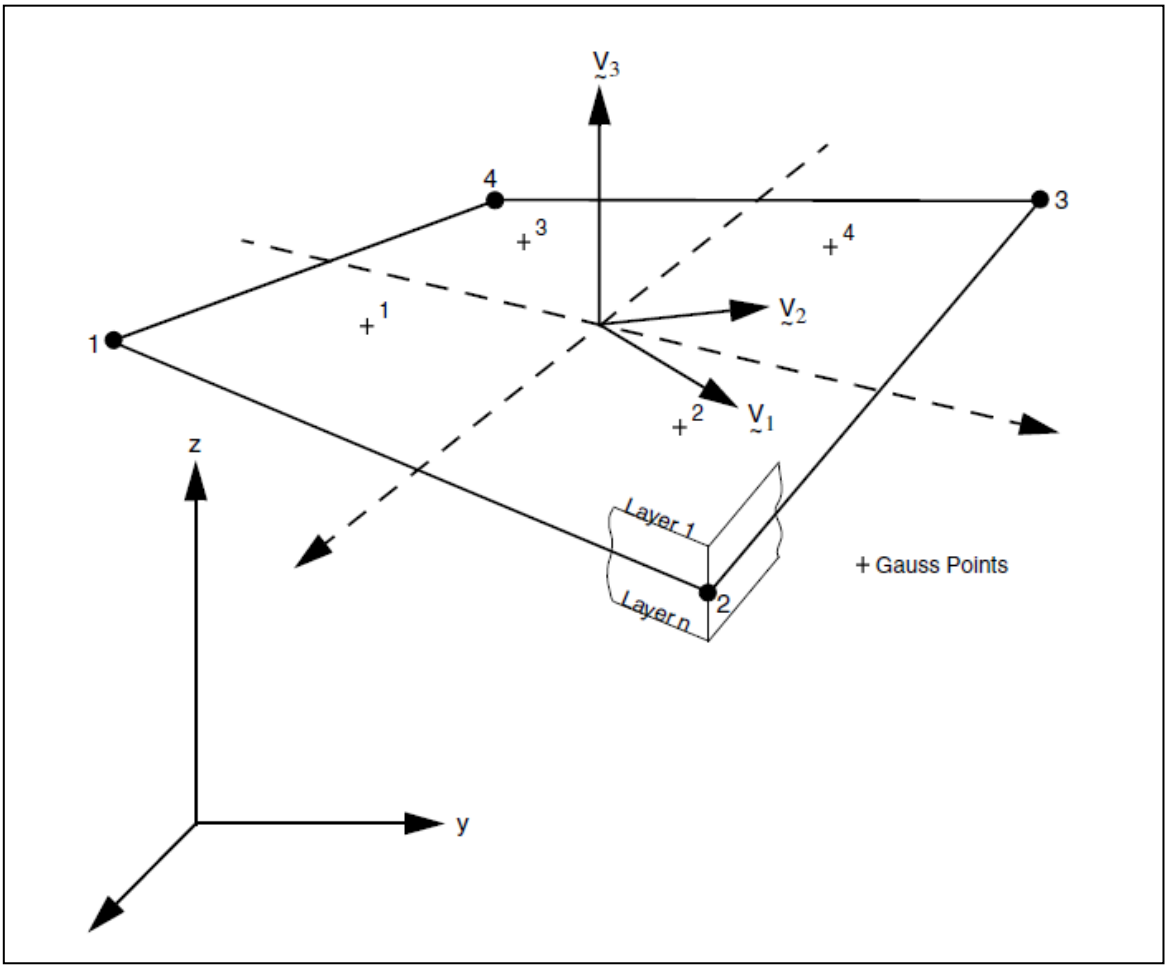

Figure 3.7: Element type 75, bilinear thick-shell element [26]

From the presented analytical solution in the previous subsection, it was shown that transverse shear has a significant effect on the actual behaviour of the sandwich panel. Therefore, a finite element analysis will be performed with transverse shear effect taken into account. By using the “enhanced transverse shear” option in the job properties of Marc Mentat, a parabolic distribution of the shear strain trough the thickness will be introduced in this particular model. In the default case, this would have been modelled with a constant shear strain distribution.

A 1 N compressive load will be applied to each node at the right edge of the sandwich panel, where after the eigenvalues are found using the buckling analysis in Marc Mentat. The product of the total applied load and the lowest found eigenvalue determines the first buckling load of the structure. The buckling mode is graphically presented by Marc Mentat and is related to the eigenvector of the corresponding eigenvalue.

The resulting buckling loads for different mesh densities are presented graphically in figure 3.8, where it will be considered that a converged solution is found when the buckling load is smaller than a factor 1.01 times the critical load found from the most refined mesh. This situation occurs for 680 elements (or an element size of 25 mm). The exact values indicated with green dots can be found in appendix C.

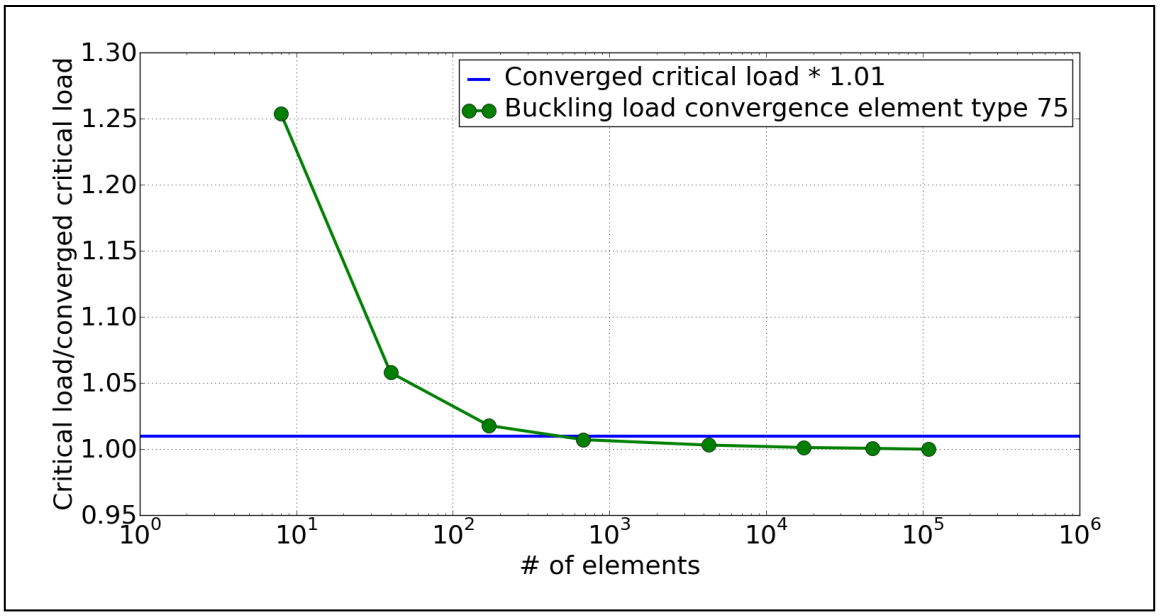

Figure 3.8: Convergence of the buckling load, using element type 75

3.3.2. Core type 7 (brick) and face sheet type 75 (shell)

Another possible way to model the behaviour of the sandwich panel is when the foam core is modelled by using 3D solid elements, as shown in figure 3.9. The face sheets are modelled by type 75 elements, which are compatible with the solid element.

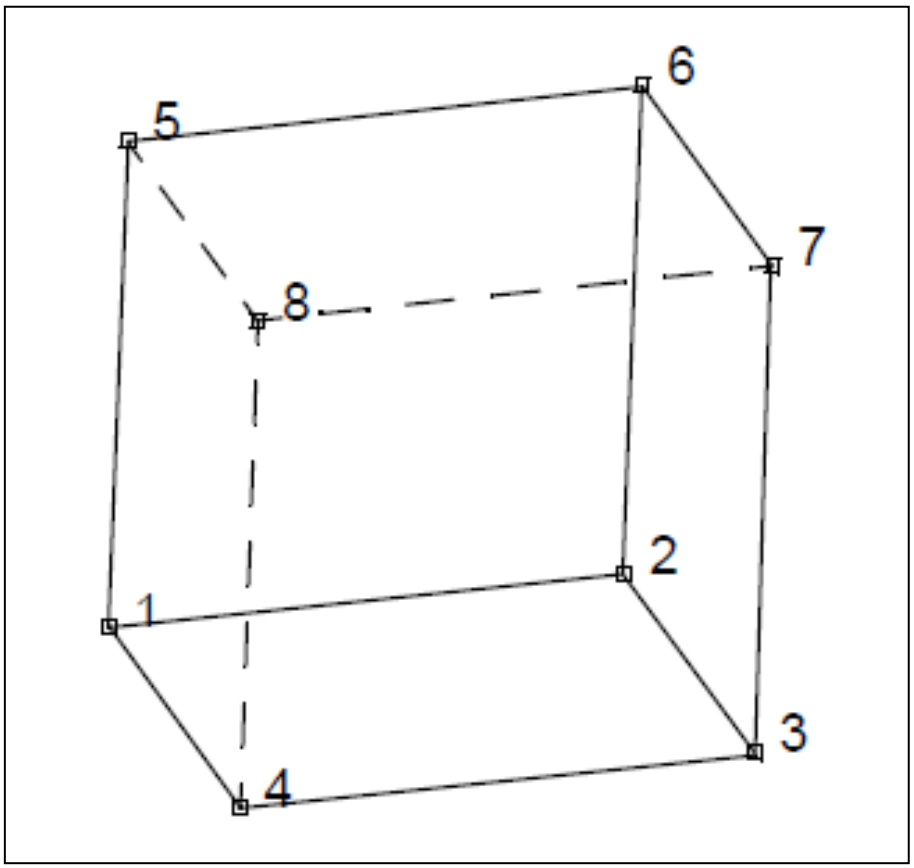

Figure 3.9: Element type 7, eight-node brick element [26]

Again, an eigenvalue analysis is performed. Since the panel is modelled in 3D, transverse shear effects are expected to be included in the analysis. The found buckling loads for increasing mesh densities are graphically presented in figure 3.10. The values indicated in the graph by the green dots can be found in appendix C.

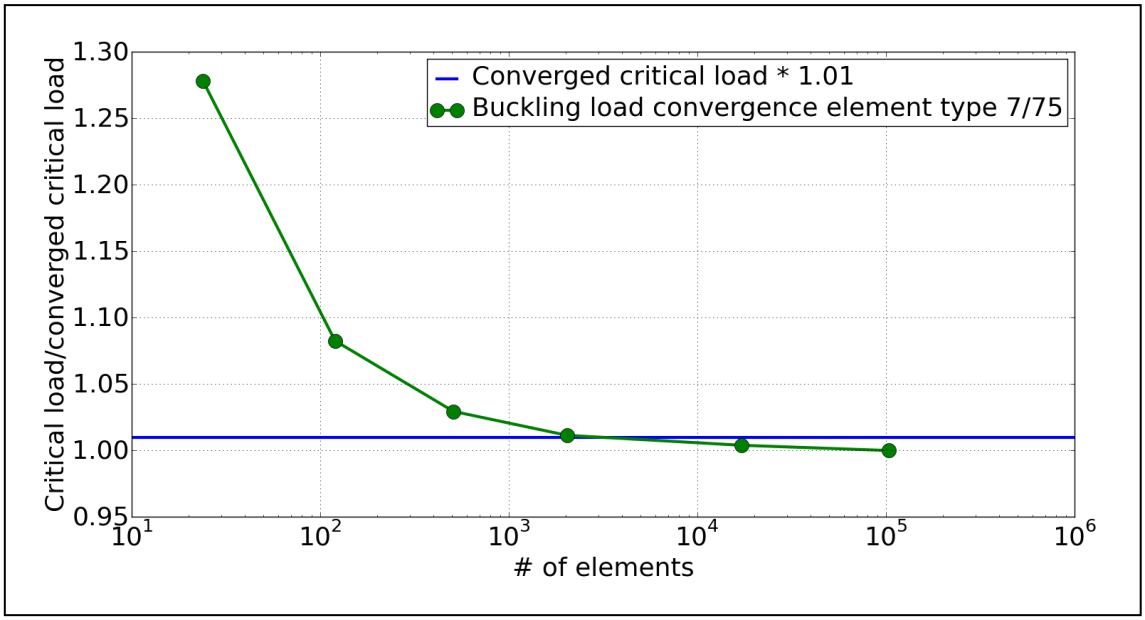

Figure 3.10: Convergence of the buckling load, using element type 7 and 75

From the graph, it can be seen that by using a mesh of 17200 elements (or element size of 10 mm), the buckling load is within a factor of 1.01 times the critical load with the most refined mesh.

3.3.3. Core type 21 (brick) and face sheet type 22 (shell)

The third and final model used to analyse the sandwich panel is build from higher order 3D solid elements and higher order shell elements, shown in figure 3.11. Having 20 and 8 nodes respectively, the elements are more expensive than the ones used so far, but a lower number of elements is expected to be used in order to obtain a converged solution.

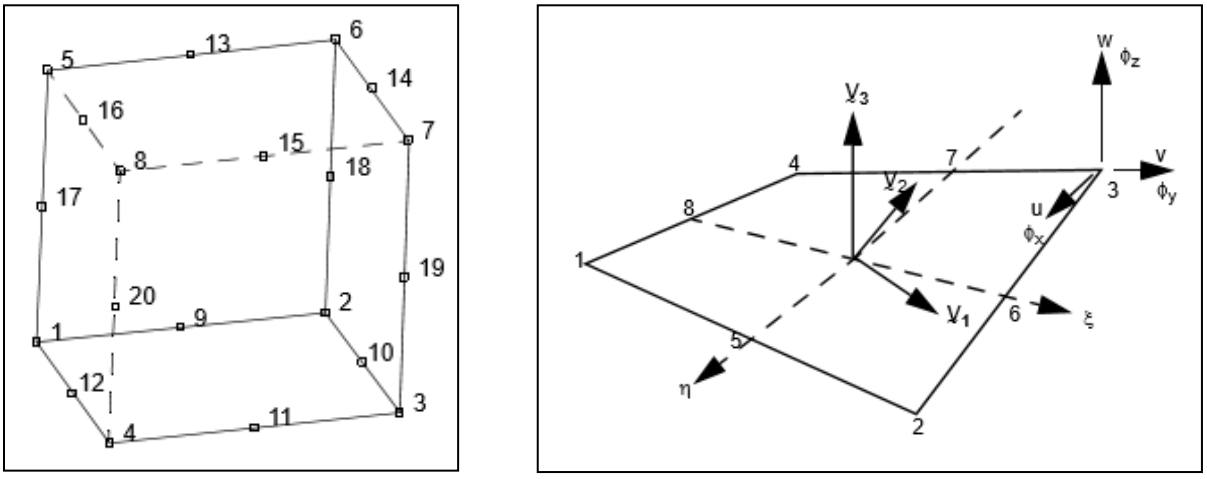

Figure 3.11: Element type 21, twenty-node brick element and element type 22, eight-node thick shell element [26]

The buckling eigenvalue analysis is performed for a range of element densities, of which the results are graphically presented in figure 3.12 below. The values of the data-points can be found in

appendix C. A fast convergence can be recognized for a total of 756 elements (element size of 40 mm), where the expected buckling load is within a factor of 1.01 times the critical buckling load of the most refined mesh. The graph also shows an increase in the expected buckling load from 20 mm till 15 mm. This could be a result of the model having an extra solid element through the thickness of the core, while decreasing the element size. This changes the ratio between the number of elements for the core and face sheet, possibly explaining the oscillation around the critical load.

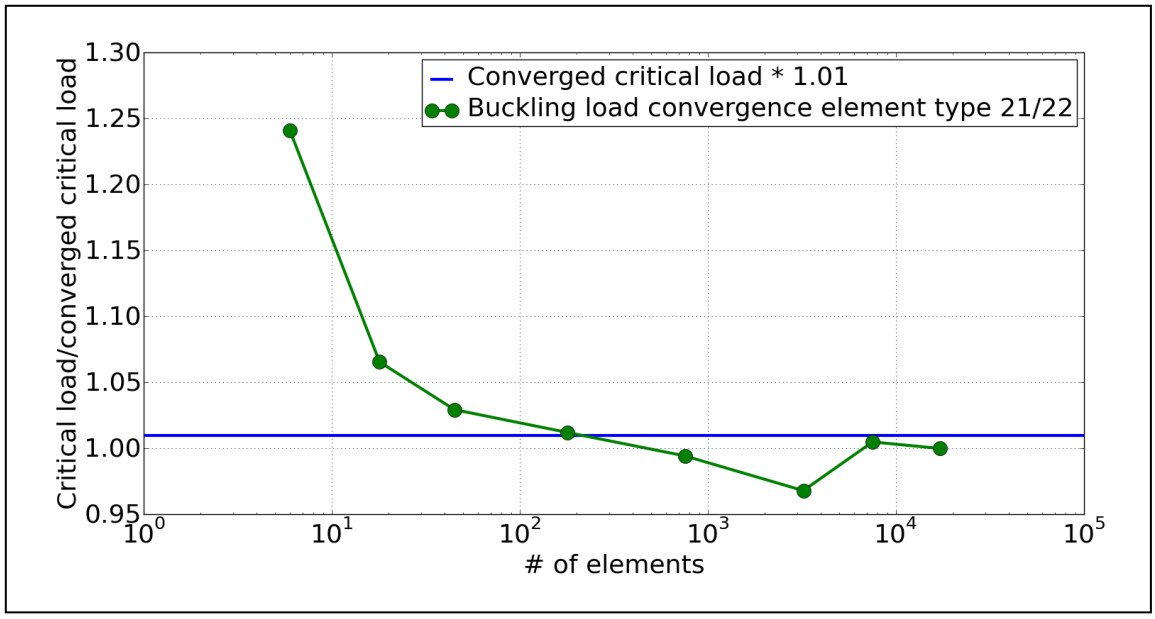

Figure 3.12: Convergence of the buckling load, using element type 21 and 22

3.3.4. Comparison of the numerical models

In order to compare the three different models presented so far, all convergence graphs are presented in figure 3.13, where the expected buckling load is given on the y-axis and the number of used elements shown on the x-axis.

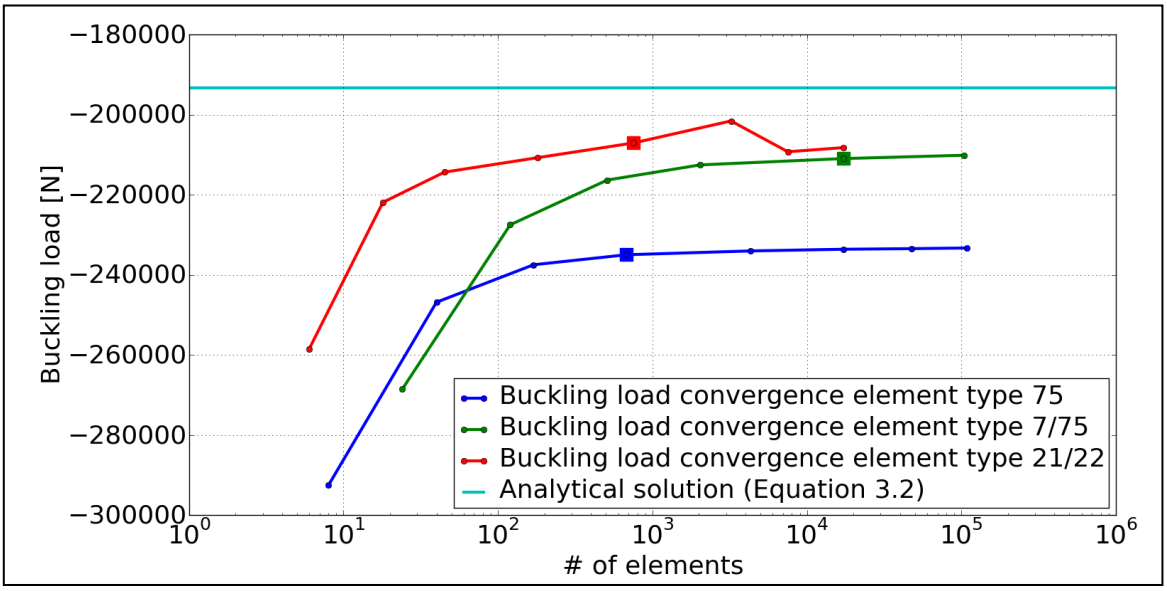

Figure 3.13: Comparison of the convergence of the numerical models described in subsection 3.3.1 (blue), 3.3.2 (green) and 3.3.3 (red)

From the figure shown, it can be seen that both the model with element type 75 converges almost as fast as the model using element type 21 and 22, while the latter is computationally much more expensive. However, comparing both solutions with the analytically expected buckling load, the model using element types 21 and 22 gives a solution which is in better agreement.
The model with element types 7 and 75 converges for a larger number of elements. The model also shows a smooth converging line towards approximately the same solution as is predicted by the model with element type 21 and 22.
The solutions, which are considered to be converged are indicated with a square in figure 3.13 and for each of those solutions, the computational time of the analysis is also found. The same CPU was used to solve the analysis, with the following results:

- Element type 75: 2 seconds
- Element type 7/75: 23 seconds
- Element type 21/22: 3 seconds

3.4 Verification of models

This section will focus on comparison between the analytical and numerical models. The focus is hereby on the global buckling failure mode of the sandwich panel. The analytical solution for this failure mode was given by equation (3.2). The expected global buckling load is analysed for five different designs shown in table 3.1, where the first design was presented in the previous subsection. The other four designs were chosen based on the goal to verify a range of possible design options. The layup of the face sheet ranges from 2 till 6 layers of biaxial glass-fibre, while increasing the core thickness up to 50 mm for the fifth design. An exception is made with the fourth design, where the core thickness is reduced relative to an increase of the face sheet thickness. This is done to verify the models for a thick face sheet with a relatively thin core as well.
For each analytically determined load, the different numerical models outlined in the previous subsection are used to calculate the expected buckling load of the particular designs. The obtained buckling loads are compared to the analytical solution in figure 3.14. The solution is obtained by using the mesh density, which was concluded to give a converged solution for each of the models. For sandwich designs 3, 4 and 5, no solution was obtained from the model with element types 7 and 75.

Table 3.1: Sandwich designs for verification of analytical and numerical models

	Sandwich 1	Sandwich 2	Sandwich 3	Sandwich 4	Sandwich 5
Facesheet layup	$[+/-45]_2$	$[+/-45]_3$	$[+/-45]_4$	$[+/-45]_5$	$[+/-45]_6$
Core thickness [mm]	19	20	40	25	50

The numerical model build from element types 21 and 22 will be used for verification of the determined low-weight designs in the next chapter, based on the following reasons:

- Computationally almost as fast as the element type 75 model and faster than the element type 7/75 model
- Global buckling prediction gives the most accurate solutions compared to the analytically determined solution, where the difference was the largest (10.2%) for sandwich design 4
- The model with element type 7/75 did not give valid results for thicker sandwich designs, making that particular model unusable

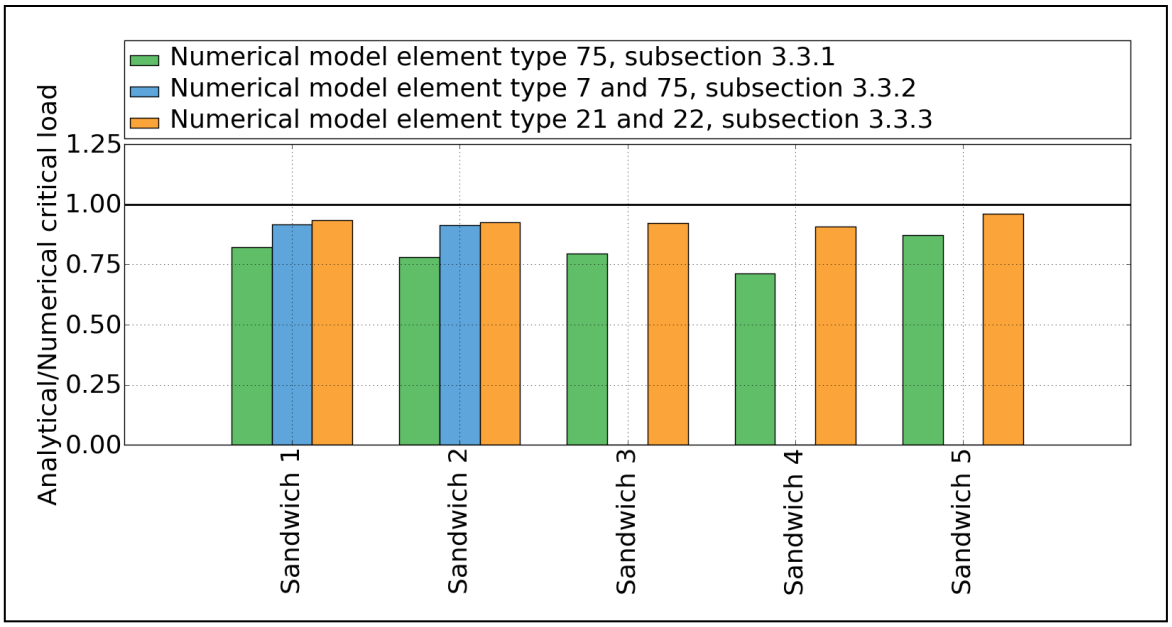

Figure 3.14: Verification of analytical global buckling solutions by numerical models

3.5 Low-weight sandwich panels

This section describes the way in which low-weight sandwich designs are found in order to make a comparison with the orthogrid structure. The brute force analysis scheme is presented in figure 3.15.

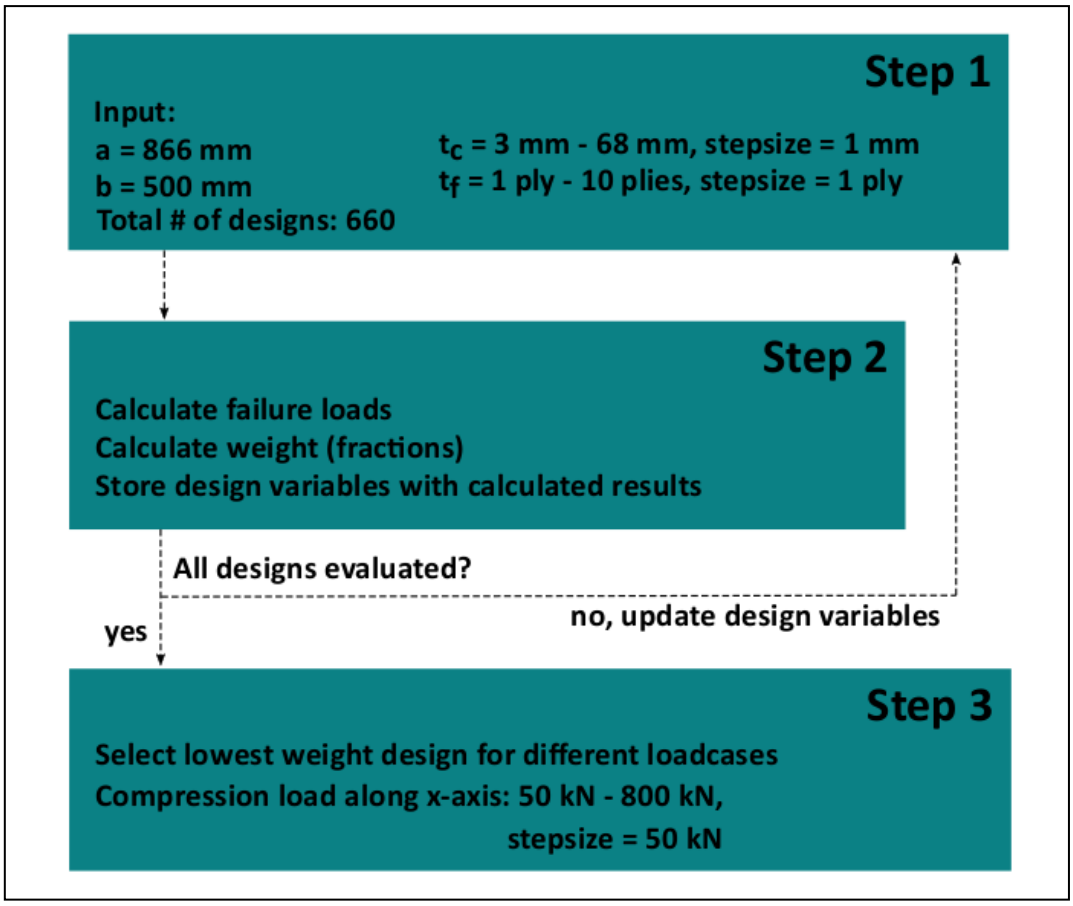

Figure 3.15: Brute force analysis scheme for low-weight sandwich panels

Step 1 of the analysis describes the different input design variables. The core thickness is available in a range from 3 mm to 68 mm in steps of 1 mm. To obtain a panel design, which is comparable to a layup used in the trailing edge of a wind turbine blade, a stacking of a multiple of [+/-45]-degree plies is used.
Step 2 calculates the failure modes and the weights of all different design variable combinations. Since the numerical analysis for global buckling was in sufficiently good agreement with the analytical solutions, the analytical methods are used in finding an optimized design for the benchmark sandwich panel. For every design, all the mentioned failure modes from section 3.2 are taken into account.
After all calculations have been made, the lowest weight design is chosen for a range of design loads in step 3. The design loads range from a compressive load of 50 kN up to and including a load of 800 kN, with a step size of 50 kN.
The resulting weight values for the found sandwich panels are shown in figure 3.16, where the combined weight of face sheet and foam core material is indicated by the blue triangles. The weight fraction of the face sheet and core are shown as percentages by the green stars and yellow circles respectively. From the figure, it can be seen that the foam core material is found to be around 20 to 25% of the total weight of the panel in this particular design and material combination.

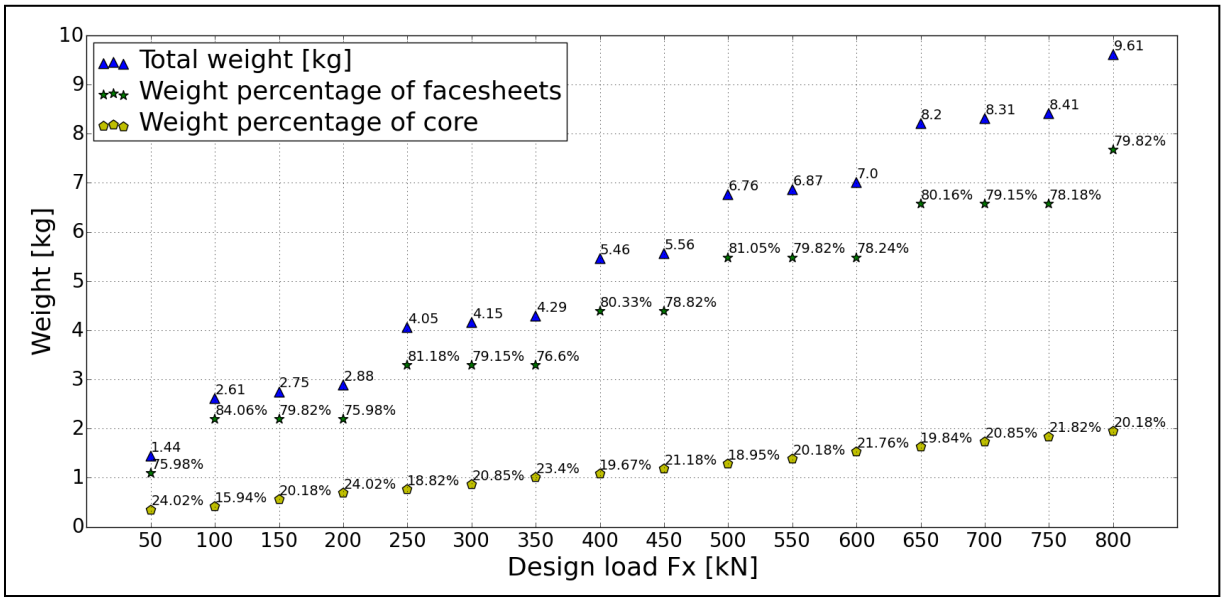

Figure 3.16: Low-weight sandwich panel weight(fractions) per design load

The design variables related to the found low-weight designs are given in table 3.2. The design load is shown in the first column. The layup of one of the two face sheets and the thickness of the foam core can be found in the second and third column respectively. The corresponding weight, which is based on the material densities given in appendix A, are repeated in the fourth column.

Table 3.2: Design variables for low-weight sandwich panels with different design loads

Design load [kN]	Layup face sheet	Core thickness [mm]	Weight [kg]
50	$[+/-45]_1$	10	1.442
100	$[+/-45]_2$	12	2.608
150	$[+/-45]_2$	16	2.746
200	$[+/-45]_2$	20	2.885
250	$[+/-45]_3$	22	4.050
300	$[+/-45]_3$	25	4.154
350	$[+/-45]_3$	29	4.293
400	$[+/-45]_4$	31	5.458

450	$[+/-45]_4$	34	5.562
500	$[+/-45]_5$	37	6.762
550	$[+/-45]_5$	40	6.866
600	$[+/-45]_5$	44	7.004
650	$[+/-45]_6$	47	8.204
700	$[+/-45]_6$	50	8.308
750	$[+/-45]_6$	53	8.412
800	$[+/-45]_7$	56	9.612

The prediction of all the different failure modes, corresponding to the low-weight designs are shown in figure 3.17. It can be seen that global buckling, face sheet wrinkling and core crimping loads are predicted relatively close to each other. According to the analysis, material failure will not be expected under the applied compressive loads.

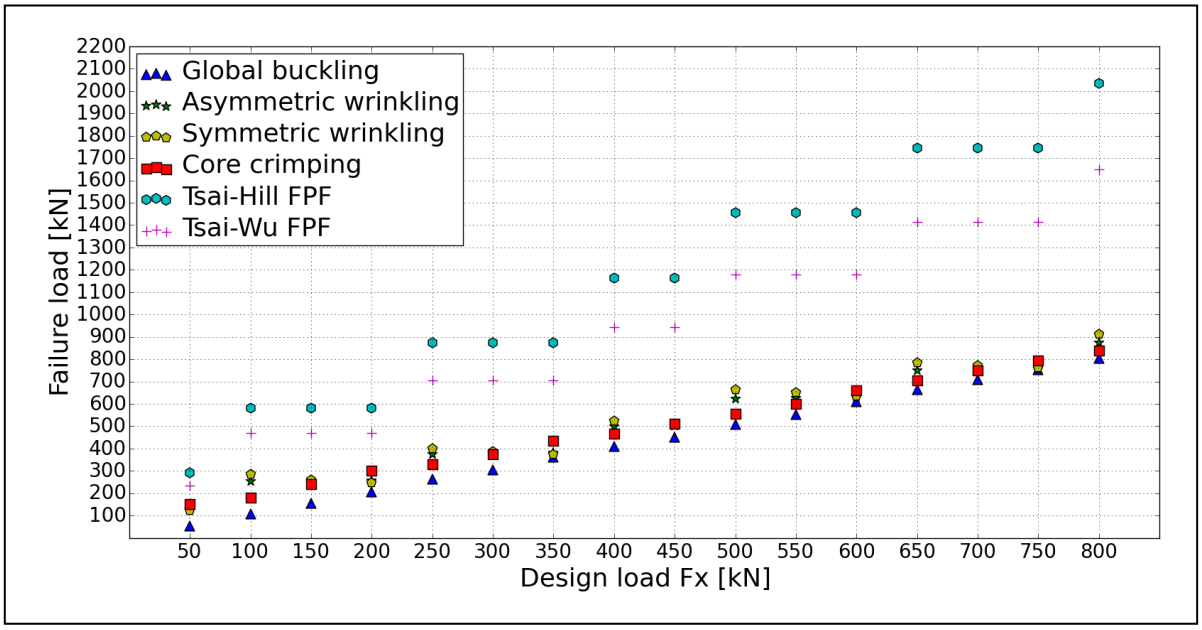

Figure 3.17: Different failure loads for the low-weight sandwich designs

From figure 3.17, it can be seen that in all cases, global buckling is determined to be the first failure mode to occur under the applied compressive load. Using the 3D numerical model with element types 21 and 22, the obtained analytical global buckling loads are verified, for which the comparison is shown in table 3.3. The first column indicates the design load, with the analytically determined global buckling load in the second column. The third column shows the numerical solution for the global buckling load, where also the eigenvalue multiplied by the applied load is written in between brackets. The fourth column gives the differences between the analytical and numerical solution and the last column indicates the number of buckling number of half waves expected during by the numerical model.

From the results, it is shown that the numerical model predicts a failure load within 8% of the critical load predicted by the analytical model for all cases. The number of buckling half waves predicted by the numerical model is however increasing up to a number of 6 for the case of 450 kN. This difference with the analytical model could be explained by the foam core not being taken into account in equation (3.1), where m determined the number of half waves. Further study or experiments should be performed to explain or validate the occurrence of multiple half waves on the numerical model.

Table 3.3: Verification of low-weight sandwich designs by numerical eigenvalue analysis with type 21 and 22 elements

Design load [kN]	Analytical solution x_1 [N]	Numerical solution from eigenvalue analysis x_2 [N] (eigenvalue * applied load)	Difference [%] $\left(\frac{x_2-x_1}{x_2} * 100\right)$	Failure mode from numerical model
50	53311	49965 (0.07931*630000)	-6.70%	2 half waves
100	106235	106722 (0.1694*630000)	+0.46%	2 half waves
150	154950	162855 (0.2585*630000)	+4.85%	2 half waves
200	206410	222012 (0.3524*630000)	+7.03%	3 half waves
250	261425	281799 (0.4473*630000)	+7.23%	4 half waves
300	303474	323694 (0.5138*630000)	+6.25%	5 half waves
350	360236	377244 (0.5988*630000)	+4.51%	5 half waves
400	407565	425817 (0.6759*630000)	+4.29%	5 half waves
450	451180	465822 (0.7394*630000)	+3.14%	6 half waves
500	507439	533232 (0.8464*630000)	+4.84%	5 half waves
550	551561	568933 (0.5633*1010000)	+3.05%	5 half waves
600	610542	621251 (0.6151*1010000)	+1.72%	5 half waves
650	663795	697102 (0.6902*1010000)	+4.78%	5 half waves
700	708267	736795 (0.7295*1010000)	+3.87%	5 half waves
750	752789	776084 (0.7684*1010000)	+3.00%	5 half waves
800	803976	860318 (0.8518*1010000)	+6.55%	5 half waves

4. Orthogrid Structure

As a potential replacement of the sandwich panel on the wind turbine trailing edge, the grid stiffened type of structure is proposed. This chapter will discuss the orthogrid type of structure, where the different design variables are explained first in section 4.1. Analytical analysis for different types of failure modes is discussed in section 4.2. A numerical model for this type of structure is set up in section 4.3, using shell elements. Verification is performed by a parametric study, where analytical and numerical methods are compared in section 4.4. The goal of this chapter is to give a clear overview of the available methods to determine the behaviour of an orthogrid stiffened panel and obtaining low-weight designs in section 4.5 with the presented models.

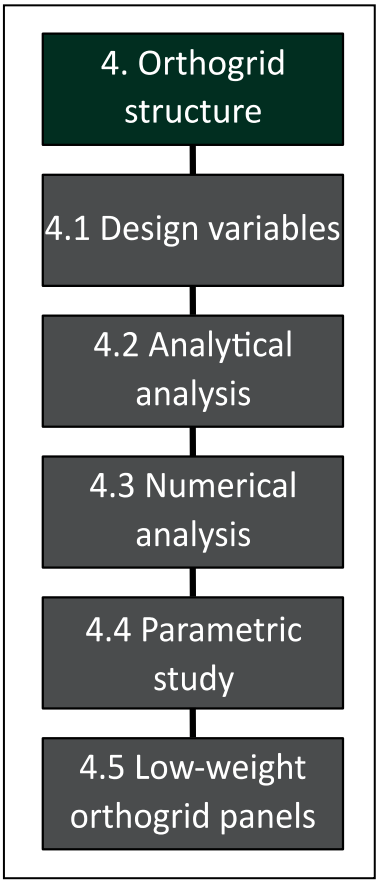

Figure 4.1: Flow chart chapter 4

4.1 Design variables

One specific type of grid stiffened structure is the orthogrid, which consists of orthogonally positioned stiffeners as is shown in figure 4.2. Xu et al. [6] describe a complete panel in terms of a unit cell vector S, where a number is added as a subscript and refers to a certain direction of the stiffener. S_3 and S_5 refer to the longitudinal stiffeners along length a of the panel and S_4 and S_6 refer to the stiffeners in transverse direction along width b of the panel. a_0 and b_0 indicate the length and width of a single unit cell respectively. For clarity, the components S_1 and S_2 would refer to diagonal stiffeners, which are not present at the orthogrid stiffened panel. The example panel given in figure 4.2 would have the unit cell vector indicated by equation (4.1).

$$S = \begin{bmatrix} S_1 \\ S_2 \\ S_3 \\ S_4 \\ S_5 \\ S_6 \end{bmatrix} = \begin{bmatrix} 0 \\ 0 \\ 1 \\ 1 \\ 0.8333 \\ 0.75 \end{bmatrix} \tag{4.1}$$

The given example shows 2 unit cells along the x-axis, resulting in 2 times S_4 and 4 times S_6. Substituting for S_4 and S_6 results in a total of 5 stiffeners, which is also drawn in figure 4.2. The same applies for 1.5 unit cells along the y-axis. This unit cell vector is used during the analytical calculation of the global buckling load in the next section.

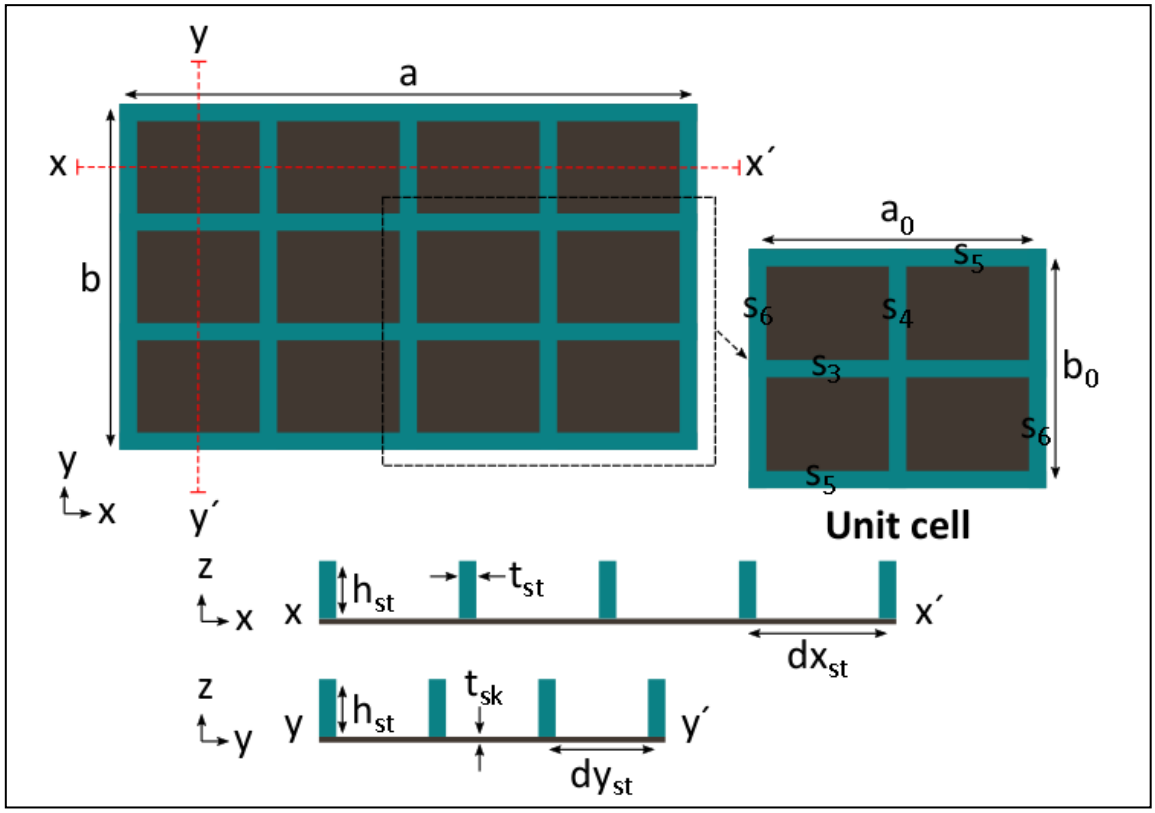

Figure 4.2: Design variables of an orthogrid structure

The design of the panel is further described by the following different variables, which are also shown in figure 4.2.

$$t_{sk}: \text{thickness of the skin [mm]} \tag{4.2}$$

$$t_{st}: \text{thickness of the stiffener [mm]} \tag{4.3}$$

$$h_{st}: \text{height of the stiffener [mm]} \tag{4.4}$$

$$dx_{st}: \text{spacing between two transverse stiffeners [mm]} \tag{4.5}$$

$$dy_{st}: \text{spacing between two longitudinal stiffeners [mm]} \tag{4.6}$$

The panel length a and width b are fixed to 866 mm and 500 mm respectively. For the skin, Saertex-812g biaxial glass-fibre layers are used, for which the properties are described in appendix A. The stiffeners will be manufactured by using unidirectional glass-fibre roving, of which the properties are assumed to be equal to a unidirectional glass-fibre fabric also described in appendix A.

4.2 Analytical analysis

Analytical methods found in literature or produced from theory are outlined in this section. Analysis of the global buckling of an orthogrid panel will first be discussed in subsection 4.2.1. The individual stiffeners within the grid could also locally buckle (crippling). A suitable displacement function is used in combination with a minimization of total potential energy to obtain the particular failure load and is described in subsection 4.2.2. The buckling of local skin segments between the stiffeners is called intracellular buckling. Methods to determine this particular failure load for rectangular sections are described in subsection 4.2.3. The separation of skin and stiffener is assumed to be a post buckling mode of failure and is briefly described in subsection 4.2.4. First ply failure within the panel is obtained by applying a Tsai-Wu, Tsai-Hill and maximum stress failure criterion in critical zones and is described in subsection 4.2.5.

4.2.1. Global buckling

Xu et al. [6] describe a smeared stiffener method to determine the global buckling strength of a grid stiffened panel. The method shows accurate predictions of the buckling strength of an orthogrid stiffened panel, compared to a finite element analysis. Since there was no success in reproducing the given values from the article exactly, the complete derivation as it was stated in the article of Xu et al. can be found in appendix D. The method as it is described in the appendix is coded and used during the rest of this project.

A brief description of the method is given here. The equivalent stiffness matrix of the grid stiffened panel should be found based on the unit cell configuration, which is a superposition of the separate skin and stiffener stiffness contributions to the ABD-matrix:

$$\begin{bmatrix} N \\ M \end{bmatrix} = \begin{bmatrix} A_{sk} + A_{st} & B_{sk} + B_{st} \\ B_{sk} + B_{st} & D_{sk} + D_{st} \end{bmatrix} \begin{bmatrix} \varepsilon_0 \\ \kappa \end{bmatrix} \tag{4.7}$$

Assuming simply supported boundary conditions, where displacement and moments are zero at the edges of the panel, the assumed displacement function is described by:

$$w(x,y) = \sum_{m=1}^{M} \sum_{n=1}^{N} C_{mn} \sin\left(\frac{m\pi x}{a}\right) \sin\left(\frac{n\pi y}{b}\right) \tag{4.8}$$

The Ritz method is used in combination with a minimization of the total potential energy. The derivative of the total potential energy is set equal to zero, resulting in the following equation to be solved:

$$\begin{aligned} \frac{\partial \Pi}{\partial \mathrm{C_{mn}}} = C_{mn} \Bigg[& m^4 D_{11} + \frac{2m^2 n^2 a^2}{b^2} D_{12} + \frac{n^4 a^4}{b^4} D_{22} + \frac{4m^2 n^2 a^2}{b^2} D_{66} - \frac{m^2 a^2}{\pi^2} N_x \\ & - \frac{n^2 a^4}{\pi^2 b^2} N_y \Bigg] \\ & - C_{ij} \Bigg[\sum_{i=1}^{M} \sum_{j=1}^{N} \left(\frac{64 m^2 a}{\pi^2 b} D_{16} + \frac{64 n^2 a^3}{\pi^2 b^3} D_{26} \right. \\ & \left. + \frac{32 a^3}{\pi^4 b} N_{xy} \right) \left(\frac{mnij}{(m^2 - i^2)(n^2 - j^2)} \right) \Bigg] = 0 \end{aligned} \tag{4.9}$$

From which the term with the summation signs only give a non-zero contribution when:

$$m \pm i = odd \quad AND \quad n \pm j = odd \tag{4.10}$$

The above results in a generalized eigenvalue problem and is given by:

$$\Big[[E] - N_{x,y,xy} [H] \Big] \{C_{mn}\} = \{0\} \tag{4.11}$$

In which:

$[E]$: matrix with all terms obtained from the equivalent D − terms

$[H]$: matrix containing all values related to the applied forces N_x, N_y and N_{xy}

$\{C_{mn}\}$: will be equal to the eigenvector after evaluation

$N_{x,y,xy}$: eigenvalue

The eigenvalue problem is solved by a Python script called scipy.linalg.eig(E, b=H). The resulting eigenvalues and eigenvectors are substituted in equation (4.11) to verify the validity of the used Python script. The largest error found within the resulting zero vector was negligible, which means the solution from the eigenvalue analysis will be considered accurate enough.
To verify the method described by Xu et al. and given in appendix D, the results will be compared with a numerical model in section 4.4, where a parametric study is performed on the orthogrid structure.

4.2.2. Stiffener crippling

Another typical failure mode of a grid stiffened structure is the local buckling or crippling of a stiffener. In order to obtain a solution for this failure mode, an exact solution for a plate under compression with three edges simply supported and one edge free is described in this subsection.
Meink et al. [13] described a displacement function for the stiffener which is used in combination with the method of minimum potential energy. A full derivation of the method for the critical stiffener crippling load is described in appendix E. Equation (4.12) is found as a solution, which is in good agreement to an exact solution found in chapter 6 of [14].

$$N_{x,sc} = D_{11}\left(\frac{m^2\pi^2}{{dx_{st}}^2}\right) + D_{12}\left(\frac{0.190}{{h_{st}}^2}\right) + D_{22}\left(\frac{0.0265{dx_{st}}^2}{m^2\pi^2{h_{st}}^4}\right) + D_{66}\left(\frac{12.285}{{h_{st}}^2}\right) \qquad (4.12)$$

When the crippling load is found, it should be related to a total force applied to the panel. This is done by relating the individual membrane stiffness of a stiffener to the equivalent membrane stiffness of the complete panel. The total force, which causes stiffener crippling is then described by equation (4.13).

$$F_{tot} = F_i * \frac{\sum_{j=1}^{N}(EA)_j}{(EA)_i} \qquad (4.13)$$

Where:

$$F_i = N_{x,sc} * h_{st} \qquad (4.14)$$

$$i: \text{single stiffener} \qquad (4.15)$$

$$N: \text{number of structural members of the cross} - \text{section} \qquad (4.16)$$

Since the panel will be tested in uni-axial compression, the transverse stiffeners are not analyzed for crippling.

4.2.3. Intracellular buckling

The intracellular buckling load is estimated by considering the skin between the stiffeners as a small simply supported plate. It is assumed that the bending/twisting coupling terms D_{16} and D_{26} are very low due to symmetry of the layup and could be neglected. The buckling load under uni-axial

compression is then easily determined by applying the method of minimum potential energy and can be described by equation (4.17) [14]:

$$N_{x,ic,ss} = \frac{\pi^2}{{dx_{st}}^2}\left[D_{11}m^2 + 2(D_{12} + 2D_{66})(AR)^2 + D_{22}\frac{(AR)^4}{m^2}\right] \quad (4.17)$$

The aspect ratio AR is based on the number of longitudinal and transverse stiffeners on the panel and is given by:

$$AR = \frac{dx_{st}}{dy_{st}} = \frac{a_0}{b_0} \quad (4.18)$$

Equation (4.17) is evaluated for m ranging from 1 to 20 and the lowest obtained load will describe the intracellular buckling load. To obtain the applied load to the complete panel causing buckling of the local skin segments, the failure load is multiplied with the width of the skin section. Equation (4.13) can then be applied to find the total applied load.
Since simply supported conditions can be too conservative, clamped boundary conditions are also analysed. Considering clamped boundary conditions for the rectangular skin pocket between the stiffeners, equation (4.19) is used as the approximated displacement function to describe the buckling load. The full derivation is given in appendix F.

$$w(x,y) = \sum_{m=1}^{M}\sum_{n=1}^{N} C_{mn}\left(1 - \cos\frac{2m\pi x}{a_0}\right)\left(1 - \cos\frac{2n\pi y}{b_0}\right) \quad (4.19)$$

The resulting buckling load under clamped conditions and an uni-axial applied load is given by equation (4.20).

$$N_{x,ic,cc} = D_{11}\left(\frac{4m^2\pi^2}{{dx_{st}}^2}\right) + D_{12}\left(\frac{8\pi^2}{3{dy_{st}}^2}\right) + D_{22}\left(\frac{4\pi^2{dx_{st}}^2}{m^2{dy_{st}}^4}\right) + D_{66}\left(\frac{16\pi^2}{3{dy_{st}}^2}\right) \quad (4.20)$$

The analytical methods using simply supported and clamped conditions will both be compared with a numerical model as verification in section 4.4.

4.2.4. Skin stiffener separation

Since there is not much literature found on analytical solutions for the separation of skin and stiffener, this particular failure mode will be assumed to occur after local buckling of skin or stiffener, where out of plane stresses will probably increase significantly due to peel stresses at the edges. Results from Shroff's experiments [20] also show this typical sequence of failure modes, where local buckling of the skin was observed prior to separation of the skin and stiffener.
Since the project is focussed on the first mode of failure, this failure mode will not be further assessed in this report.

4.2.5. First ply failure

To determine if material failure occurs as a first mode of failure, different failure theories are used to predict the critical load in the skin and the stiffeners. Since the stiffeners in the orthogrid stiffened panel will only consist of [0] degree fibres and the skin consists of [+/-45] degree plies only, not all plies have to be analysed for failure. The outer extremes of the stiffener and skin will undergo the largest strains, caused by a non-zero B-matrix and are therefore expected to be subjected to the largest stresses. Figure 4.3 shows six critical locations on the panel, which are analysed for first ply failure. The analysis for material failure is performed for the skin and stiffeners separately. The skin (locations 1 and 2) is analysed by a Tsai-Wu [31] and Tsai-Hill failure [32] criterion, since this part of the structure could be seen as a plate. The stiffeners (locations 3, 4, 5 and 6) are considered to be

beams, which are analysed by determining the stress in the direction of the stiffener. This stress is compared to the allowable tensile or compressive strength of the material.

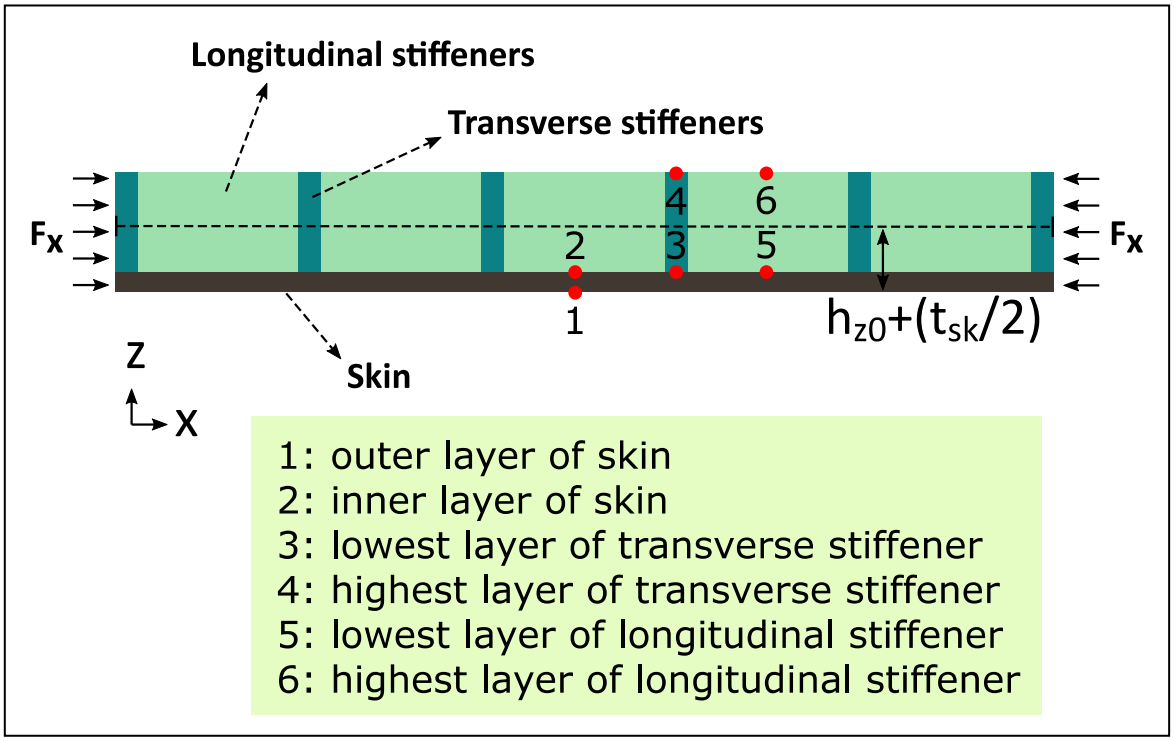

Figure 4.3: Critical locations for first ply failure analysis

The steps to determine the strains and curvatures of the orthogrid panel are outlined in appendix B, where the ABD-matrix is obtained from the smeared stiffener method described in appendix D. The global strains and curvatures are used to determine the strains at each critical location, using equation (4.21).

$$\begin{bmatrix} \varepsilon_x \\ \varepsilon_y \\ \gamma_{xy} \end{bmatrix} = \begin{bmatrix} \varepsilon_{x0} \\ \varepsilon_{y0} \\ \gamma_{xy0} \end{bmatrix} + z \begin{bmatrix} \kappa_x \\ \kappa_y \\ \kappa_{xy} \end{bmatrix} \tag{4.21}$$

The z value is the distance between the calculated neutral axis using the smeared stiffener method used for global buckling and the z-location of the ply. The neutral axis is assumed to lie at the z location, where the stiffeners are smeared over the area. The determination of this value is outlined in appendix D and is shown in figure 4.3 as:

$$h_{z0} + \left(\frac{t_{sk}}{2}\right) \tag{4.22}$$

The critical locations could now be analysed using their specific failure theory.

Skin (location 1 and 2)

For the skin, the exact same method as is further described in appendix B is used to obtain the failure load within the plies. The most conservative of the Tsai-Wu or Tsai-Hill criterion is used for comparison with the failure loads found for the transverse and longitudinal stiffeners. From the analysis, it was found that the orthogrid panel bends towards the grid side of the panel under compression as a result of the asymmetry of the structure. This results in higher compressive stresses at location 2 of the skin and with that, a lower reserve factor.

Transverse stiffeners (location 3 and 4)

It is assumed that the complete orthogrid panel stretches and bends as one integral structure, based on the found ABD-matrix. Due to the relatively thin and small cross-section of the stiffener, it is also assumed that the stiffener behaves like a beam, with stretching in the direction of the stiffener only and bending around the out-of-plane axis only. Since the transverse stiffeners lie parallel to the y-direction of the panel, equation (4.21) is then simplified to the strains in the transverse direction as follows:

$$\varepsilon_y = \varepsilon_{y0} + z * \kappa_y \tag{4.23}$$

In equation (4.23), the strain in the direction of the stiffener is multiplied with the stiffness of the unidirectional glass-fibre, resulting in the stress at the critical locations of the transverse stiffener.

$$\sigma_{\text{transverse stiffener}} = \mathrm{E}_{11}\varepsilon_y \tag{4.24}$$

The stress is compared to the allowable compressive or tensile strength of the unidirectional glass-fibre material, resulting in the reserve factor (RF) for the applied load:

$$RF = \frac{\sigma_{t11}}{\sigma_{\text{transverse stiffener}}} \quad or \quad RF = \frac{\sigma_{c11}}{\sigma_{\text{transverse stiffener}}} \tag{4.25}$$

The expected critical failure load per mm width of the panel is obtained by multiplying the RF with the initially applied load. The total critical material failure load is obtained by multiplication with the width of the panel.

Longitudinal stiffeners (location 5 and 6)

For the longitudinal stiffeners, the exact same method is used as is described for the transverse stiffeners. In this case, the strain along the longitudinal stiffener is obtained by taking the strains in longitudinal direction from equation (4.21):

$$\varepsilon_x = \varepsilon_{x0} + z * \kappa_x \tag{4.26}$$

Comments on the first ply failure analysis

Since the low-weight designs to be found in the next chapter, are expected to be stability driven designs, the first ply failure model described in this subsection will only be used as a quick method to determine if this failure mode would occur prior to one of the stability driven failure modes.
In future studies, the accuracy could be improved by introducing the transverse and shear stresses present in the stiffener.

4.3 Numerical analysis

The numerical model of the orthogrid structure is build by element type 75, shown in figure 3.7, which is used for both the skin and the stiffeners of the panel. This subsection will outline different convergence studies related to global buckling, stiffener crippling and intracellular buckling of the grid stiffened panel. The goal is to make an assumption on the required mesh density to find converged solutions on a range of designs. The convergence study is performed by analysing six examples of orthogrid structures. Subsection 4.3.1 gives two examples of an orthogrid panel, where intracellular buckling is predicted by the analytical models. In subsection 4.3.2, two designs predicting stiffener crippling are outlined. The last two example designs show convergence towards a global buckling solution and are discussed in subsection 4.3.3. A brief summary and sub conclusions are given at the end in subsection 4.3.4.

4.3.1. Convergence study for intracellular buckling

By using the analytical models from the previous subsection, two different designs were obtained for analyzing the intracellular buckling failure mode. Both are shown in figure 4.4 and 4.5, where the latter has relatively more stiffeners than the first design. It is expected that a more refined mesh should be used to obtain a converged solution for the design with more stiffeners, because local modes of skin instability are expected to be found.

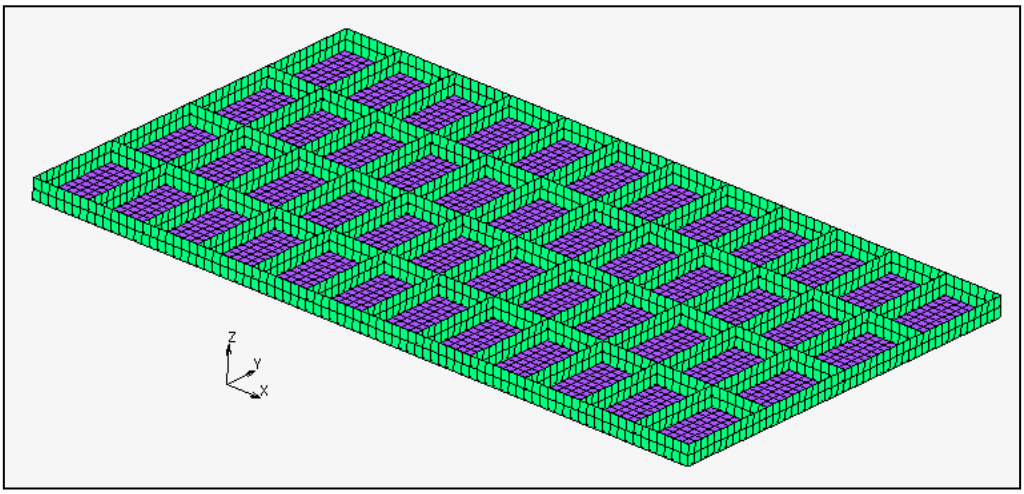

Figure 4.4: Orthogrid design, skin layup: $[+/-45]_3$, stiffener layup: $[0]_5$, h_{st}: 25.0 [mm], 5 longitudinal stiffeners and 13 transverse stiffeners

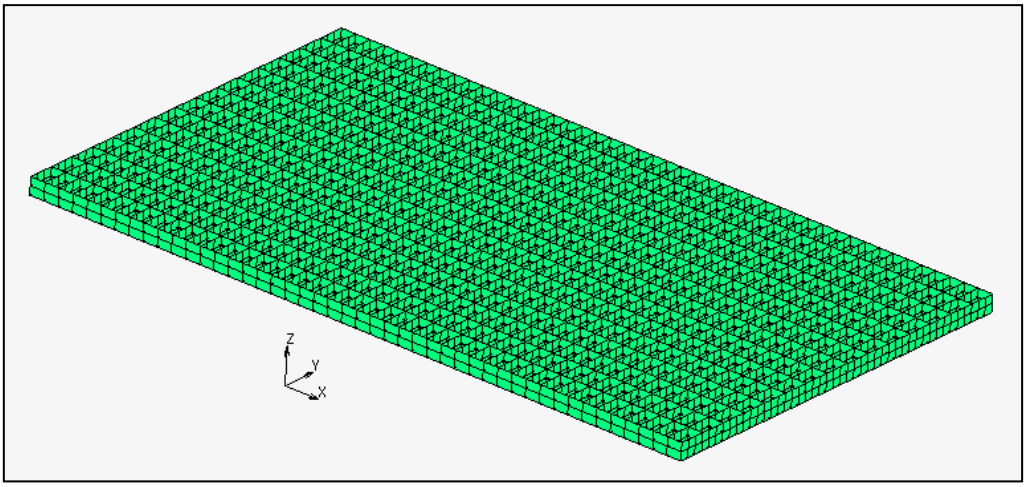

Figure 4.5: Orthogrid design, skin layup: $[+/-45]_1$, stiffener layup: $[0]_2$, h_{st}: 21.0 [mm], 16 longitudinal stiffeners, 47 transverse stiffeners

Starting with the design shown in figure 4.4, the orthogrid panel is first modelled with a coarse mesh and results using more refined meshes are found afterwards. The results from the analysis are graphically presented in figure 4.6, for which the exact values from the numerical analysis can be found in appendix G. For a coarse mesh, where the panel is modelled by only 260 elements, the predicted mode of failure shows global buckling. By refining the mesh, the expected failure mode changes to a combination of intracellular buckling and stiffener crippling. This was not expected from the analytical model, where the lowest failure mode was given for intracellular buckling. This expected combined mode of failure should be taken into account and more insight could probably be obtained from experiments. The solution is converged when the panel is modelled by 27500 elements (or approximate element size of 5 mm), where the solution is within a factor of 1.01 times the solution obtained with the most refined mesh.

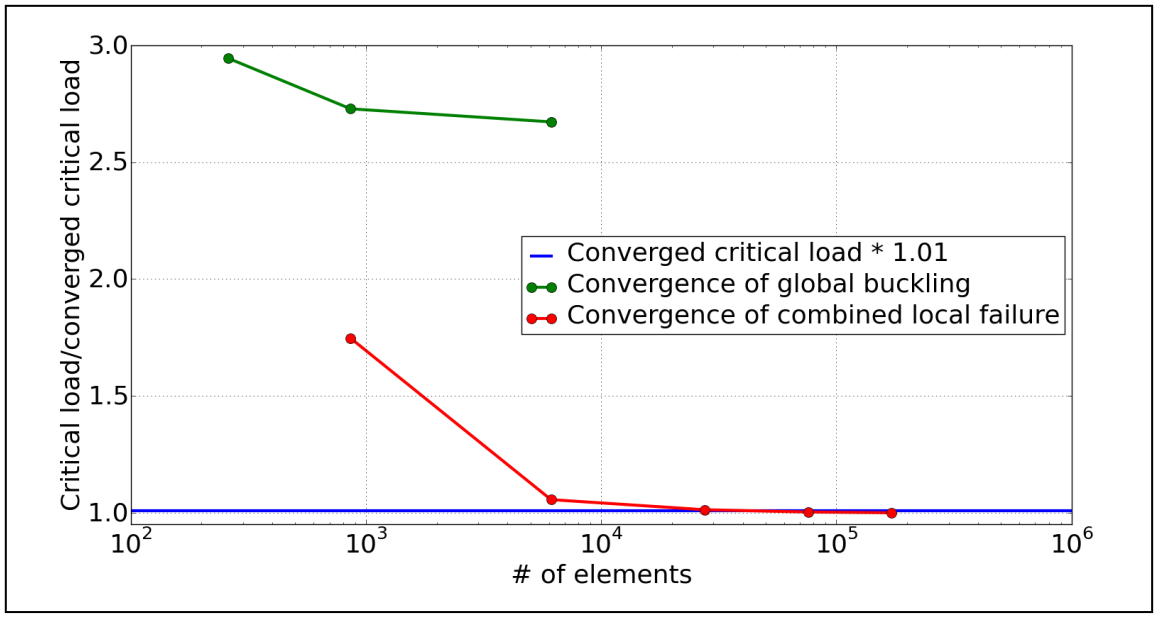

Figure 4.6: Convergence of orthogrid design of figure 4.4

In the previous example, global buckling was found as the initial failure mode, when modelling the panel by a relatively coarse mesh. In this case it already changed to a combination of stiffener crippling and intracellular buckling quickly when refining the mesh.
From the analysis of the second design in figure 4.5, it is not very obvious that intracellular buckling (or a combined local failure) will occur, due to the high amount of stiffeners reducing the size of the skin cells. Figure 4.7 shows the results of the convergence study of the buckling analysis, of which the exact values can be found in appendix G.

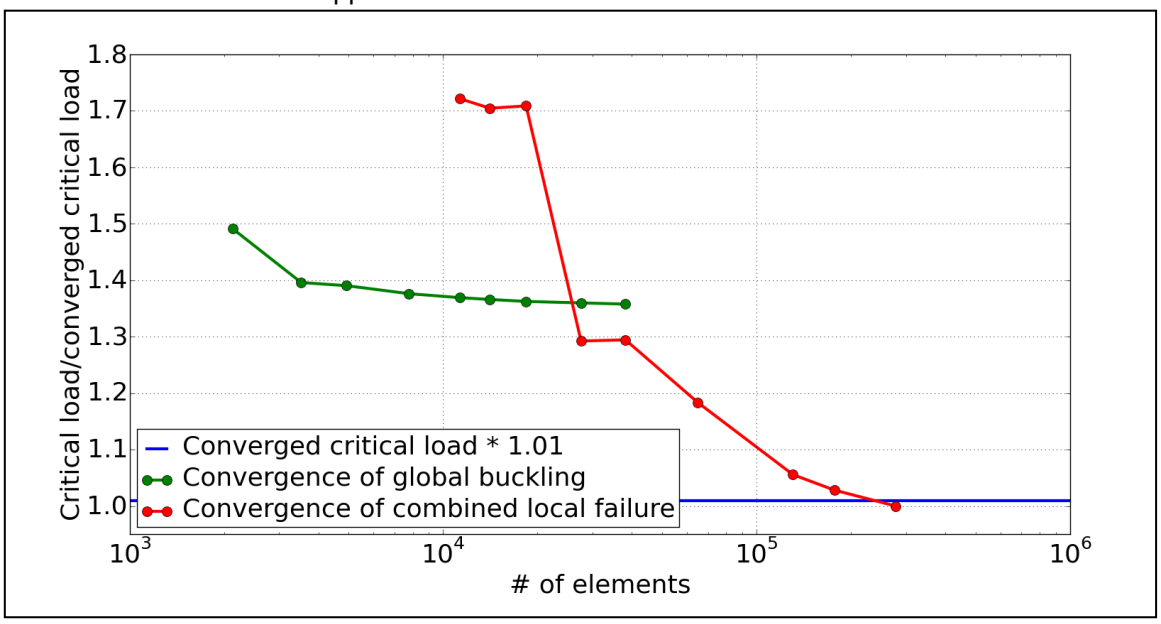

Figure 4.7: Convergence of orthogrid design of figure 4.5

From these values, the solution tends to converge to the global buckling case. However, when a refined mesh of 27549 elements is reached, the predicted failure mode switches to intracellular buckling. From that point, the mesh should be refined much more to obtain a converged solution for this typical design. This results in a computationally very expensive analysis, where the computational limit has been reached on the ability to perform the buckling analysis.

Effect of cell size on intracellular buckling

As a comparison between the two analysed orthogrid designs, the number of elements along the length and width of a skin cell are calculated.
The considered converged solution of the first design was modelled with an element length and width of 5 mm, which resulted in 13 elements along the length of a cell and 25 elements along the width of the cell. This resulted in a total of 325 elements per skin cell, resulting in an accurate solution with respect to an even finer mesh.
The second design was modelled with an approximate element length and width of 2 mm as the most refined mesh. This model resulted in 9 elements along the length and 16 elements along the width of a cell. A total of 144 elements was then used to model each of the skin cells, which was not considered sufficiently accurate.
In order to obtain at least the same element density within one skin cell, the second model should be build from an approximate element size of 1 mm, which was found to be too expensive computationally for the available computers.
Future study could possibly determine the mesh density required within a cell in order to find a converged solutions for the intracellular buckling load.

4.3.2. Convergence study for stiffener crippling

This subsection shows the numerical convergence with respect to the stiffener crippling mode. Two example designs are obtained by using the analytical methods described in the previous subsection. The two designs are shown in figure 4.8 and 4.9, where the main difference is found in the amount of stiffeners between the two.

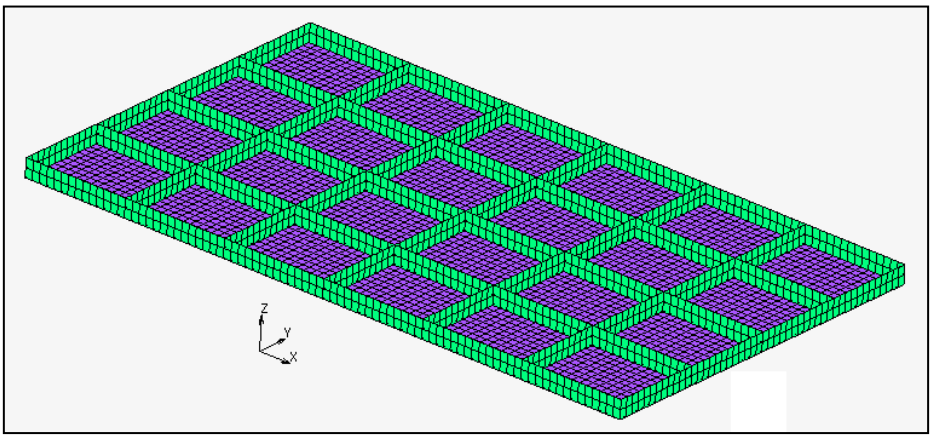

Figure 4.8: Orthogrid design, skin layup: $[45]_4$, stiffener layup: $[0]_3$, h_{st}: 25.0 [mm], 5 longitudinal stiffeners and 7 transverse stiffeners

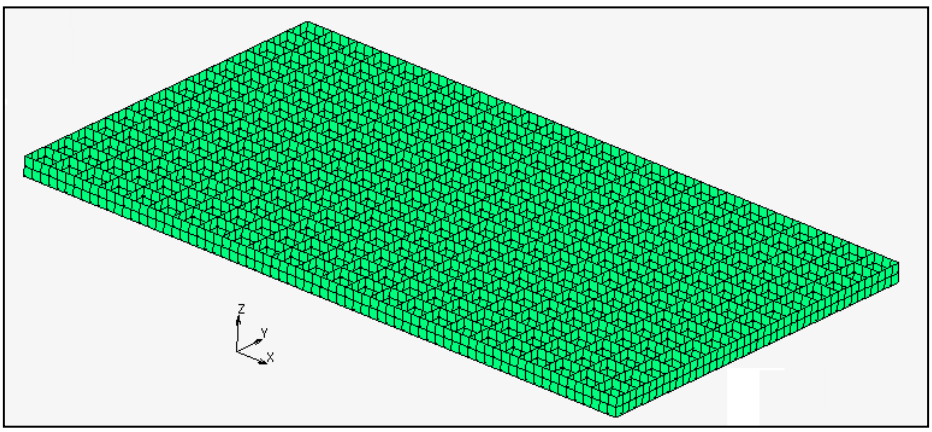

Figure 4.9: Orthogrid design, skin layup: $[45]_4$, stiffener layup: $[0]_3$, h_{st}: 25.0 [mm], 15 longitudinal stiffeners and 25 transverse stiffeners

4.3 Numerical analysis

The convergence study, related to the design shown in figure 4.8, is graphically presented in figure 4.10, of which the data-point values are outlined in appendix G. It is shown that the numerical model initially predicts a failure mode of global buckling for a model consisting of only 82 elements. After increasing this number of elements, stiffener crippling is expected and eventually converges when 24500 elements are used. This solution is within a factor of 1.01 times the numerical solution obtained with the most refined mesh.

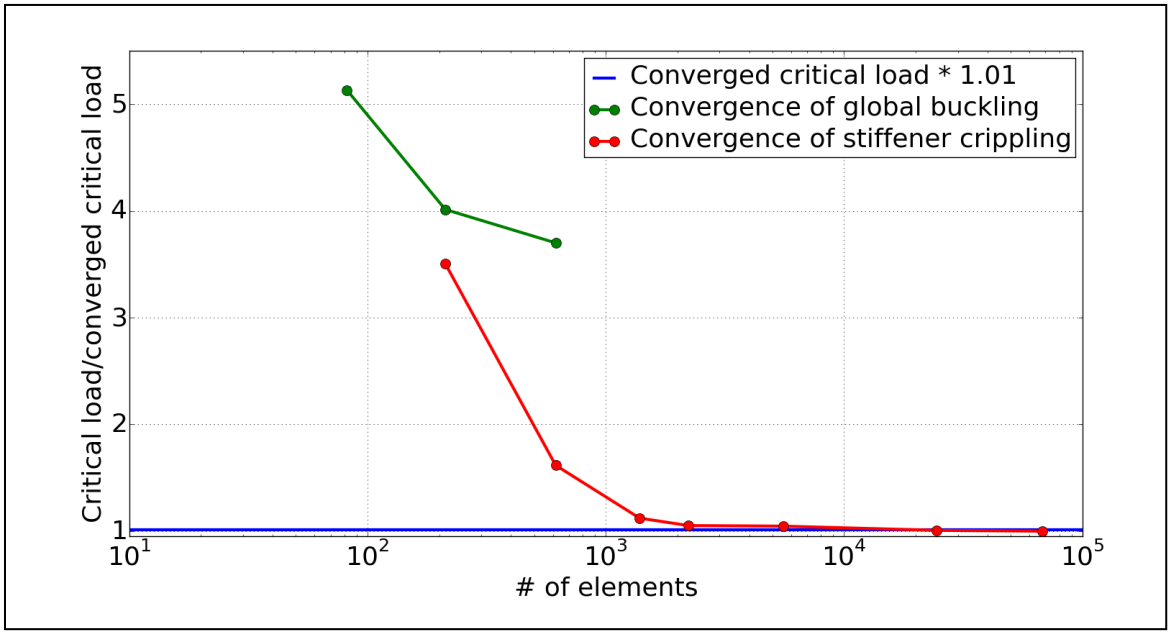

Figure 4.10: Convergence of orthogrid design of figure 4.8

The same convergence study is performed for the design of figure 4.9. The resulting values of the convergence study are drawn in figure 4.11, for which the exact values can be found in appendix G. In this case, stiffener crippling is already observed to be the first mode of failure from the analysis. However, a very refined mesh should be used to find a converged result for the particular design. Modelling the panel with 109712 elements results in a solution within 1 percent of the solution with the most refined mesh.

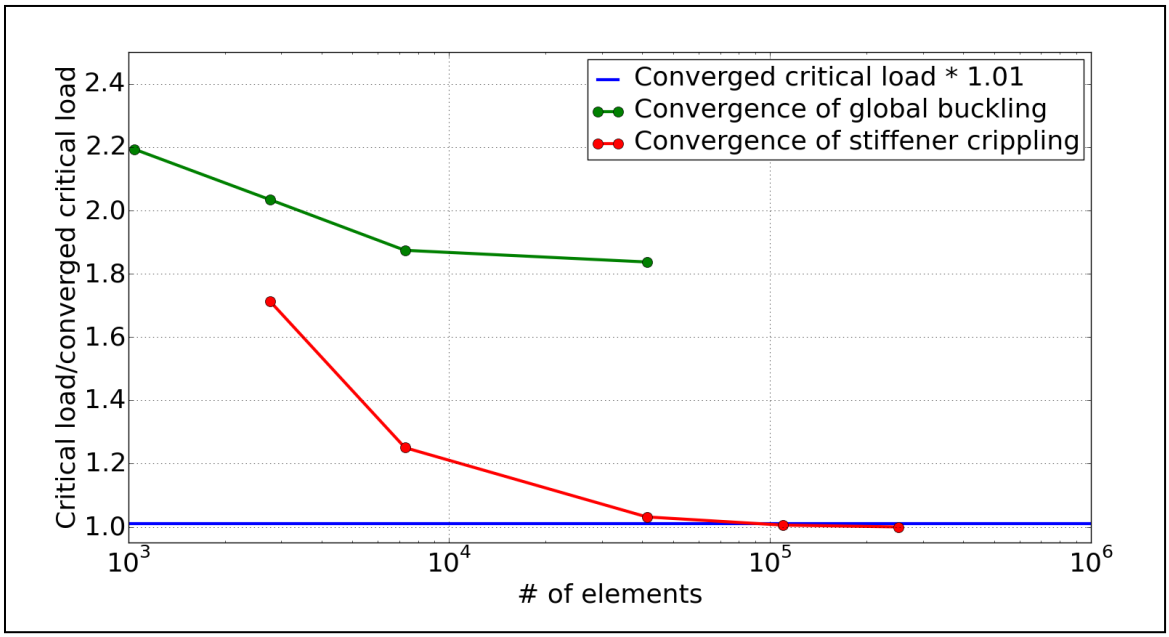

Figure 4.11: Convergence of orthogrid design of figure 4.9

4.3.3. Convergence study for global buckling

This subsection provides insight in the convergence of two orthogrid designs, which fail in global buckling according to the analytical models. The first design is shown in figure 4.12 and consists of less stiffeners than the second orthogrid design given in figure 4.13.

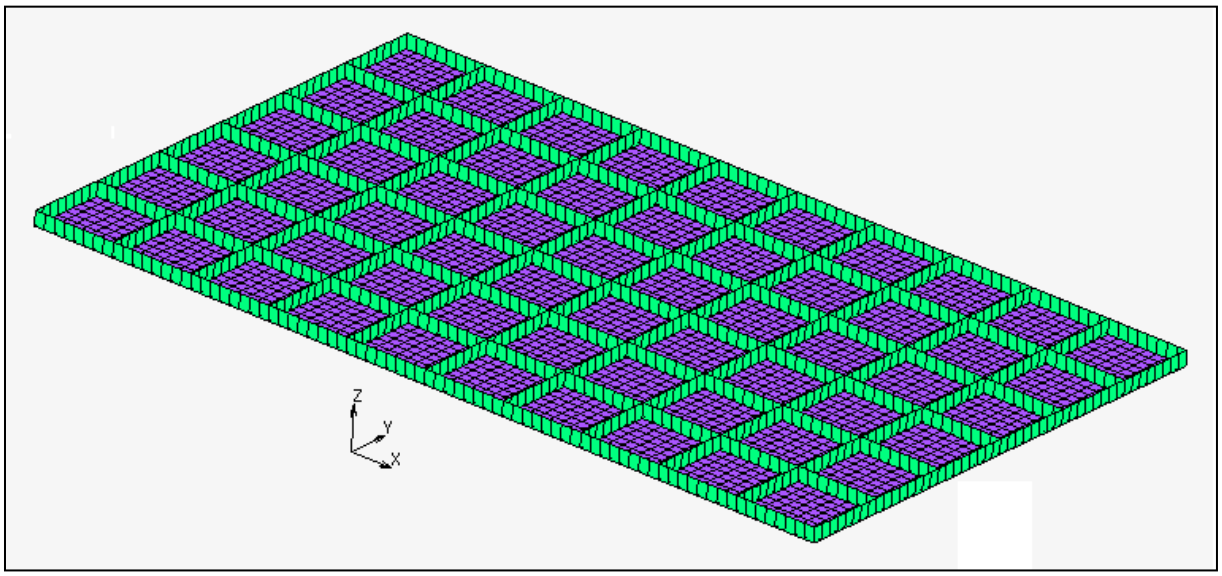

Figure 4.12: Orthogrid design, skin layup: $[45]_3$, stiffener layup: $[0]_3$, h_{st}: 15.0 [mm], 7 longitudinal stiffeners and 11 transverse stiffeners

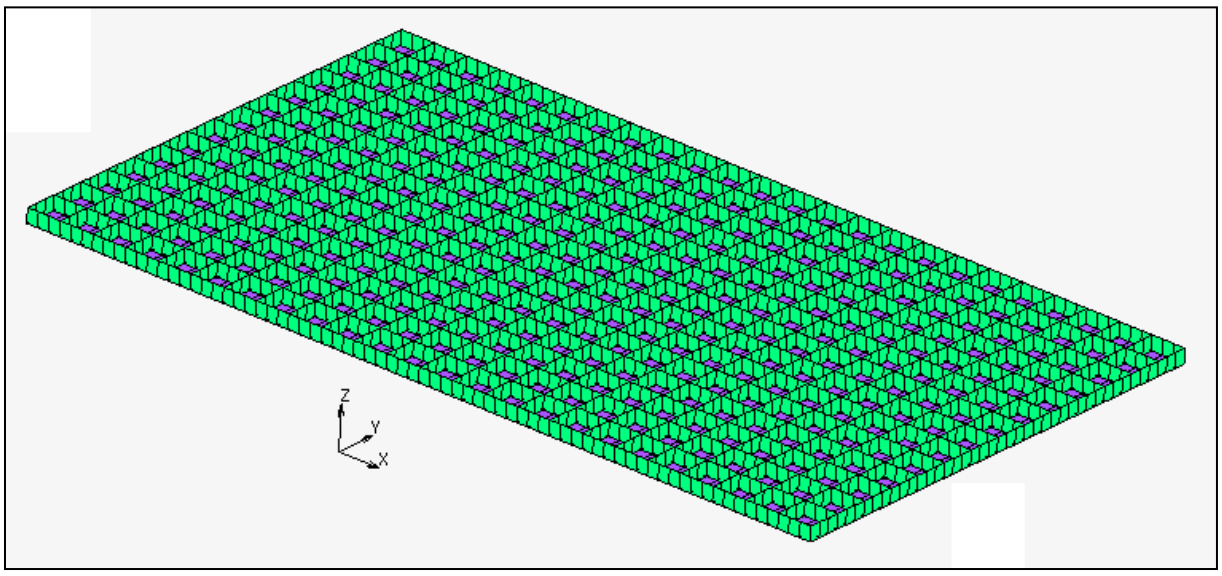

Figure 4.13: Orthogrid design, skin layup: $[45]_2$, stiffener layup: $[0]_3$, h_{st}: 15.0 [mm], 15 longitudinal stiffeners and 25 transverse stiffeners

The results from the numerical models of the first design are graphically presented in figure 4.14 and the exact values are given in appendix G. From this convergence graph, it can be seen that the model converges relatively quick and a very refined mesh is not necessary to find the global buckling failure mode. Only 512 elements are sufficient to obtain a result which is within a factor of 1.01 times the numerical solution found by using 64070 elements. A combined local failure mode was also found, but was related to a higher eigenvalue.

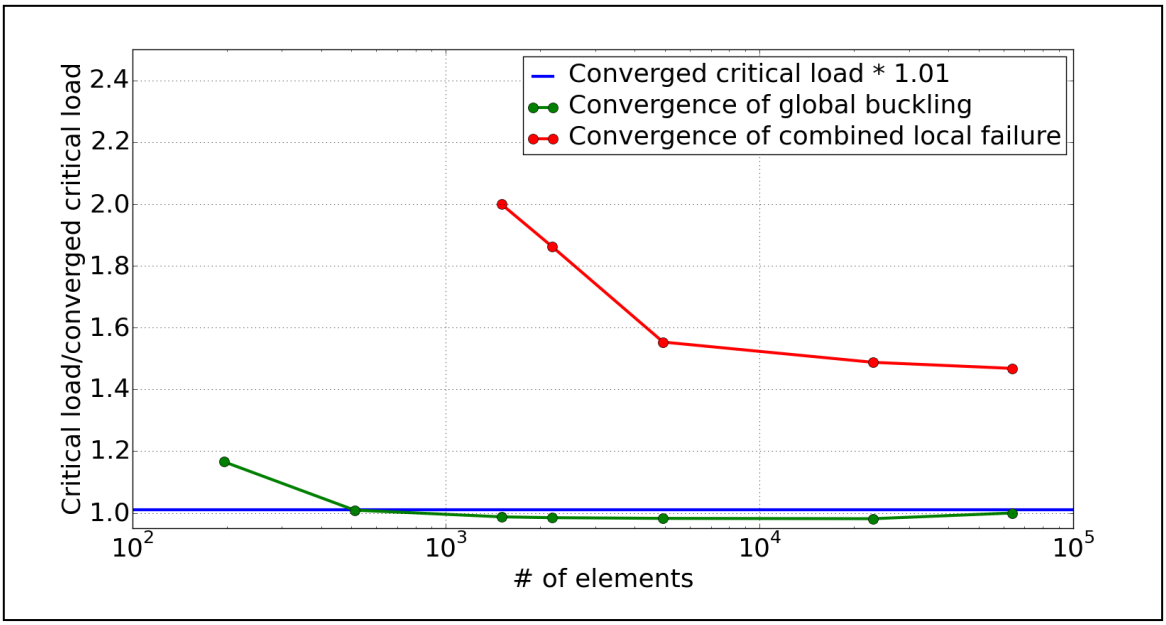

Figure 4.14: Convergence of orthogrid design of figure 4.12

In figure 4.15, the convergence study related to the example orthogrid design from figure 4.13 is shown. The data-point values are written down in appendix G. A relatively fast convergence is shown for the predicted global buckling failure mode. A combined failure mode was also found, which converged to a higher critical load at a very fine mesh.

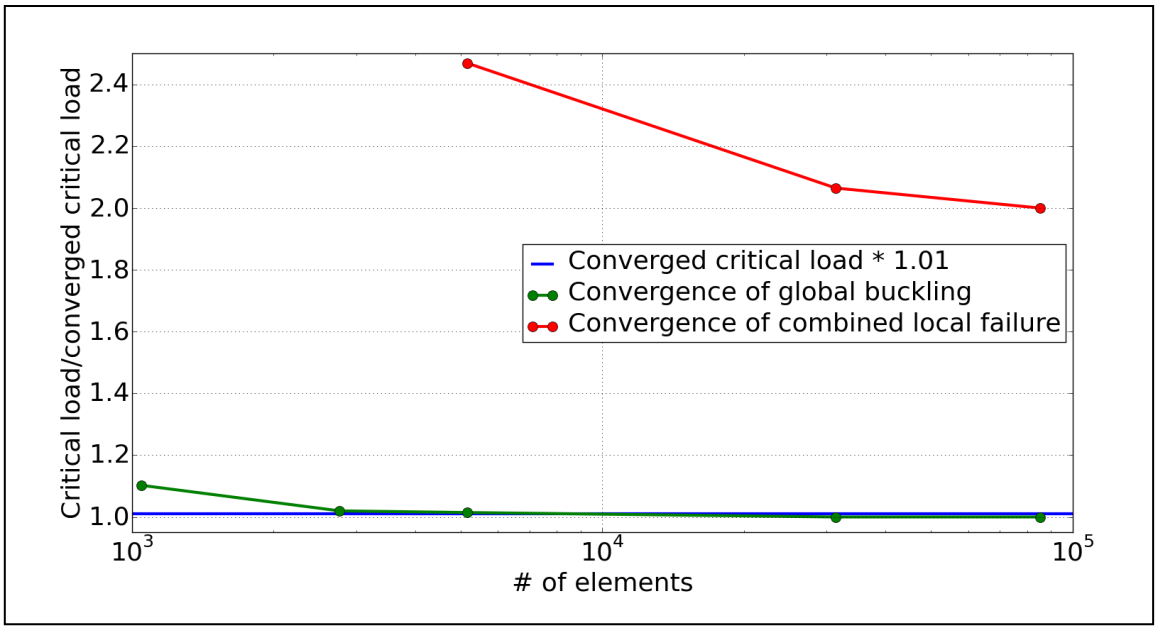

Figure 4.15: Convergence of orthogrid design of figure 4.13

4.3.4. Discussion on numerical convergence orthogrid

Converged solutions were found for five of the six analysed designs and it was found that local failure modes had to be modelled with finer element meshes in order to obtain a converged solution. For designs with small skin cells or stiffener sections, the computational limit was even reached, before an actual converged solution was found.

From the six analysed example orthogrid designs, some simplifying decisions will be made in order to speed up the process of finding low-weight designs in the next chapter. In order to find converged solutions using the presented numerical model, an element size of approximately 2 mm will be considered as accurate enough. Using this element size, only the second example panel did not show a clearly converged solution, where the number of transverse and longitudinal stiffeners was very high. If designs with a high number of stiffeners are found, an extra check could be considered with modelling the specific design with a coarser mesh as comparison.
For future study, computational cost could possibly be reduced by using different element types to model the orthogrid structure. Smaller sections of a design could also be modelled and analysed in order to capture local failure modes within grid stiffened structural designs.

4.4 Parametric study

In order to verify the analytical and numerical models, a comparison between the two will be made, combined with a parametric study. This parametric study is performed to obtain more insight on the influence of an orthogrid design variable on a typical failure mode. To start, a benchmark design is chosen, which allows a change of a design variable in a negative and positive sense. The design was also chosen to approximately have a weight percentage of 40% in the skin and 60% in the stiffeners, since the stiffeners are expected to give the main contribution to the structural stiffness and strength. Taking the above into account, the following design variables are chosen for the benchmark design used in the parametric study:

- Skin layup: $[+/-45]_4$
- Stiffener layup: $[0]_8$
- Stiffener height: 20 [mm]
- Number of longitudinal stiffeners: 10
- Number of transverse stiffeners: 15
- Length a: 866 [mm]
- Width b: 500 [mm]

The cross-section of a transverse or longitudinal stiffener with a portion of the skin is shown in figure 4.16.

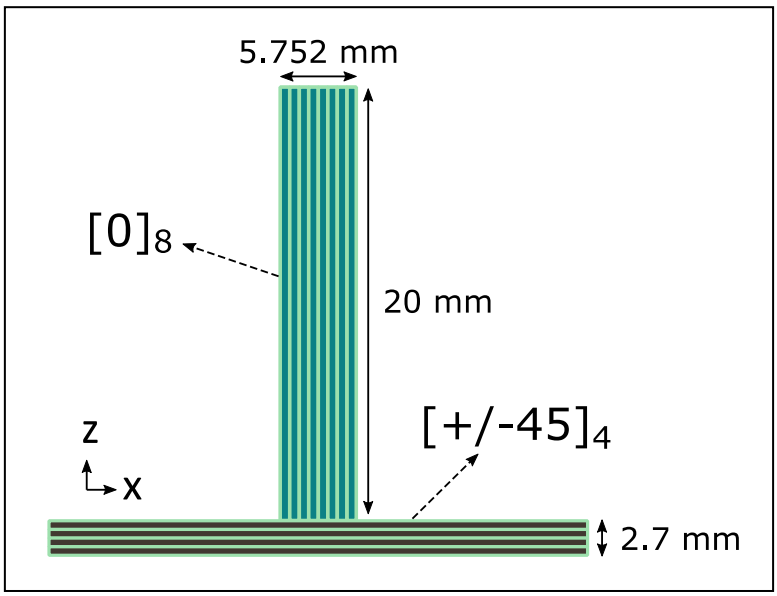

Figure 4.16: Cross-section of a stiffener of the benchmark orthogrid design

4.4 Parametric study

From this benchmark design, each design variable will be changed and the influence it has on the analytical and numerical results will be shown. In subsections 4.4.1 till 4.4.5, the following design variables will be changed accordingly:

4.4.1. Skin thickness
4.4.2. Stiffener thickness
4.4.3. Stiffener height
4.4.4. Number of longitudinal stiffeners
4.4.5. Number of transverse stiffeners

A discussion on the performed parametric study will be performed in subsection 4.4.6, where the most important sub conclusions regarding this section are also drawn.

4.4.1. Skin thickness

The skin layup of the benchmark design will be changed from 1 till 10 layers of biaxial glass-fibre. The influence of the skin thickness, when the other design variables are fixed, is drawn in figure 4.17. The exact values of the data-points from the numerical models are given in appendix H.
The global buckling load predicted by the analytical and numerical model are in very good agreement. A local failure mode is predicted in two different ways. The buckling analysis shows pure skin cell buckling for a skin layup of 1 or 2 biaxial glass fibre plies. The other solution shows a combination of skin and stiffener buckling at the same time. This combined local failure mode tends to follow the line between intracellular buckling under simply supported and clamped conditions. However, at the moment stiffener crippling becomes more apparent as a local failure mode, the graph follows the green curve of stiffener crippling. The analytical solution of stiffener crippling is however over predicting the failure load with respect to the numerical solution.

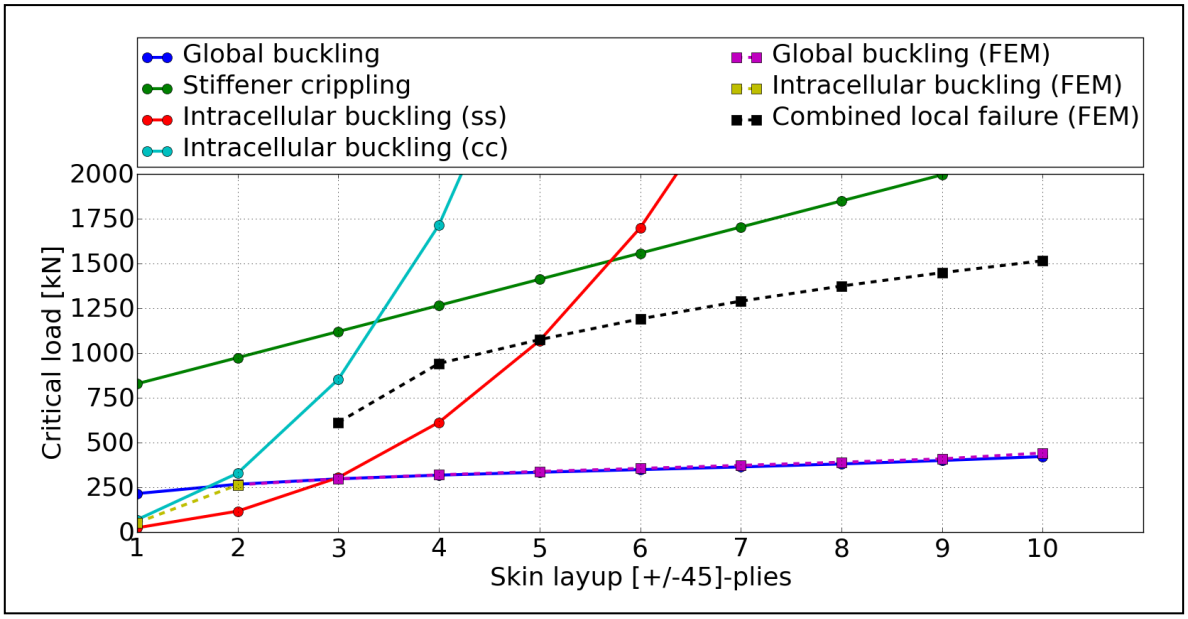

Figure 4.17: Influence of skin thickness on the stability driven failure modes

4.4.2. Stiffener thickness

The stiffener thickness of the benchmark design will be changed from 2 till 20 layers, using a step size of 2 layers. The influence of the stiffener thickness on the different failure modes, when the other design variables are fixed, is drawn in figure 4.18. The values of the data-points for the numerically predicted failure modes are given in appendix H.

The numerical and analytical model to determine global buckling are in very good agreement. The local failure modes predicted by the numerical model are following the line of stiffener crippling initially. When the thickness of the stiffeners increase to 6 plies, a combined failure mode of stiffener crippling and intracellular buckling is predicted by the numerical model. At the point, where the thickness of the stiffener is build of 12 plies, the stiffener crippling failure mode is not shown in the results of the numerical model anymore. From this point, intracellular buckling is shown from the numerical result, which is predicted between the analytical models based on simply supported and clamped boundary conditions.

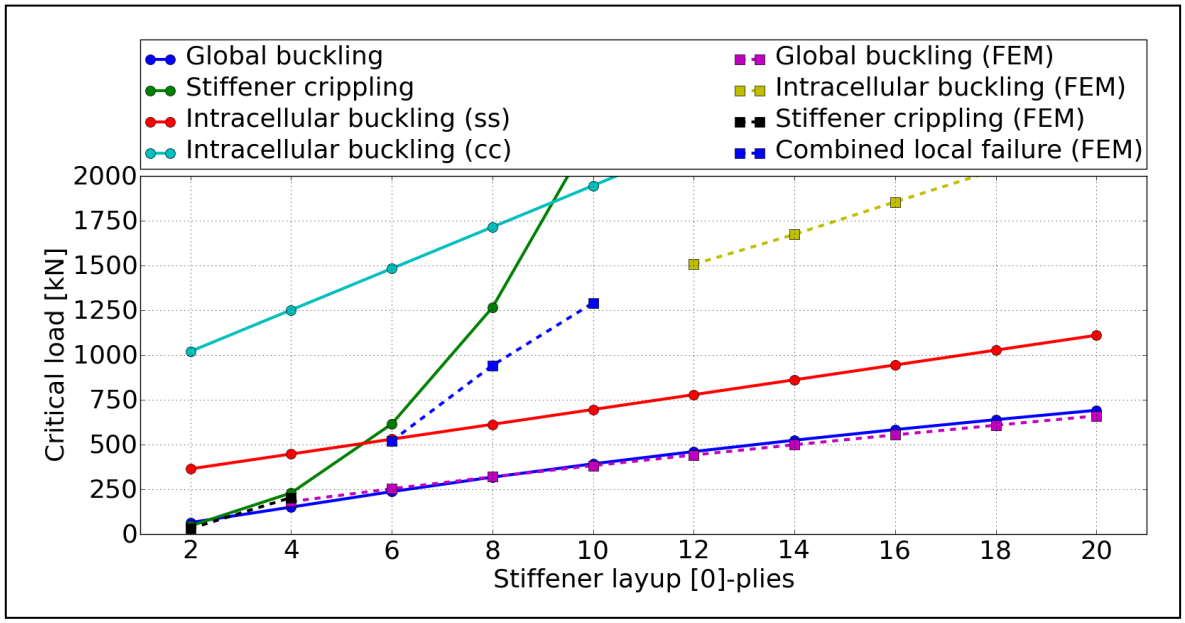

Figure 4.18: Influence of stiffener thickness on the stability driven failure modes

4.4.3. Stiffener height

The stiffener height of the benchmark design will be changed from 2 till 40 mm, using a stepsize of 2 mm. The influence of the stiffener height on the different failure modes when the other design variables are fixed, is drawn in figure 4.19. The values of the data-points for the numerically predicted failure loads are given in appendix H.

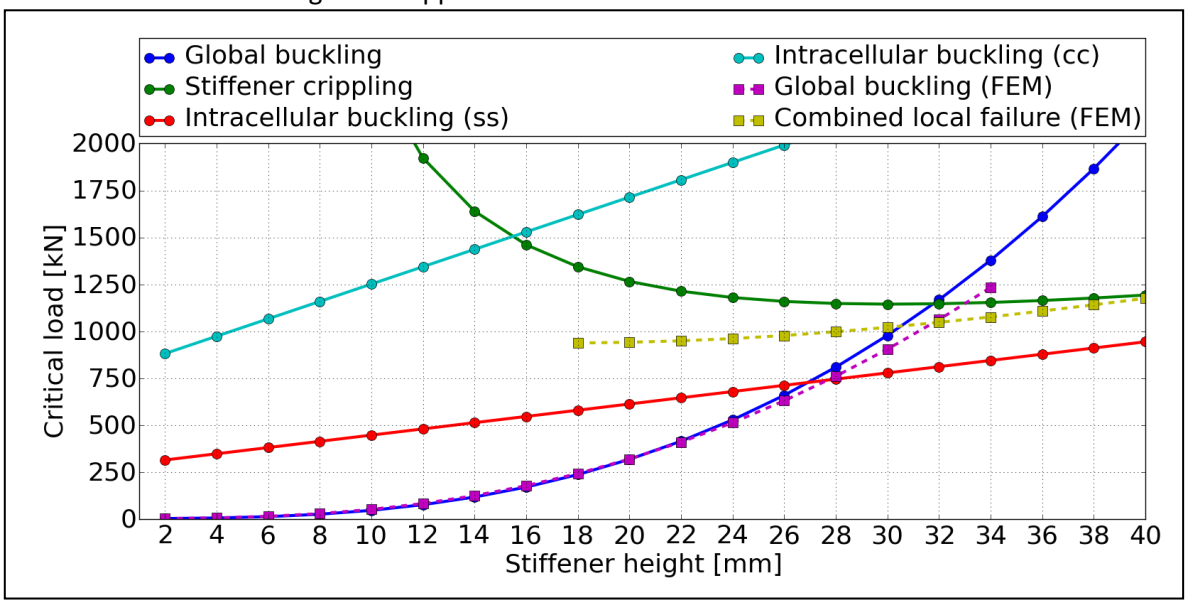

Figure 4.19: Influence of stiffener height on the stability driven failure modes

The predicted failure load for global buckling by the analytical and numerical model is in good agreement. The difference between the two solutions seems to deviate a little for increasing stiffener heights, but remains within 10%. The local failure modes predicted by the numerical model is of the combined case. The yellow line stays between the analytical models for intracellular buckling assuming simply supported and clamped boundary conditions. However, the decreasing critical load of stiffener crippling by height seems to influence the numerical prediction, because the difference with the clamped case of intracellular buckling becomes larger.

4.4.4. Longitudinal stiffeners

The number of longitudinal stiffeners for the benchmark design will be changed from 2 till 30 stiffeners in steps of 2. The results from the analytical and numerical models are shown in figure 4.20. The values of the data-points related to the numerical analysis can be found in appendix H.

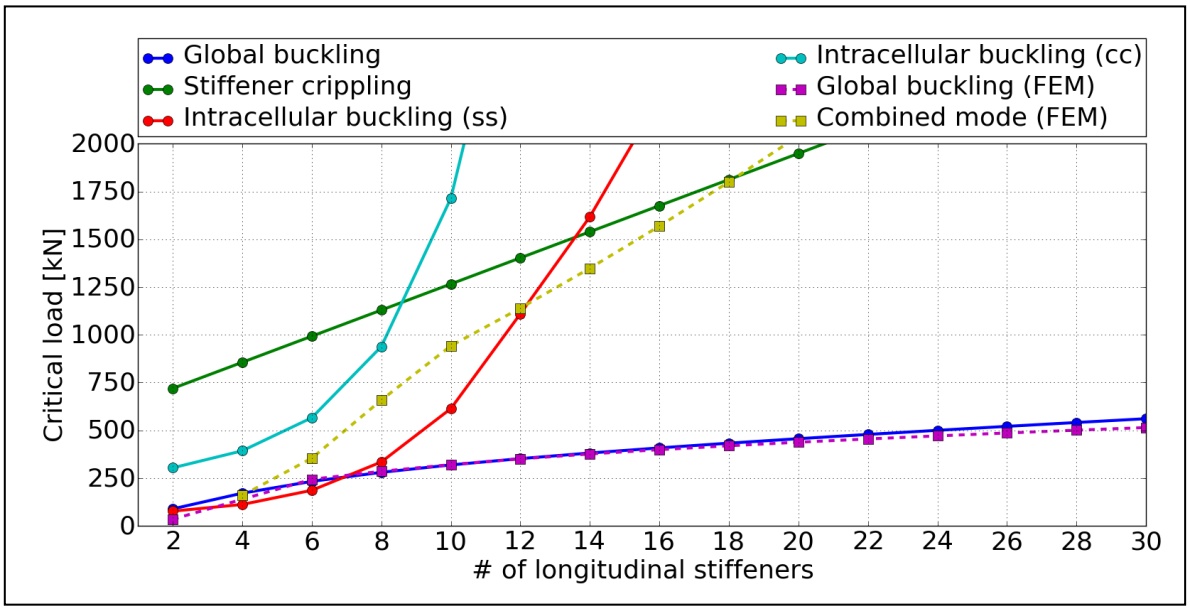

Figure 4.20: Influence of number of longitudinal stiffeners on the stability driven failure modes

The global buckling predictions obtained from the numerical and analytical solutions seem to be in good agreement. The case, where only two or four stiffeners are present, the solution is not accurate or no solution was found respectively. For two stiffeners, this could be explained by knowing that the two stiffeners were modelled at the unloaded edges and were therefore part of the boundary conditions where a constraint was placed on the out-of-plane displacement.
A combined failure mode of stiffener crippling and intracellular buckling was found along the whole range of the number of longitudinal stiffeners. For the lower amount of longitudinal stiffeners, between 4 and 10, the graph follows the intracellular buckling models with simply supported and clamped conditions. For 12 and more longitudinal stiffeners, the numerical result follows the stiffener crippling case. For 20 or more stiffeners, the numerically predicted load eventually crosses the analytical solution for stiffener crippling.

4.4.5. Transverse stiffeners

The number of transverse stiffeners are changed over a range from 3 until 41 stiffeners in steps of 2 stiffeners. The predicting failure loads obtained from the analytical and numerical models are presented in figure 4.21. The values of the data-points for the numerical results are found in appendix H.
For this last graph of this parametric study, the global buckling load obtained from both the numerical and analytical model is again in good agreement.

The combined failure mode predicted by the numerical model, seems to follow the stiffener crippling prediction initially. At the moment, where the prediction of the intracellular buckling load is more apparent to occur with respect to stiffener crippling, the numerical line follows its path between the lines of intracellular buckling.
A note should be made about the analytically determined intracellular buckling load, where the transverse stiffeners do not have an influence on the intracellular buckling load initially. However, having more than 19 transverse stiffeners, the aspect ratio of the skin cell becomes lower than 1 and the stiffener spacing in x direction becomes very small. This eventually leads to the first term of equation (4.17) and (4.20) to be the dominating factor of the typical failure load.

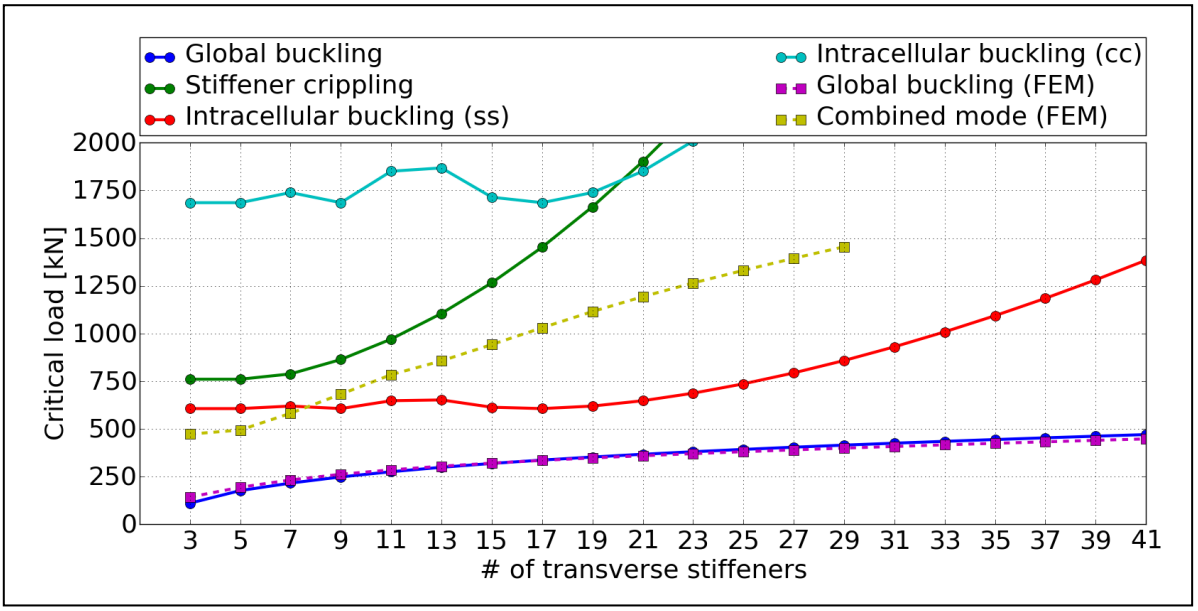

Figure 4.21: Influence of number of transverse stiffeners on the stability driven failure modes

4.4.6. Discussion

In order to find low-weight designs in the next section, the analytical models will be used to find a preliminary design, which are verified and improved by the numerical model afterwards. It was shown from the parametric study, that the analytical models deviate from the numerical models. However, since a sufficiently good trend was found between both models, a knockdown factor could be placed on the analytical predicted failure loads in order to find preliminary designs, which are conservative. After a comparison between the obtained results from this subsection, the knockdown factors shown in table 4.1 will be applied to the analytical models. The knowledge about the influence of each design variable on the different failure modes could be used for further improving the obtained designs in the next section.

Table 4.1: Knockdown factors on analytical models

Failure mode	Knockdown factor
Intracellular buckling (clamped boundary conditions)	0.506
Stiffener crippling	0.621
Global buckling	0.894

From all these design variables, it seems that the number of transverse stiffeners have a low influence on the different failure modes in comparison to the other design variables. Only when the number of transverse stiffeners become significantly high, the stiffeners improve the local failure modes by lowering the stiffener and skin cell in length. This effect of changing the aspect ratio could also be obtained by introducing angled stiffeners as a replacement of the transverse stiffeners. For

future studies, an isogrid stiffened structure could therefore be analysed as well in order to obtain more efficient designs. It was also shown in appendix D, equation (D.64), that angled stiffeners would improve the torsional stiffness of the structure, which is not taken into account during this study. In the case of isogrid stiffened structures, Chen et al. [30] present an approximating displacement functions to model triangular skin sections, which could then be used to analytically determine the intracellular buckling load of an isogrid stiffened structures. In addition, transverse stiffeners could be modelled and manufactured with lower thickness than the longitudinal stiffeners, to further improve the designs. This introduces an extra design variable, which is for now outside the scope of the study.
The analytical models used to determine stiffener crippling and intracellular buckling are not very accurate, but the comparison with the numerical model shows that the influence of the design variables could be guessed. In order to improve the analytical models for the local failure modes, one could try to find the influence of the skin and stiffener thickness on the boundary conditions. As an example, a thicker stiffener could result in stiffer boundaries between stiffener and stiffener or between stiffener and skin.
An overview of the influence on the different failure modes by changing different design variables is shown in table 4.2. The increase of each of the design variables, results in a change of the failure modes, indicated by "+", "-" and "squared" signs. A "+"-sign indicates a slowly (almost) linear increase of the failure load. A "++"-sign is related to a faster (almost) linear increase of the failure load. When the "+"-sign is indicated with a "square"-sign, the failure mode tends to increase in an exponential way. The "$(+/-)^2$"-sign is used when the influence could either be negative or positive, depending on the values of the design variables themselves.

Table 4.2: Influence of the design variable on the different stability-driven failure modes

Design variable	Global buckling	Stiffener crippling	Intracellular buckling
Skin layup	+	++	$(++)^2$
Stiffener layup	+	$(++)^2$	+
Stiffener height	$(++)^2$	$(+/-)^2$	+
# of longitudinal stiffeners	+	++	$(++)^2$
# of transverse stiffeners	+	$(+)^2$	$(+/-)^2$

4.5 Low-weight orthogrid panels

A trial and error based technique will be used to obtain low-weight orthogrid designs. In 4.5.1, theoretical optimum solutions will be designed, where the design variables of the orthogrid panel have no constraints. In 4.5.2, potential manufacturing limitations are taken into account on the stiffener thickness, resulting in more practically oriented designs.

4.5.1. Theoretical low-weight orthogrid designs

The analytical models are used first to obtain a preliminary design on each of the load cases, because the numerical models used so far are computationally expensive. As a result of the parametric study, the knockdown factors from table 4.1 are used on the analytical models to obtain a preliminary design for each of the load cases. An improved brute-force analysis is used for finding the lowest-weight design within the following ranges for the different design variables:

- Skin layup: ranging from 1 till 5 in steps of 1 ply
- Stiffener layup: ranging from 1 till 10 in steps of 1 ply
- Stiffener height: ranging from 10 till 50 in steps of 1 mm
- Number of longitudinal stiffeners: ranging from 3 till 30 in steps of 1 stiffener
- Number of transverse stiffeners: ranging from 4 till 50 in steps of 1 stiffener

The found preliminary design from the knocked down analytical models are shown in table 4.3. All the failure load predictions (without knockdown factor) from the designs listed in this table are graphically presented in figure 4.22, along with the numerically predicted failure load by a buckling analysis. All of the numerical models were build by an approximate element size of 2 mm, which was assumed to give converged solutions for designs with a relatively low number of stiffeners. The obtained preliminary designs have a lot of longitudinal and transverse stiffeners and it can therefore not be assumed that the obtained solutions from the numerical model are converged. The theoretical preliminary designs will however be further improved to obtain the final theoretical low-weight orthogrid designs. A convergence study could be performed for each of the final designs in order to give a conclusion about the convergence. This is not performed during this study, due to time limitations.

Table 4.3: Preliminary orthogrid designs by analytical solutions (theoretical)

Design load [kN]	Skin layers [+/-45]	Stiffener layers [0]	Longitudinal stiffeners	Transverse stiffeners	Stiffener height [mm]	Weight [kg]
50	1	2	17	34	15.0	1.831
100	1	2	20	47	18.0	2.529
150	1	2	28	49	20.0	3.177
200	2	3	15	35	21.0	3.685
250	2	4	13	27	22.0	4.033
300	2	3	13	45	24.0	4.373
350	2	3	15	46	25.0	4.735
400	2	3	19	45	25.0	5.035
450	2	3	19	48	26.0	5.350
500	2	4	16	35	27.0	5.661
550	3	5	9	30	28.0	5.946
600	2	4	17	38	28.0	6.188
650	2	4	17	39	29.0	6.448
700	3	5	9	34	30.0	6.658
750	2	4	17	42	30.0	6.875
800	3	5	10	35	31.0	7.110

In order to further improve the preliminary designs, figure 4.22 is used to try and make some improvements and lower the weight. Each of the load cases is shown on the x-axis and the y-axis gives insight in the critical load of each failure mode with respect to the design load. The legend indicates the different predicted failure modes, of which the first five are obtained from the analytical solutions and the last two vertical bars are determined by the numerical model. All the exact values related to the histogram are presented in appendix I.

As an example, for the 50 kN design load, a 50% higher combined local failure mode is found with respect to the design load. From the parametric study, it was observed that the number of transverse and longitudinal stiffeners have a small influence on the global buckling load and a larger influence on the local failure modes. The design could therefore be improved, by removing some of the transverse and longitudinal stiffeners, up to the point where the numerically determined critical load is still higher than the design load.

For each of the design loads, this trial and error scheme is used to obtain a design, where the numerically determined buckling load is still above the design load.

In addition, some of the designs predict an early first ply failure, based on the analytical solution. From the different designs, it can be seen that the ones with a low first ply failure critical load also have a low number of longitudinal stiffeners (550, 700 and 800 kN). The preliminary designs are therefore also improved by increasing the first ply failure load on some of the designs.

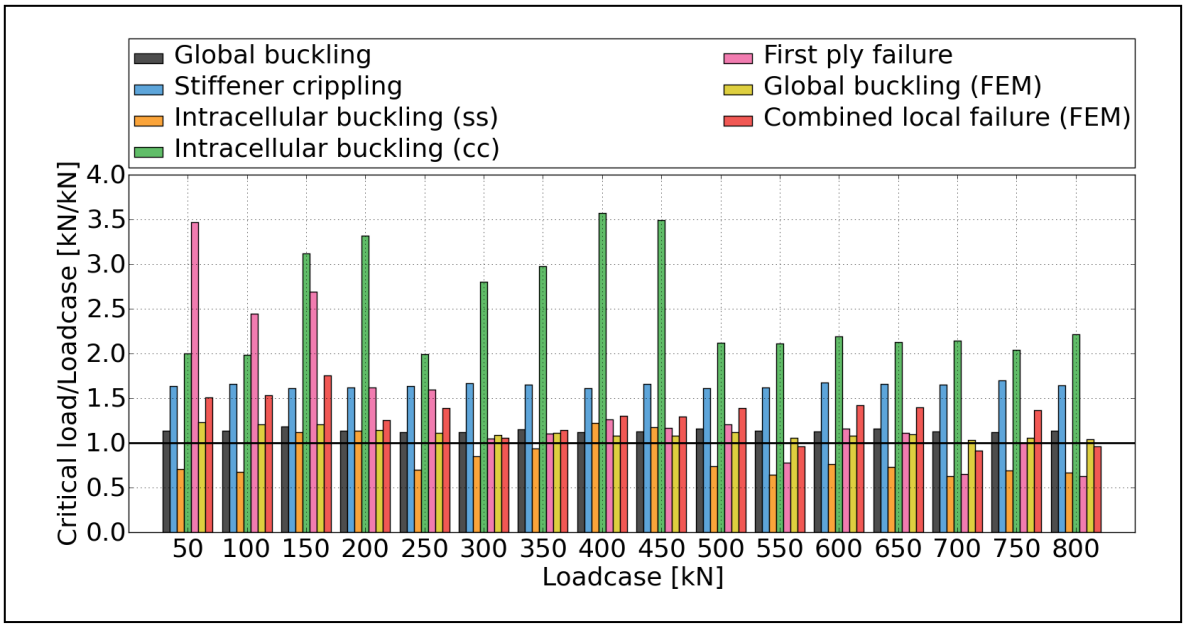

Figure 4.22: Different failure loads for the preliminary orthogrid designs (theoretical)

The improved final designs, obtained after the performed numerical analysis on each of the load cases, are shown in table 4.4. The analytically and numerically determined failure loads related to the found low-weight orthogrid designs are graphically presented in figure 4.23. The exact failure modes related to the vertical bars in the histogram are presented in appendix I.
As was mentioned before, the designs found cannot be considered converged, due to the high number of stiffeners present.

Table 4.4: Improved low-weight orthogrid designs by trial and error (theoretical)

Design load [kN]	Skin layers [+/-45]	Stiffener layers [0]	Longitudinal stiffeners	Transverse stiffeners	Stiffener height [mm]	Weight [kg]
50	1	2	17	25	15.0	1.649
100	1	2	27	33	17.0	2.376
150	1	2	23	41	20.0	2.728
200	1	2	25	43	22.0	3.108
250	1	2	30	43	23.0	3.492
300	1	2	31	49	24.0	3.871
350	2	3	18	36	25.0	4.492
400	2	3	19	37	26.0	4.772
450	2	3	20	39	26.0	4.968
500	2	3	22	37	27.0	5.197
550	2	3	23	40	27.0	5.455
600	2	3	23	40	28.0	5.616
650	2	3	24	41	29.0	5.938
700	2	4	18	31	30.0	6.125
750	2	4	19	32	30.0	6.346
800	2	4	20	34	30.0	6.648

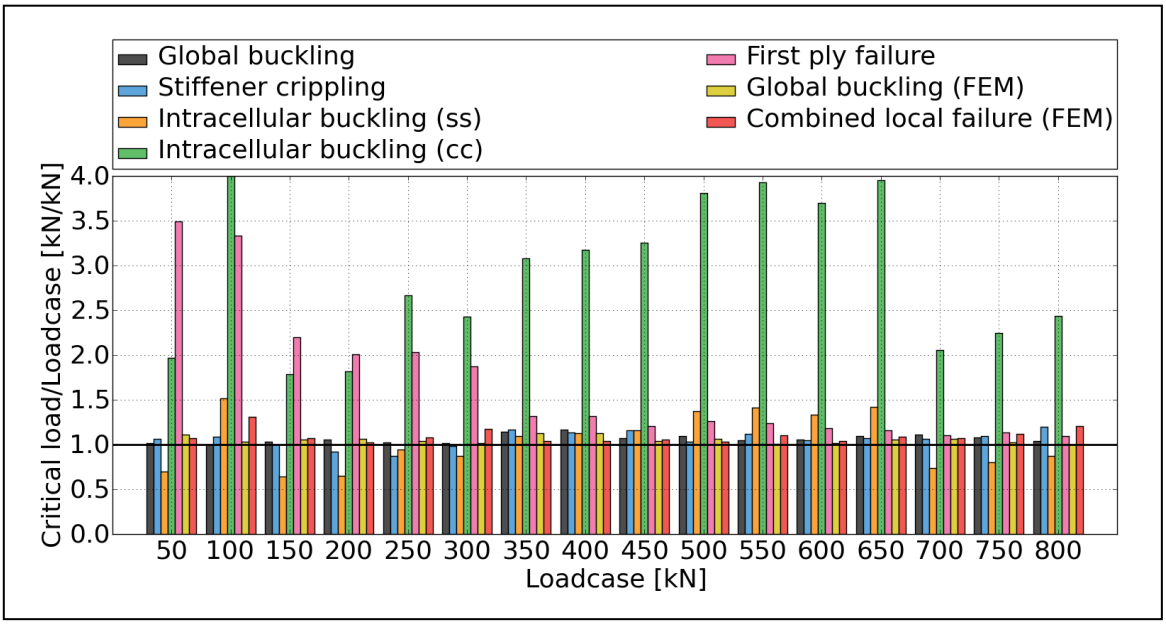

Figure 4.23: Different failure loads for the improved low-weight orthogrid designs (theoretical)

Figure 4.24 graphically presents the increase in weight of the orthogrid panel, when the compressive load is increased. The weight percentage for the grid and skin are also shown in the graph. Low-weight solutions tend to have as less weight as possible in the skin. The weight of the skin will increase when the intracellular buckling load is the critical failure mode and cannot be further improved by applying more longitudinal stiffeners.

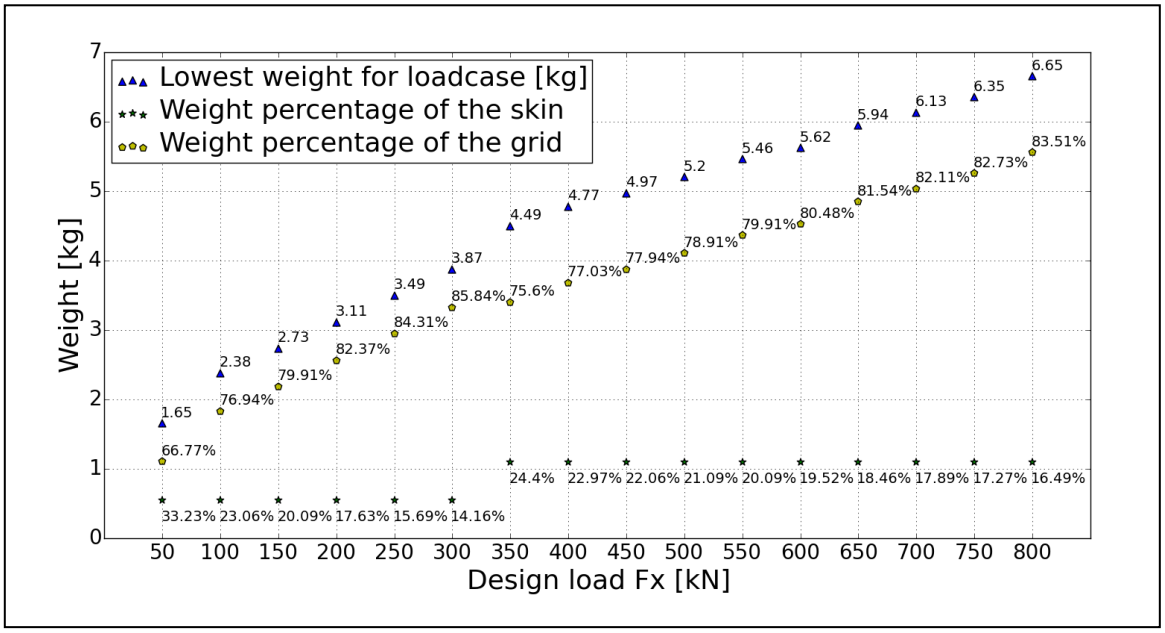

Figure 4.24: Theoretical low-weight orthogrid panel weight(fractions) per load case

4.5.2. Practical low-weight orthogrid designs

The high amount of stiffeners found in the previous subsection, resulted in very small stiffener thicknesses. This could result in manufacturing problems, where tolerance issues could result in a bad quality product. In terms of an automated process using fibre layup, tolerances could also become a problem, where the robot head is not able to steer exactly over the small stiffener or the thin stiffener will be crushed under the applied pressure from the machine.
Another optimum result is therefore found from the numerical models, where a minimum stiffener thickness is introduced. A preliminary design is found by using the analytical models, from which a trial and error procedure is again used to find low-weight designs for the range of load cases. The manufacturing of a thin stiffener was the main problem, which is why this design variable is given a minimum of 5 mm, resulting in at least 7 layers of unidirectional layers of glass-fibre trough the thickness of the stiffener. The preliminary designs are then obtained from the following ranges:

- Skin layup: ranging from 1 till 5 in steps of 1 ply
- Stiffener layup: ranging from 7 till 15 in steps of 1 ply
- Stiffener height: ranging from 10 till 50 in steps of 1 mm
- Number of longitudinal stiffeners: ranging from 3 till 30 in steps of 1 stiffener
- Number of transverse stiffeners: ranging from 4 till 50 in steps of 1 stiffener

The resulting designs from the improved brute-force analysis are shown in table 4.5. The designs are verified by the numerical model and are presented in figure 4.25 along with the analytically determined critical loads. The data related to the failure loads of the preliminary designs are presented in appendix J.

Table 4.5: Preliminary orthogrid designs by analytical solutions (practical)

Design load [kN]	Skin layers [+/-45]	Stiffener layers [0]	Longitudinal stiffeners	Transverse stiffeners	Stiffener height [mm]	Weight [kg]
50	1	7	13	5	14.0	2.366
100	2	7	9	6	18.0	2.929
150	2	7	10	5	21.0	3.308
200	2	7	11	6	22.0	3.697
250	2	7	12	7	23.0	4.111
300	2	7	13	9	23.0	4.516
350	3	8	9	9	24.0	4.826
400	3	9	9	7	26.0	5.207
450	3	10	9	5	27.0	5.391
500	3	11	9	4	29.0	5.856
550	3	7	11	17	26.0	6.067
600	3	7	11	18	27.0	6.364
650	3	8	11	15	27.0	6.602
700	4	12	8	5	30.0	6.768
750	3	9	11	13	28.0	7.089
800	4	8	9	17	29.0	7.288

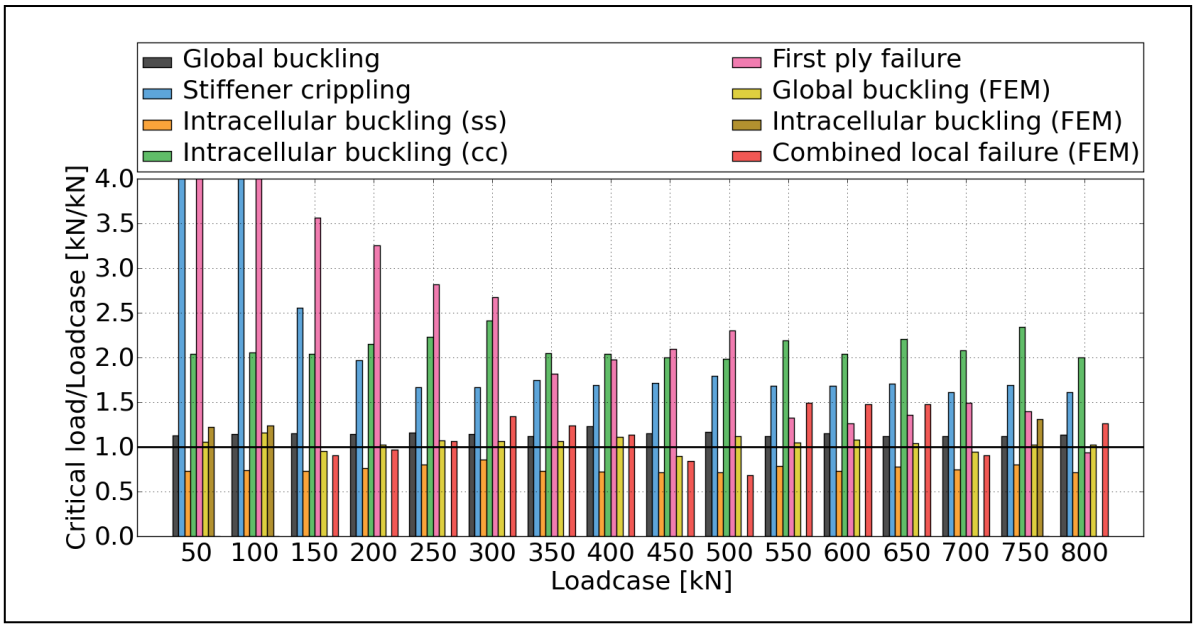

Figure 4.25: Different failure loads for the preliminary orthogrid designs (practical)

The preliminary designs will be improved by (re)moving material of the specific design. With the knowledge of the parametric study, a trial and error solution technique is used to obtain lower weight designs for each of the design loads. For some of the preliminary designs, an improvement with respect to the first ply material failure load has to be made. Increasing the number of longitudinal stiffeners should give this increase on the critical load.
Table 4.6 shows the improved designs, for which the critical loads are presented with a histogram in figure 4.26 and the related data can be found in appendix J.

Table 4.6: Improved low-weight orthogrid designs by trial and error (practical)

Design load [kN]	Skin layers [+/-45]	Stiffener layers [0]	Longitudinal stiffeners	Transverse stiffeners	Stiffener height [mm]	Weight [kg]
50	1	7	13	5	14.0	2.366
100	2	7	9	5	18.0	2.845
150	2	7	10	7	20.0	3.391
200	2	7	11	7	21.0	3.677
250	2	7	12	8	22.0	4.084
300	2	7	12	9	23.0	4.328
350	3	8	9	7	25.0	4.689
400	3	8	9	8	26.0	4.951
450	3	9	9	8	26.0	5.365
500	4	9	7	9	27.0	5.652
550	3	8	11	9	27.0	5.728
600	3	7	11	15	27.0	5.982
650	3	8	11	11	28.0	6.182
700	4	8	9	12	29.0	6.506
750	3	9	11	10	29.0	6.755
800	4	8	11	10	30.0	6.892

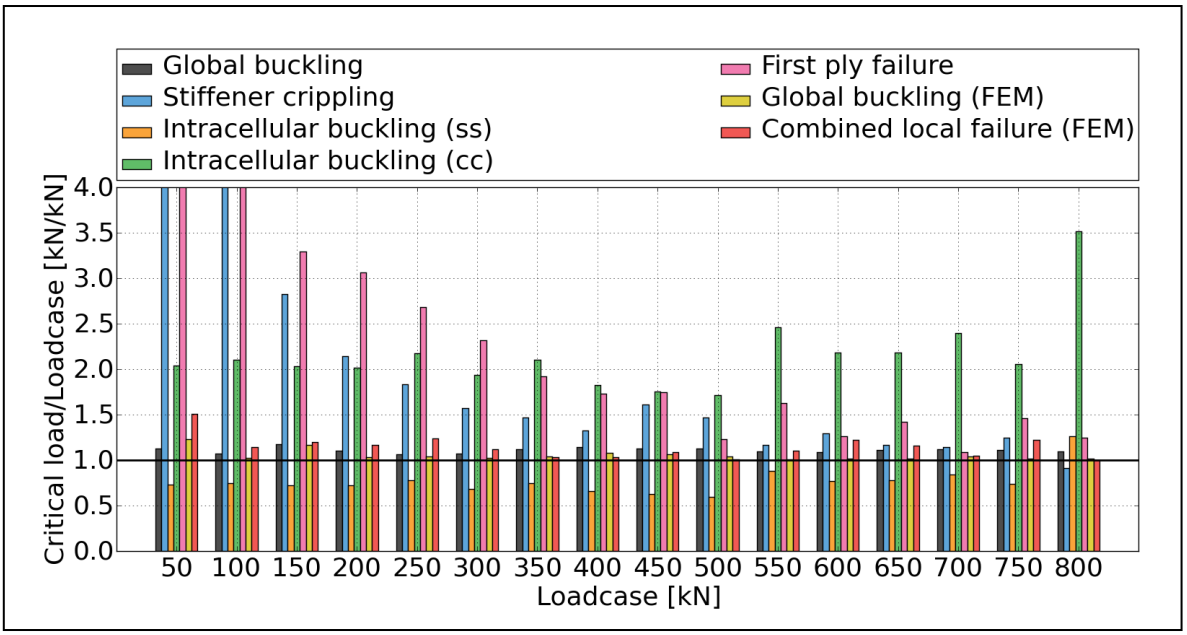

Figure 4.26: Different failure loads for the improved low-weight orthogrid designs (practical)

The resulting weights of the improved designs are presented in figure 4.27. The weight fraction in the grid and skin are also presented, where it is observed that most of the weight is present in the grid of the panel. Compared to the theoretical low-weight designs, the weight percentage in the skin is slightly higher. This could be explained by the fact that the skin requires more thickness in order to prevent intracellular buckling, which is more apparent to occur as a result of the larger skin cells.

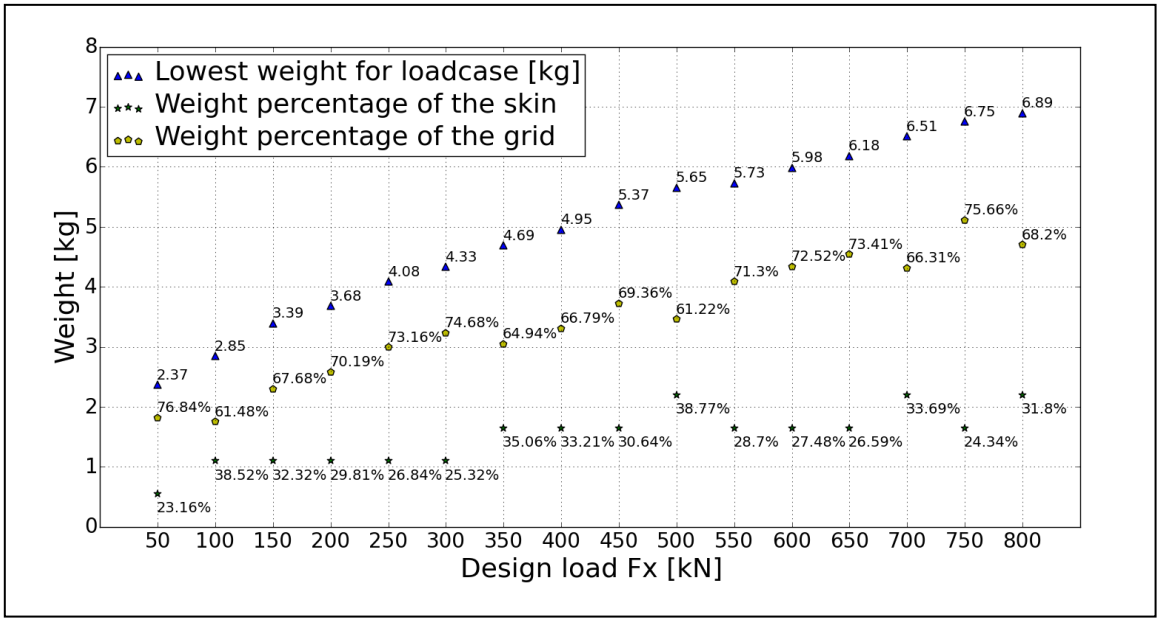

Figure 4.27: Practical low-weight orthogrid panel weight(fractions) per load case

5.Comparison of Low-Weight Designs

In the previous two chapters, different analytical and numerical models have been analysed and verified. With those models, low-weight designs were obtained for a sandwich and an orthogrid structure. A comparison between the obtained low-weight solutions is made in section 5.1. In order to validate these compared results, different panels which will be manufactured and tested are described in section 5.2.

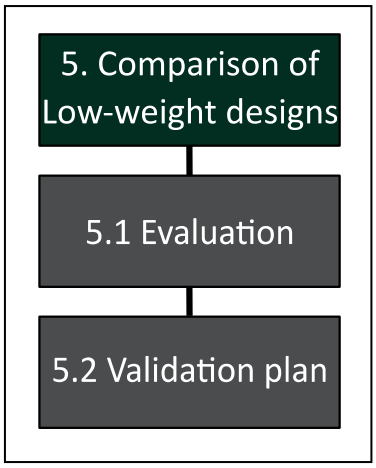

Figure 5.1: Flow chart chapter 5

5.1 Evaluation

The obtained low-weight solutions found in the two previous chapters are drawn together in figure 5.2. It is observed that for lower load cases, both types of structure perform equally well. For higher load cases, a reduction in weight is observed for the orthogrid structure compared to the sandwich structure.
Wang [1] stated the following in her optimization study on orthogrid wind turbine blade trailing panels:

“At the same time, a minimum skin thickness of 1.7688 mm (40% of the average face sheet thickness of the sandwich trailing panels of the reference blade) is set to avoid the local skin buckling due to the ultrathin skin”

The average thickness of the face sheet on the reference blade is therefore approximately 4.4 mm and can be compared to a lay-up of at least 6 layers of biaxial glass-fibre used during this project. The range of designs with 6 biaxial glass-fibre layers or more are indicated with the grey background colour in figure 5.2. The practical low-weight orthogrid designs show a weight reduction between 19.7% till 28.3% with respect to the low-weight sandwich panels.
The theoretical orthogrid design shows lower weight solutions, but the weight reductions seem to be negligible for higher load cases. The large amount of stiffeners on the theoretical designs also introduce a lot of stiffener crossings. These locations are not taken into account in the analysis, but could have negative effects on the performance of the structure, because fibres are steered at these locations during manufacturing. In addition, convergence of the numerical solutions for the theoretical designs cannot be assumed. The theoretical designs do show lower skin thicknesses, which could improve the performance as a result of a lower level of asymmetry of the structure.
Future studies could focus on finding lower-weight solutions for the grid stiffened structure, by introducing more design variables. As an example, the isogrid type of structure could be analysed or transverse stiffeners could be modelled with varying stiffener thicknesses. Another option could be

the introduction of longitudinal and transverse stiffener, which have different heights compared to each other.

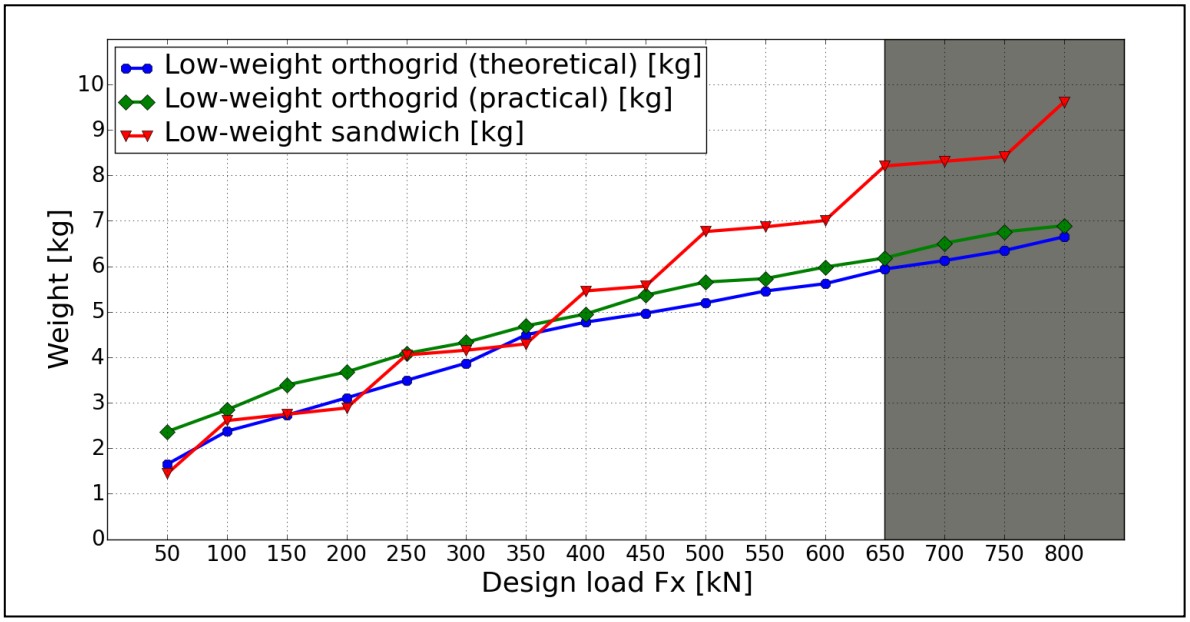

Figure 5.2: Comparison of the low-weight sandwich and orthogrid designs

5.2 Validation plan

In order to validate the analysis performed so far, manufacturing and testing of the designs will be performed. Taking the time available during a master thesis into account, it has been decided to manufacture and test the two designs shown in figure 5.3 and figure 5.4, which are related to the design load of 100 kN. This lower load case is chosen, because the fibre roving used for the stiffened grid has to be wound manually. Higher design loads can result in manual glass-fibre winding taking up to a couple of weeks to finish only one panel. For the orthogrid panel, it was also decided to test the manufacturing process for a very dense grid structure, based on the theoretical low-weight solutions. This should result in a conclusion on design limits for the manufacturing process.

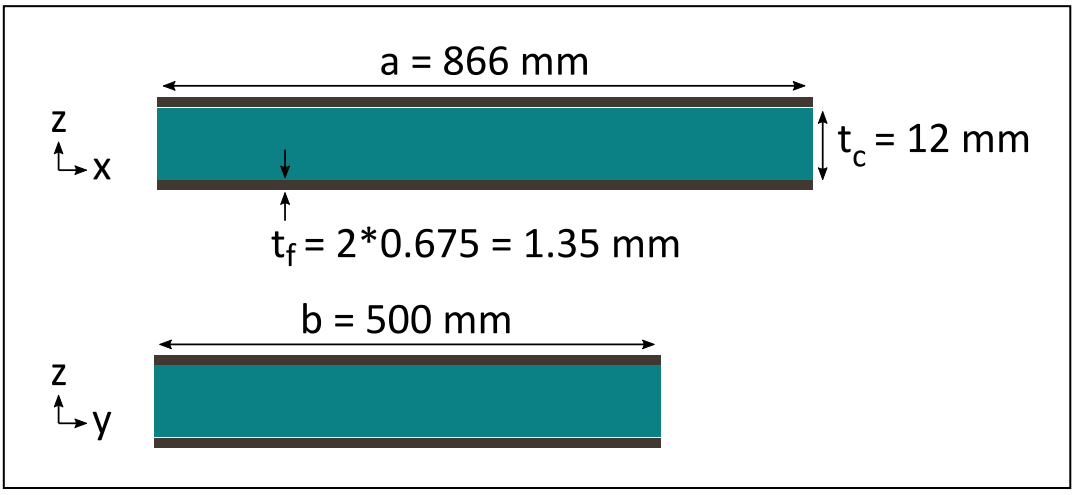

Figure 5.3: Low-weight sandwich design for a design load of 100 kN

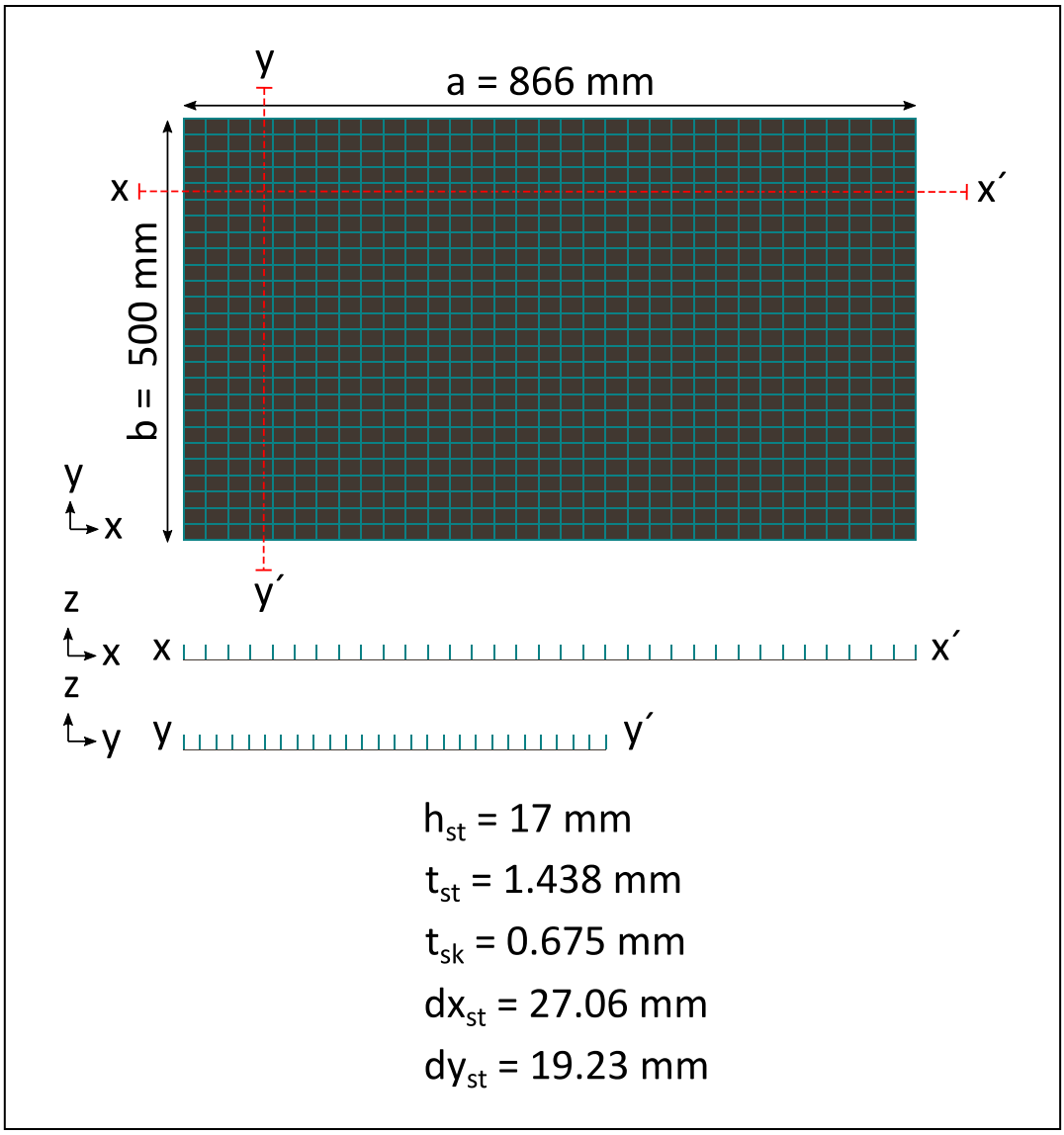

Figure 5.4: Low-weight orthogrid design (theoretical) for a design load of 100 kN

In order to evaluate the manufacturing process for the orthogrid structure specifically, two sample panels are manufactured in parallel to the design and analysis part of the project. These two panels are also tested in order to see if improvements on the test set-up could be made for the larger panels at a later stage of the project. The design for the sample orthogrid panel is shown in figure 5.5. The design variables of the panels shown in figures 5.3 till 5.5 are given in table 5.1 and 5.2.

Table 5.1: Design variables of sandwich panel to be manufactured and tested

Loadcase [kN]	Layup face sheet	Core thickness [mm]	Weight [kg]
100	$[+/-45]_2$	12	2.608

Table 5.2: Design variables of orthogrid panels to be manufactured and tested

Loadcase [kN]	Skin layers [+/-45]	Stiffener layers [0]	Longitudinal stiffeners	Transverse stiffeners	Stiffener height [mm]	Weight [kg]
Small panel	3	7	3	3	20.0	0.426
100	1	2	27	33	17.0	2.376

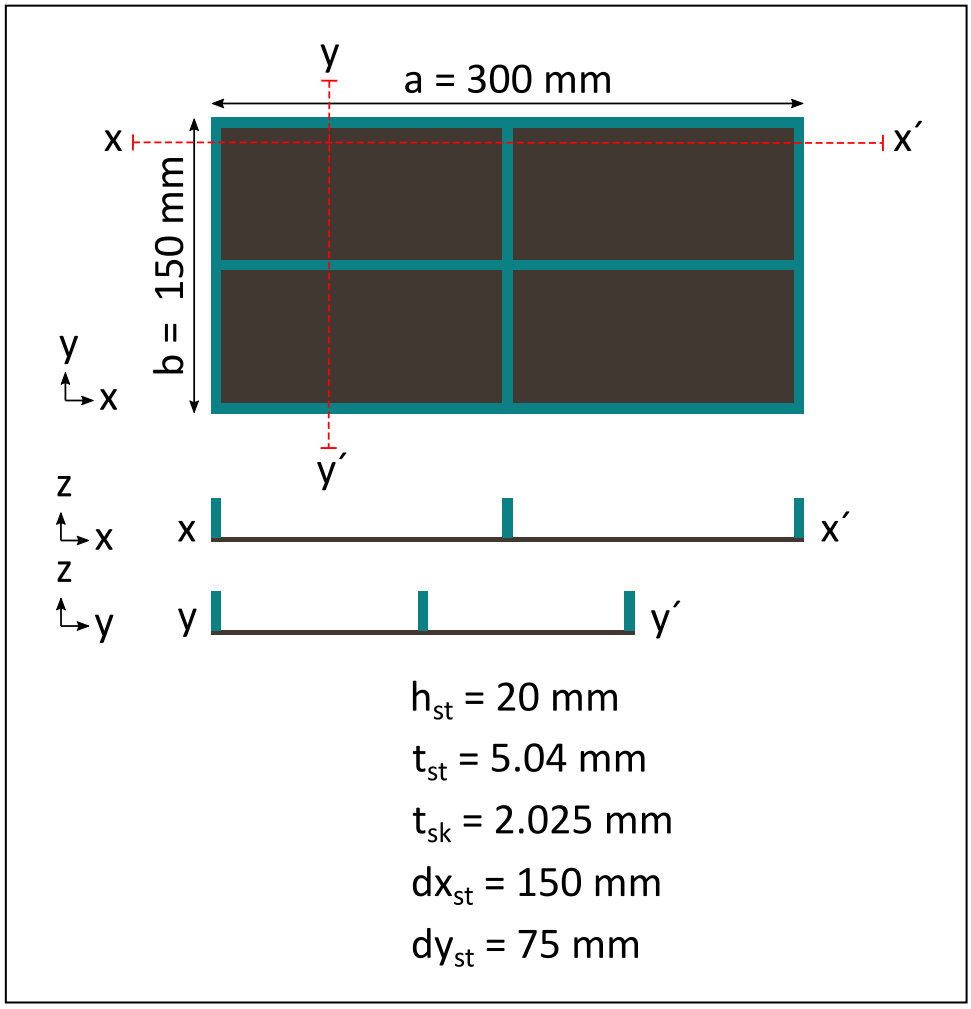

Figure 5.5: Sample orthogrid design

PART II: VALIDATION

In order to validate the low-weight designs obtained, the results will be compared to experimental data. Manufacturing and testing of the panels is therefore outlined in chapter 6. Evaluation of the test data and improvements to the initial models are discussed in chapter 7.

6. Manufacturing and Testing

This chapter is written in chronological order of manufacturing and testing of the different panels, because results from the performed experiments were taken into account to improve the next test. The manufacturing and testing of the sample orthogrid panels will be described first in section 6.1 and was done in parallel with the analytical and numerical work performed during the project. This was done to prevent any delay to the project in case issues with respect to the complexity of the manufacturing and testing would have occurred. The sandwich design to be manufactured and tested is outlined in section 6.2. The larger orthogrid panel design will be dealt with in section 6.3. Finally, concluding remarks will be given on the manufacturing and testing process in section 6.4, where options for further improvements are discussed.

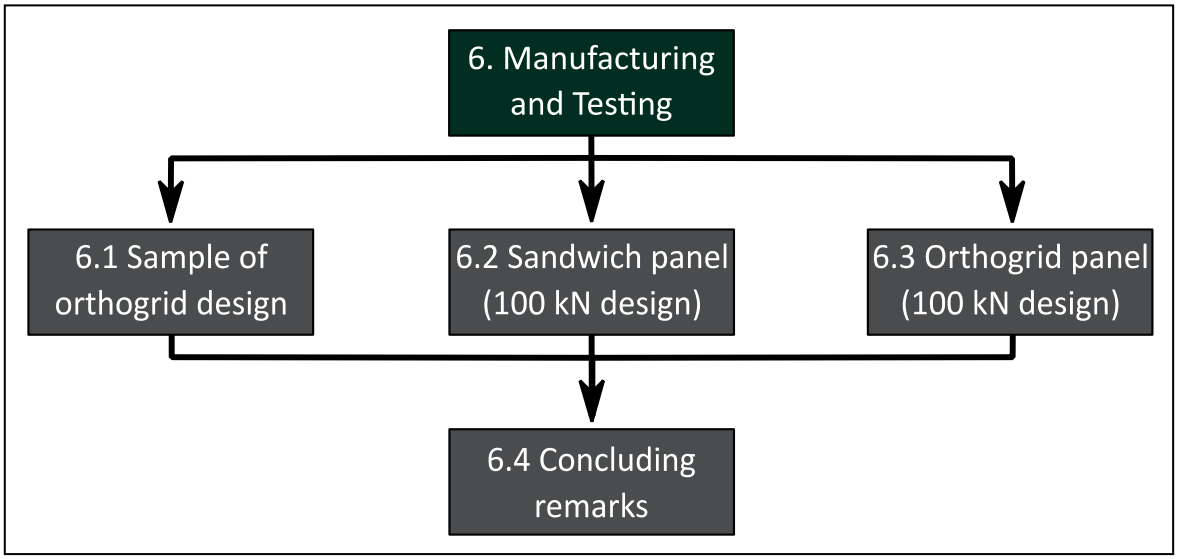

Figure 6.1: Flow chart chapter 6

6.1 Sample of orthogrid design

Since the manufacturing process of flat grid stiffened panels is more complex than the fabrication of flat sandwich panels, the process itself will be analysed and tested before applying it on the larger low-weight designs. Subsection 6.1.1 describes the different steps of the manufacturing process. Testing of two sample orthogrid panels will be outlined in subsection 6.1.2. The last subsection 6.1.3 will evaluate the quality of the final product and will give a conclusion on which method is most suitable for obtaining a high quality product.

6.1.1. Manufacturing process

The complexity of the design results in a difficult manufacturing process. The steps to manufacture two sample orthogrid panels for the project are shown on the flow chart in figure 6.2. Each of the steps from A till G, will be explained in this subsection.

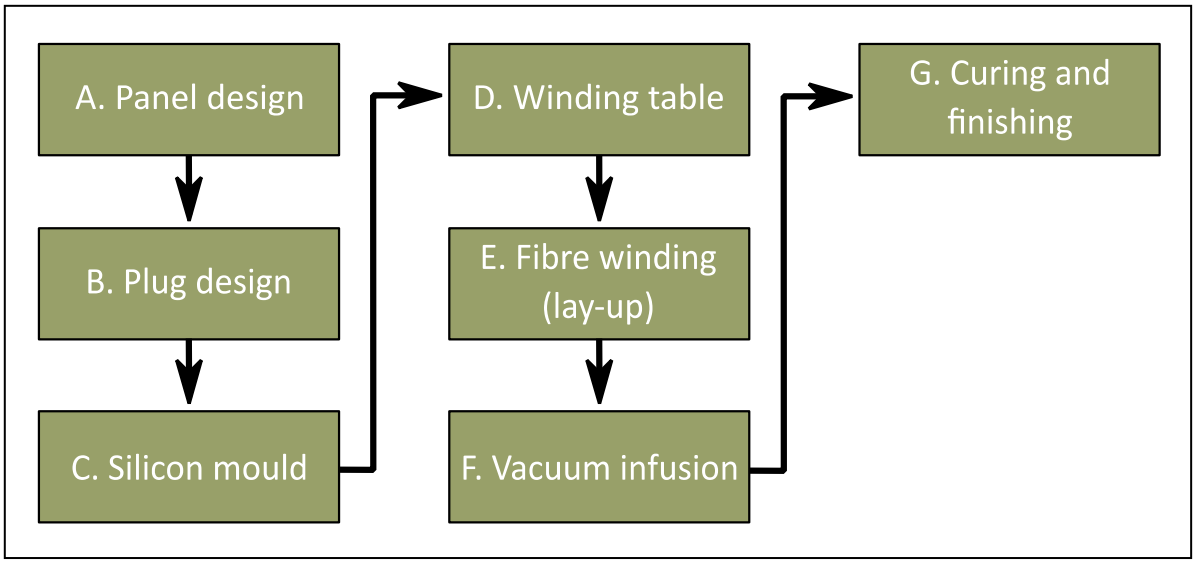

Figure 6.2: Flow chart of the manufacturing steps for the sample orthogrid panels

Step A: Design the panel

The process will start with the determination of all the design variables of the grid stiffened panel. Since tabs should be applied around the complete panel before testing under a compressive load, each side is extended by 50 mm as is indicated in figure 6.3. The added material will also contribute to the quality of the final product, since the edges are normally not as smooth as the material away from the edges. At the node locations, where the transverse and longitudinal stiffeners are crossing each other, extra volume is added by applying a fillet, to obtain sufficient volume for the fibres. This extra volume should prevent the fibre at the nodes to build up twice as fast as the fibre in the stiffener sections. The radius of the fillet at the nodes is equal to the thickness of the stiffener, which should result in the same fibre volume fraction at the nodes and at the stiffener sections.

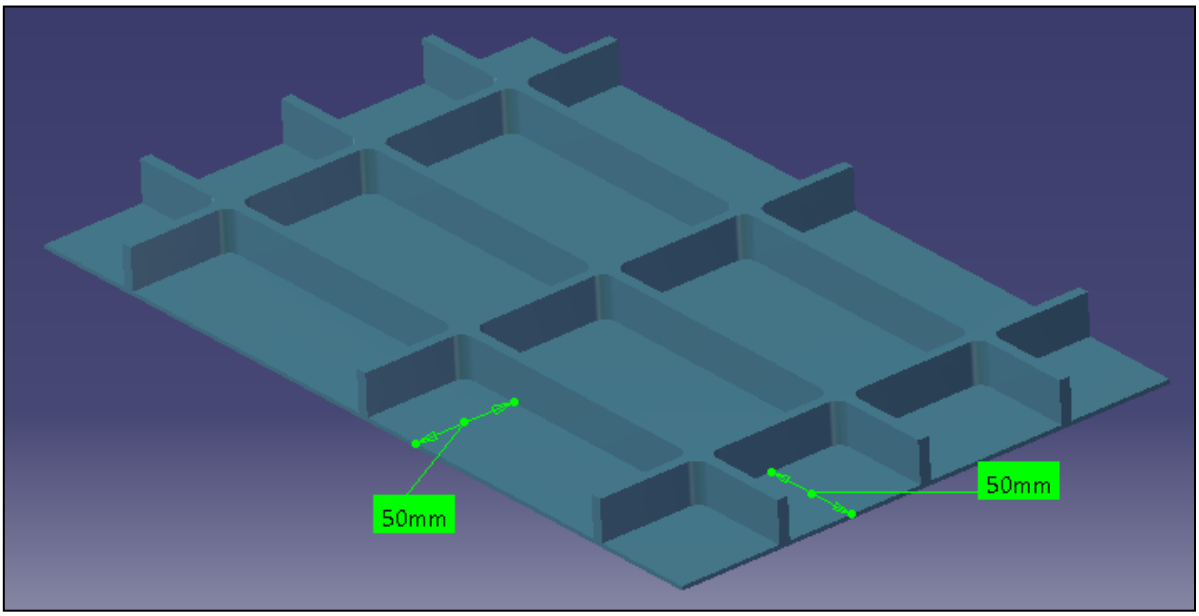

Figure 6.3: Design of sample orthogrid panel

Step B: Build a plug of the design

Knowing the design variable values, a plug of the panel was build with walls around it. The plug of the small orthogrid panel, shown in figure 6.4, was made by milling two layers of 10 mm thick tab material in order to create the designed stiffener height. Two extra layers of 10 mm were milled for obtaining sufficiently high walls on each side of the plug. A flat bottom plate of 2 mm thick tab material was finally milled. The five parts were glued together by applying epoxy resin between all the layers. After curing of the epoxy resin, a test was performed on the water tightness of the plug. This was done to prevent leaking of the silicon during the next step of the process.

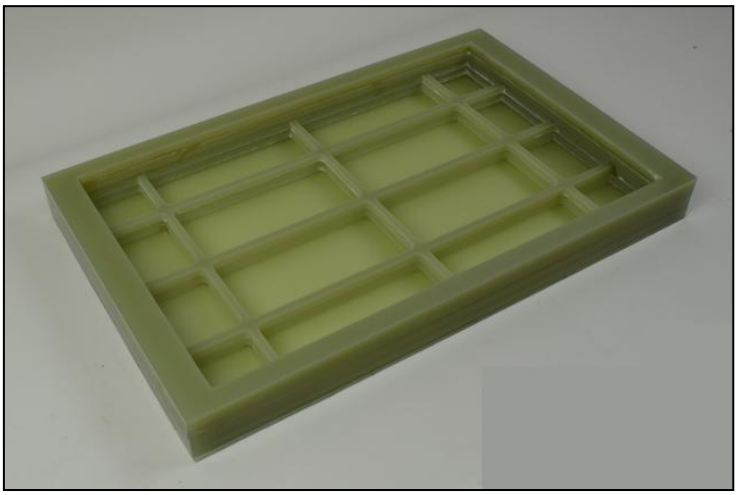

Figure 6.4: Plug of sample orthogrid panel

Step C: Making and post-processing silicon mould

The produced silicon mould is shown in figure 6.5. Uncured silicon is poured in the plug, to form a silicon mould for laying up the dry glass-fibre roving at a later stage. A sufficient amount of silicon was poured into the plug in order to obtain a thick layer connecting the different blocks of silicon. The silicon material used for the mould has a hardness of shore 15. This soft variant of silicon was chosen to enable easy removal of the mould from the product after infusion. Tolerances on the stiffener thickness after manufacturing could be a drawback of the soft mould. As a final step, the mould is inspected on small films of silicon, which could be present inside the channels of the mould. These should be removed to prevent them from influencing the quality of the final product.

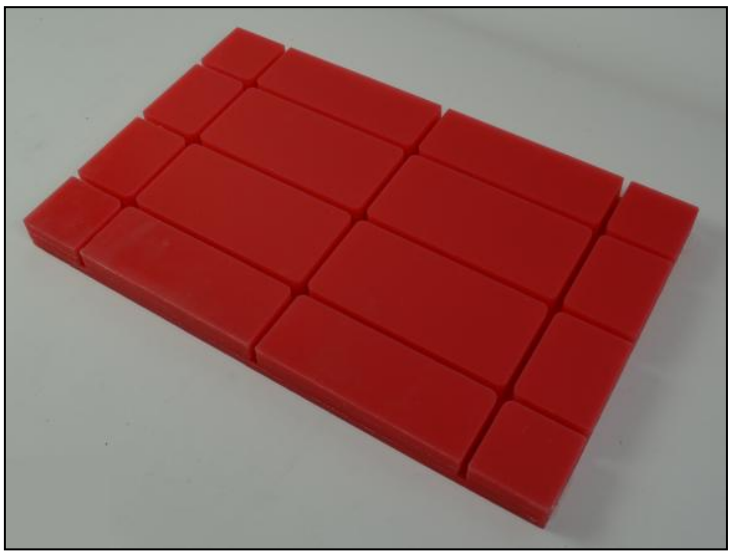

Figure 6.5: Silicon mould of sample orthogrid panel

Step D: Design and build winding table

A winding table shown in figure 6.6 was made to enable the layup of the glass-fibre roving. A sketch of the grid design and the position of the mould was drawn and printed on an A1 sheet. The paper was positioned on a plywood panel along with the silicon mould. Large nails were hammered at the locations indicated by the large red dots on the A1 sheet. Finally, smaller pins were placed at the node locations in the mould and on the sides where the channels are present. This is done to guide the pins through the channels as straight as possible. To ensure accurate and fast placement of these small pins, pin placement tools were used as indicated in figure 6.7.

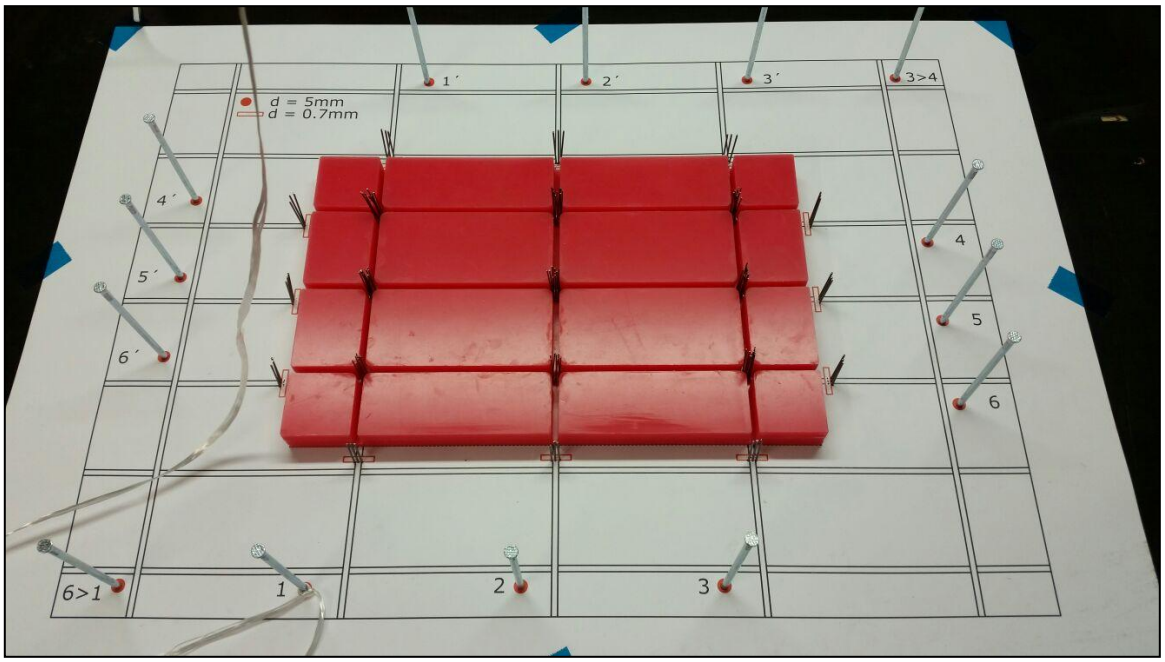

Figure 6.6: Winding table design

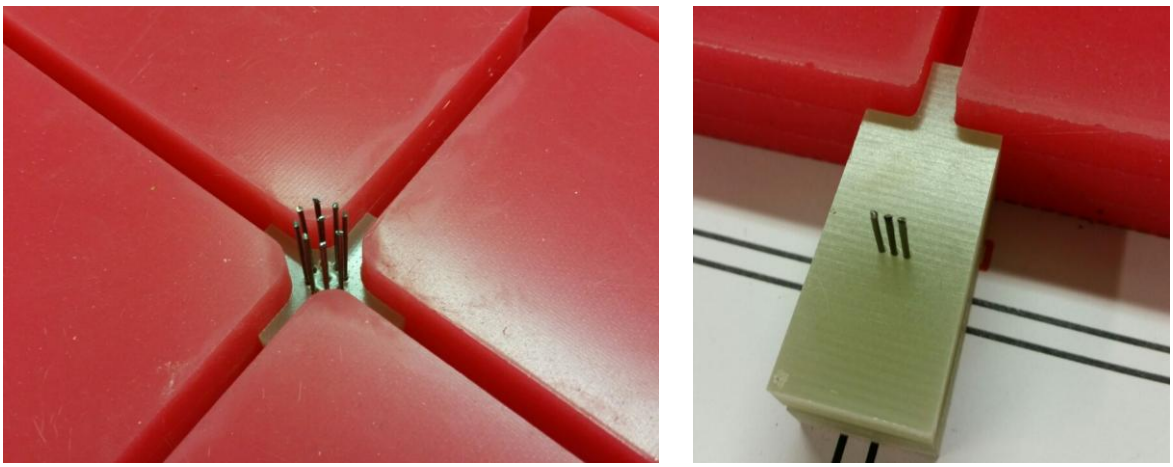

Figure 6.7: Pin placement tools

Step E: Winding of glass-fibre roving manually

Using the winding table, the glass-fibre roving was wound through the channels of the silicon mould as is shown in figure 6.8. The roving was wound through the mould until it was filled to the top of the channels. The filled mould was then prepared for vacuum infusion, which is shown in figure 6.9. All pins were removed and excess glass-fibre roving was cut. The loose roving was connected by tape along the edges of the mould.

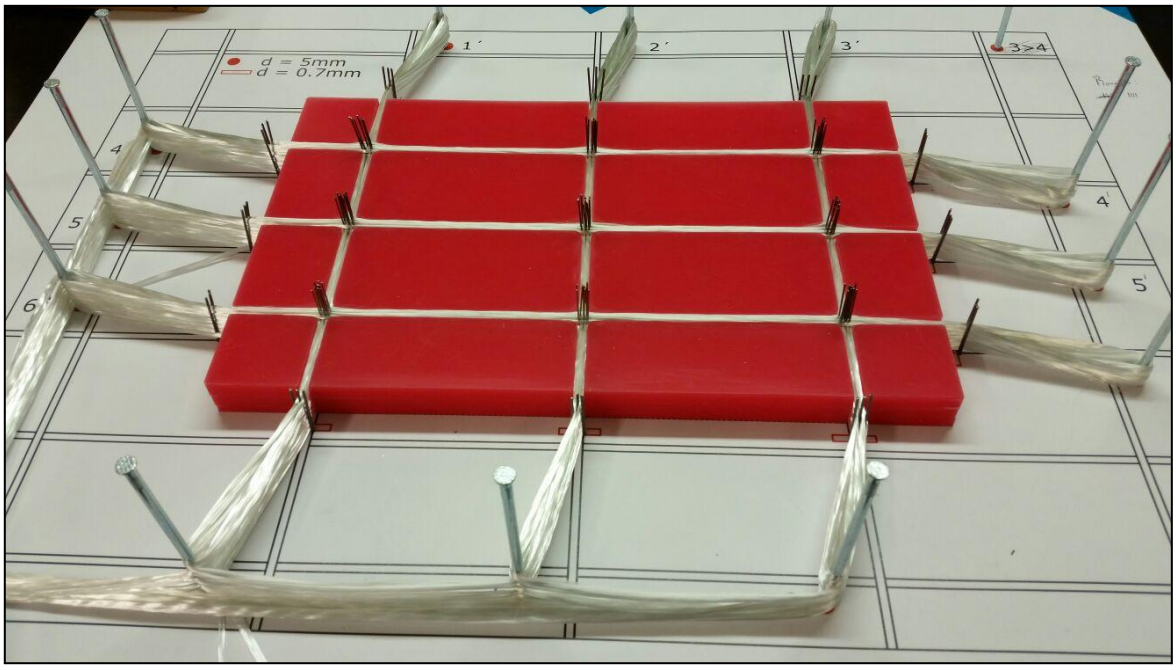

Figure 6.8: Glass-fibre roving wound through the silicon mould

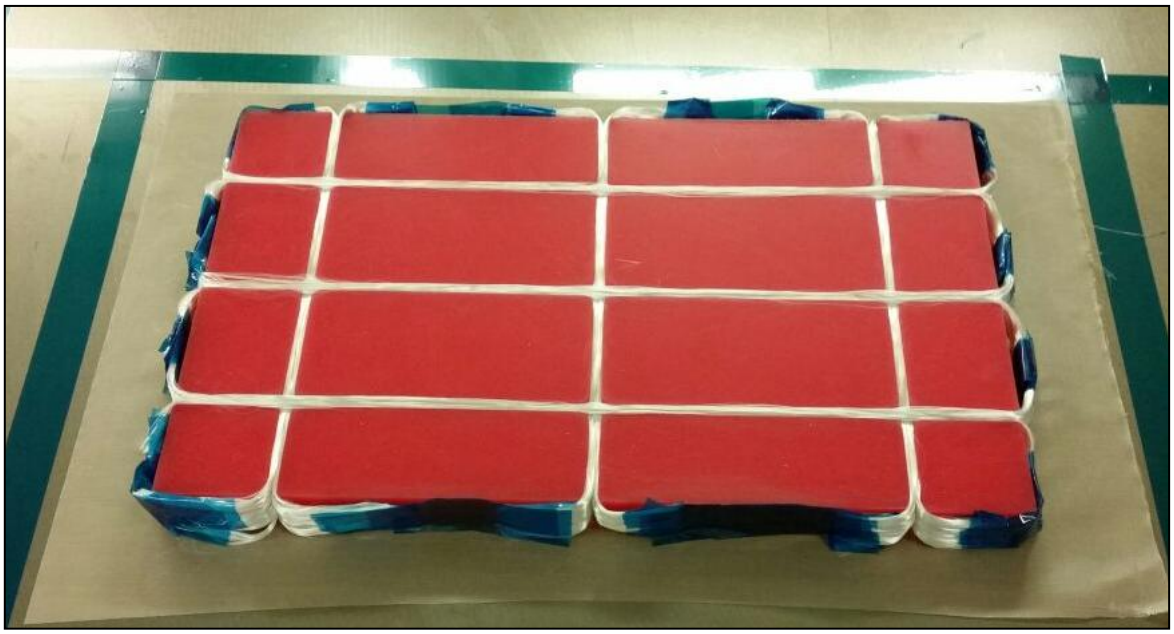

Figure 6.9: Silicon mould, filled with dry glass-fibre roving

Step F: Design vacuum infusion set-up

Impregnation of the dry fibres with resin will be performed with vacuum infusion. In this process, two different set-ups were tried in order to obtain a high-quality orthogrid panel, schematically presented in figure 6.10.

The first set-up (top figure) has the biaxial skin layers placed on top of the silicon mould. A peel ply is placed on both sides of the silicon mould to prevent different layers sticking to each other.

In the second set-up (bottom figure), the filled silicon mould is turned upside down after laying up the glass-fibre skin plies, a peel ply, a flow mesh and another peel ply on top of the silicon mould. Since the silicon mould was relatively small, the turning of the mould can be performed without the glass-fibre falling out of it. In case of a larger mould, an extra plate should be used to turn the mould

upside down. When the mould is laying with the skin on the bottom, the resin flow during the vacuum infusion is supposed to run through the skin first and exit the mould on top. For this, holes were already drilled in the silicon mould prior to winding the glass-fibre roving. These holes can be drilled by using a drill with a 2 mm diameter. In addition, holes at the grid nodes were present due to the steel pins placed during the preparation of the winding table.
The lay-up on top of the most outer peel ply is the same for both infusion set-ups. In figure 6.11, a semi-permeable membrane is placed on top of the peel ply, which only allows air to go through, resulting in vacuum over the full product during the whole infusion process. A breather, caul plate and another breather are placed on top of the membrane to apply an even pressure along the panel and to keep vacuum over the full surface.

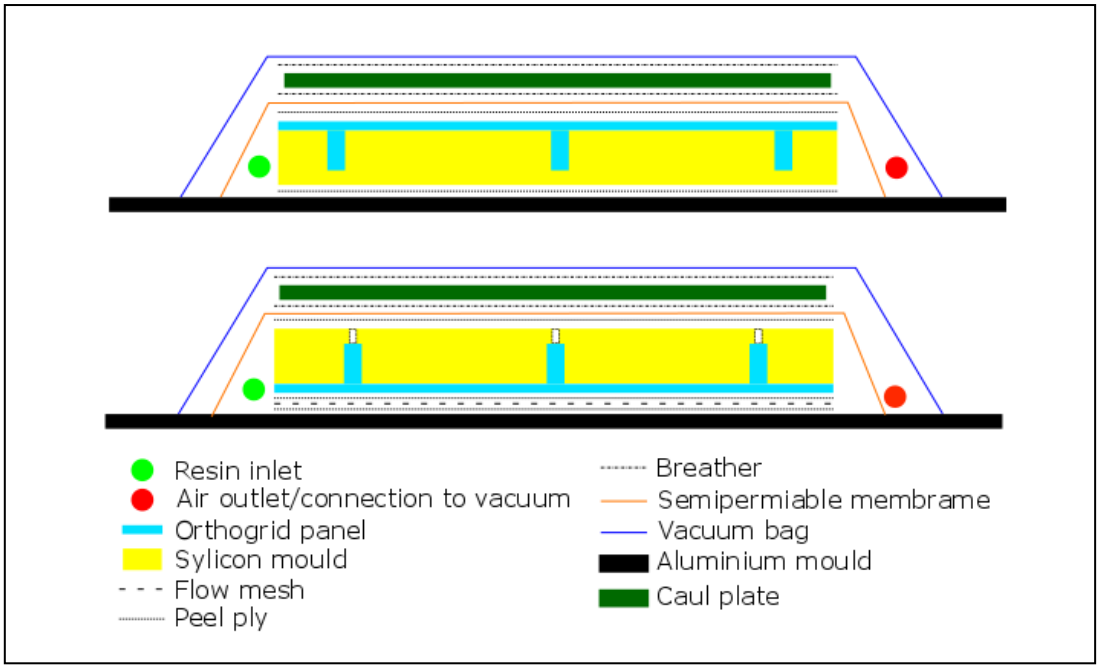

Figure 6.10: Vacuum infusion set-ups for the sample orthogrid panel

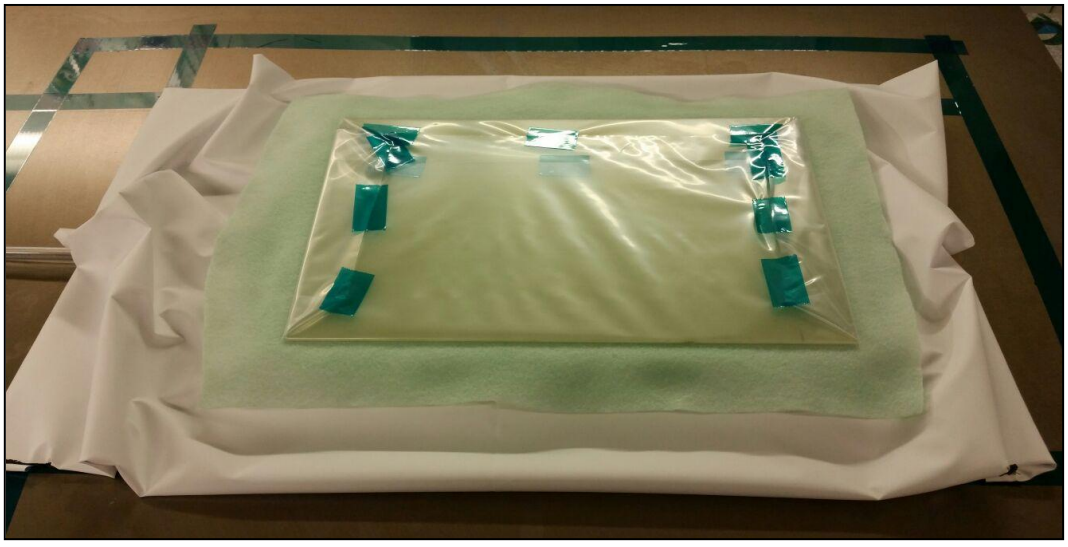

Figure 6.11: Semi-permeable membrane with a breather and caul plate on top

Using a vacuum bag and positioning the air outlet inside, the infusion can be performed as is shown in figure 6.12.

Figure 6.12: Sample orthogrid panel under vacuum

Step G: Curing, post-curing and preparing for testing

The resulting sample orthogrid panels from infusion set-up 1 and set-up 2 are shown in figure 6.13 and 6.14 respectively. The infusion was finished after an hour, where the mould was heated to 30 degrees. An initial cure cycle of 2 hours was performed at 50 degrees Celsius, where after it was cured for 24 hours at room temperature. After removing the product from the silicon mould, a post-cure cycle of 10 hours was performed at 70 degrees Celsius.

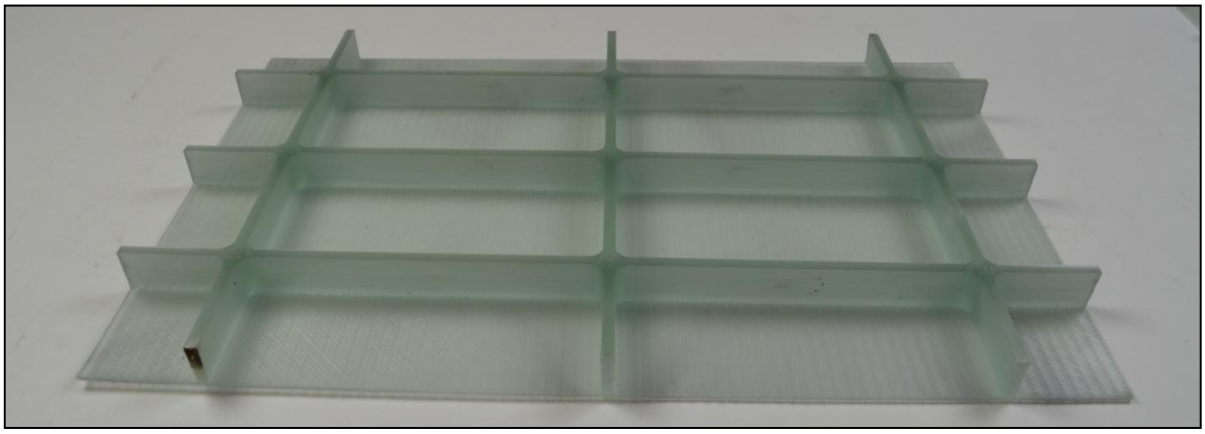

Figure 6.13: Sample orthogrid panel 1

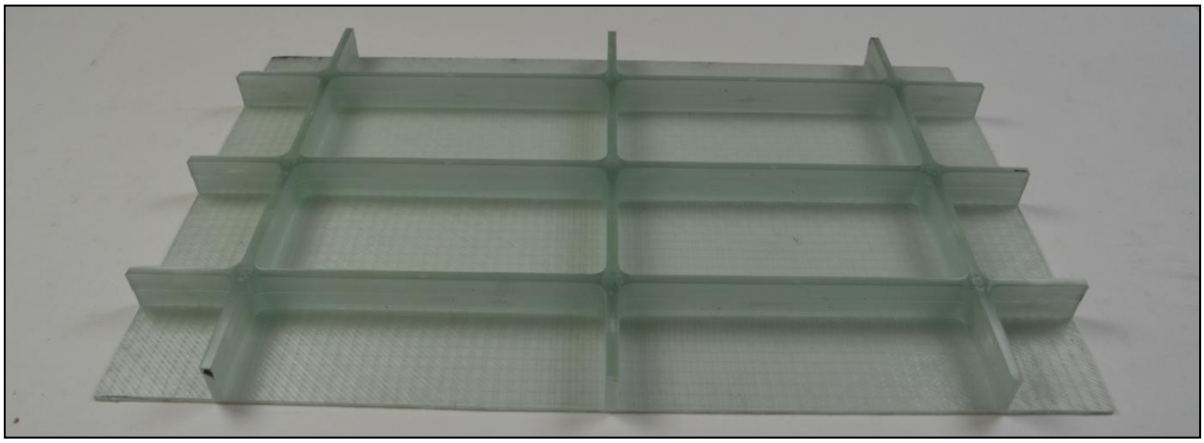

Figure 6.14: Sample orthogrid panel 2

The first panel shows a warpage, which is a result of the asymmetric skin layup. The biaxial glass-fibre plies were a lay-up of [+45] and [-45] degree layers. The layup was corrected for the second panel to [-45, 45, -45, 45, 45, -45], which is still not fully symmetric, but did improve the warpage of the resulting panel.
With the naked eye, voids were found on the first panel, exactly at the middle of each stiffener section as is indicated in figure 6.15. For the second panel, the drilled air outlet holes in the silicon mould, were therefore chosen at the middle of each of the stiffeners. This reduced the size of the voids for the second panel. Holes were not drilled at the small stiffeners at the edges of the panel, where the same voids were found as is shown in figure 6.16.

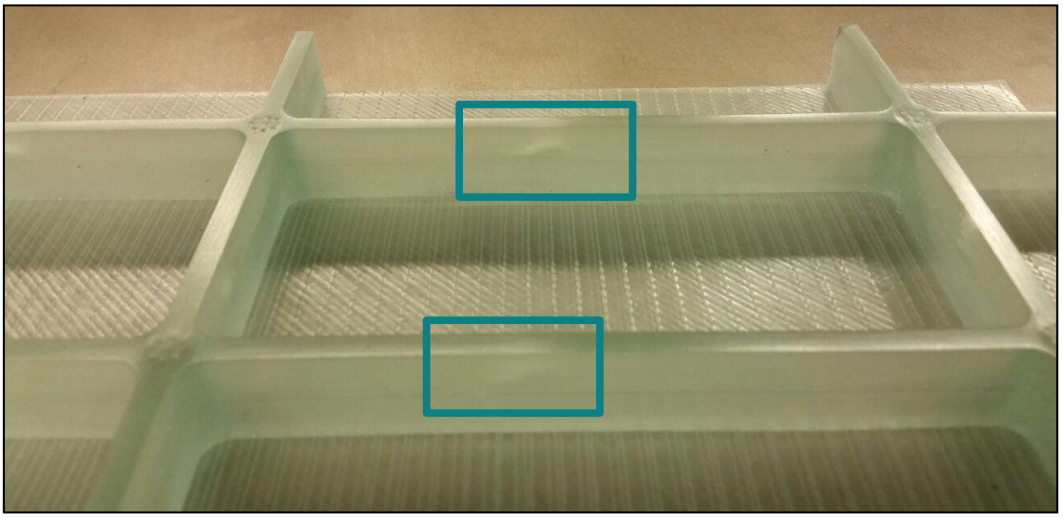

Figure 6.15: Voids at the middle of the stiffeners of sample orthogrid panel 1

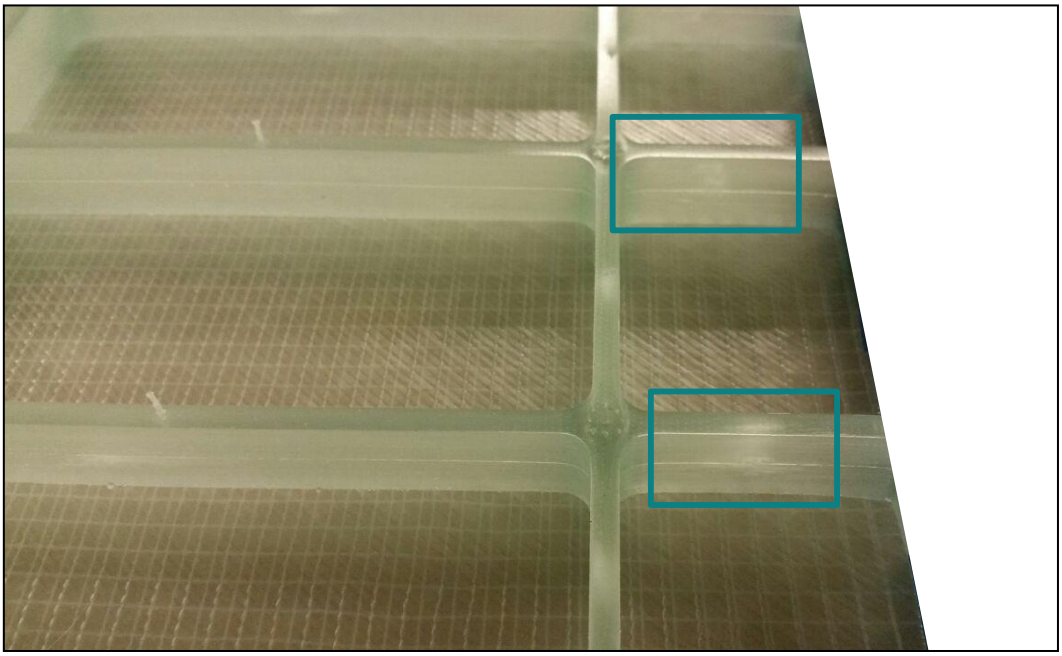

Figure 6.16: Voids at the small stiffener sections at the edges of sample orthogrid panel 2

The infused panels finally have to be prepared for testing. One of the resulting specimens is shown in figure 6.17. The infused panels are supposed to be tested in a compression machine, where the load should be introduced in the structure without crushing the loaded edges. The loaded top and bottom edges of the panels are therefore tabbed and the adjacent cells are filled with bonding paste (green colour). The unloaded edges are also tabbed, because they are supposed to be simply supported during the test. Extra out-of-plane stability is added at the unloaded edges, to prevent local buckling

of the skin or tab material at those locations. This is done by putting small stiffeners between the skin and the applied tab material, without influencing the stiffness in the loading direction. The final panel length a is milled to 380 mm and the width b is milled to 190 mm.

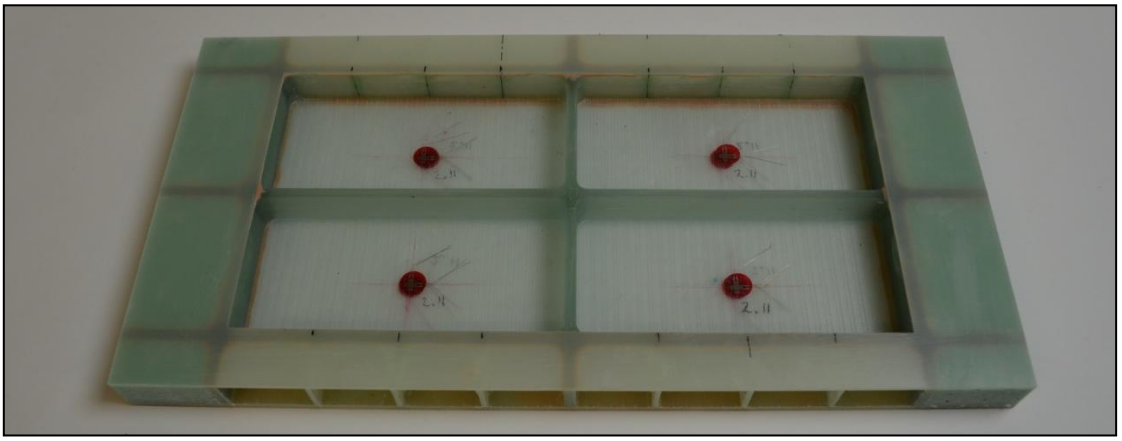

Figure 6.17: Sample orthogrid panel 1, ready for testing

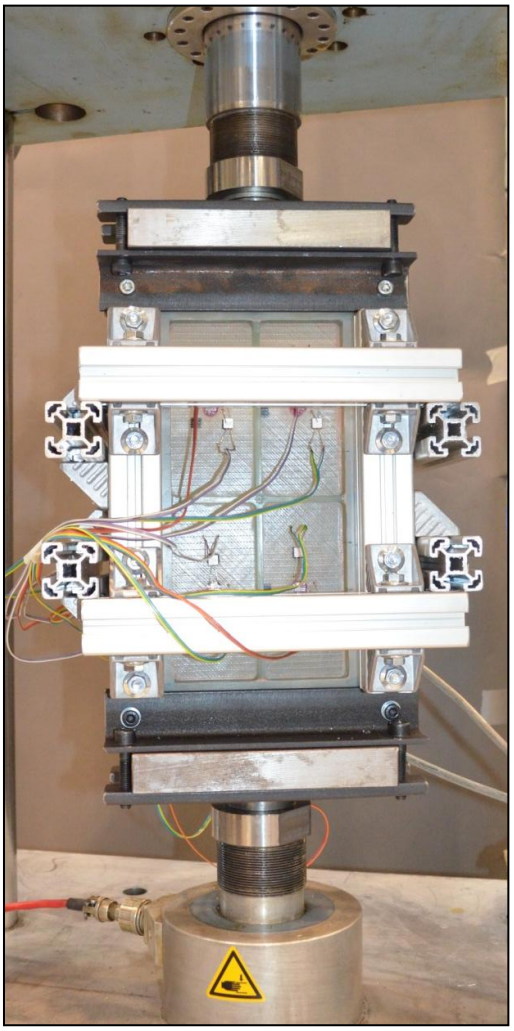

Figure 6.18: Test set-up of sample orthogrid panel 1

6.1.2. Test set-up and general results compression test

This subsection describes the test set-up of the compression test and the general results. Evaluation of the data is written in the next chapter. Since all the analytical and numerical models are based on simply supported boundary conditions, the test set-up is designed in order to simulate these conditions as close as possible. In a general compression test machine, the top and bottom can easily be fixed or supported by the machine. However, the unloaded edges are free to move in the out-of-plane direction, which would result in different behaviour during the test. To introduce the simply supported conditions at the unloaded edges, an aluminium frame is build around the panel as is shown in figure 6.18, which enables the panel to only slide along the frame in the plane of the panel. To prevent the test machine from compressing the frame, the aluminium frame was given a height which enabled the machine to compress the panel up to its critical load without touching the frame. In this particular case, a safety factor of 3 was chosen with respect to the displacement at failure obtained from a non-linear analysis on the numerical model.
Both of the sample orthogrid panels were compressed until final failure occurred. The first orthogrid panel showed combined local buckling of skin and stiffener and finally failed due to the separation of the skin and stiffener as is shown in figure 6.19. The final failure load, where the skin and stiffener separated was found to be a compressive load of 123 kN.

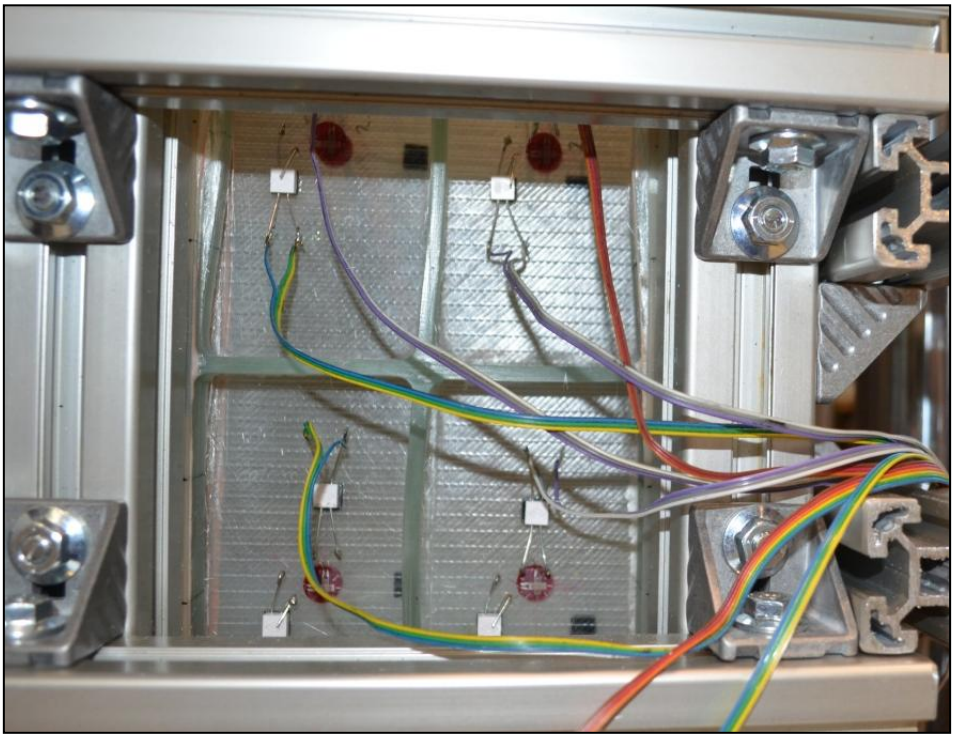

Figure 6.19: Final failure of sample orthogrid panel 1 at -123 kN

The second panel was also undergoing combined local buckling of the skin and stiffener, but the first material failure occurred due to the delamination of the middle bottom stiffener as can be seen in figure 6.20 at a compressive load of 110 kN. After this first stiffener failure, the panel was able to hold the applied force and increased to a compressive load of 112 kN, where the stiffener on the left bottom also failed as is shown in figure 6.21. An image of the skin side after final failure is shown in figure 6.22.

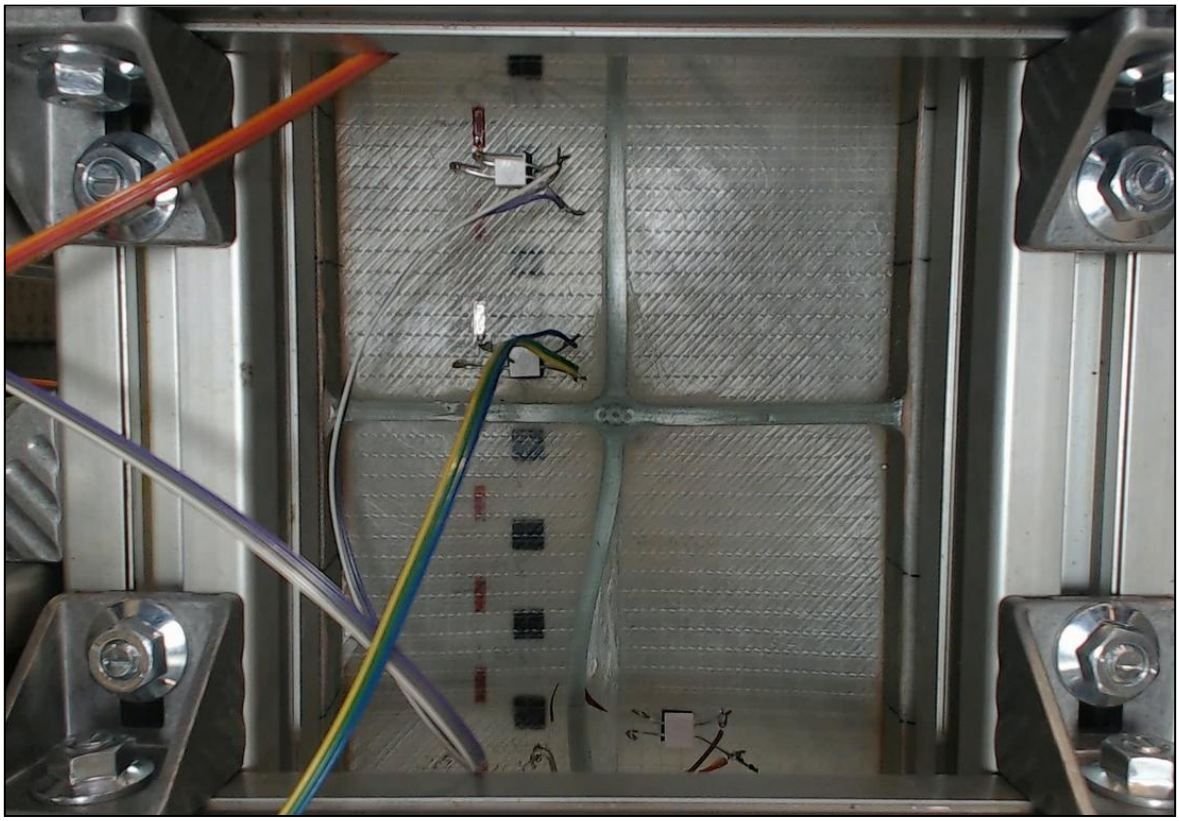

Figure 6.20: Stiffener delamination of sample orthogrid panel 2 at -110 kN

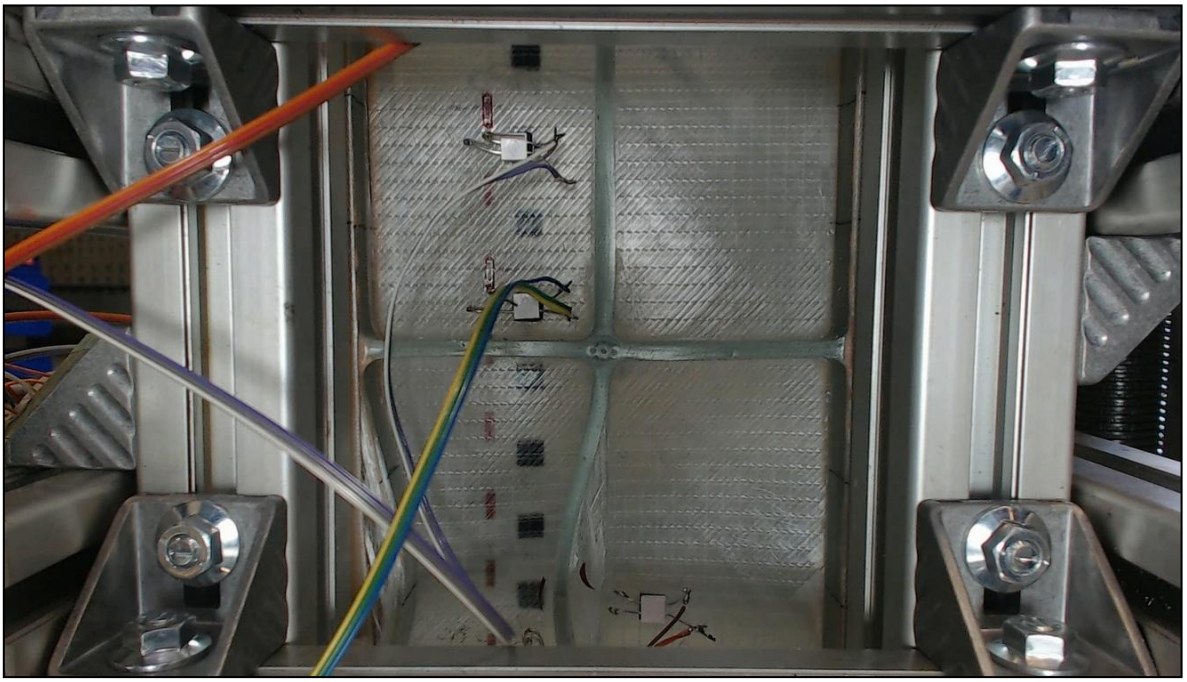

Figure 6.21: Stiffener delamination of sample orthogrid panel 2 at -112 kN

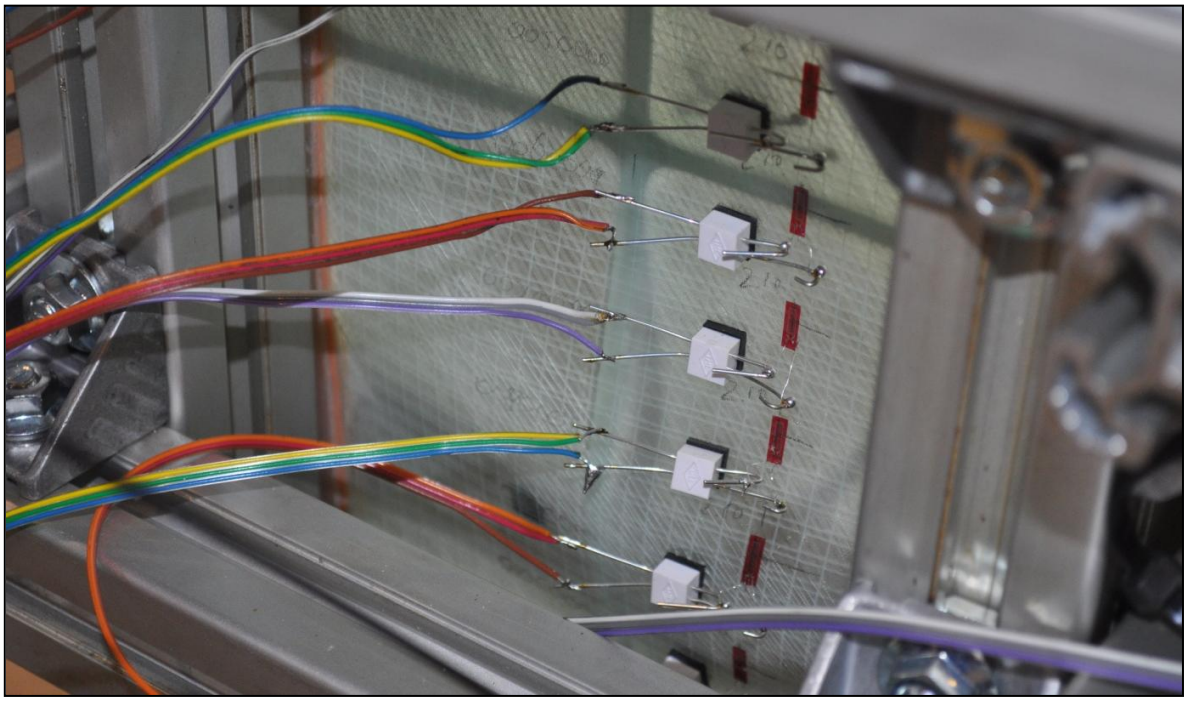

Figure 6.22: Buckled skin after final failure of sample orthogrid panel 2

After both tests, it was observed that the front and aft of the aluminium frame were pressed apart. This was a result of the connection between the front and aft being too weak to counteract the out-of-plane reaction forces. This observation is used to improve the test set-up for the larger panels, where steel wire is used to connect the front and aft aluminium frame.

6.1.3. Quality analysis

This subsection describes the influence of the manufacturing process on the different design variables and summarizes the main deviations found with respect to the design of the sample panels. The fully extended quality analysis and all its measurements can be found in appendix K.
The following design parameters are analysed in this quality analysis:

- Skin thickness
- Stiffener height
- Stiffener thickness
- Stiffener spacing
- Fibre volume fractions

The thickness of the skin was found to be 1.74 mm compared to the design value of 2.025 mm. This lower value will probably result in a lower intracellular buckling load than initially expected, which is why it should be changed in the model in the next chapter.
The stiffener height showed a reduction of 1 mm and 0.7 mm for the first and second sample orthogrid panel respectively, which could be a result of the applied vacuum on the product during the resin infusion.
The largest deviations are found for the stiffener thickness, where measurement are made at 3 locations along the height. The average of the stiffener thickness of sample orthogrid panel 1 was found to be 4.56 mm and for the second sample orthogrid panel an average thickness of 4.32 mm is measured.

As a result of the lower stiffener thickness, the measurements of the stiffener spacing resulted in higher values than initially designed.
The final measurements on the sample panels were performed after the compression test. The fibre volume fractions found for the stiffener and skin are presented in table 6.1.
The stiffeners show a fibre volume fraction of approximately 40%. The material properties for designing the stiffeners are designed with a fibre volume fraction of 50%. The difference should be taken into account, when the numerical model will be improved after evaluation of the test results in the next chapter.
The fibre volume fraction of the skin is found to be 50% and is in good agreement with the material properties used for design.
A negative void volume fraction is found for the skin of the second panel. The void volume measurements are a result of estimated densities for the glass-fibre and the epoxy. Tolerances on these densities could be the explanation of this practically impossible negative void volume fraction.

Table 6.1: Fibre volume fractions sample orthogrid panel 1 and 2

	Fibre Volume Fraction (%)	Resin Volume Fraction (%)	Void Volume Fraction (%)
Panel 1 stiffener	40.15	58.27	1.58
Panel 1 skin	49.58	50.15	0.27
Panel 2 stiffener	40.93	58.06	1.01
Panel 2 skin	51.20	50.88	-2.08

The difference of fibre volume fraction should be adjusted in the numerical model in the next chapter. The stiffness in the fibre direction should be adjusted by first calculating the stiffness of the glass-fibre roving by equation 6.1.

$$E_{\text{fibre}} = 2 * (E_{\text{total}} - E_{\text{resin}} * RVF) = 76300\ [MPa] \tag{6.1}$$

In which:

$$E_{\text{total}} = 39500\ [MPa] \tag{6.2}$$

$$E_{\text{resin}} = 2700\ [MPa] \tag{6.3}$$

$$RVF\text{: Resin Volume Fraction} = 0.5 \tag{6.4}$$

The adjusted total stiffness E_{11} for the glass-fibre roving can then be calculated by:

$$E_{\text{total}} = FVF * E_{\text{fibre}} + RVF * E_{\text{resin}} \tag{6.5}$$

The new values for sample panel 1 and 2 are 32208 MPa and 32797 MPa respectively.

Overall, the quality of both panels showed good results with respect to the quality of the infusion, where low void content was found. The largest tolerances were found for the thickness of the stiffener, especially on the bottom location, where it is connected to the skin. This is probably a result of the silicon mould being pressed into the stiffener at that location.
Method 2 will be chosen to manufacture the larger orthogrid panel, since less voids are found by observations.
The tolerances found during the manufacturing process on the different design variables will be taken into account for the next panel. The design variables will therefore be adjusted prior to manufacturing as such that the final product will have the intended design values.

6.2 Sandwich panel (100 kN design)

The manufacturing process of a sandwich panel is performed by a vacuum infusion. The set-up will be described in subsection 6.2.1. The performed compression test is described in subsection 6.2.2, along with the general observations during the test. A quality analysis will then follow in subsection 6.2.3 to determine the geometric and material properties of the test panel.

6.2.1. Vacuum infusion process

The vacuum infusion process, which is used to make the low-weight sandwich panels is schematically presented in figure 6.23. First, a peel ply is placed on the mould in order to remove the product easily after the infusion process. On top of this peel ply, a flow mesh is placed, to let the resin flow relatively fast along the bottom of the panel. Another peel ply is then applied to prevent the flow mesh to adhere to the product after the epoxy has cured. The product itself is then layed up, using 2 plies of [+45/-45] degree glass fibre material for both face sheets and a foam core of 12 mm thickness in between. On top of the product another peel ply and flow mesh are placed. The final layer will be the vacuum bag.

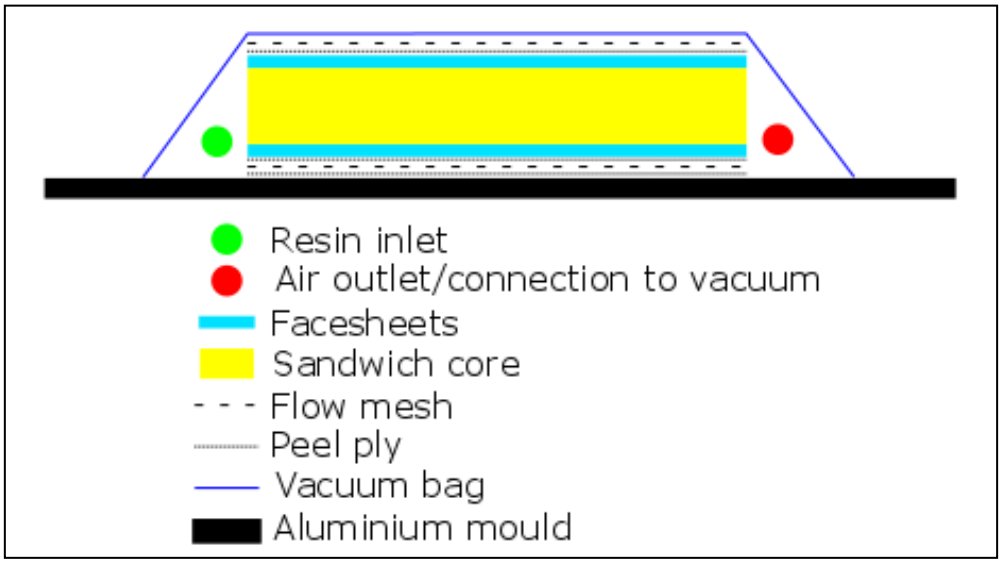

Figure 6.23: Schematic drawing of sandwich panel vacuum infusion process

In order to introduce the loads during the compression test without crushing the panel at the edge, a block of tab material was placed at both loaded edges. The blocks were infused along with the full product, from which the side view is schematically drawn in figure 6.24. Since the block of tab material has a thickness of 10 mm, additional layers of biaxial glass-fibre were placed to create a panel of uniform thickness.

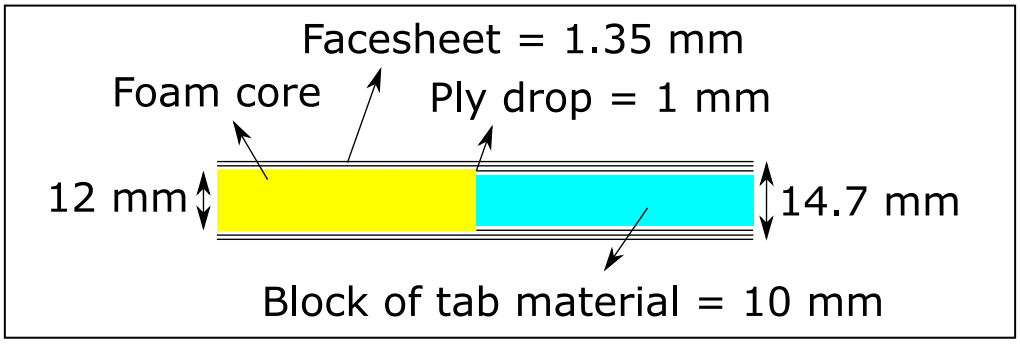

Figure 6.24: Schematic side view of the sandwich loaded edge

All around the panel, tab material of 2 mm thickness is also applied on both sides as is shown in figure 6.25. The tab material will be sliding along the aluminium frame at the unloaded edges during the compression test. Since these tabs are applied, the total length a of the panel is increased from 866 mm to 946 mm. The total width b of the panel is increased with 20 mm on both sides up to a total of 540 mm. Initially, the panel size was manufactured with larger outer dimensions, since the edges are not always of good quality. These lower quality edges were milled from the panel, ending up with the final product.
As a final comment, a dry spot is observed at the top left in figure 6.26, showing the top side of the sandwich panel. This was a result of the vacuum infusion, where the resin was flowing faster on the bottom through the flow mesh. Due to the faster flow on the bottom, the flow front did not go linearly along the length of the panel at the top. This resulted in the encapsulation of some air. This could be improved by shortening the flow meshes above and below the panel.

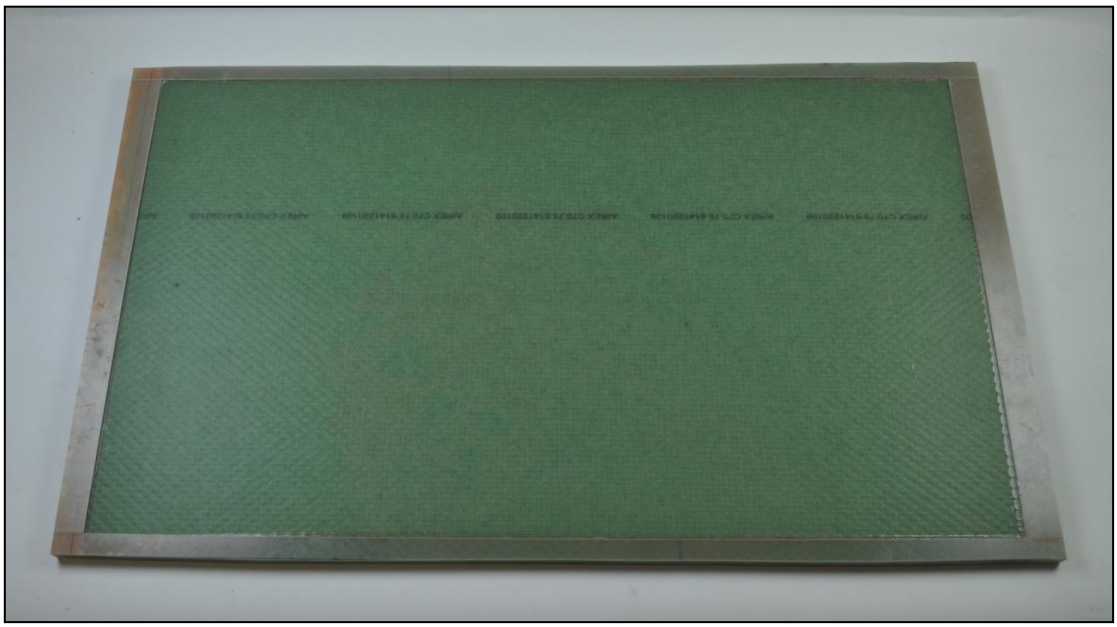

Figure 6.25: Vacuum infused sandwich panel (bottom)

Figure 6.26: Vacuum infused sandwich panel (top)

6.2.2. Test set-up and general results compression test

This subsection described the improved test set-up used for the larger panel tests and gives the general results observed during the test. Evaluation of the compression test data is performed in the next chapter.
The full test set-up as it was designed initially is shown in figure 6.27. Video cameras were positioned along with lighting on both sides of the compression machine. The aluminium bars connecting the front and aft frame are replaced by steel wire on three locations along the height of the frame. This replacement should prevent the frame from moving out of its plane. However, as indicated in figure 6.28, the wire elongated as a result of the out-of-plane forces from the sandwich panel, which started to bend. Due to the stretching of the wire, the test was aborted, because any damage to the test frame as a result from a breaking wire had to be prevented.

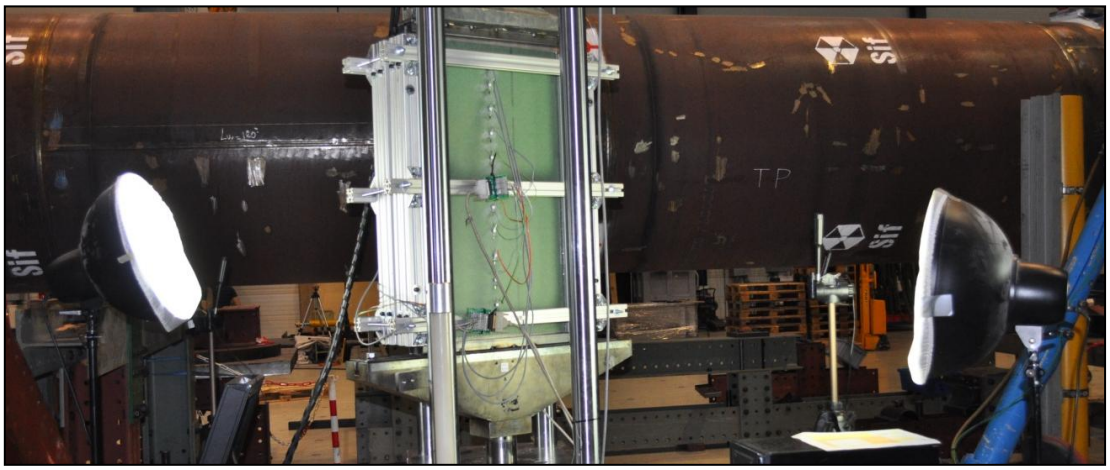

Figure 6.27: Test set-up sandwich panel

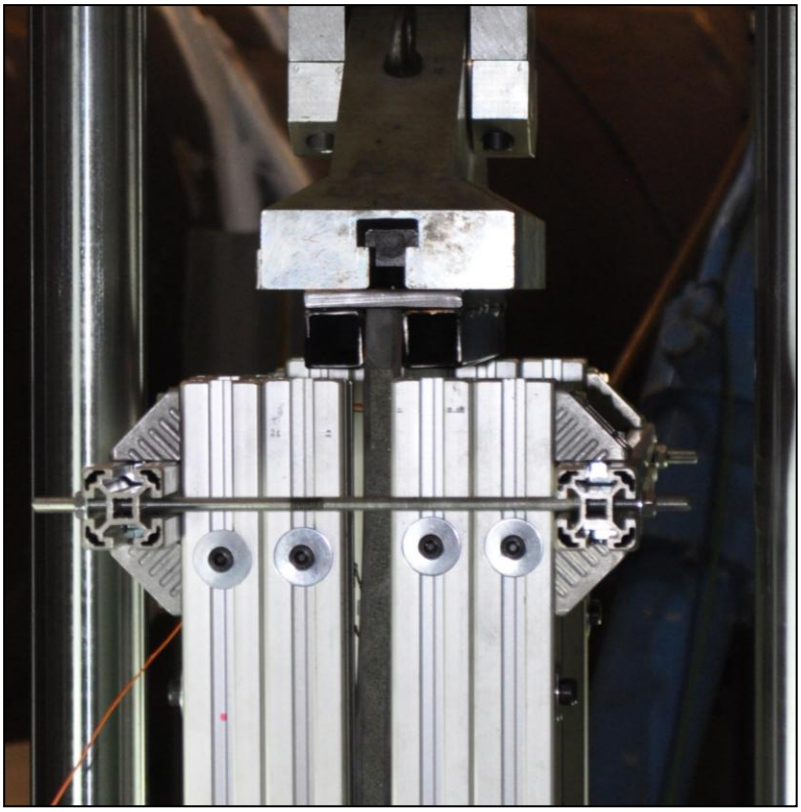

Figure 6.28: Elongation of the steel wire after sandwich bending

In order to improve the test set-up and prevent the aluminium frame from moving out-of-plane, additional stiffness to counter the reaction forces is introduced by applying steel L-profiles connected by thick steel bolts, as shown in figure 6.29. The already tested sandwich panel was compressed again in order to conclude if the extra stiffness would improve the test.
The second test did not show any observable out-of-plane movement of the aluminium frame anymore and was therefore considered successful. The sandwich panel was loaded up to its final failure at a compressive load of 149 kN.

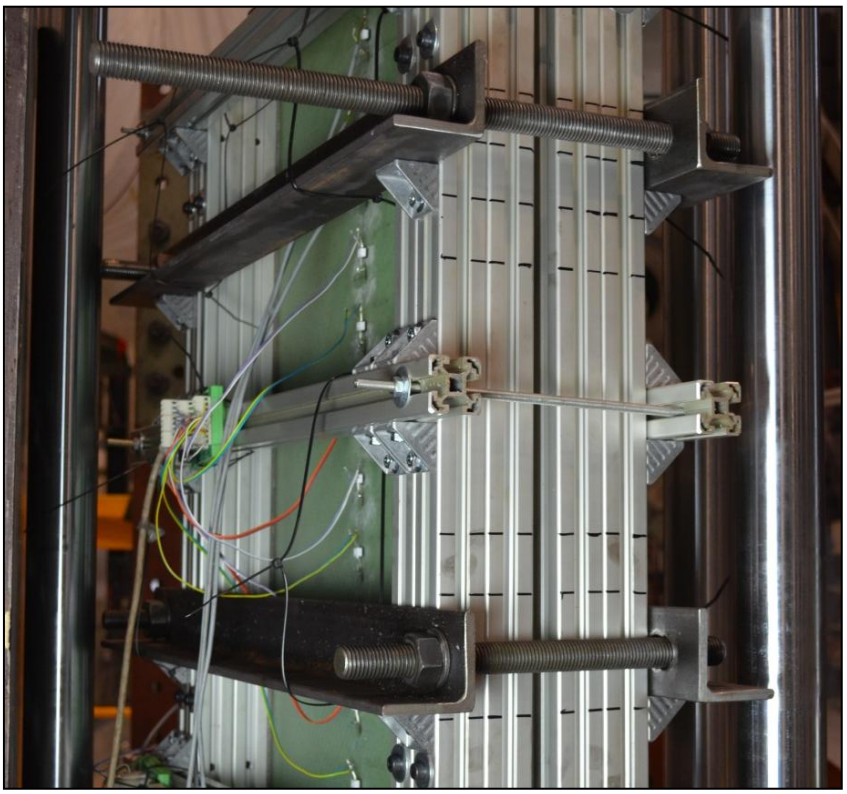

Figure 6.29: Improved aluminium frame, supported by thick steel wire

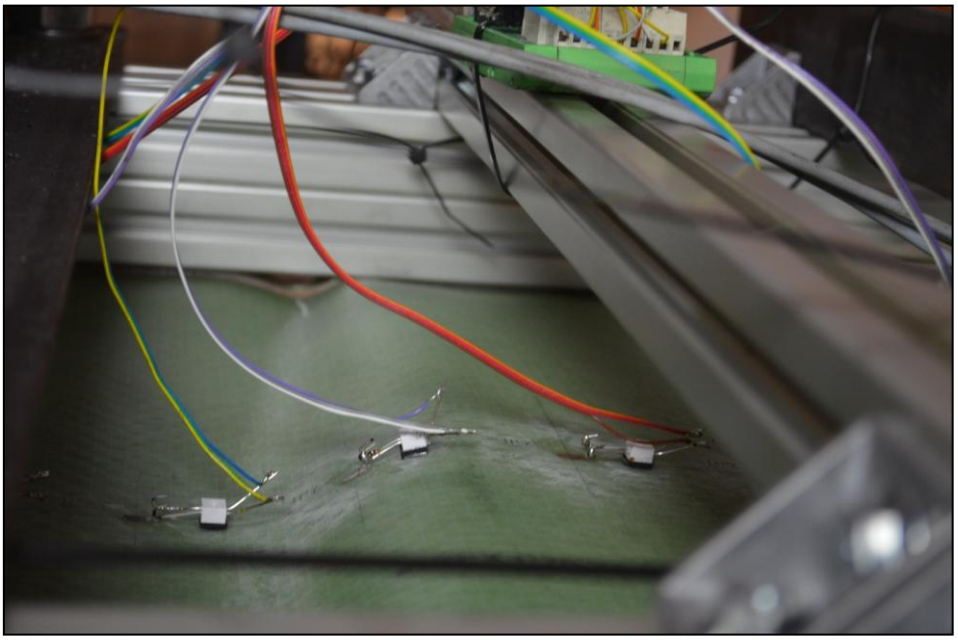

Figure 6.30: Final failure of the sandwich panel after the second (improved) test

Buckling of the panel initiated at approximately -135 kN, where after the final failure occurred as it is shown in figure 6.30. The face sheets had wrinkled along the width of the panel.

6.2.3. Quality analysis

To determine the quality of the sandwich panel, geometric and material properties are measured. The full quality analysis, with all the performed measurements can be found in appendix L. These can be divided in the following measurements:

- Total thickness
- Thickness foam core
- Thickness face sheet
- Fibre volume fractions

The average total thickness of the panel was measured to be 14.473 mm, which is 0.227 mm thinner than the designed value.
The foam core thickness was measured prior to manufacturing and has an average of 12.155 mm, which is slightly higher than the design value of 12 mm. The difference is explained by manufacturing tolerances of the foam core material.
The thickness of the face sheets are determined by subtracting the foam core thickness from the total average thickness. This results in a value of 2.318 mm of both face sheets. Since one face sheet is a stacking of 2 layers of biaxial glass-fibre, 1 ply is giving a thickness of 0.580 mm. This is different from the thickness used for design, where 1 ply was considered 0.675 mm.
Fibre volume fraction measurements are performed on different locations on the sandwich panel, both on the bottom (figure 6.25) and the top (figure 6.26) of the panel. This was done by cutting pieces of the sandwich panel and sawing the foam core from the small cuts. The excess foam core material was sanded and polished until no foam core material was present on the surface of the piece of face sheet.
The average fibre volume fraction for the top and bottom is taken from a total of 3 measurements each. The small difference is addressed to tolerances in the measurements, since the sanding and polishing of the foam core from the piece of face sheet influences the measurements. A total average of approximately 49% could therefore be given for the fibre volume fractions, which is considered to be in sufficient agreement with the datasheet of the material.
The resin and void volume fraction show no considerable values and are therefore not further taken into account.

Table 6.2: Fibre volume fractions sandwich panel

	Fibre Volume Fraction (%)	Resin Volume Fraction (%)	Void Volume Fraction (%)
Facesheet (top)	48.44	51.05	0.51
Facesheet (bottom)	49.53	49.77	0.70

6.3 Orthogrid panel (100 kN design)

The theoretical low-weight orthogrid design for a design load of 100 kN will be manufactured and tested. Subsection 6.3.1 describes the manufacturing process, of which some steps are changed with respect to the earlier sample orthogrid panels as a result of the larger dimensions. A description of the test set-up and the general observations are outlined in subsection 6.3.2. The quality analysis is summarized in subsection 6.3.3.

6.3.1. Manufacturing process

The different steps involved in the manufacturing of the larger orthogrid panel are the same as for the sample panel, but some have been changed as a result of the increased size. The flow chart in figure 6.31 shows the different steps.

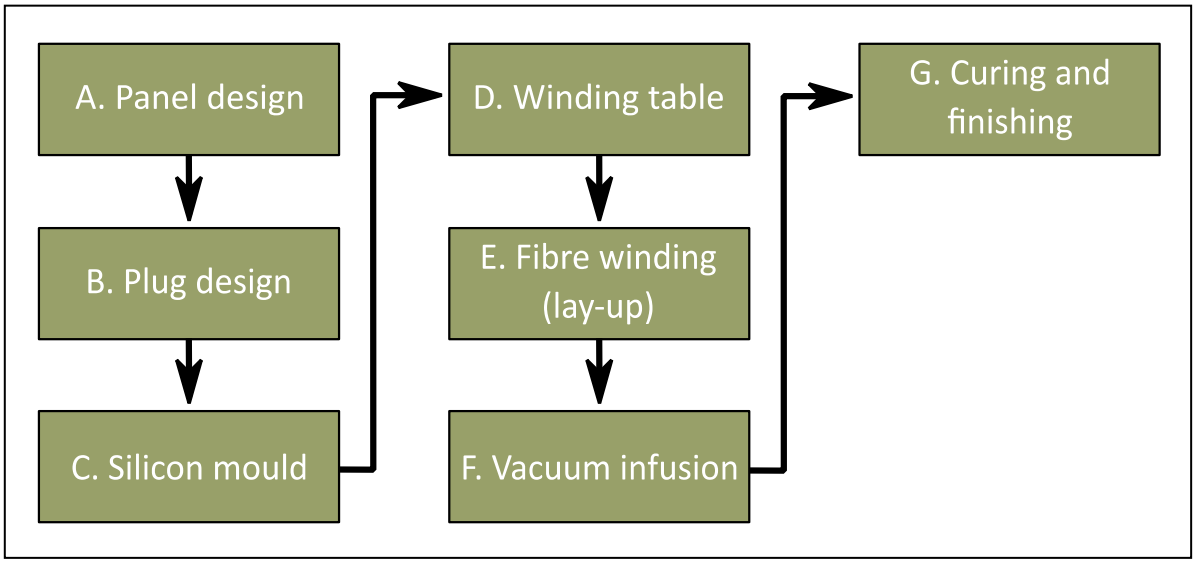

Figure 6.31: Flow chart of the manufacturing steps for the large orthogrid panel

Step A: Design the panel

The design of the 100 kN orthogrid is based on the theoretical found low-weight solution and is shown in figure 6.32. An extra 60 mm is added to the length of the design at both sides, which is used for tabbing and supporting the orthogrid panel to the compression test machine. The width b is extended with 40mm on both sides, because tab material will be placed to be simply supported to the aluminium frame during the test.

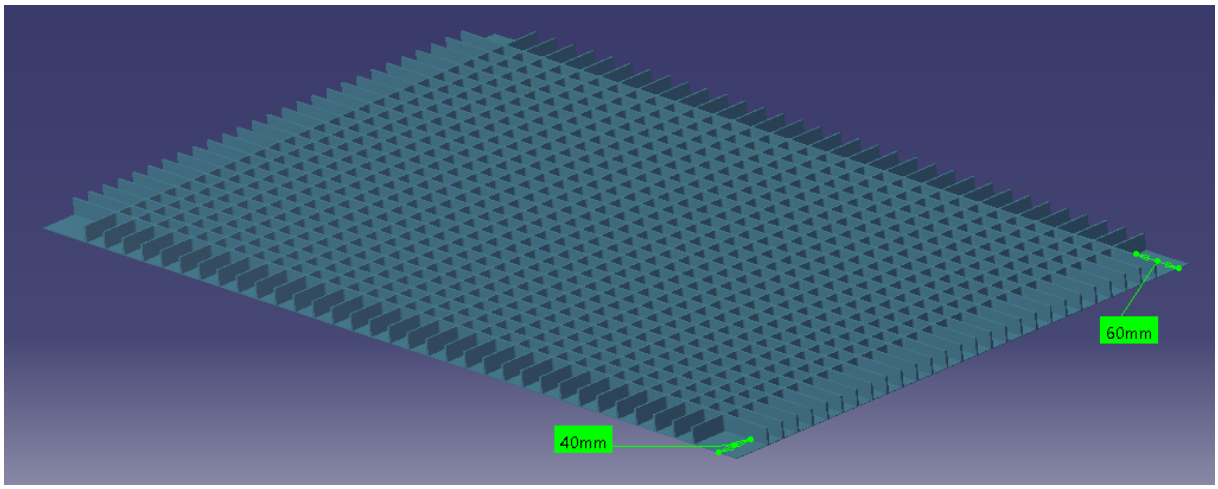

Figure 6.32: Theoretical low-weight orthogrid design, design load of 100 kN

From the quality analysis of the sample orthogrid panel, mainly the stiffener thickness was reduced by tolerances on the plug manufacturing, pouring of the silicon mould and the vacuum infusion of the final product. These tolerances are taken into account, in order to obtain a final product having the initially designed dimensions.

6.3 Orthogrid panel (100 kN design)

Table 6.3 shows the additions to the skin thickness taken into account. The orthogrid design has a stiffener thickness of 1.438 mm. On average the thickness of the stiffener was reduced by approximately 0.67 mm from the mould to the product, which explains the factor in the third column. Since the plug cannot be manufactured by milling as a result of the size of the panel, a 3D printed grid was ordered in eight parts. Since tolerances were not known for the 3D printing technique, no additional thickness was added. The grid was therefore 3D printed with a stiffener thickness of 2.11 mm. The other design variables are printed as initially designed.

Table 6.3: Tolerances during manufacturing process

Design variable	Product	Factor	Mould	Factor	Plug
Stiffener thickness	1.438	(1.438)+0.67	2.11	(2.11)+0.0	2.11

Step B: Build a plug of the design

Due to the size and number of stiffeners, milling of the plug was not an option anymore. The grid was therefore 3D printed in 8 several parts, of which one is shown in figure 6.33. The 3D printing method used was Fused Deposition Modeling (FDM) with a layer thickness of 200 microns. The quality of the 3D prints were relatively good and low tolerances allowed to glue the 8 parts together with bonding paste as is shown in figure 6.34. The bottom and walls of the plug were cut from tab material and were glued and made watertight by using a silicon sealant.

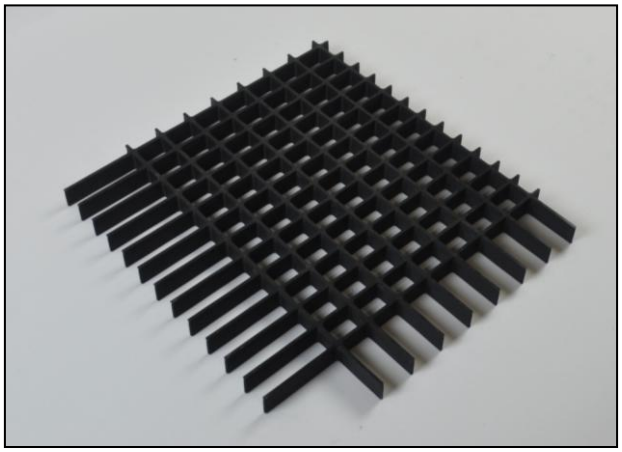

Figure 6.33: Piece of 3D printed grid for the plug

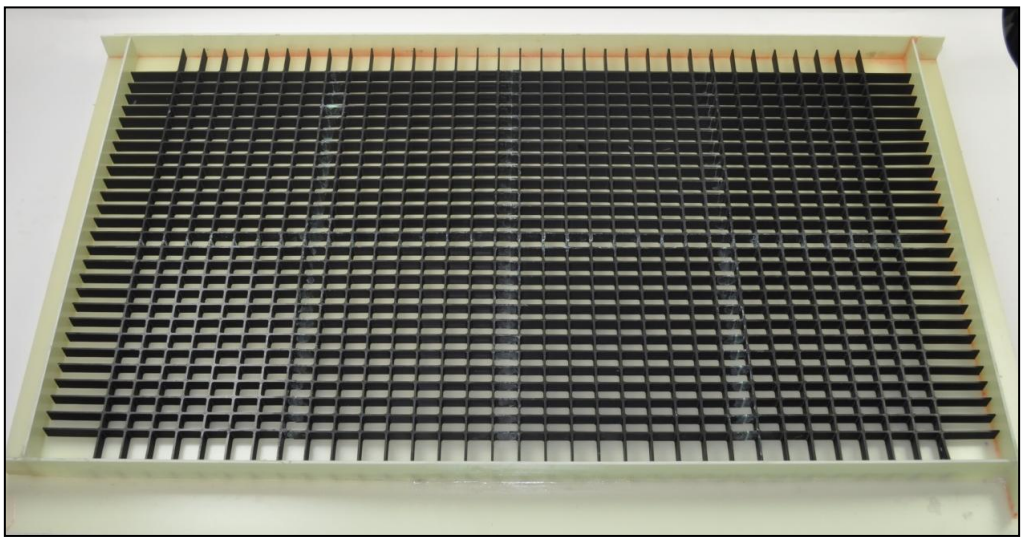

Figure 6.34: Plug of the 100 kN orthogrid design

Step C: Making and post-process silicon mould

The shore-15 silicon was poured into the 3D printed plug as is shown in figure 6.35. After 24 hours of curing, the mould could be removed. After the cured mould was removed from the plug, some post-processing steps had to be performed in order to make it ready for winding the glass-fibre roving and vacuum infusion.

The first step was to peel off all the excess silicon, which was present at the top of all channels. This excess silicon was a thin film as a result of the 3D printed plug not completely glued to the bottom plate. This post processing step could be prevented when the whole 3D printed grid was fixed to the bottom plate over the full surface.

The second step was the drilling of holes at the bottom of the silicon mould at every middle location of the stiffener, in order to have a sufficient number of air outlets during the vacuum infusion process. A total of 952 (34*28) holes were drilled, using a drill of 2 mm in diameter.

The finished silicon mould is shown in figure 6.36.

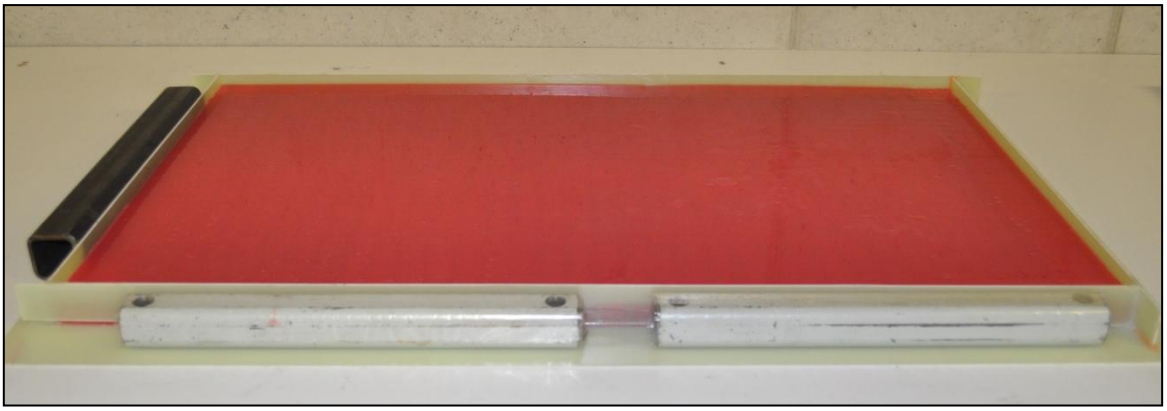

Figure 6.35: Silicon curing in the 3D printed plug

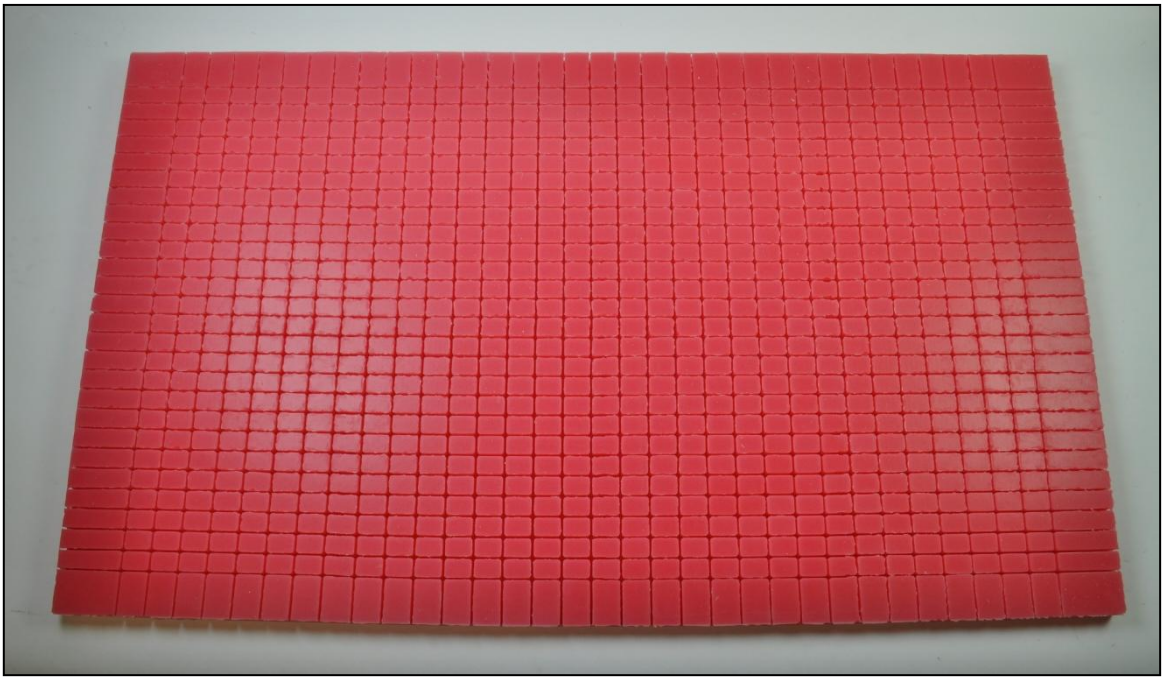

Figure 6.36: Finished silicon mould of the theoretical low-weight orthogrid panel

Step D: Design and build winding table

The winding table is shown in figure 6.37. A drawing of the positions of the nails on the edges and the location of the silicon mould was printed on A0 paper and it was taped to a plywood board. The silicon mould itself was first placed on a wooden plate, because it had to be turned upside down after the winding process had finished.

As a last step, a total of 891 pins were placed at each stiffener crossing in order to steer the fibre in two directions. The aim is to prevent the fibre from building up twice as fast as in the stiffener sections. The pins also introduced an extra hole in the mould, which could improve the air outlet during the vacuum infusion.

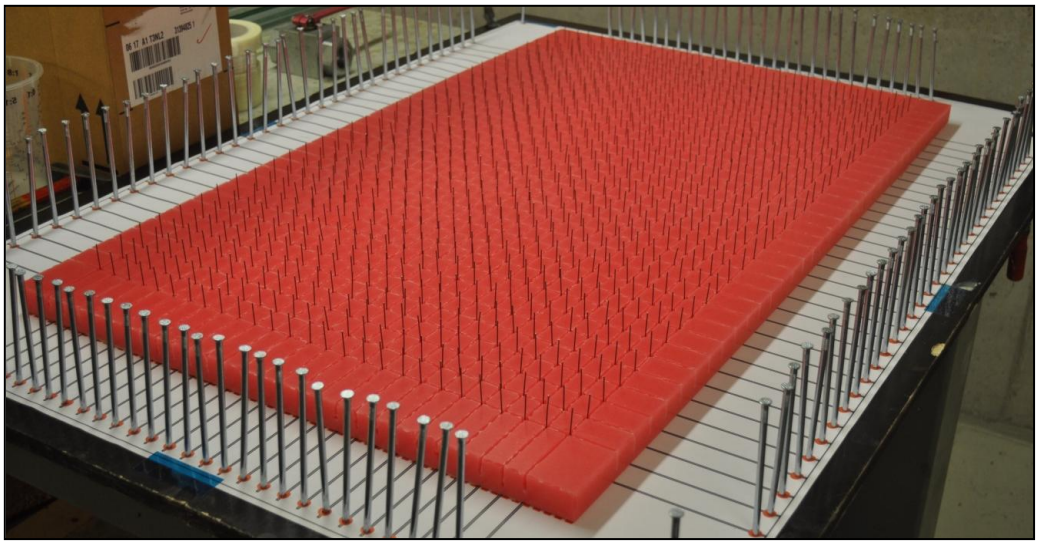

Figure 6.37: Winding table of the theoretical low-weight orthogrid panel

Step E: Winding of glass-fibre roving manually

The glass fibre was wound manually through the silicon mould, as is partially shown in figure 6.38. A total of approximately 750 meter of glass-fibre roving completely filled the silicon mould, which took almost 3 full days to finish. After the silicon mould was fully filled, the nails were removed and the excess roving was taped together at the side as shown in figure 6.39.

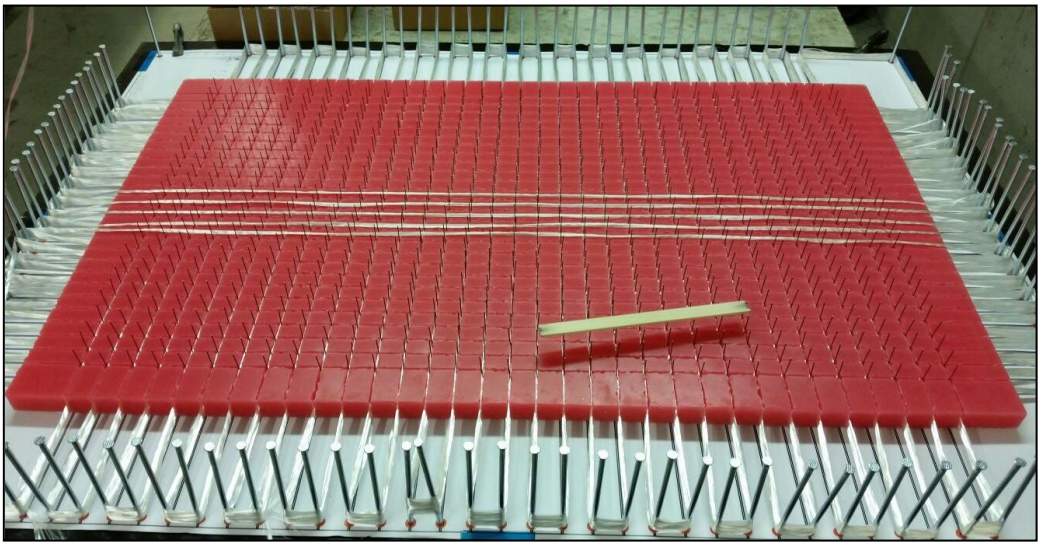

Figure 6.38: Winding of the glass-fibre roving of the theoretical low-weight orthogrid panel

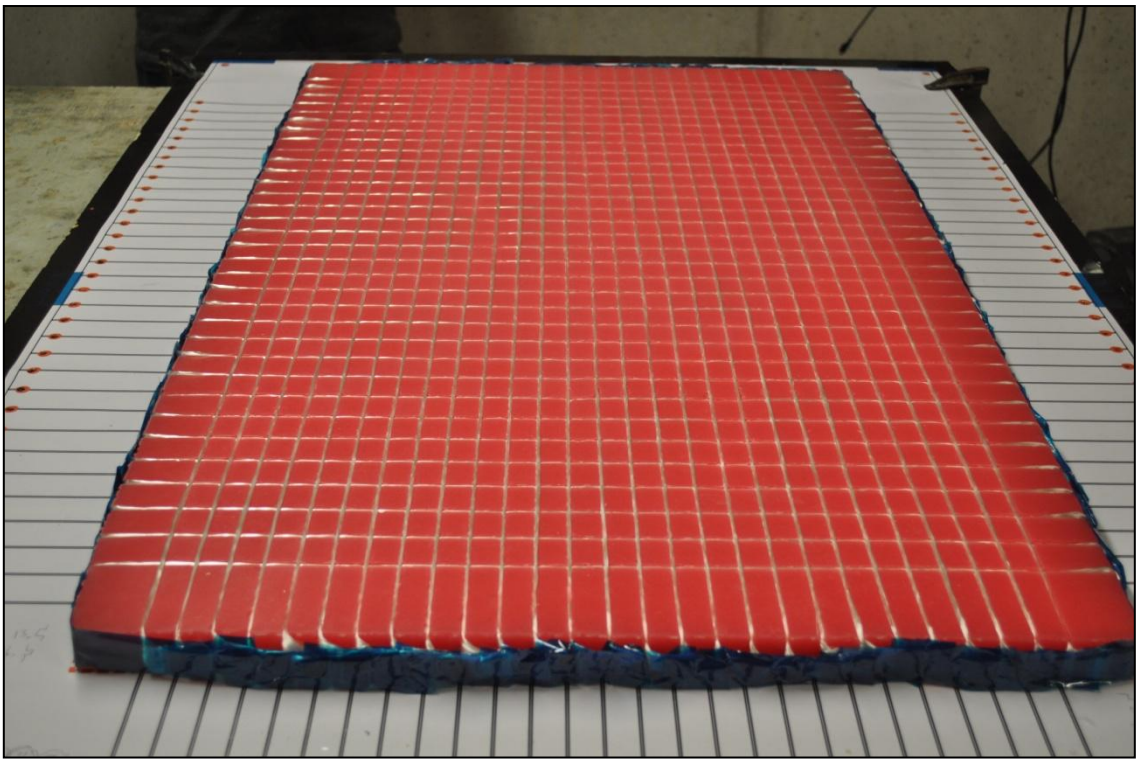

Figure 6.39: Finished state after winding the glass-fibre roving

Step F: Design vacuum infusion set-up

The same infusion set-up as the one for the second sample orthogrid panel was used to infuse the large orthogrid panel. In order to turn the mould upside down on the aluminium mould, an extra plate was placed on top. Along with the earlier wooden plate positioned on the bottom of the silicon mould, the dry glass-fibre layup can be turned around without disturbing the lay-up.

Figure 6.40 shows the vacuum infusion lay-up, before the semi-permeable membrane is applied on top. The figure shows the resin runner placed around the silicon mould. The green flow mesh is supposed to spread the resin along the skin laying on the bottom. The resin will then move upwards through the silicon mould and flow out through the drilled holes.

Before applying the vacuum bag, the semi-permeable membrane, a breather, caul plate and another breather are layed up as is shown in figure 6.41. The full set-up is tested for air tightness, where the minimum measured air pressure on the outlet was 8 mbar.

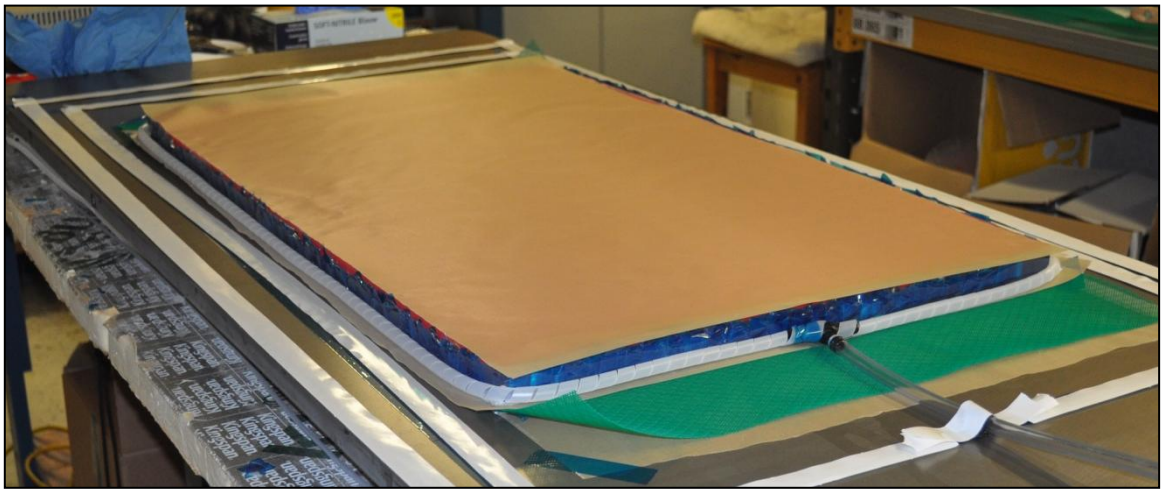

Figure 6.40: Vacuum infusion set-up, before applying semi-permeable membrane

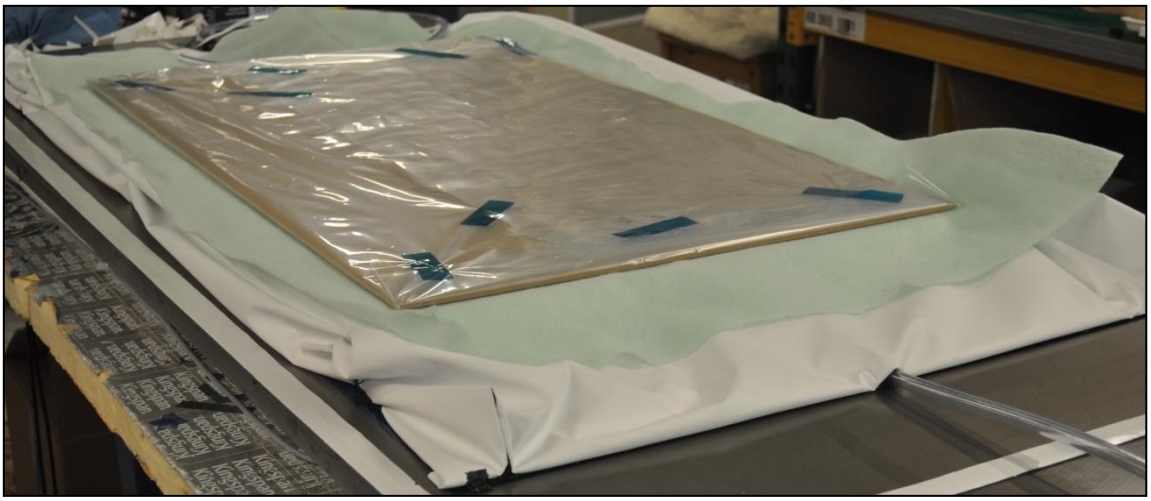

Figure 6.41: Semi-permeable membrane with a breather and caul plate on top

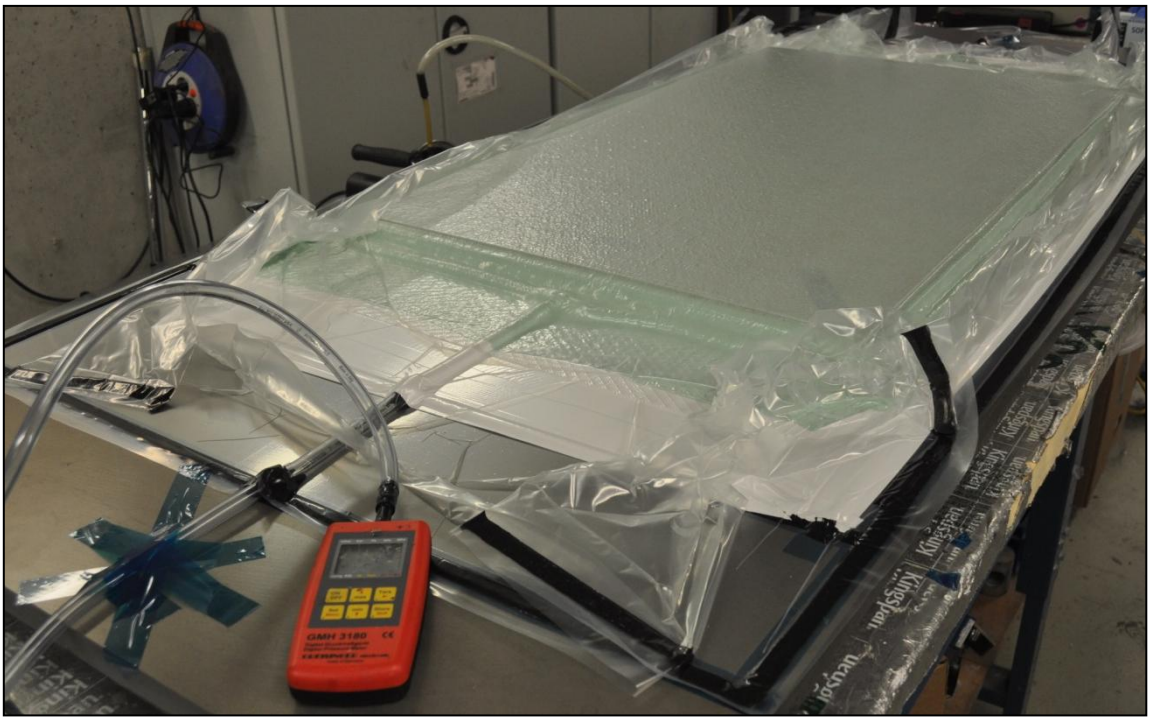

Figure 6.42: Vacuum infusion set-up tested on air tightness

Step G: Curing, post-curing and preparing for testing

After the infusion was performed, the product was cured for 24 hours at room temperature. After removing the product from the mould, a post-cure session was followed, which had a duration of 10 hours at 70 degree Celsius.

The product showed very good quality, where the resin infusion had reached all parts of the orthogrid panel. At the locations, where the 3D printed grid parts were glued together, the surface was found to be rough, which was expected. A photo of the full panel is shown in figure 6.43 and a close-up shot is taken from the grid and shown in figure 6.44. The rough points on top of the grid are a result of the holes in the silicon mould, which acted as air outlets. The rough surface was easily removed with sanding paper.

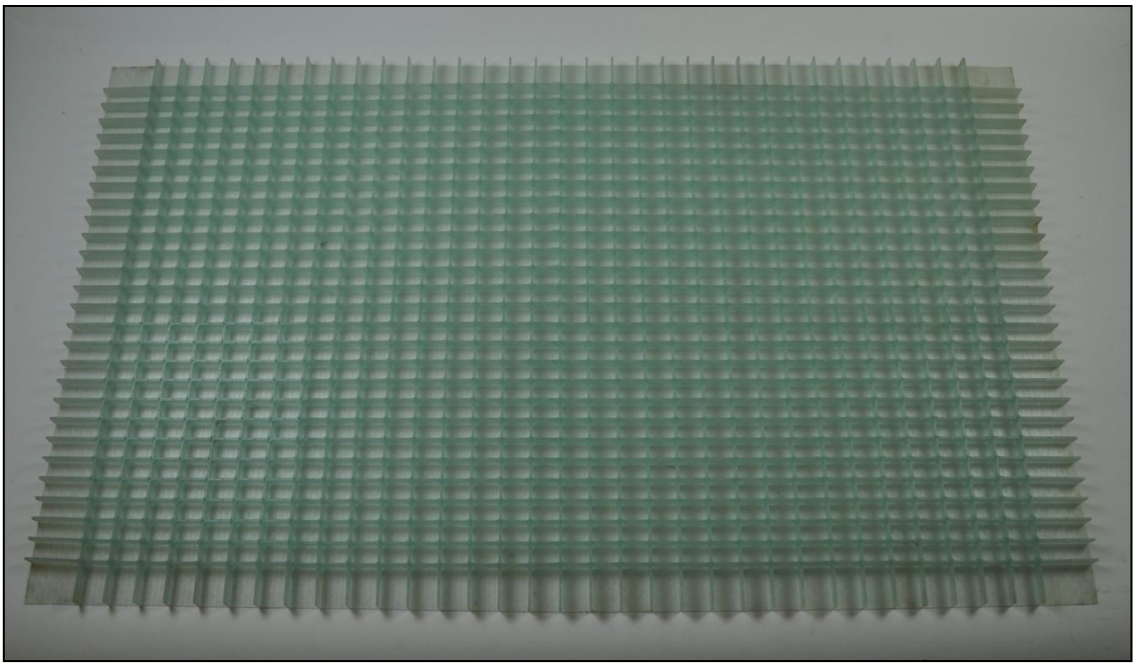

Figure 6.43: Orthogrid panel (100 kN) design, final product

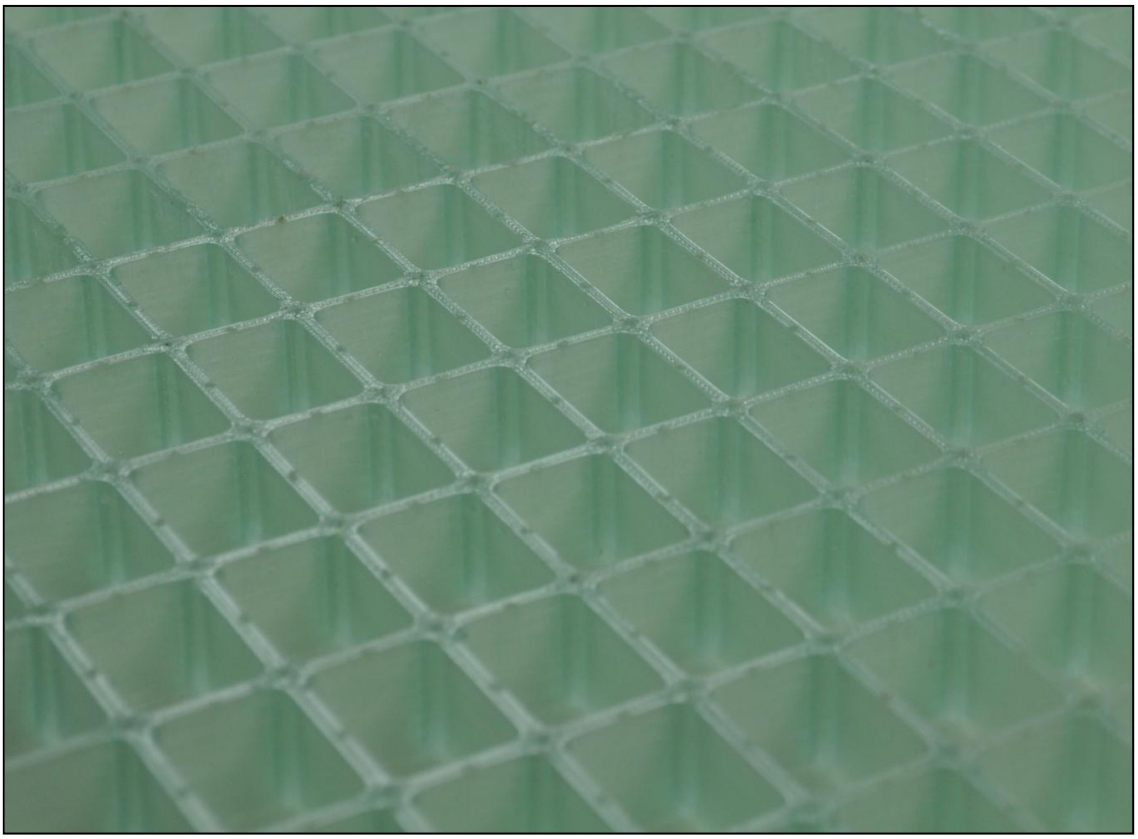

Figure 6.44: Close-up orthogrid panel (100 kN) design, final product

6.3.2. Test set-up and general results compression test

The test set-up is shown in figure 6.45. Two video cameras were positioned to film both sides of the panel during the test. The aluminium frame was again stiffened with the steel L-profiles and thick bolts to prevent out-of-plane displacement of the unloaded edges. The fixtures on the loaded edges had been adapted to the total thickness of the panel, from which a close-up view is shown in figure 6.46.

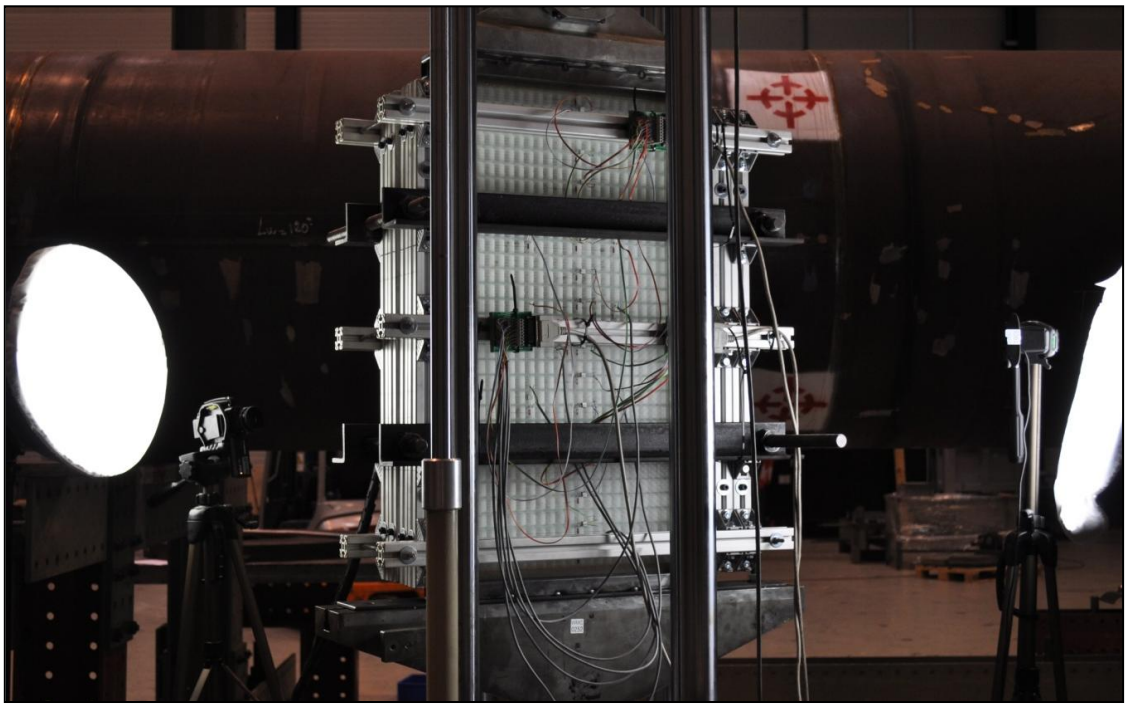

Figure 6.45: Test set-up orthogrid panel

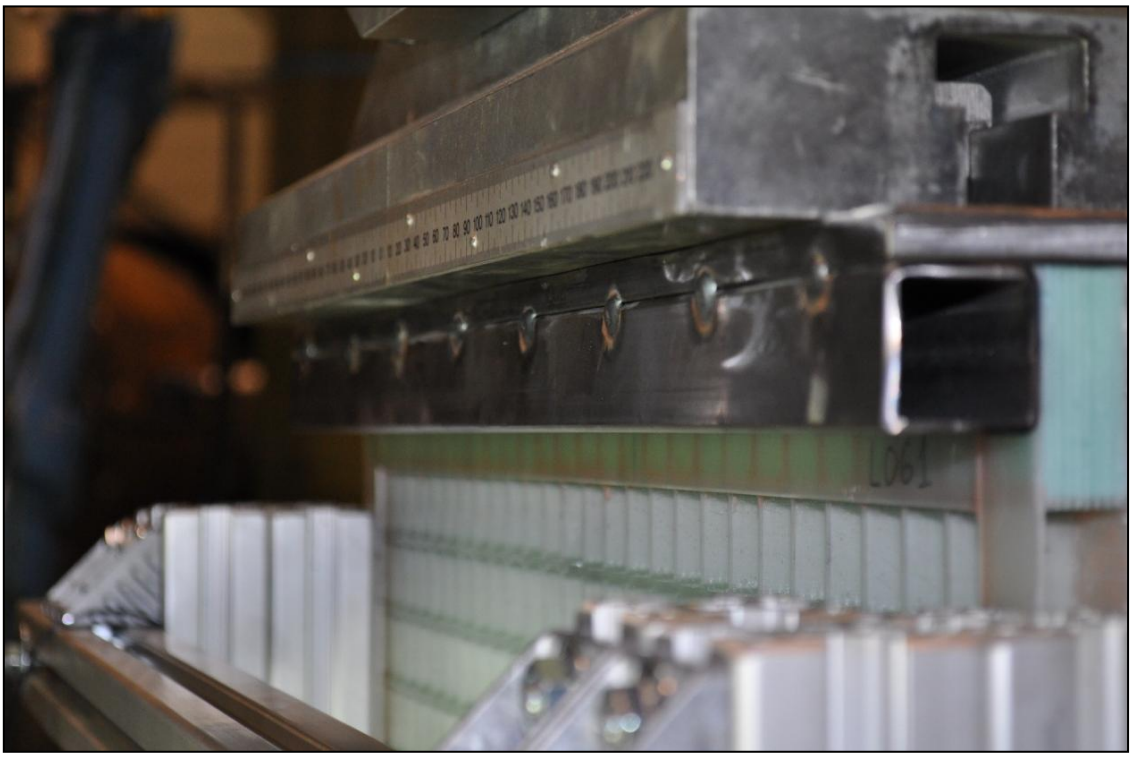

Figure 6.46: Orthogrid panel fixture at the top loaded edge

According to the test results, global buckling initiated at a compressive load of 95 kN. Final failure occurred at a compressive load of 163 kN, due to a combination of skin stiffener separation and a compression failure of the stiffener as is shown in figure 6.47 and figure 6.48/6.49 respectively. The failure at this location could be a result of the simply supported conditions missing over a small range of the length. The strain gauge result at the top of the panel will give more insight in the next chapter.

Figure 6.47: Skin delamination of the orthogrid panel at -163 kN

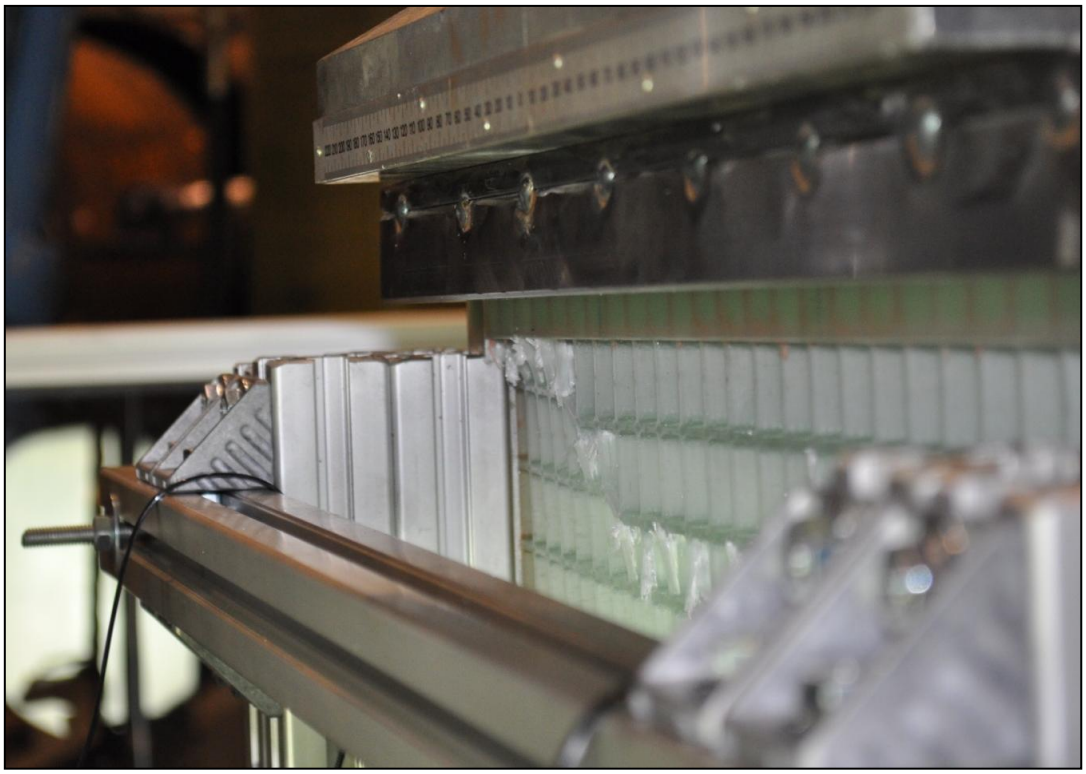

Figure 6.48: Compression failure of the grid at -163 kN (1)

Figure 6.49: Compression failure of the grid at -163 kN (2)

6.3.3. Quality analysis

A summary of the performed quality analysis is given in this subsection. Additional information with respect to the performed measurements can be found in appendix M. The following measurement were performed:

- Total thickness
- Stiffener spacing
- Skin thickness
- Stiffener height
- Stiffener thickness
- Fibre volume fractions

The average of the measurements on the total thickness was found to be 17.44 mm, where the designed value was given by 17.675 mm.
The average stiffener spacing in x and y were 24.61 mm and 16.96 mm respectively. These values are both lower than the designed values of 24.89 mm and 17.04 mm. A relatively large standard deviation can also be observed, which can have significant influence on the thin stiffeners.
The stiffener height was in relatively good agreement, where an average of 16.91 mm was found. This is only 0.09 mm lower than the design value.
The skin thickness is calculated by subtracting the average stiffener height from the measured average total thickness. This resulted in a skin thickness of 0.53 mm, which is lower than the design value of 0.675 mm. However, since a large scatter in results of the average total thickness is present, the skin thickness value could be easily influenced by the performed calculation. Measuring the thickness of the skin after cutting pieces out of the panel, the average skin thickness was found to be 0.676 mm and is therefore considered to be in sufficient agreement with the designed value.
The stiffener thickness was measured on the bottom, middle and top location along the stiffener height. Taking the average of all measurements together, an average stiffener thickness of 2.30 mm is found. This is 0.19 mm thicker than the plug design and 0.862 mm thicker than the low-weight design found in chapter 4.
Table 6.4 shows the fibre volume fractions measured after the compression test. Both stiffeners and skin have lower values than were found during the manufacturing of the sample orthogrid panels. This is a result of the higher void volume fractions found from the measurements.
Using equations 6.1 till 6.5, the stiffness E_{11} of the stiffener is adjusted to 30043 MPa.

Table 6.4: Fibre volume fractions orthogrid panel (100 kN design)

	Fibre Volume Fraction (%)	Resin Volume Fraction (%)	Void Volume Fraction (%)
Stiffener	37.29	58.90	3.81
Stiffener node	35.86	61.01	3.13
Skin	47.16	46.59	6.25

6.4 Concluding remarks

Based on the performed work with respect to manufacturing and testing, some conclusions and recommendations can be set-up for future research. A short discussion is therefore given on the findings related to manufacturing in subsection 6.4.1 and related to testing in subsection 6.4.2.

6.4.1. Discussion on manufacturing

From the experience obtained on manufacturing of grid stiffened structures during this project, a couple of involved aspects can be discussed.
The first aspect is the obtained quality of the product from the vacuum infusion process. The used method has shown to result in a good quality product with a low number of voids present. To reduce the number of voids further, the resin flow could be assessed by filming the process with an infrared camera, with the aim to see the flow pattern and get a better understanding of the reason behind the dry spots which were mainly found in the middle of the stiffeners.
Besides the good infusion of the panels, the low fibre volume in the stiffeners and the tolerances for the stiffener thickness should be further investigated and techniques should be developed to increase the fibre volume and improve the tolerances on mainly the stiffener thickness.
The second aspect involves the complexity of the process. A lot of steps have to be undertaken to infuse one panel, which heavily increase the total time of manufacturing. The large orthogrid panel has taken two weeks in total from plug manufacturing up to the final product. Improving or removing certain steps from the process, would lead to faster and possibly cheaper manufacturing. In that perspective, automation of the fibre winding process is relevant in order to manufacture larger structures, because this step alone had cost 3 days in total to finish by hand.
The third aspect is related to the complexity of the structure itself. During this project, constant design variables were used in the design of the panels. When different stiffener heights have to be manufactured along the width and length of the structure, ply drops have to be introduced, which is a handling that cannot be performed with the present technique.

6.4.2. Discussion on testing

The developed testing method during this project had shown good results in general. The main challenge on further improving the test set-up is to improve the boundary conditions, in order to enable an accurate translation to the boundary conditions applied on the numerical models. The aluminium frame could therefore be improved by replacing it with a more stiff steel frame, where the frame itself can be build with a lower number of parts to speed up the building of the set-up. The simply supported boundary conditions on the unloaded edges can also be improved by applying them over the full length of the panel. To enable this, the width of the fixture applying the compressive force on the panel should then be changed to the distance between the two supports on the left and right of the panel.
Another improvement can be made by increasing the visibility on the test specimen, which could possibly be reached when a stiffer steel frame is introduced. With the extra visibility on the specimen, the test could be expanded by introducing digital image correlation to determine the strains on the skin side of the panel. As a result, the application of a lot of strain gauges could be prevented and a comparison with a finite element model could easily be made.

7.Evaluation and Improvements

In this chapter, the obtained results of the compression tests are evaluated and compared to the numerical models. The performed quality analysis is used to adjust the model dimensions and properties in order to improve the results. Differences between the model and the experimental results still present after the improvements are explained and recommendations on potential improvements for future research is given. A flow chart of this chapter is shown in figure 7.1. The evaluation and improvements of the sample orthogrid panels, the sandwich and the orthogrid panel are outlined in section 7.1, 7.2 and 7.3 respectively.

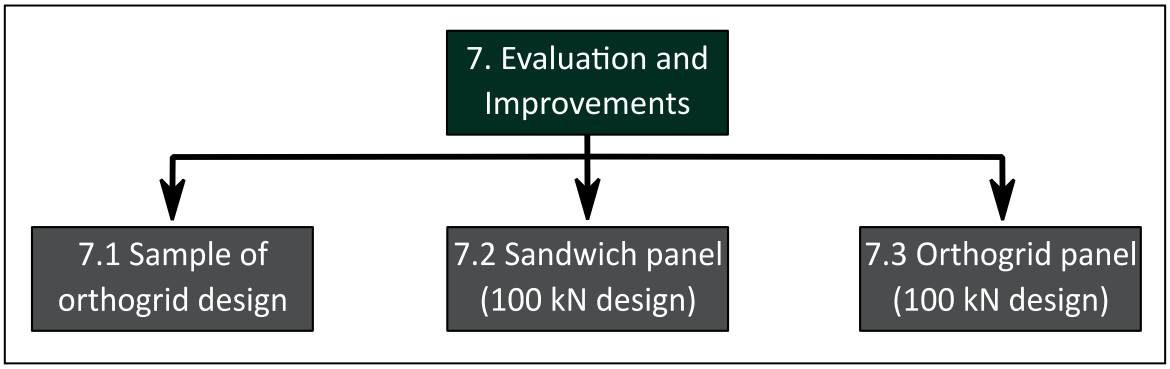

Figure 7.1: Flow chart chapter 7

7.1 Sample of orthogrid design

This section contains the evaluation of the two compression tests of the sample orthogrid panels. The experimental data obtained from the machine displacement and the strain gauges will be compared to the numerical model. Sample orthogrid panel 1 will be addressed first in subsection 7.1.1. and the evaluation and improvements for the second sample orthogrid panel will be outlined in subsection 7.1.2.

7.1.1. Sample orthogrid panel 1

The evaluation of the results is carried out by comparing the load/displacement curve and the load/strain curves at the locations of the strain gauges. In order to model the compression test numerically and compare it with test results, a non-linear analysis is performed with Marc Mentat. An example of the set-up of the numerical model is given in appendix N.

The full model of the sample orthogrid panel consists of a total of 33140 elements, where the extended edges with tab material are also included. The material properties of the tab material were requested at the supplier and were slightly less stiff than the Saertex-812g biaxial glass-fibre used for the skin. This change in stiffness has been taken into account. On each edge, simply supported boundary conditions were applied to the numerical model and the final failure load during the compression test of 120 kN will be applied with a time step of 0.005. Since the model is symmetric along the xz-plane of the panel, a load imperfection is applied to the middle longitudinal stiffeners as an initial unit load. This should allow the stiffeners to cripple under the applied load as is expected by the buckling analysis and was also observed during the test. After the numerical analysis has been performed, the data of the force, displacement and strains is extracted from the results file.

The locations of the strain gauges are shown in figure 7.2, where 1&5, 2&6, 3&7 and 4&8 are positioned as a pair on two sides of the skin. A comparison between the strains of the compression test and the numerical model are shown in figure 7.3. From the symmetry of the numerical model, the strains at each strain gauge location were found to be relatively similar, which is why only 1 load/strain curve is plotted. From the resulting graphs, it is observed that the numerical model

predicts stiffer behaviour and shows a higher intracellular buckling load than is observed during the compression test. The model is therefore improved on some aspects.

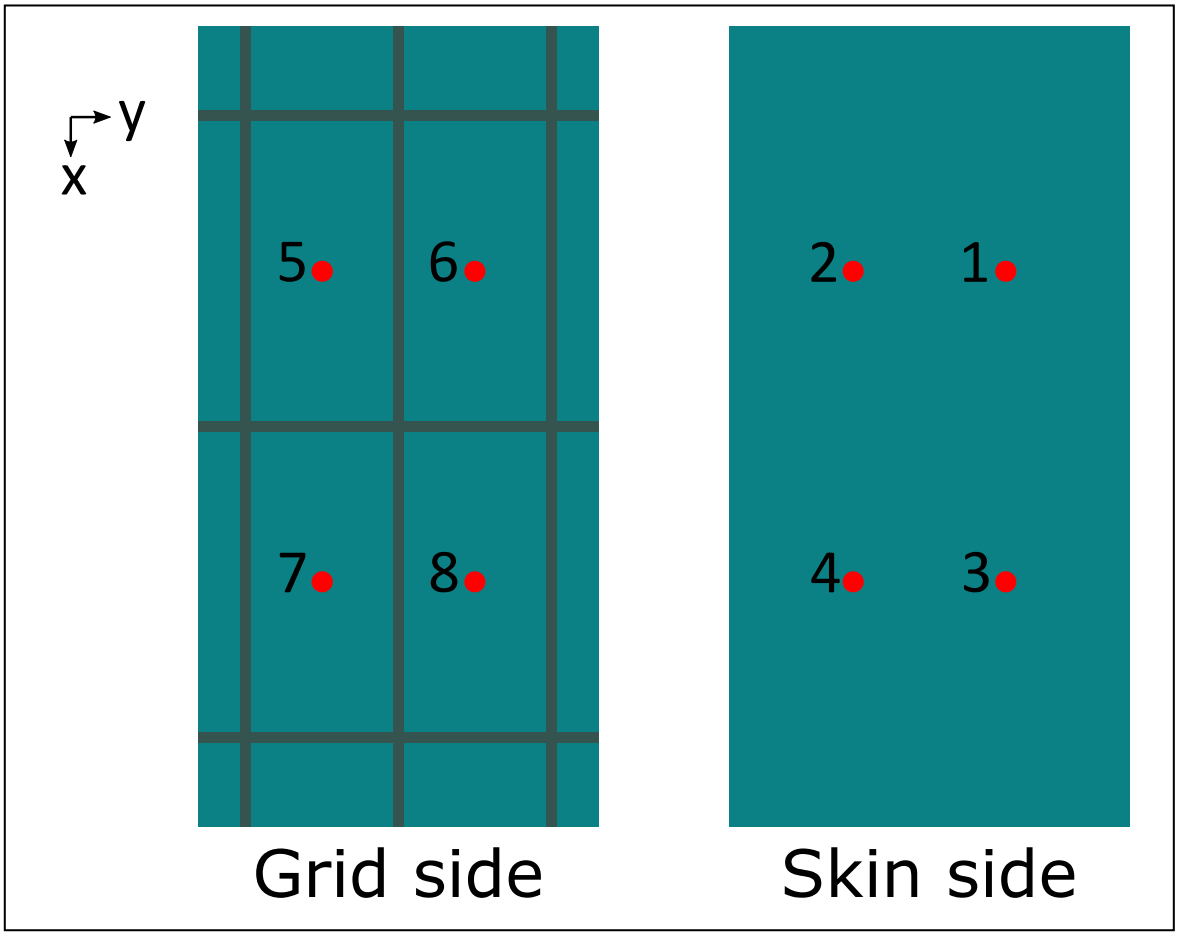

Figure 7.2: Strain gauge locations on sample orthogrid panel 1

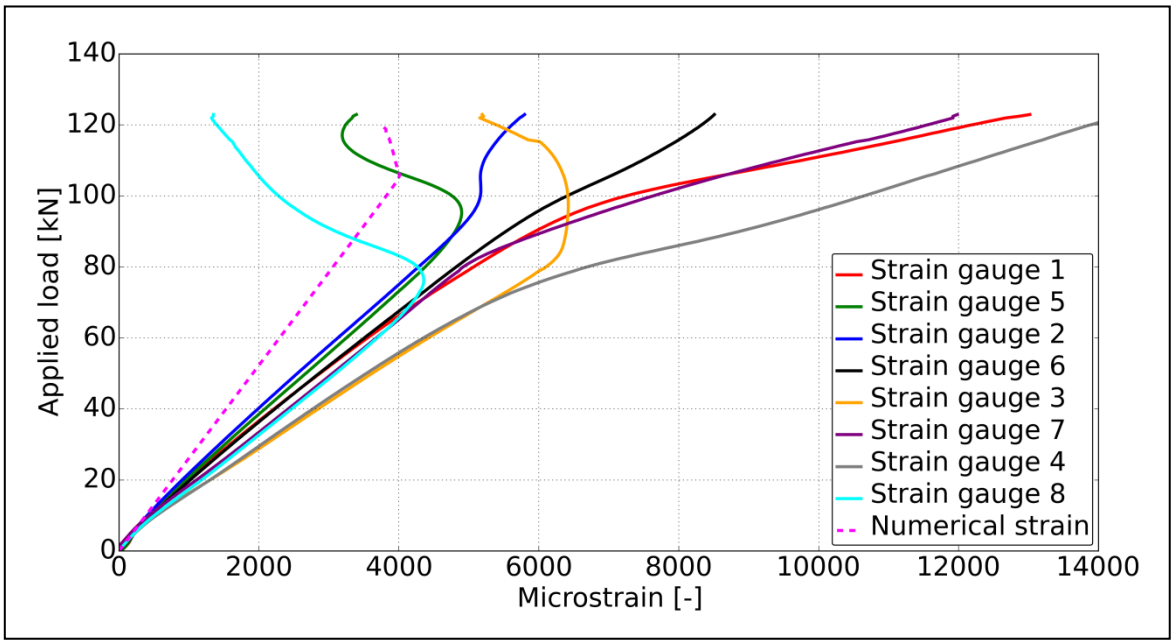

Figure 7.3: Load/strain curve of experiment and numerical model, sample orthogrid 1

7.1 Sample of orthogrid design

It was shown in the quality analysis that not all design variables were accurately manufactured. The numerical model is therefore improved to the measured values in the quality analysis subsection of the previous chapter:

- Skin thickness: changed from 2.025 mm to 1.74 mm
- Stiffener height: changed from 20.0 mm to 19.0 mm
- Stiffener thickness: changed from 5.04 mm to 4.56 mm
- Stiffener stiffness: changed from 39500 MPa to 32208 MPa

The influence of the different improvements on the strain obtained from the non-linear model is shown in figure 7.4. The largest influence on the intracellular buckling load is observed by the reduction in skin thickness, which could be expected since a thin skin decreases the intracellular buckling load exponentially. The adjusted stiffness of the stiffeners shows the largest influence on the slope of the load/strain curve.

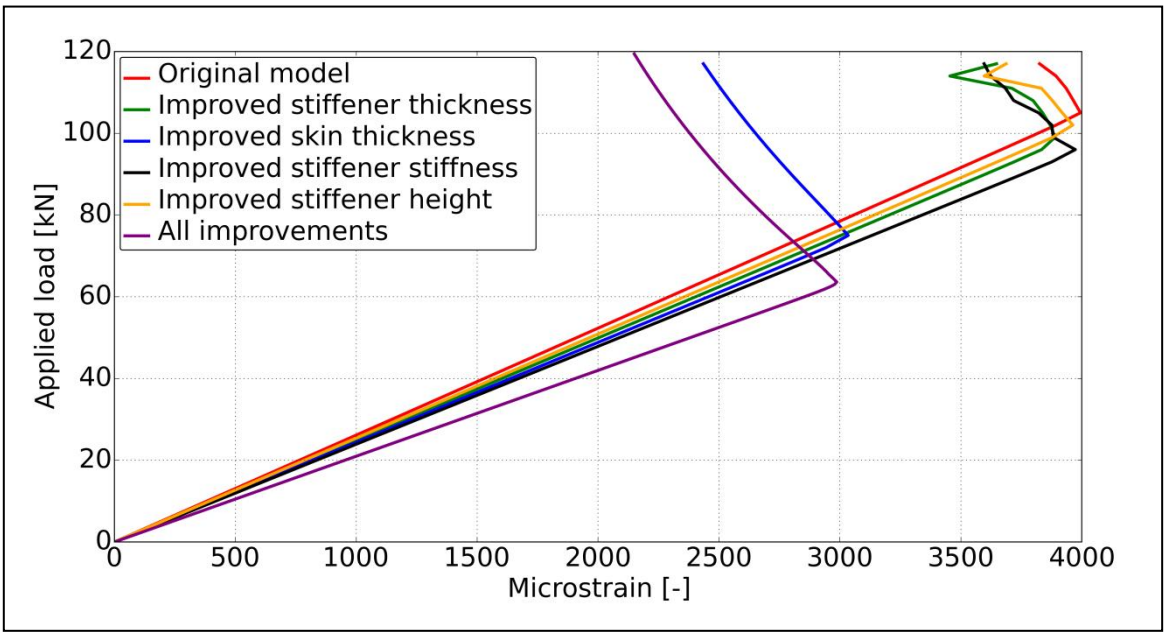

Figure 7.4: Influence of the adjustments on the strains, sample orthogrid panel 1

The superimposed model improvements are compared to the strain gauges measurements in figure 7.5. The overall stiffness still shows some stiffer behaviour in comparison with the experimental results obtained from the strain gauges. The initiation of intracellular buckling is however predicted with a large error of 20.5% at a compressive load of 63.6 kN with respect to an approximate load of 80 kN shown by the data from the strain gauges.
The main reason behind this lower value could be that the shell elements introduce wider and longer skin cells in comparison with the manufactured panel, because the thickness of the stiffener is not taken into account. The differences of the length and width of the skin cells are outlined in table 7.1. From plate buckling theory, it is known that the width of a panel has a significant effect on the buckling load. A difference of 10% for the width was found, which gives approximately a decrease of 20% according to analytical models presented in chapter 4. Based on this statement, the model could possibly be improved by modelling the stiffeners of the orthogrid with 3D solid elements to accurately model the length and width of the cells.
In order to test the above statement in a simplified way, the cells could be modelled smaller. Since the decrease of the cell size, would result in more influence of the added tab material, the complete panel has also been modelled with a lower width b of the panel. The results of the non-linear numerical model with the actual measured cell sizes are presented in figure 7.6.

It could be observed that the critical failure load is in much better agreement with the compression test results.
A reason for the scatter of the intracellular buckling load in the different cells, could be a result of the different skin thicknesses. Relatively small changes on the skin thickness already introduce a significant effect on the critical buckling load as is also shown in figure 7.4. Measurements on the skin thickness should therefore be as accurate as possible in order to have an accurate model for intracellular buckling.

Table 7.1: Real and numerical skin cell length and width of sample orthogrid panels

	Sample panel 1	Numerical model	Difference [%]
Skin cell length [mm]	142.1	150	5.56
Skin cell width [mm]	67.7	75	10.8

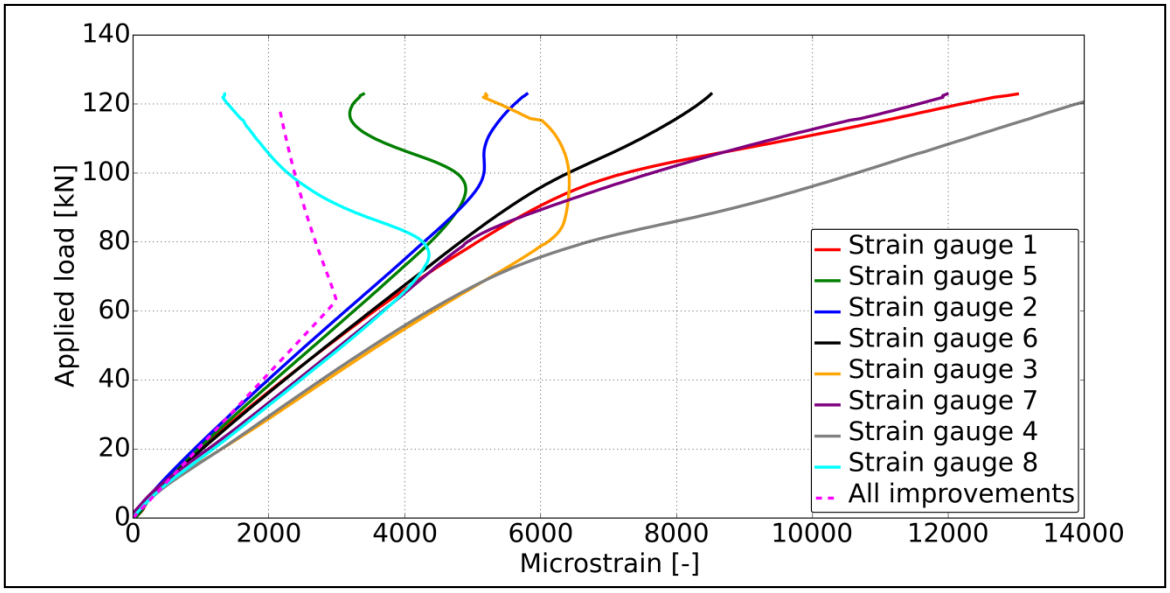

Figure 7.5: Load/strain curves of experiment and improved numerical model, sample orthogrid 1

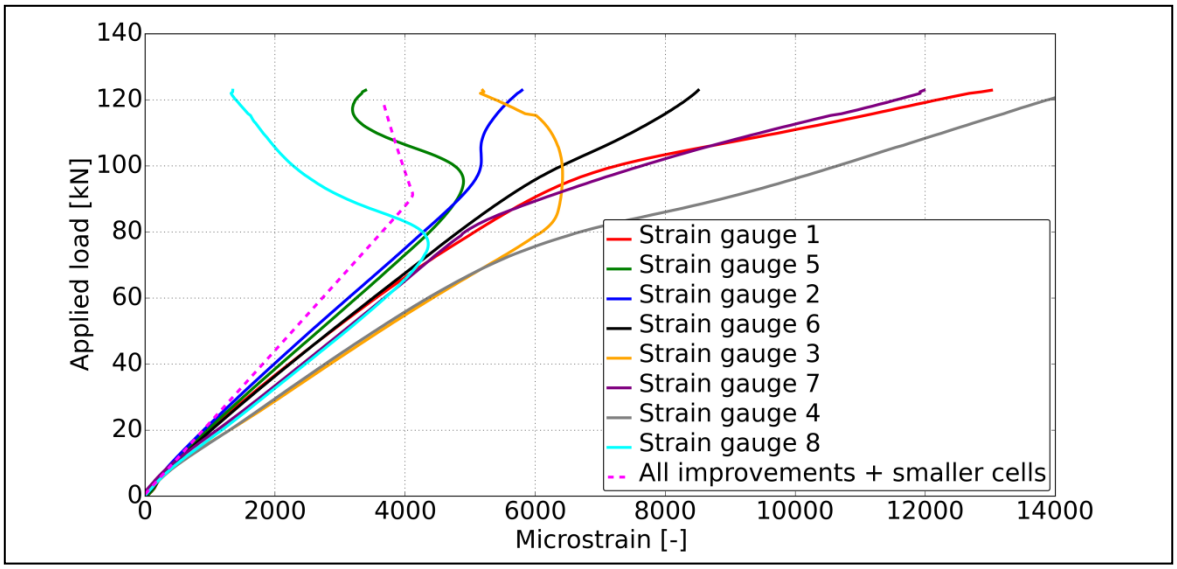

Figure 7.6: Load/strain curves of experiment and improved numerical model with smaller cells, sample orthogrid 1

7.1 Sample of orthogrid design

The higher overall stiffness of the numerical model as was shown in the load/strain curves, is also shown in the force/displacement curves drawn in figure 7.7. The red line indicates the data obtained from the compression test and the green and blue line show the results from the non-linear analysis for the original and the improved model respectively.
It can be seen that the improved model does give better results when compared to the experimental load/displacement curve, but the difference is still present.
This could partially be explained by the start of the compressions test, where the test specimen has a low stiffness initially and probably has to deform until the applied compression is completely distributed through the panel. After a displacement of 0.25 mm at approximately 10 kN, the slope is relatively linear.
Another explanation of the lower stiffness could be related to the boundary conditions of the unloaded edges. It was observed during the test, that the aluminium frame did not hold the edges from bending out-of-plane completely. This ability of deformation could have resulted in less stiff behaviour during the test. However, this explanation was tested by removing the boundary conditions at the unloaded edges of the numerical model and did not result in a lower stiffness of the numerical model.
The most logical explanation could be found in the stiffness of the stiffeners. From figure 7.4 it was already shown that this parameter had a significant influence on the slope of the load/strain curve. Since the glass fibre roving was placed by hand and had to be steered at every stiffener crossing, the fibre could lose some more of its stiffness properties as a result of the layup process. More research should therefore be performed on the influence of the stiffener crossings.
In addition, the unidirectional fibre was not under tension anymore at the moment of infusion, resulting in possible waviness of the fibres through the stiffeners. With respect to hand lay-up, automated processes [17] have been proven to be far more accurate for laying up fibres and also resulted in higher quality products.
The material properties of the fibre roving could also be different, as they were assumed to be the same as the measured values of the unidirectional fabrics. A different twist or processing technique could have resulted in changed stiffness properties of the glass-fibre. Accurate material properties should therefore be available to give a conclusion on this statement.
In an attempt to strengthen the above explanation, a knockdown factor could be placed on the stiffness of the stiffeners. This knockdown factor is determined by the ratio of the linear stiffness regions in figure 7.7 (30 kN to 70 kN), for the test machine displacement and the improved numerical model. The knockdown factor is then determined to be 0.696.

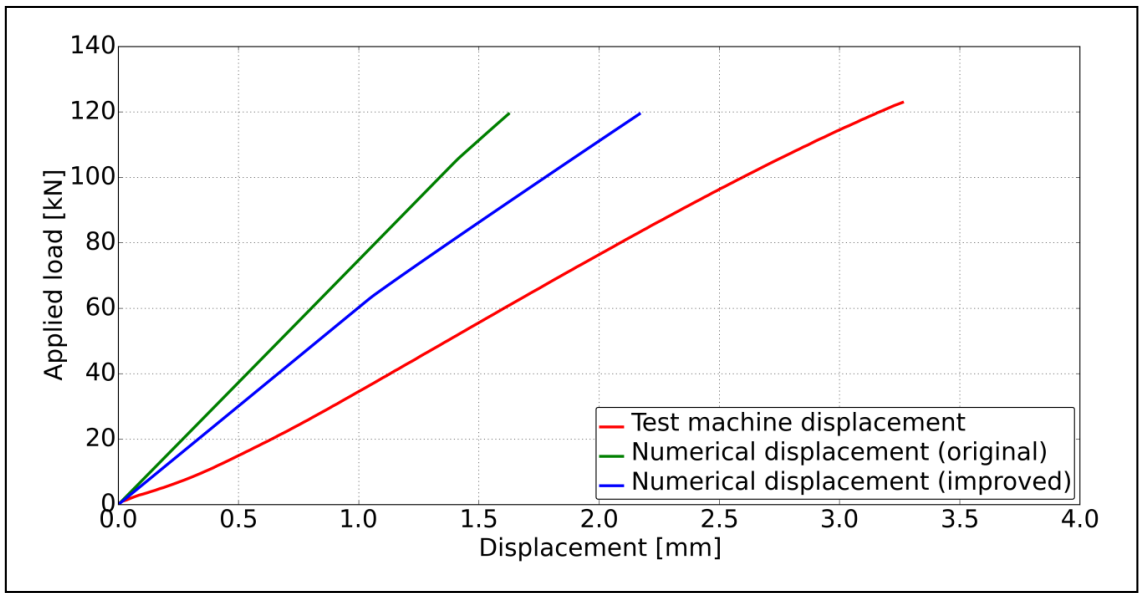

Figure 7.7: Force/displacement curve of experiment and numerical model, sample orthogrid 1

The stiffness is then further reduced to 22417 MPa and when introduced on the model with the small cells, the load/strain curves are obtained as they are shown in figure 7.8.

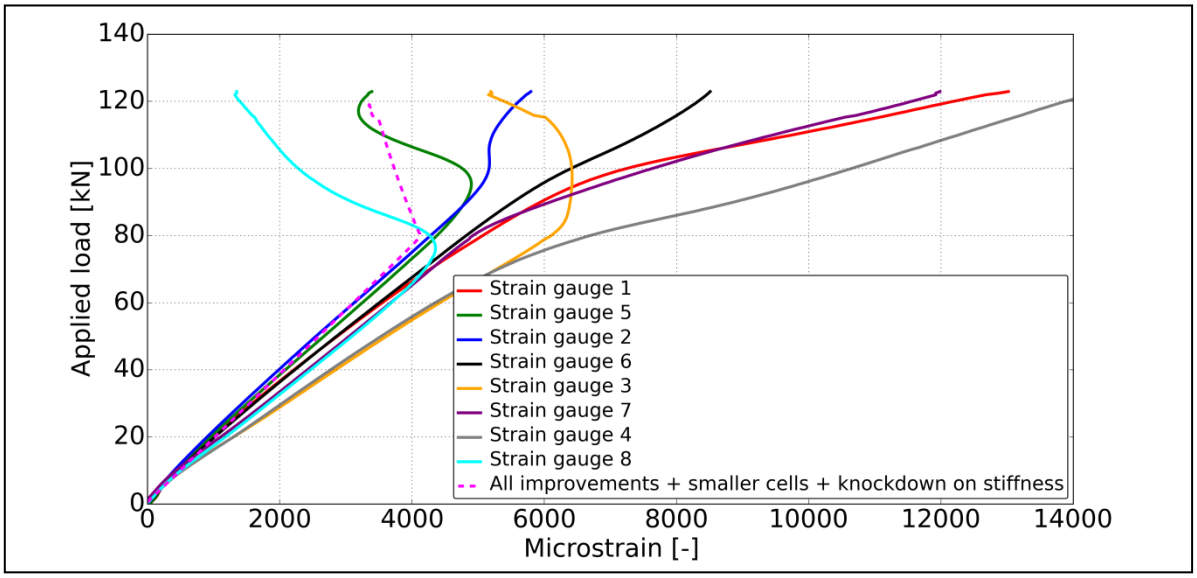

Figure 7.8: Load/strain curves of experiment and improved numerical model with smaller cells and knock-down on stiffener stiffness, sample orthogrid 1

Finally, the non-linear model (without smaller cells and knock down factor) is compared to the buckling analysis performed in chapter 4. This resulted in an estimated intracellular buckling load of 63429 N (214N*296.4), which is good agreement with the non-linear analysis. The asymmetry of the orthogrid panel therefore seems to have no influence on the intracellular buckling load determined by the eigenvalue analysis, which is based on a linear static analysis.

7.1.2. Sample orthogrid panel 2

For the second sample orthogrid panel, the data from the compression test is evaluated and compared to the numerical model in this subsection. The data obtained from the compression test consists of the applied load and the related machine displacement and strains obtained from the strain gauges. The same non-linear model is used as was described for the first sample orthogrid panel. The applied load was only changed to 110 kN, since failure had occurred earlier at the second panel. The strain gauges were placed on different positions in order to determine the buckling mode along the length of the panel and within each of the cells. They are schematically indicated in figure 7.9. A total of 11 strain gauges are placed along the length of the panel at the skin side. In the top left cell on the grid side, 3 additional strain gauges are placed, which are opposite to the strain gauges on the skin side. These are placed in order to compare the strains on the grid and skin side during intracellular buckling. Since the original design was not in good agreement with the actual test for the first panel, the design is immediately improved by the measurements performed in the quality analysis subsection of the previous chapter:

- Skin thickness: changed from 2.025 mm to 1.74 mm
- Stiffener height: changed from 20.0 mm to 19.3 mm
- Stiffener thickness: changed from 5.04 mm to 4.32 mm
- Stiffener stiffness: changed from 39500 MPa to 32797 MPa

In addition, the length a and width b are adjusted to 377 mm and 187 mm, because more material was milled away than intended before the test.

7.1 Sample of orthogrid design

The load/strain curves of the strain gauges positioned in the top left cell are shown in figure 7.10, along with the improved numerical model. Only one load/strain curve from the numerical model is presented to indicate the expected failure load, since the linear region was the same for each position. A big error in determining the intracellular buckling load is found. This error was also observed for the first sample orthogrid panel, of which the possible explanation is given in subsection 7.1.1. Decreasing the skin cell size resulted in better comparison between the numerical model and the compression test.

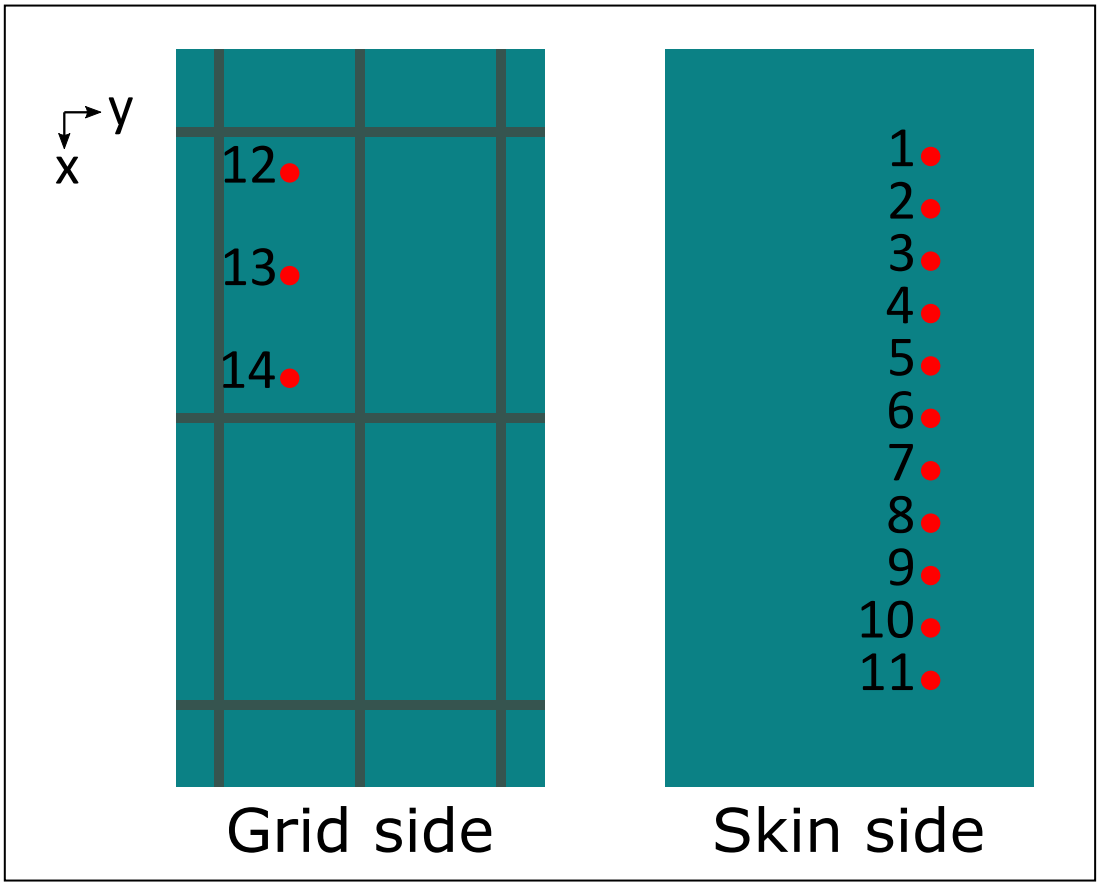

Figure 7.9: Strain gauge locations on sample orthogrid panel 2

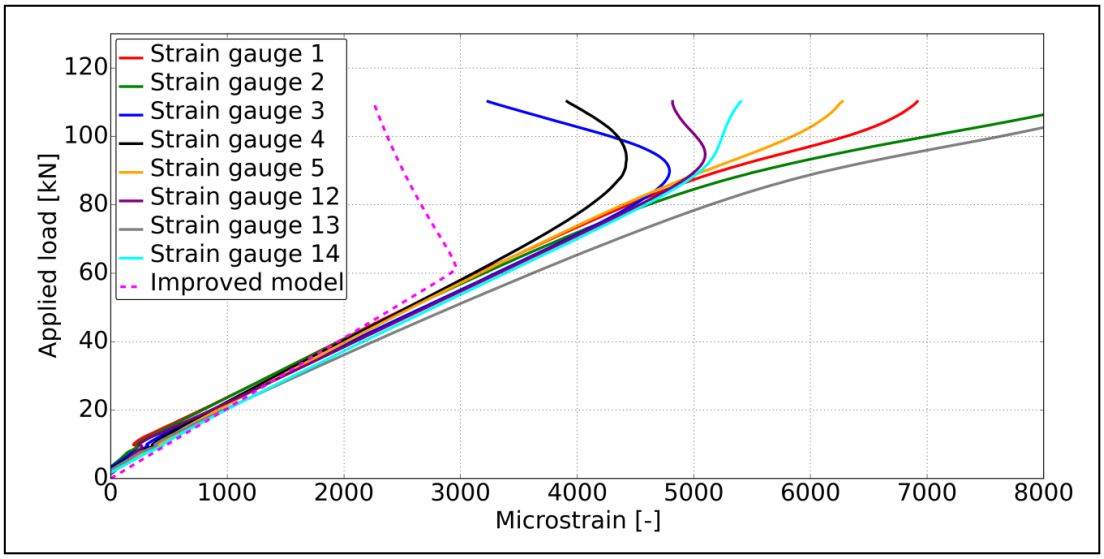

Figure 7.10: Load/strain curves of experiment and improved numerical model, sample orthogrid 2

The load/displacement curve is shown in figure 7.11, where the test result is shown along with the original model and the improved design. The region of low stiffness at the start of the compression test is more visible here. Different possible explanations on the lower stiffness have already been described in subsection 7.1.1.

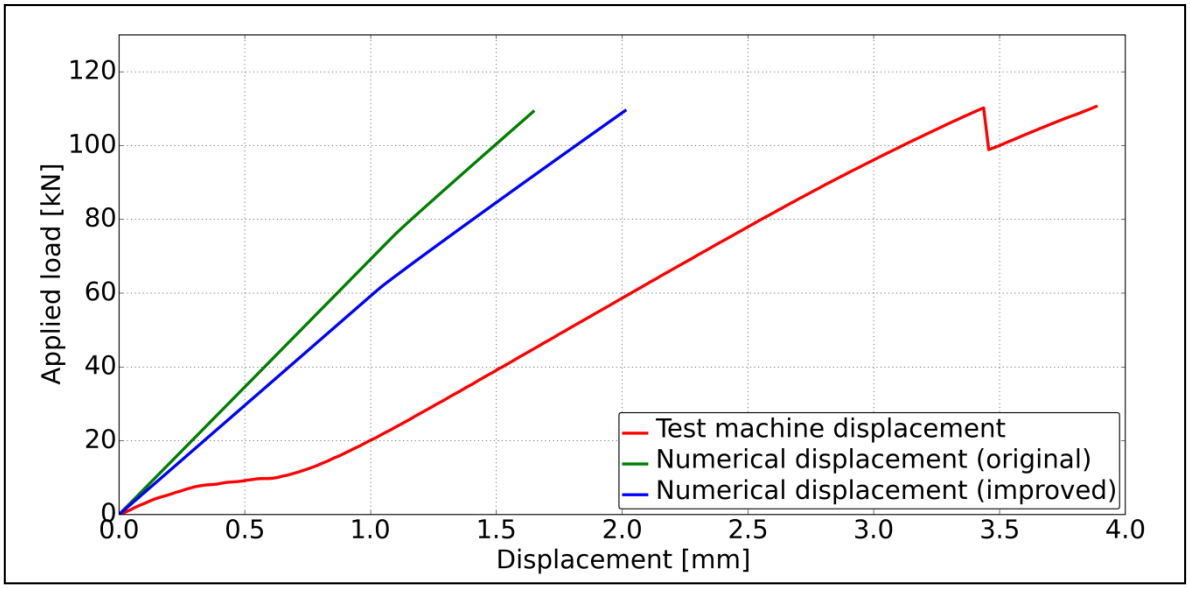

Figure 7.11: Force/displacement curves of experiment and numerical model, sample orthogrid 2

When trying to analyse the intracellular buckling mode, results of strain gauges 1 to 11 are plotted at different load levels in figure 7.12. The figure shows 2 buckling half waves in each cell (1 to 5 and 7 to 11), which is not in agreement with the results from the numerical analysis shown in figure 7.13, where 3 half waves are predicted. This could again be a result of the width and length of the skin cell, which is lower in reality.
It could also be a result of edge conditions. Since there are only 2 cells along the length, this local behaviour could be influenced by the boundary conditions of the test. The applied bonding paste at both loaded edges could have influenced the boundaries of the cells.

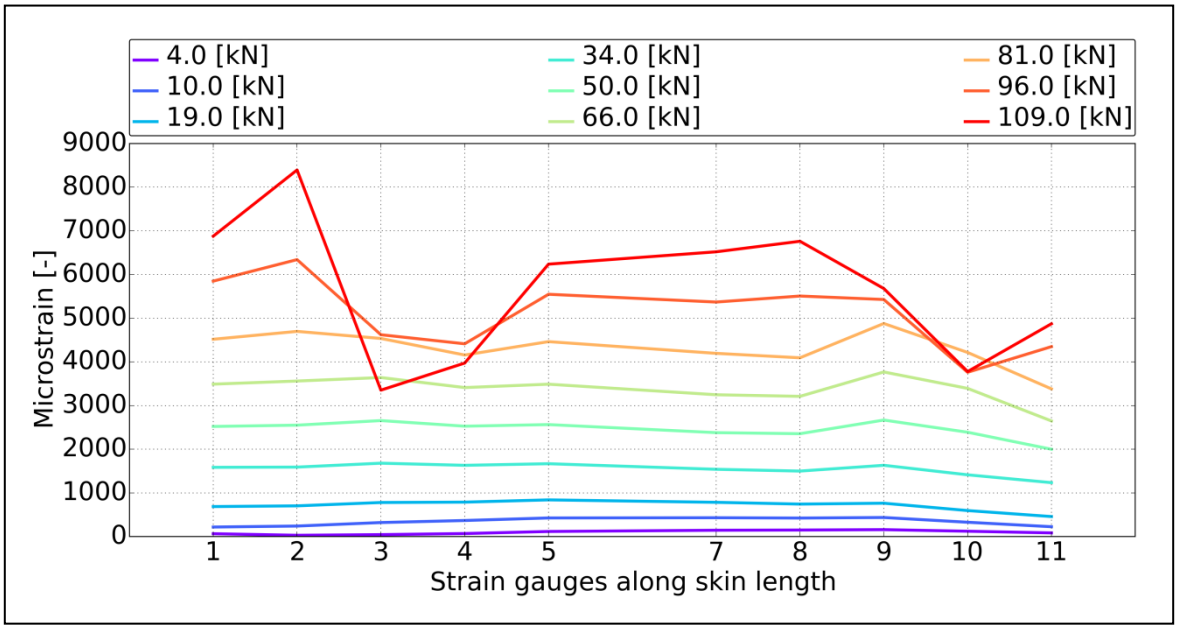

Figure 7.12: Strain gauge results along the skin length at different load levels

Based on the results, it is also advised to use a different experimental method in determining the buckling mode, since figure 7.12 is not very clear when only using 5 strain gauges along the skin length. The use of digital image correlation would be a possibility to determine the strains gradually along the skin cell.

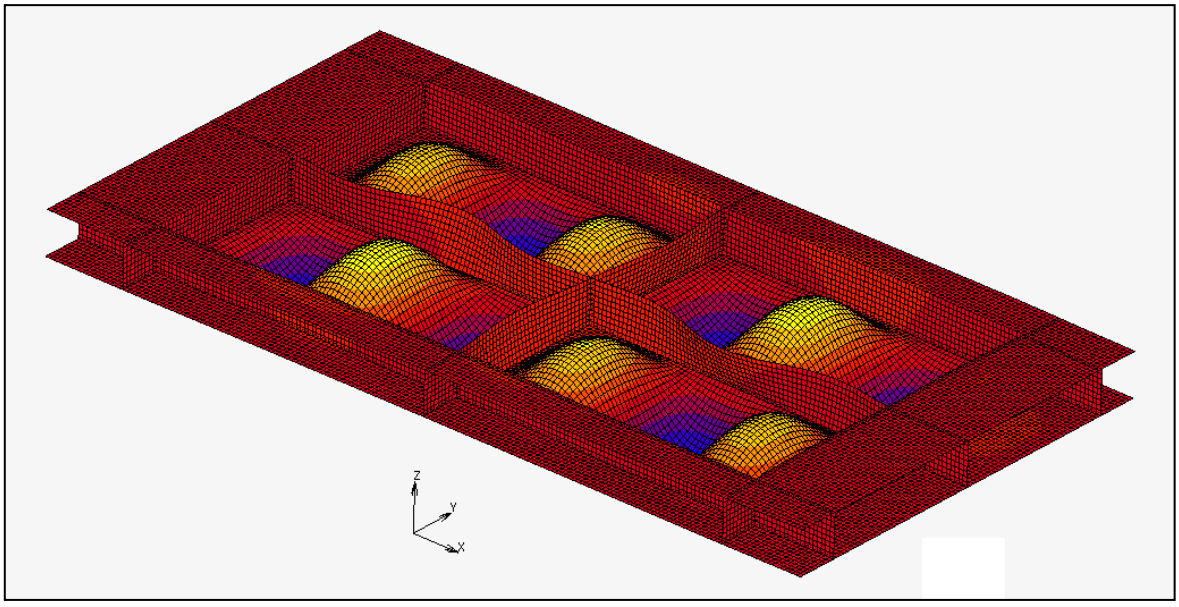

Figure 7.13: Screen shot of the buckling mode of the improved numerical model (exaggerated out-of-plane displacements)

Finally, using the buckling eigenvalue analysis performed in chapter 4, a load of 61572 N is predicted, which is in agreement with the predicted result from the non-linear model in figure 7.10.

7.2 Sandwich panel (100 kN design)

This section describes the evaluation of the obtained data from the compression test performed on the sandwich panel. As the first compression test on the sandwich panel was not going as planned and had to be aborted prior to failure, the extracted data will be evaluated first, where after a comparison is made with the numerical model.
The strain gauges are positioned on multiple locations on both sides of the panel, which are shown in figure 7.14. On both sides of the panel, a row of 11 strain gauges is placed to determine the buckling mode during the test. In all the graphs, an “a” or a “b” will be added to the strain gauge number, which correspond to the first and second compression test respectively.
The resulting load/strain curves of strain gauge 1 to 11 of the first test are drawn in figure 7.15. It is clearly observable that the strain gauges measure different strain along the length of the panel, where the largest strains are found in the middle. This is probably a result of bending of the panel as was already mentioned in figure 6.28.
At the start of the test, it is even noted that at the location where no aluminium frame is present, a tensile strain is measured by the strain gauge. This is a result of bending of the panel at this location, which can be clearly shown by plotting the obtained strains of gauge 1 and 2 against the results from gauges 12 and 13 on the opposite side of the panel. The related graphs are plotted in figure 7.16.

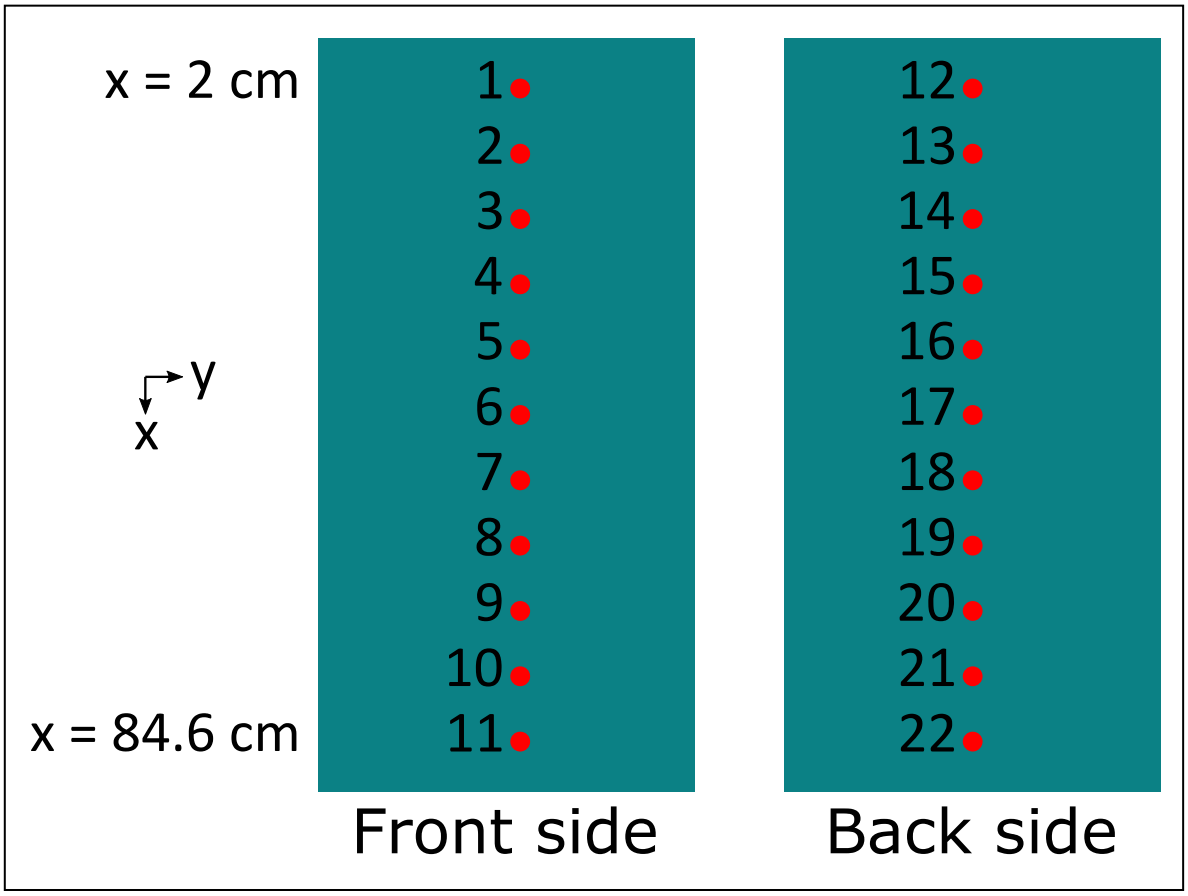

Figure 7.14: Strain gauge positions on the sandwich panel

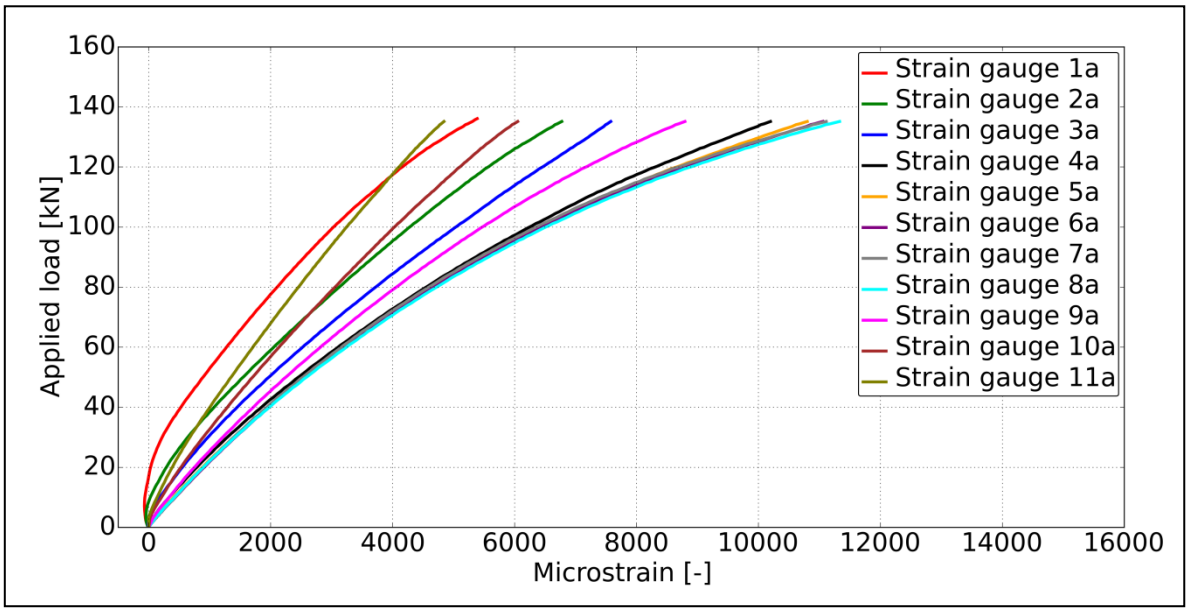

Figure 7.15: Load/strain curves of test a on the sandwich panel

7.2 Sandwich panel (100 kN design)

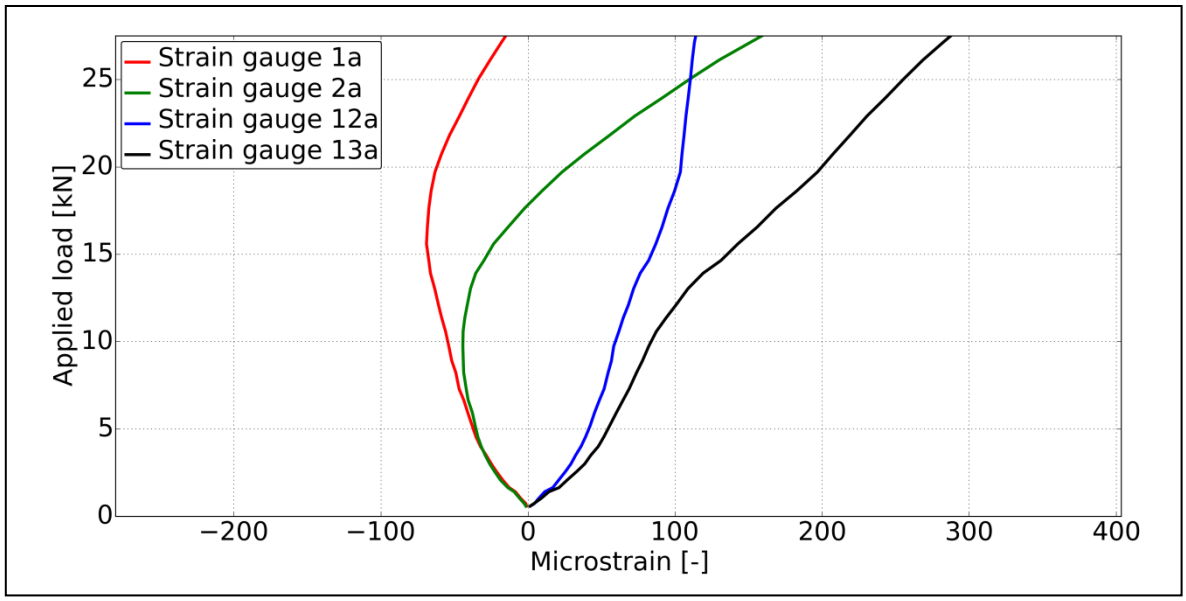

Figure 7.16: Load/strain curves at the start of the sandwich compression test a

The second test on the same sandwich panel was performed with an improved design of the aluminium frame, where extra steel support was applied to prevent out-of-plane displacements at the unloaded edges. Since the sandwich panel was already loaded up to 90% of its final failure during the first test, possible damage already present to the sandwich panel invalidates this second test.
During the second test, final failure was reached after global buckling of the panel was shown on the video recording. In order to approximately determine this load, the results of both rows of strain gauges at different load levels are plotted in figure 7.17. The solid line represents strain gauges 1 to 11 (front of the panel), ranging from 2 to 84.6 cm along the x-axis. The dashed lines indicates strain gauges 12 to 22 (aft of the panel). Each load level is indicated by a different colour and at a load level between 116 kN and 130 kN, the strains on the front and aft of the panel seems to deviate at an increased rate. This indicates buckling of the panel, where at approximately 30 cm and 50 cm, the strains are equal. These two points of equal strain, indicate 3 half waves of global buckling.

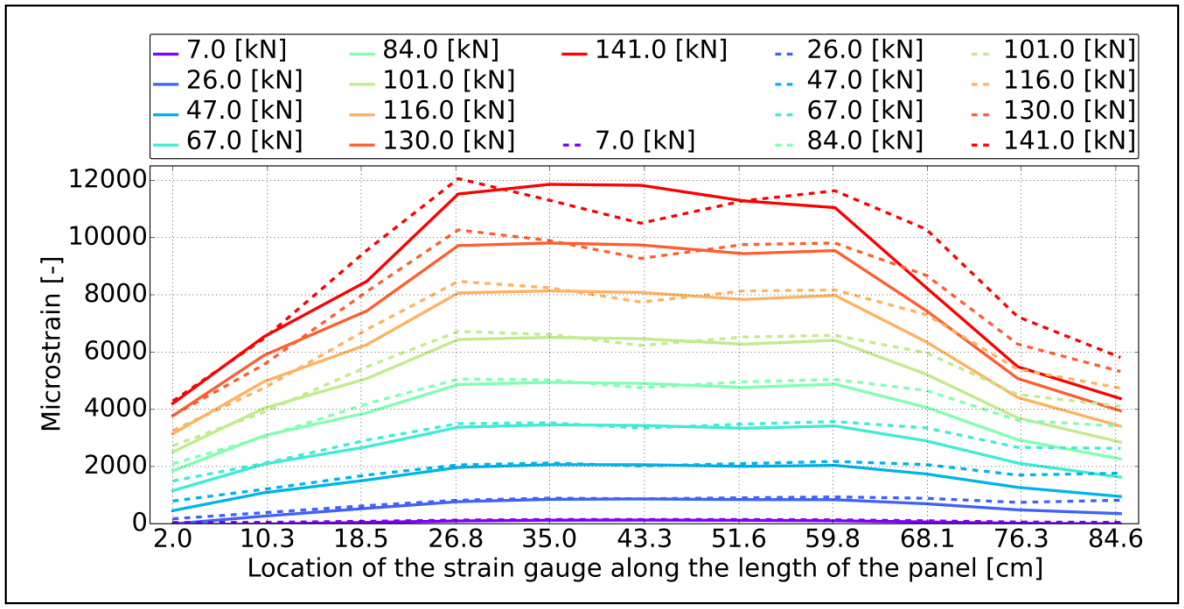

Figure 7.17: Strain curves along the length of the panel, solid lines represent strain gauges 1 to 11, dashed lines represent strain gauges 12 to 22, (improved compression test b)

The larger strains in the middle of the panel, could however not be explained. In order to further investigate this test, it is advised to redesign the load introduction, where a more gradual ply drop should be used. In addition, the aluminium frame could be improved to obtain more realistic boundary conditions during the test.
In order to have an idea between the test data and the initially expected behaviour obtained from the numerical model, the load/displacement curves are shown in figure 7.18. The load/displacement curves of the first and second test are red and green respectively, which show relatively the same behaviour. The second test follows a more stiff curve as a result of the extra applied steel support around the frame. The original design and improved design are also numerically modelled with the tab material included. Based on the manufacturing and quality analysis of the sandwich panel, the following improvements were made to the model:

- Face sheet thickness: changed from 1.35 mm to 1.16 mm
- Foam core thickness: changed from 12 mm to 13.16 mm
- Added the block of tab material at the loaded edges
- Added tie links at the loaded edge

The foam core was increased to 13.16 mm, because the face sheets are modelled by shell elements, which do not represent the mid-plane of the face sheet at the correct distance from the neutral axis. The large difference in displacement is addressed to the large strains observed in the middle of the panel, for which no explanation has yet been found and needs further investigation.

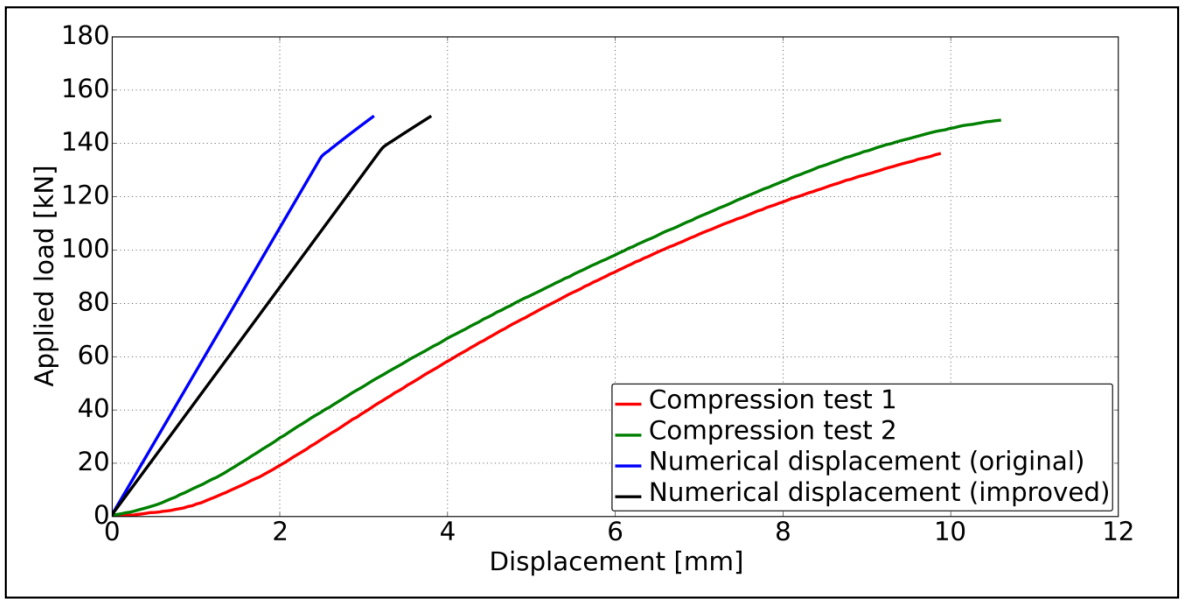

Figure 7.18: Force/displacement curves of experiment and numerical model, sandwich panel

Where the load/displacement curve does not show any agreement between the numerical model and the experiment, the failure load does show some comparison. When performing the eigenvalue analysis from chapter 3 and including the improvements, a global buckling load of 136109 N is expected. This value is compared with the load/strain curves of the second test in figure 7.19. At almost exactly this load level, the two opposing strain gauge 6 and 17 at the middle of the panel start to diverge, which indicates buckling of the panel.

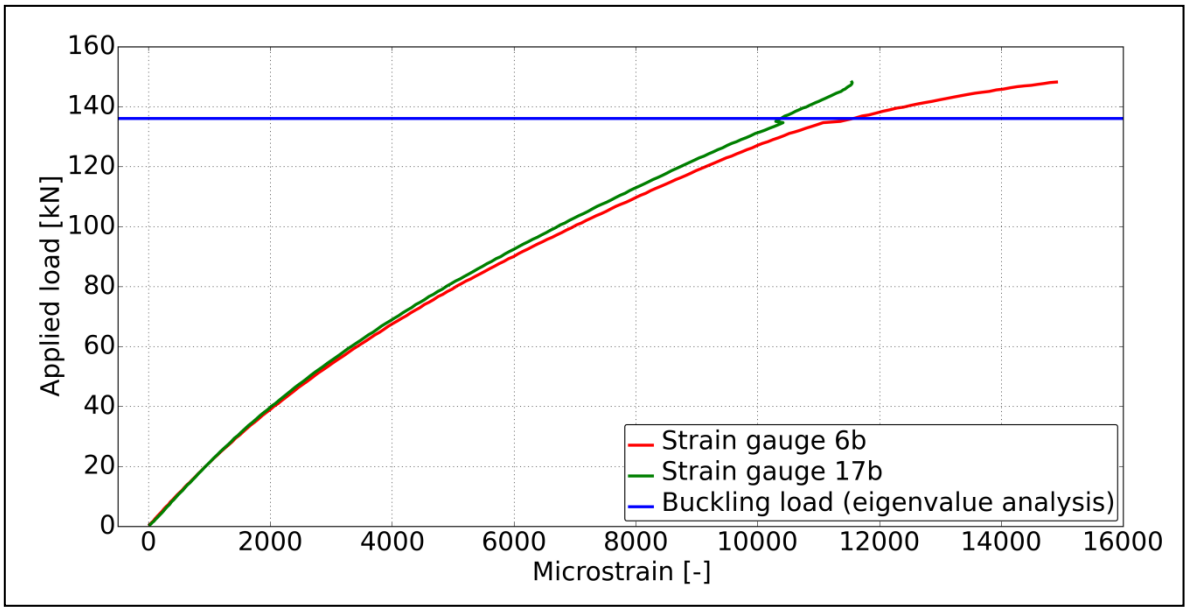

Figure 7.19: Load/strain curve of strain gauges 6 and 17 during second test compared to predicted buckling load

7.3 Orthogrid panel (100 kN design)

The obtained data from the compression test of the large orthogrid panel is evaluated in the section. During the test, a final failure load of -163 kN was observed. In order to compare it with the numerical model, the complete panel is remodelled with its increased length and width and the added tab material. An example of the set-up of the numerical model is shown in appendix N. The model consists of a total of 130686 elements and all the nodes at the edges are fixed in the out-of-plane direction. At one loaded edge, the nodes are fixed in both the in-plane directions, where the other loaded edge is fixed in y-direction and has nodal ties in order to create a uniform displacement as a result of the applied load.
From the quality analysis performed on the panel, the following material and geometric improvements will be implemented in the numerical model:

- Stiffener thickness: Changed from 1.438 mm to 2.3 mm
- Stiffener stiffness: Changed from 39500 MPa to 30043 MPa

The load/displacement curves of the non-linear analysis and the test results up to final failure are graphically shown in figure 7.20. The red curve, indicating the results obtained from the compression test, indicates a lower stiffness initially. From a load of 20 kN at approximately 1 mm displacement, a linear stiffness region is observed. This linear region is compared with the numerical models in table 7.2. The improved model, shows an increased stiffness of the panel, deviating from the experimental result. This higher stiffness from the numerical model was also found for the sample orthogrid panels. The most likely explanation so far thought of is the lower stiffness properties of the grid of stiffeners, of which the causes were outlined in subsection 7.1.1. The influence of the stiffener crossings could be significant since there are 33 along the loading direction of the panel.

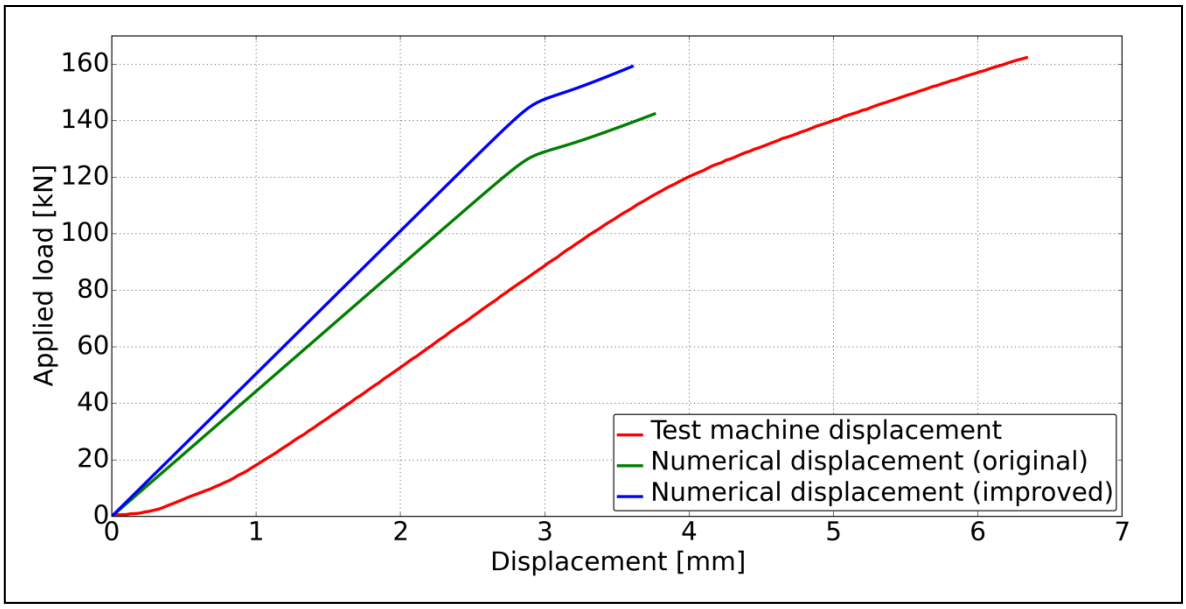

Figure 7.20: Force/displacement curves of experiment and numerical models, orthogrid panel

Table 7.2: Overall panel stiffness of the large orthogrid panel (experiment and numerical models)

	Experiment (40 kN -100 kN)	Original model (5 kN – 60 kN)	Improved model (5 kN – 60 kN)
$\frac{\Delta F}{\Delta d}$ $\left[\frac{kN}{mm}\right]$	35.64	44.27	50.44

The initiation of global buckling of the orthogrid panel can be observed from the strain gauge results. Since the cells on the grid side of the panel were too small, no strain gauges can be applied to this side. A total of 24 strain gauges were applied in order to obtain sufficient results from the test. The locations are schematically presented in figure 7.21. Strain gauge 1 to 17 are applied to obtain the buckling mode of the panel, since global panel buckling is expected initially. Strain gauges 18, 19, 20, 21, 23 and 24 are applied to determine the buckling shape along the y-axis. Strain gauge 22 is applied next to strain gauge 10 at a neighbour skin cell in order to see if the cells locally buckle in different out-of-plane directions as a result of the ultra thin skin.

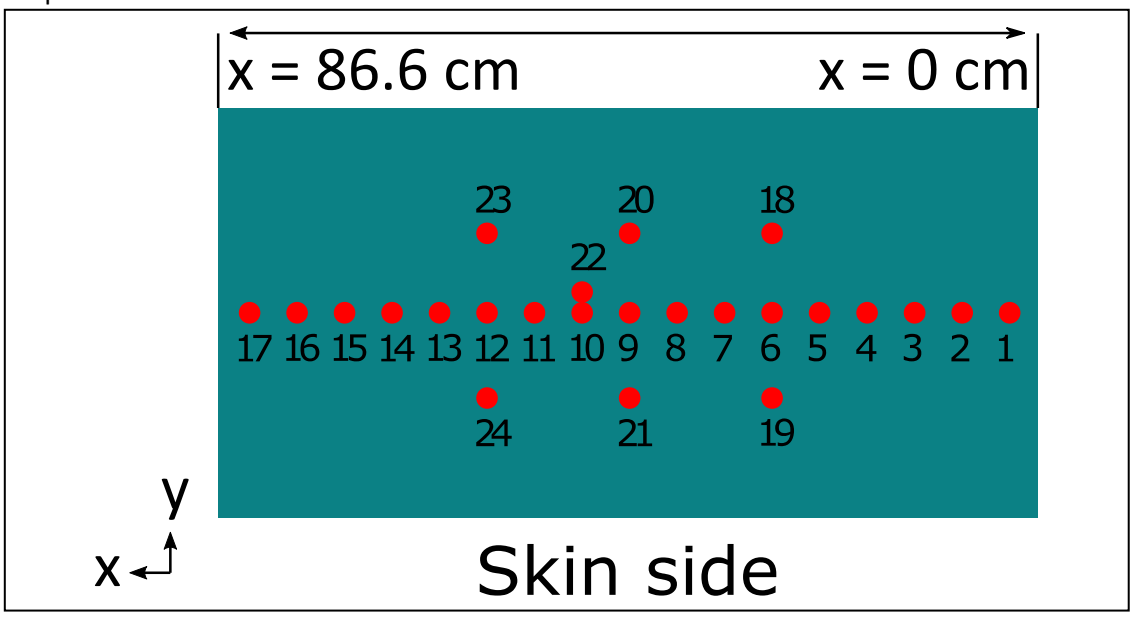

Figure 7.21: Strain gauge locations at the skin side of the orthogrid panel

7.3 Orthogrid panel (100 kN design)

The load/strain curves from strain gauges 1, 3, 5, 7, 9, 11, 13, 15 and 17 are shown in figure 7.22, where it is observed that buckling initiates in the range of 90 to 100 kN. Strain gauge 1 is positioned at the side of the panel, where the aluminium frame is not fully constraining the edges from out-of-plane deflection. It is observed that it induces a very small buckling half wave as a result of this lack of constraint.

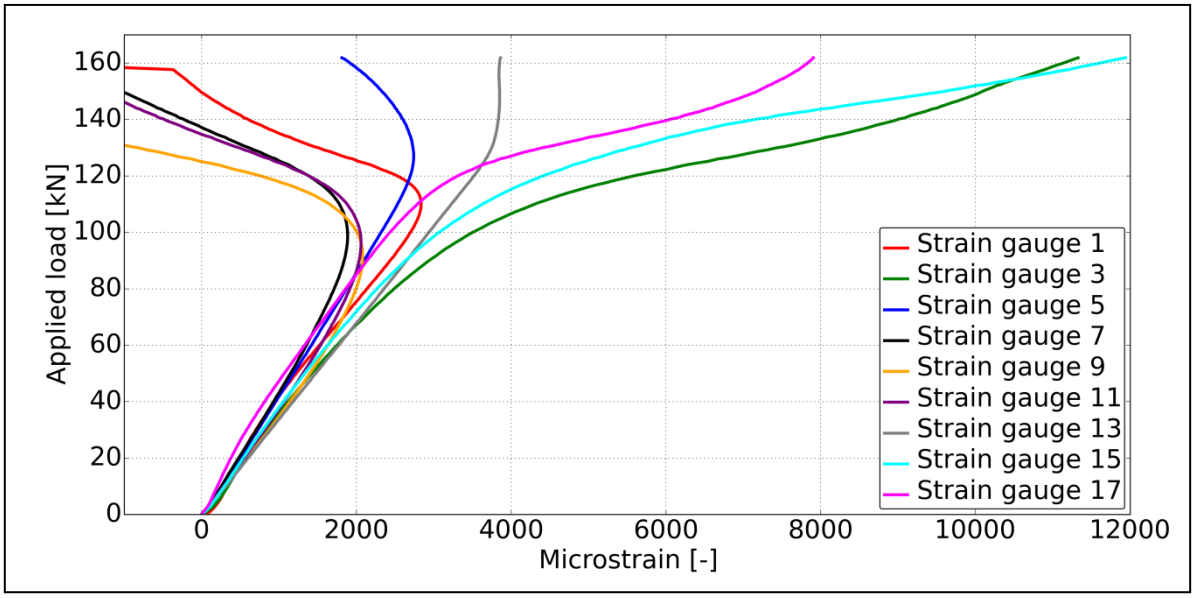

Figure 7.22: Load/strain curves from the compression test of the orthogrid panel

To show the difference more clearly, a comparison is made with the improved numerical model in figure 7.23. Only strain gauges 1 till 9 and their related numerical solution are shown. From the numerical model, strains at 1, 2 and 3 all follow a curve where the strain increases at a faster rate after buckling initiates. Here, it is also apparent that strain gauge 1 shows opposite behaviour as a result of the aluminium frame not covering the full edge. It is therefore be recommended to improve the design of the test set-up, as this could result in unwanted failure during the test.
The linear region of the load/strain curves of both the experiment and the numerical data show good agreement. The initiation of the buckling load is however predicted at a higher load by the numerical model, which will be analysed now.

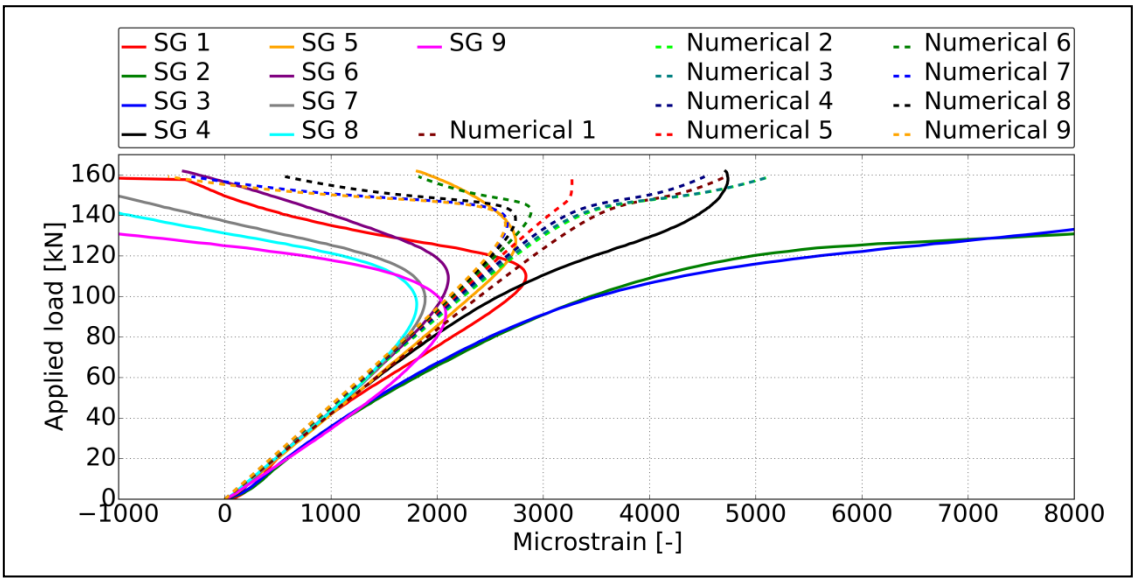

Figure 7.23: Comparison of load/strain curves from the compression test and the numerical model

The buckling mode observed during the compression test of the large panel is presented in figure 7.24. Every curve indicates a certain load level, where on the x-axis, the location of the strain gauge on the panel along the length is indicated. From the experimental results, 3 half waves along the length can clearly be observed, which initiates between the lines of 83 and 105 kN.

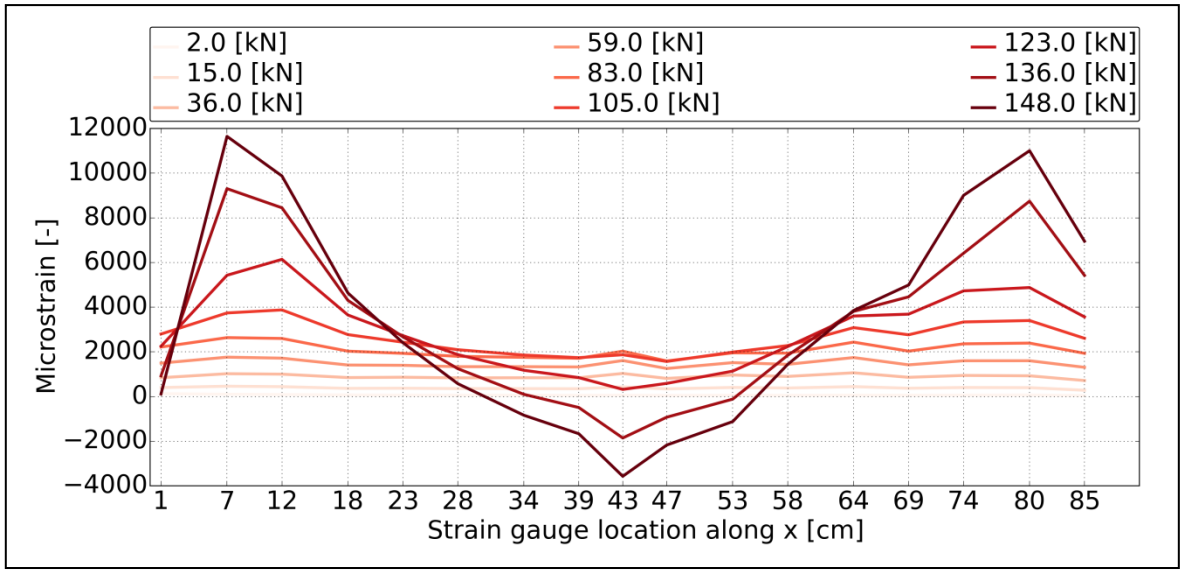

Figure 7.24: Strains along the panel length on different load levels during compression test

A comparison with the improved numerical model is made in figure 7.25, where the dashed lines indicate the results from the numerical model. The improved numerical model also shows 3 half waves, but the expected buckling load is much higher than the experimental value, which could possibly be addressed to the stiffness of the grid.

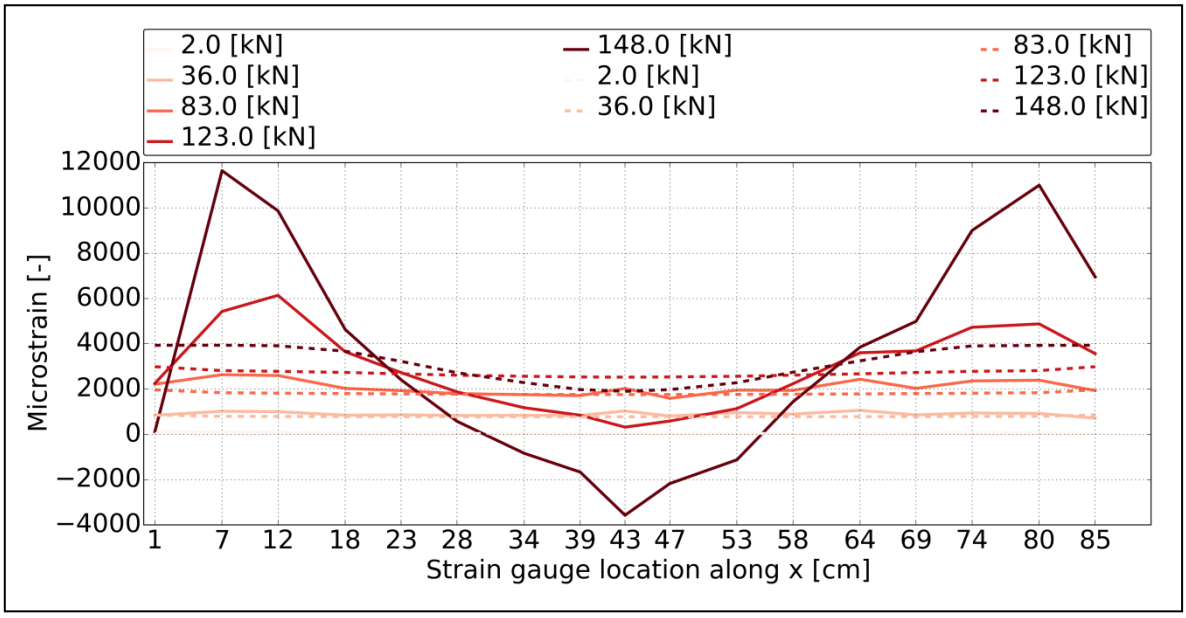

Figure 7.25: Strains along the panel length on different load levels from the improved numerical model

The explanation of the stiffness of the grid being lower as a result of hand lay-up, influence of stiffener crossings and the glass-fibre roving material could be tested by introducing a knockdown factor on the grid stiffness in the numerical model. This factor is chosen by the values stated in table 7.2. Dividing the experimental value by the improved model value, results in a knockdown factor of

0.707. The stiffness of the unidirectional roving is therefore lowered to a value of 21240 MPa. Comparing the compression test results again with the numerical results with a knockdown factor on the stiffness of the stiffeners results in figure 7.26. Initiation of global buckling predicted by the numerical model shows a much better result compared to the experimental data. However, the global buckling load is still slightly over predicted and the post-buckling strains at the edges are higher in reality.

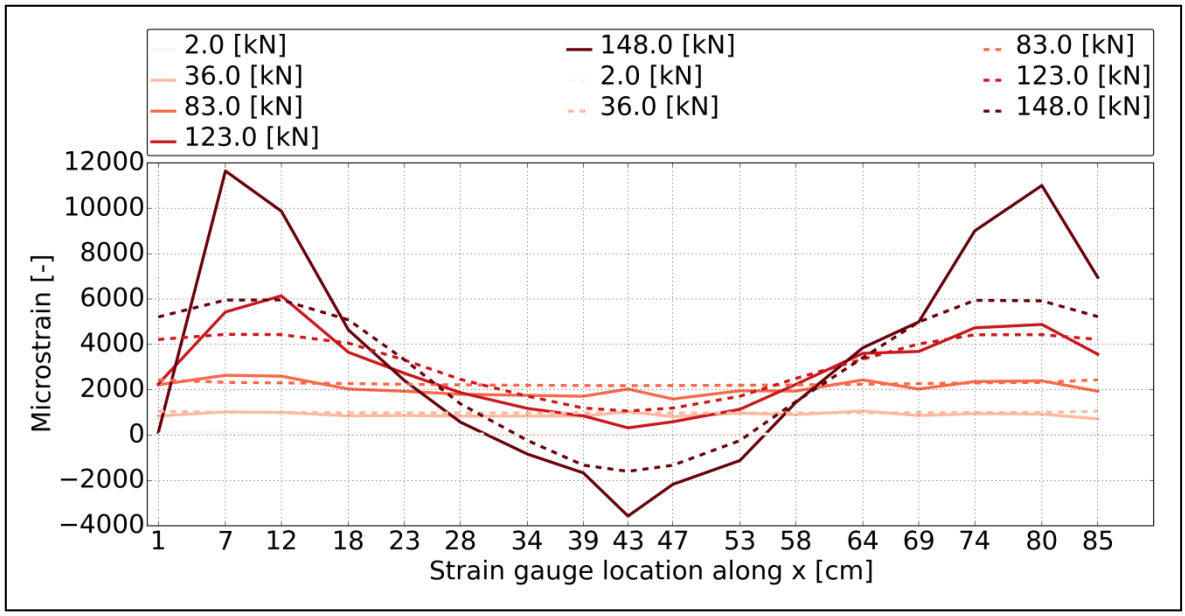

Figure 7.26: Strains along the panel length on different load levels with a knockdown factor on the stiffness of the grid

The strains and critical buckling load could be influenced by material and structural imperfections, which are not taken into account in the numerical model.
In the experiment, the boundary conditions at the unloaded edges were improved with the stiff steel profiles and thick bolts. A small out-of-plane displacement is however always allowed since the aluminium frame is not clamping the sides.
Based on the initial stage of the load/displacement curve from the panel, it is advised to improve the load introduction, because this could be the cause of this low stiffness at the initial applied load. The boundary conditions at the load introduction could also be an explanation of the large strains at the loaded edges and the early global buckling.
From a numerical analysis perspective, different element types could be used, which could possibly improve the results of the high post buckling strains as a result of the large curvatures. A higher order shell element is therefore recommended as a more accurate solution.

The strain results along the y-axis can also be plotted for different load levels. Since at each of the three rows of strain gauges along the y-axis, the same behaviour of 1 half wave is shown, only the results from strain gauges 20, 9 and 21 are plotted in figure 7.27. This result is in agreement with the numerical model.

Strain gauge 22 was placed in order to see if any skin cell buckling would have occurred during the test. The load/strain curve is therefore compared to strain gauge 10, which is placed in an adjacent skin cell. Both curves are not exactly showing the same strains, but both skin cells do bend in the same direction, explained by the fact that the strain gauges both measured compressive strain first and change into a tensile strain after global buckling initiates. The assumption here is made, that only one half wave would be present in case of intracellular buckling. For obtaining accurate results on these questions in the future, digital image correlation on the skin side of the panel is advised.

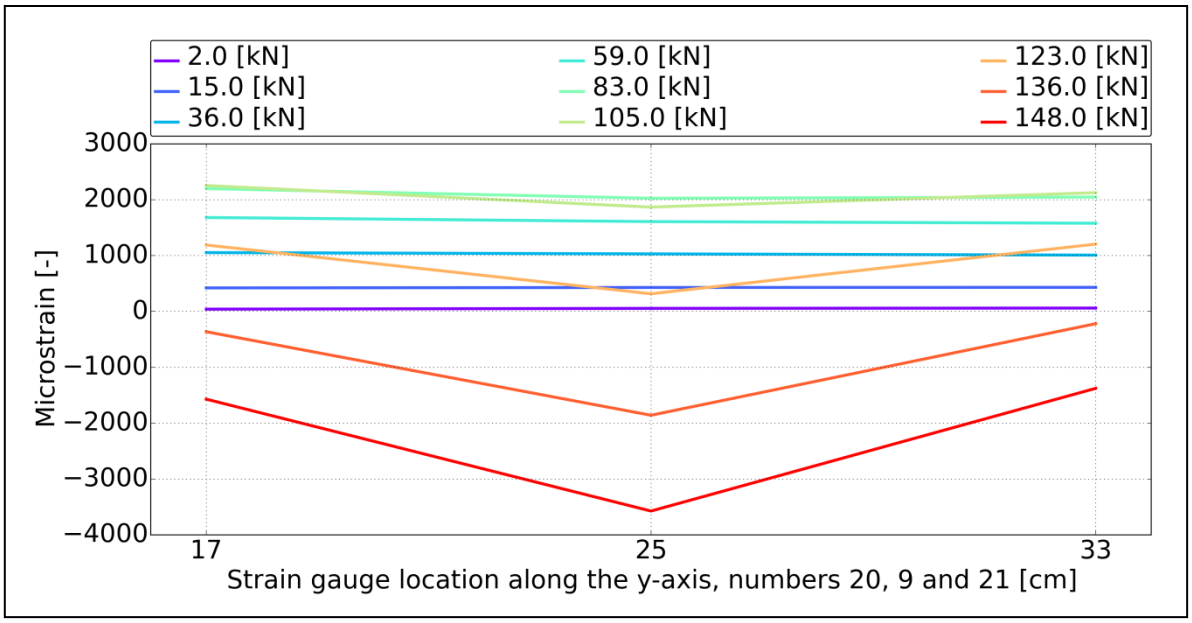

Figure 7.27: Strains along the panel width on different load levels obtained from the compression test

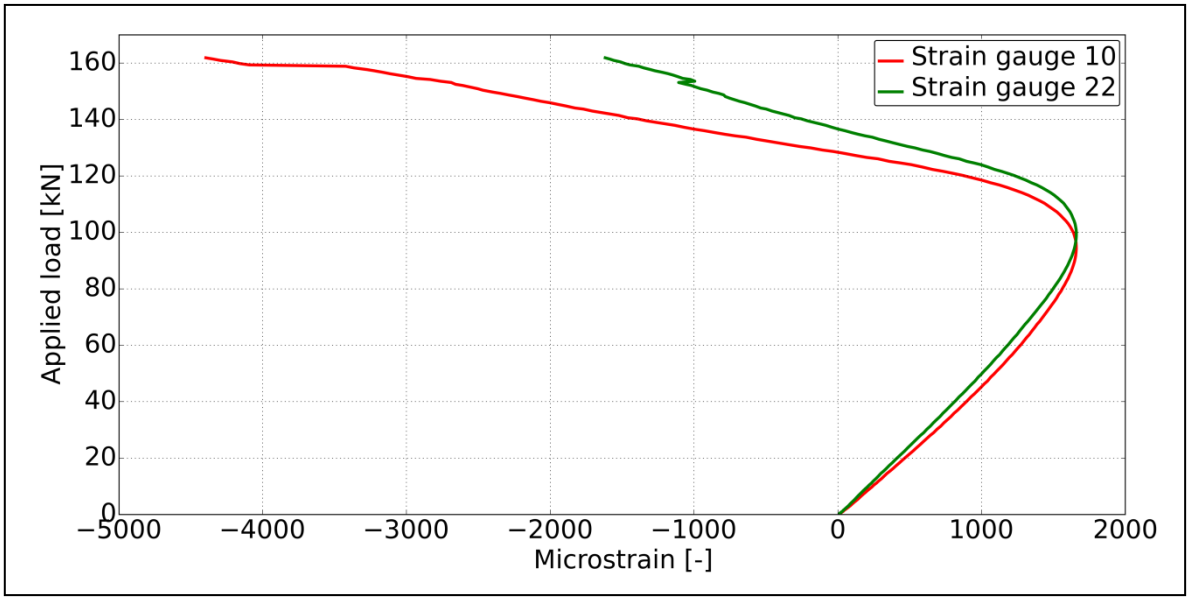

Figure 7.28: Load/strain curves of strain gauge 10 and 22, positioned in two adjacent cells

In order to make a comparison with the low-weight designs found by the linear static eigenvalue analysis, the non-linear model is compared to the used eigenvalue analysis. In this calculation, the skin thickness has a reduced value of 0.53 mm. This is a result of the initial skin thickness calculations, which were later found to be inaccurate. With an applied load of 446 N, the lowest eigenvalue obtained from the analysis is 328.9. This results in a prediction of 146689 N for the buckling load. It was observed from the non-linear numerical model that global buckling initiated at approximately 130000 N, which is 11.4% lower than the critical load from the eigenvalue analysis. The geometric non-linearity of the orthogrid panel is therefore expected to give lower global buckling load than initially expected by the linear static eigenvalue analysis. This penalty should be taken into account as a result of the asymmetry of the grid stiffened structure.

8.Conclusions and Recommendations

As a result of the performed study described in this report, conclusions and recommendations are given for future research in this chapter. The conclusions in section 8.1 will evaluate the main and sub research questions, which where stated at the beginning of the project. Based on the findings and drawn (sub)conclusions, section 8.2 is devoted to recommendations for new studies related to the subject.

8.1 Conclusions

In order to give a clear conclusion to the main research question at the end of this section, an overview of the findings and sub conclusions are given first. A division is made between the two different parts of the project. The first part is evaluated in 8.1.1, where the sandwich and grid stiffened structure are designed, analysed and compared. The second part related to validation, including the manufacturing and testing of the designed structures, is outlined in subsection 8.1.2. The final conclusion is then given in subsection 8.1.3.

8.1.1. Sub conclusions on verification

The first part of the thesis, including the design and analysis of the sandwich and othogrid structure, is outlined in this subsection.

In order to obtain a benchmark design for this study, the sandwich structure was designed and analysed. Different analytical and numerical models were set up to calculate different failure loads of the sandwich panels. In this study, the numerical model consisting of element type 21 and element type 22 resulted in the most accurate prediction of the buckling load compared to the analytical model. In addition, the computational cost was low compared to the other two presented models.
Using the analytical models, low-weight sandwich designs have been found and were verified by the numerical model. Since the low-weight designs were obtained from all possible combinations of design variables, they could be considered the lowest-weight solutions of the sandwich panel. However, the analytical models used to analyse the sandwich structure were found in literature, where they were not validated over a full range of designs. This results in uncertainties about the validity of the used analytical models, which should be proven in future studies.
From all the different calculated failure loads, the assumed material failure load predicted by the Tsai-Wu and Tsai-Hill criterion do not seem to limit the low-weight designs of sandwich panels, since both show high failure loads with respect to the other modes of failure. Therefore, a low-weight design seems to be driven by stability of the face sheets and the strength of the core material.

The studied innovative design was the orthogrid structure, on which different modes of failure are applicable. Analytical and numerical models were set up for the structure. Each of the different models was verified by a parametric study. Global buckling predictions obtained from the analytical [6] and the numerical model have shown good agreement over a broad range of designs. The analytical models predicting stiffener crippling and intracellular buckling are not in very good agreement with the numerical models, but based on the parametric study, the influence of different design variables on both of the local failure modes could be determined relatively well. The influence of the different design variables on the failure modes were found to be as follows:

- Increasing the skin thickness resulted in an exponential increase of the intracellular buckling load predicted by the analytical and numerical model.
- Increasing the number of longitudinal stiffeners and as a result, decreasing the stiffener spacing in transverse direction, resulted in an exponential increase of the intracellular buckling load predicted by the analytical and numerical model.

- Increasing the stiffener thickness results in an exponential increase of the stiffener crippling load predicted by the analytical and numerical model.
- Increasing the stiffener height resulted in an exponential increase of the global buckling load predicted by the analytical and numerical model.
- The influence of transverse stiffeners on the different failure modes seem to be low, where it is assumed that their main function is to lower the length of the longitudinal stiffener sections of the grid. This improvement could also be realized by applying angled stiffeners, which could also improve the torsional and shear stiffness of the orthogrid panels.

Using knockdown factors on the analytical models of the orthogrid structure, preliminary low-weight designs were obtained for a range of design loads. The preliminary designs were further improved by (re)moving material along the panel. The resulting low-weight designs were found for an orthogrid structure without any design constraint and for a design with a lower limit of 5 mm on the stiffener thickness. The weight for grid stiffened panels could possibly be further decreased, when more design variables are taken into account.

In the final chapter of part I, the benchmark sandwich design and the orthogrid designs were compared. Based on a linear elastic buckling analysis, it is concluded that the structural performance of the orthogrid structure improves faster in relation to the sandwich structure when the applied compressive loads increase. Low-weight grid stiffened designs were found with and without design constraints. The theoretical low-weight designs did however not give very high improvements with respect to the more practical designs.
A drawback of the theoretical low-weight design could be the high number of transverse and longitudinal stiffeners, having a low thickness. This results in a high number of stiffener crossings, which could influence the performance of the structure. The thin stiffeners could also result in a bad quality product as a result of the tolerances on the manufacturing process.
A positive effect could be obtained by the small skin thickness found for the theoretical low-weight designs as a result of the smaller skin cells. This lower skin thickness could be beneficial in relation to the asymmetry of the panel, which introduces a stretching/bending coupling.

8.1.2. Sub conclusions on validation

The second part of the thesis, including the manufacturing and testing of the sandwich and orthogrid panels, is outlined in this subsection. A validation plan was set up in an attempt to give a solid conclusion on the designed low-weight panels.

The sandwich panel was manufactured by a relatively straight forward vacuum infusion process and the overall quality seemed to be sufficient for testing. In order to obtain a good quality orthogrid structure, two small sample orthogrid panels were initially manufactured by a more complex vacuum infusion process. After obtaining a sufficiently good quality product for testing, a larger orthogrid panel was also manufactured.
The largest tolerances on the manufacturing process were found for the stiffener thickness. The two sample orthogrid panels had a smaller stiffener thickness than designed for and resulted in an average fibre volume fraction of 40.15% and 40.93%. The larger orthogrid panel had a higher stiffener thickness than it was initially designed for and the average fibre volume fraction measured was 37%. It seems that a lower stiffener thickness has a positive influence on the fibre volume fractions. This could be a result of the expansion of the mould, which compresses the dry fibres in the stiffeners. Therefore, in order to obtain high fibre volume fractions in the grid, a good compaction during the vacuum infusion process is required. In the case of observable voids, they were mainly found at the middle locations of the stiffener sections.

8.1 Conclusions

A limitation of the used manufacturing process was the time involved. The stiffened grid was hand layed up by winding a glass-fibre roving into the silicon mould. Making larger panels or panels with even more meters of glass-fibre roving in the grid can result in weeks of manual winding.

All the manufactured panels were tested with a developed test set up, where all edges were supposed to behave as simply supported. The results from these first tests seems to be promising, but improvements to the test set-up can and should be made in order to obtain better agreement between the numerical model and the compression test:

- The boundary conditions of the test set-up should be further improved to prevent bending at one of the loaded edges at the start of the test.
- The load introduction on the test panels should be improved to potentially improve the results from the compression test.

The machine displacements and the strain gauge results were also compared to a non linear numerical model. During the evaluation of the results, the quality analysis of all the panels was used to introduce model improvements, in order to explain any differences.
Intracellular buckling on the sample orthogrid panels was not predicted accurately by the numerical model. The obtained results were conservative, probably by the cell being modelled wider than they actually are. This possible explanation was tested by reducing the cell size on the numerical model, resulting in a more accurate intracellular buckling load. It was also found that the skin thickness had a large influence on this mode of failure and any scatter or imperfections along the surface of the skin could therefore lead to early intracellular buckling.
The overall stiffness on all the orthogrid panels were predicted too high by the numerical models. Different possible explanations were proposed:

- The influence of fibre waviness at the stiffener crossings were not taken into account.
- During the manufacturing process, the fibres were not under tension, resulting in possible waviness through the grid.
- The glass-fibre roving could have different stiffness properties compared to the measured material properties obtained from a unidirectional fabric. It was initially assumed that both fibres would have approximately the same properties, but potential twist or a different processing technique of the fibre could influence these properties.

The three possible reasons are not proven, but by introducing a knockdown factor on the stiffness of the grid, a much better agreement between the compression test and the numerical model was found.
Since the actual goal was to validate the low-weight designs from the first part of the project, the non-linear analysis was compared to the linear static eigenvalue analysis. For the two sample orthogrid panels, failing in a combined mode of intracellular buckling and stiffener crippling, the eigenvalue analysis predicted the same load as the non-linear model. For the large orthogrid panel, failing in global buckling, a difference of 11.4% was found. This lower critical failure load predicted by the non linear numerical model should be taken into account and is a result of the asymmetry of the grid stiffened structure.
The sandwich panel compression test did not run according to plan and it had to be aborted prior to failure in the first test. With an improved test set-up, where the aluminium frame was stiffened, the sandwich panel was loaded up to final failure. The sandwich panel critical failure load was predicted at approximately the same value as obtained from the eigenvalue analysis, but a large difference in the load/displacement curves were observed. Any conclusions on the test and the design therefore requires further study and explanation.

8.1.3. Main research question

At the start of the project, the following main research question was stated:

“Is it possible to create a lighter weight trailing edge panel design by using an orthogrid stiffened panel, with remaining strength and stiffness properties at equal or lower cost?”

Based on the research performed in this study, a strong conclusion cannot be given, because there are still limitations to be solved.
Besides the fact that numerical analysis shows promising results about the reduction of the weight of the structure by using a grid stiffened structure, the loading conditions were simplified. In reality, the introduction of shear or torsion could result in bad performance of the grid stiffened structure. Another limitation could be the simplified analysis as a result of the computational cost of the numerical model of a grid stiffened structure. As was shown for the large orthogrid panel, a non-linear analysis introduces a penalty of 11.4% on the result of the performed eigenvalue analysis.
The manufacturing has been limited to a grid structure with uniform heights. As the height of the grid is found of major influence on the global buckling load of the grid stiffened panel, the ability to manufacture panels with stiffeners of varying heights along the length of the blade is of great importance. An automated process for winding or laying up the stiffened grid is also necessary to enable the manufacturing of larger structures.
Since there are not many test methods known on sub component level for wind turbines trailing panels, a large gap between manufacturing and testing of small specimens and a full wind turbine blade exists. New test methods are therefore required to design and test low-weight grid stiffened structures of intermediate size.

8.2 Recommendations

The implementation of grid stiffened structures in wind turbine blade trailing panels still has a lot of research questions to answer, as was outlined in the conclusion of this study. However, the technology is still promising to investigate as a substitution of sandwich panels for the following reasons:

- With the addition of more design variables and state-of-the-art optimization techniques, improved weight reduction could possibly be found.
- No use of balsawood or foam core material is required, where the balsawood possesses non-uniform material properties and has the drawback that it can rot, resulting in high repair and maintenance costs.
- An automated manufacturing process can significantly drop the cost of production
- Good damage tolerance of the grid stiffened structure

In order to benefit from the above advantages, recommendations for future studies on the subject are given on design and analysis, manufacturing and testing.

Design and analysis

Since the computational cost is limiting the accuracy of the models, improved techniques should be developed to determine the different failure modes. Especially the local behaviour of the skin cells and the stiffeners should be investigated and simple and efficient numerical models should be developed to accurately predict these failure modes. In order to gain these insights, different element strategies could be compared. Another option to determine the local modes of failure is to compare small sections of a grid with the behaviour of the full panel and try to obtain comparable results by setting the right boundary conditions and introducing the correct loading conditions.

8.2 Recommendations

As was already mentioned, introducing more design variables could lead to more efficient designs. Different design variables, which could lead to lower weight designs are:

- Different thickness of the transverse and longitudinal stiffeners
- Different heights of the transverse and longitudinal stiffeners
- Different angles of stiffeners or introducing the isogrid type of structure

An important aspect to take into account is the design load of the panels, where only a compression load was used in this study. Making the load case more complex by introducing torsion and shear, results in a more realistic design for the panel and with that, a more fair comparison with the sandwich structure.

Manufacturing

Related to the production process of the grid stiffened panels, automation is possibly one of the most important aspects to further develop. This would lead to the ability to upscale the structures to be tested or faster production of small test specimens.
The fibre volume content of the stiffeners has also been found to have a relatively low value and methods to improve this with the present techniques would result in higher quality products. In the same line of thought, further improving the manufacturing techniques with respect to tolerances is recommended.
Finally, along the length of the blade, the height of the stiffeners will change in value, which requires manufacturing techniques to obtain these ply drops in the stiffeners. Using the transverse stiffener to facilitate for these ply drops could be an option, where the fibres are directed from the transverse stiffener into the longitudinal stiffener and with that, increasing the amount of roving and the stiffener height.

Testing

With respect to testing it is recommended to continue the study on subcomponent level tests and develop new tests for wind turbine trailing panels, potentially with more realistic loading conditions. Grid stiffened structures could then be tested, prior to immediately manufacturing large structures or full blade sections.
The test set-up used in this study could be further improved by adjusting the boundary conditions, where full contact between the frame and the unloaded edges of the panel is present. More tests should also be performed to improve the similarity of the boundary conditions of the numerical model and the experimental test.

Other recommendations for the wind turbine trailing panels

Different aspects, which were stated in the literature study, but not addressed in this research project are still interesting topics to consider for future studies. Grid stiffened structures could possibly be beneficial with respect to the conventional wind turbine blade structure after obtaining answers on the following questions:

- What is the influence of grid stiffened structures on maintenance and repair?
- How are the load introductions designed for grid stiffened structures?
- How are the top and bottom trailing panels adhered at the trailing edge and does it have any advantages or disadvantages with respect to the present sandwich structure?
- How does a grid stiffened structure perform under fatigue loading obtained from the periodic rotations of the blade?

REFERENCES

[1] INNWIND.EU: Deliverable 2.22, New lightweight structural blade designs and blade designs with build- in structural couplings, INNWIND.EU technical report, *Deliverable 2.22 available at www.innwind.eu*, November 2017.

[2] INNWIND.EU: Deliverable 2.24, Manufactured and laboratory tested scaled blades and parts of the blade, INNWIND.EU technical report, *Deliverable 2.24 available at www.innwind.eu*, November 2017.

[3] Burton, T., Jenkins, N., Sharpe, D., & Bossanyi, E. (2011). Wind energy handbook. John Wiley & Sons.

[4] Hau, E., & Von Renouard, H. (2000). Wind turbines: fundamentals, technologies, application, economics (Vol. 2). Munich: Springer.

[5] Jaunky, N., Knight, N. F., & Ambur, D. R. (1996). Formulation of an improved smeared stiffener theory for buckling analysis of grid-stiffened composite panels. *Composites Part B: Engineering*, 27(5), 519-526.

[6] Xu, Y., Tong, Y., Liu, M., & Suman, B. (2016). A new effective smeared stiffener method for global buckling analysis of grid stiffened composite panels. *Composite Structures,* 158, 83-91.

[7] Kidane, S., Li, G., Helms, J., Pang, S. S., & Woldesenbet, E. (2003). Buckling load analysis of grid stiffened composite cylinders. *Composites Part B: Engineering,* 34(1), 1-9.

[8] Wang, D., & Abdalla, M. M. (2015). Global and local buckling analysis of grid-stiffened composite panels. *Composite Structures,* 119, 767-776.

[9] Shi, S., Sun, Z., Ren, M., Chen, H., & Hu, X. (2013). Buckling resistance of grid-stiffened carbon-fiber thin-shell structures. *Composites Part B: Engineering,* 45(1), 888-896.

[10] Li, G., & Cheng, J. (2007). A generalized analytical modeling of grid stiffened composite structures. *Journal of Composite Materials,* 41(24), 2939-2969.

[11] Wand, B., Hao, P., Li, G., Tian, K., Du, K., Wang, X., … & Tang, X. (2014). Two-stage size-layout optimization of axially compressed stiffened panels. *Structural and Multidisciplinary Optimization,* 50(2), 313-327.

[12] Wodesenbet, E., Kidane, S., & Pang, S. S. (2003). Optimization for buckling loads of grid stiffened composite panels. *Composite Structures,* 60(2), 159-169.

[13] Meink, T. E., Huybrechts, S., Ganley, J., & Shen, M. H. (1999). The effect of varying thickness on the buckling of orthotropic plates. *Journal of composite materials,* 33(11), 1048-1061.

[14] Kassapoglou, C. (2013). Design and analysis of composite structures: with applications to aerospace structures. John Wiley & Sons.

[15] Weber, M. J., & Middendorf, P. (2014). Semi-analytical skin buckling of curved orthotropic grid-stiffened shells. *Composite Structures,* 108, 616-624.

[16] Sorrentino, L., Marchetti, M., Bellini, C., Delfini, A., & Albano, M. (2016). Design and manufacturing of an isogrid structure in composite material: Numerical and experimental results. *Composite Structures,* 143, 189-201.

[17] Sorrentino, L., Marchetti, M., Bellini, C., Delfini, A., & Del Sette, F. (2017). Manufacture of high performance isogrid structure by Robotic Filament Winding. *Composite Structures,* 164, 43-50.

[18] Huybrechts, S. M., Meink, T. E., Wegner, P. M., & Ganley, J. M. (2002). Manufacturing theory for advanced grid stiffened structures. *Composites Part A: Applied Science and Manufacturing*, *33*(2), 155-161.

[19] Shroff, S., & Kassapoglou, C. (2015). Progressive failure modelling of impacted composite panels under compression. *Journal of Reinforced Plastics and Composites*, *34*(19), 1603-1614.

[20] Shroff, S., Acar, E., Kassapoglou, C (2017). Design, analysis, fabrication, and testing of composite grid-stiffened panels for aircraft structures. *Thin-Walled Structures*, v119, 0263-8231

[21] McDonnell Douglas Astronautics Company (1973). *Isogrid Design Handbook*, *1600*, G4295A.

[22] Kim, T. D. (1999). Fabrication and testing of composite isogrid stiffened cylinder. *Composite structures*, *45*(1), 1-6.

[23] Kim, T. D. (2000). Fabrication and testing of thin composite isogrid stiffened panel. *Composite structures, 49(1), 21-25.*

[24] Vinson, J. R. (2006). *Plate and panel structures of isotropic, composite and piezoelectric materials, including sandwich construction* (Vol. 120). Springer Science & Business Media.

[25] Daniel, I. M. & Ishai, O. (2006). *Engineering mechanics of composite materials*. Oxford university press

[26] MSC Software Corporation, Marc 2016, *Volume B: Element Library*

[27] Heder, M. (1991). Buckling of sandwich panels with different boundary conditions—A comparison between FE-analysis and analytical solutions. *Composite structures*, *19*(4), 313-332.

[28] Community Research and Development Information Service – CORDIS, http://cordis.europa.eu/project/rcn/106004_en.html

[29] Vadakke, V., & Carlsson, L. A. (2004). Experimental investigation of compression failure mechanisms of composite faced foam core sandwich specimens. *Journal of Sandwich Structures and Materials*, *6*(4), 327-342.

[30] Chen, H. J., & Tsai, S. W. (1996). Analysis and optimum design of composite grid structures. *Journal of composite materials*, *30*(4), 503-534.

[31] Tsai, S. W., & Wu, E. M. (1971). A general theory of strength for anisotropic materials. *Journal of composite materials*, *5*(1), 58-80.

[32] Azzi, V. D., & Tsai, S. W. (1965). Anisotropic strength of composites. *Experimental mechanics*, *5*(9), 283-288.

[33] Lahuerta Calahorra, F. (2017). Thickness effect in composite laminates in static and fatigue loading.

Appendix A

MATERIAL PROPERTIES USED FOR DESIGN

This appendix shows the different material properties, which are used in the calculations during the project. The required properties from the epoxy resin are shown in table A.1. The material properties of the biaxial glass fibre fabric are given in table A.2 [33]. It should be noted that the fabric is a lay-up of [+45] and [-45] degree plies, resulting in an asymmetric ply. The values given in the table are also based on a fibre volume fraction of 50%. The properties of the core material used for the sandwich panel are described in table A.3. The unidirectional roving used in the grid of the orthogrid stiffened structures are outlined in table A.4. As well as for the biaxial glass fibre, the values given for the unidirectional roving are also based on a fibre volume fraction of 50%.

Table A.1: Properties of the epoxy resin

EPIKOTE Resin MGS RIMR 135 EPIKURE Curing Agent MGS RIMH 137		
Elastic modulus [MPa]	E_{xx}	3000
Density epoxy [kg/m^3]	ρ_{resin}	1150

Table A.2: Properties of biaxial glass-fibre impregnated with EPIKOTE RIMR 135 [33]

Biax 12 Type E Glass Fibre		
Elastic modulus [MPa]	E_{11}	26000
	E_{22}	26000
	E_{33}	13190
Poisson [-]	ν_{12}	0.15
	ν_{23}	0.15
	ν_{31}	0.08
Shear modulus [MPa]	G_{12}	13535
	G_{13}	3535
	G_{23}	3535
Tension strength [MPa]	σ_{t11}	424.5
Compression strength [MPa]	σ_{c11}	315
Shear strength [MPa]	τ_{12}	250
Tension strength [MPa]	σ_{t22}	424.5
Compression strength [MPa]	σ_{c22}	315
Shear strength [MPa]	τ_{23}	43.5
Tension strength [MPa]	σ_{t33}	85
Compression strength [MPa]	σ_{c33}	147
Shear strength [MPa]	τ_{13}	43.5
Layer thickness [mm]	t_{ply}	0.675
Density epoxy [kg/m^3]	ρ_{resin}	1150
Density glass fibre [kg/m^3]	ρ_{fibre}	2600
Assumed fibre volume fraction [%]	FVF_{biax}	50
Density GFRP [kg/m^3]	ρ_{biax}	1875

Table A.3: Properties of the sandwich core material

Airex C7075		
Elastic modulus [MPa]	E_{xx}	66
Poisson [-]	ν_{12}	0.3
Shear modulus [MPa]	G_{xy}	30
Thickness (availability) [mm]	t_{core}	3 till 68, stepsize = 1
Density [kg/m^3]	ρ_{core}	80

Table A.4: Properties of unidirectional glass-fibre roving impregnated with EPIKOTE RIMR 135 [33]

UD roving Type E Glass Fibre		
Elastic modulus [MPa]	E_{11}	39500
	E_{22}	13190
	E_{33}	13190
Poisson [-]	ν_{12}	0.26
	ν_{23}	0.26
	ν_{31}	0.08
Shear modulus [MPa]	G_{12}	3535
	G_{13}	3535
	G_{23}	3535
Tension strength [MPa]	σ_{t11}	849
Compression strength [MPa]	σ_{c11}	630
Shear strength [MPa]	τ_{12}	43.5
Tension strength [MPa]	σ_{t22}	85
Compression strength [MPa]	σ_{c22}	147
Shear strength [MPa]	τ_{23}	43.5
Tension strength [MPa]	σ_{t33}	85
Compression strength [MPa]	σ_{c33}	147
Shear strength [MPa]	τ_{13}	43.5
Layer thickness [mm]	t_{ply}	0.719
Density epoxy [kg/m^3]	ρ_{resin}	1150
Density glass fibre [kg/m^3]	ρ_{fibre}	2600
Assumed fibre volume fraction [%]	FVF_{UD}	50
Density GFRP [kg/m^3]	ρ_{UD}	1875

Appendix B

CALCULATION OF FIRST PLY FAILURE BY TSAI-WU AND TSAI-HILL FAILURE CRITERIA

The theory described in this appendix can be found in different composite handbooks [14, 25]. By using the classical laminate theory the global strains of the panel can be obtained from the ABD matrix equation:

$$\begin{bmatrix} N_{x,st} \\ N_{y,st} \\ N_{xy,st} \\ M_{x,st} \\ M_{y,st} \\ M_{xy,st} \end{bmatrix} = \begin{bmatrix} A_{11} & A_{12} & A_{16} & B_{11} & B_{12} & B_{16} \\ A_{21} & A_{22} & A_{26} & B_{21} & B_{22} & B_{26} \\ A_{61} & A_{62} & A_{66} & B_{61} & B_{62} & B_{66} \\ B_{11} & B_{12} & B_{16} & D_{11} & D_{12} & D_{16} \\ B_{21} & B_{22} & B_{26} & D_{21} & D_{22} & D_{26} \\ B_{61} & B_{62} & B_{66} & D_{61} & D_{62} & D_{66} \end{bmatrix} * \begin{bmatrix} \varepsilon_x^0 \\ \varepsilon_y^0 \\ \gamma_{xy}^0 \\ \kappa_x \\ \kappa_y \\ \kappa_{xy} \end{bmatrix} \qquad (B.1)$$

By using the inverse relation and applying a load of 1 kN/mm in x-direction, the corresponding strains and curvatures can be found. Knowing the strains and curvatures, the strain in each ply trough the thickness can be obtained by:

$$\begin{bmatrix} \varepsilon_x \\ \varepsilon_y \\ \gamma_{xy} \end{bmatrix} = \begin{bmatrix} \varepsilon_{x0} \\ \varepsilon_{y0} \\ \gamma_{xy0} \end{bmatrix} + z \begin{bmatrix} \kappa_x \\ \kappa_y \\ \kappa_{xy} \end{bmatrix} \qquad (B.2)$$

Knowing the strain in each ply, the stress in each ply can be determined based on the angle of the fibres in each layer. The relation between the stress and strain within each ply is described as:

$$\begin{bmatrix} \sigma_x \\ \sigma_y \\ \tau_{xy} \end{bmatrix} = \begin{bmatrix} Q_{11} & Q_{12} & Q_{16} \\ Q_{12} & Q_{22} & Q_{26} \\ Q_{16} & Q_{26} & Q_{66} \end{bmatrix} \begin{bmatrix} \varepsilon_x \\ \varepsilon_y \\ \gamma_{xy} \end{bmatrix} \qquad (B.3)$$

Where:

$$Q_{11} = m^4 * Q_{xx} + n^4 * Q_{yy} + 2m^2n^2 * Q_{xy} + 4m^2n^2 * Q_{ss}$$

$$Q_{22} = n^4 * Q_{xx} + m^4 * Q_{yy} + 2m^2n^2 * Q_{xy} + 4m^2n^2 * Q_{ss}$$

$$Q_{12} = m^2n^2 * Q_{xx} + m^2n^2 * Q_{yy} + (m^4 + n^4) * Q_{xy} - 4m^2n^2 * Q_{ss}$$

$$Q_{66} = m^2n^2 * Q_{xx} + m^2n^2 * Q_{yy} - 2m^2n^2 * Q_{xy} + (m^2 - n^2)^2 * Q_{ss}$$

In which m = cos(θ) and n = sin(θ) and:

$$Q_{xx} = \frac{E_x}{1 - v_{xy} * v_{yx}}$$

$$Q_{yy} = \frac{E_y}{1 - v_{xy} * v_{yx}}$$

$$Q_{xy} = \frac{v_{xy} * E_y}{1 - v_{xy} * v_{yx}} = \frac{v_{yx} * E_x}{1 - v_{xy} * v_{yx}}$$

$$Q_{ss} = G_{xy}$$

To substitute the stress from each ply in the failure criteria, the stress found in the xy-axis system should be transformed to the direction of the fibres. These depend on the angle θ and the local axis system is described as the 12-axis system. The transformation is given by:

$$\begin{bmatrix}\sigma_1\\ \sigma_2\\ \tau_{12}\end{bmatrix} = \begin{bmatrix} m^2 & n^2 & 2mn \\ n^2 & m^2 & -2mn \\ -mn & mn & m^2-n^2\end{bmatrix}\begin{bmatrix}\sigma_x\\ \sigma_y\\ \tau_{xy}\end{bmatrix} \qquad (B.4)$$

The local stresses in the fibre directions obtained from the above, can now be substituted along with the material strength values in the Tsai-Hill or Tsai-Wu failure criterion. The expression for Tsai-Hill failure theory is given by:

$$\frac{\sigma_1^2}{X^2} - \frac{\sigma_1\sigma_2}{X^2} + \frac{\sigma_2^2}{Y^2} + \frac{\tau_{12}^2}{S^2} = 1 \qquad (B.5)$$

Where the X and Y strength values depend on the sign of their corresponding stresses. For instance, the compressive strength of the ply in 1 direction should be substituted if σ_1 is negative.
The Tsai-Wu failure criterion is given as follows:

$$\frac{\sigma_1^2}{X^tX^c} + \frac{\sigma_2^2}{Y^tY^c} - \sqrt{\frac{1}{X^tX^cY^tY^c}}\sigma_1\sigma_2 + \left(\frac{1}{X^t} - \frac{1}{X^c}\right)\sigma_1 + \left(\frac{1}{Y^t} - \frac{1}{Y^c}\right)\sigma_2 + \frac{\tau_{12}^2}{S^2} = 1 \qquad (B.6)$$

Where the superscripts t and c refer to tension and compression respectively.
Multiplying the stresses with a reserve factor in equations (B.5) and (B.6) and solving for it, results in the failure load for first ply failure.

Appendix C

DATA-POINTS FOR NUMERICAL CONVERGENCE STUDY ON THE SANDWICH PANEL

The numerical convergence graphs shown in subsection 3.1.3 are based on the values given in the tables below. Table C.1 refers to the values related to the numerical model with element type 75. Table C.2 gives the values from the graph found by modelling the sandwich panel with element types 7 and 75. Table C.3 outlines the obtained values obtained from the numerical analysis, using element types 21 and 22. For each of the tables, the first column indicates the exact number of elements of the model. The element size is between brackets and is an approximate size of the element. The second column shows the applied load to the panel, resulting from the point loads give to each node on one side of the loaded edges. From the Marc Mentat buckling analysis, multiple eigenvalues are found, from which the lowest is presented in the third column. Multiplying the applied load with the lowest eigenvalue results in the expected buckling load. The mode predicted by the Marc Mentat model is also given in the most right column.

Table C.1: Buckling analysis element type 75, including transverse shear effects

# of elements (element size)	Applied load [N]	Lowest eigenvalue	Buckling load [N]	Buckling mode
8 (200 mm)	-3	97500	-292500	2 half waves
40 (100 mm)	-6	41140	-246840	2 half waves
170 (50 mm)	-11	21590	-237490	2 half waves
680 (25 mm)	-21	11190	-234990	2 half waves
4300 (10 mm)	-51	4589	-234039	2 half waves
17300 (5 mm)	-101	2313	-233613	2 half waves
47808 (3 mm)	-167	1398	-233466	2 half waves
108250 (2 mm)	-251	929.5	-233304	2 half waves

Table C.2: Buckling analysis, using type 7 and type 75 elements

# of elements (element size)	Applied load [N]	Lowest eigenvalue	Buckling load [N]	Buckling mode
24 (200 mm)	-240000	1.119	-268560	3 half waves
120 (100 mm)	-120000	1.896	-227520	3 half waves
510 (50 mm)	-22000	9.834	-216348	3 half waves
2040 (25 mm)	-42000	5.061	-212562	3 half waves
17200 (10 mm)	-153000	1.379	-210987	3 half waves
103800 (5 mm)	-505000	0.8323	-210155	3 half waves

Table C.3: Buckling analysis, using type 21 and type 22 elements

# of elements (element size)	Applied load [N]	Lowest eigenvalue	Buckling load [N]	Buckling mode
6 (320 mm)	-80000	3.231	-258480	1 half wave
18 (240 mm)	-130000	1.707	-221910	2 half waves
45 (160 mm)	-180000	1.191	-214380	3 half waves
180 (80 mm)	-330000	0.6387	-210771	3 half waves
756 (40 mm)	-630000	0.3287	-207081	3 half waves
3225 (20 mm)	-1280000	0.1575	-201600	3 half waves
7524 (15 mm)	-269000	0.7780	-209282	3 half waves
17200 (10 mm)	-405000	0.5142	-208251	3 half waves

Appendix D

DERIVATION OF GLOBAL BUCKLING OF A GRID STIFFENED PANEL

The subsequent steps to derive the global buckling load of a grid stiffened panel are outlined in this appendix. The method is described by Xu et al. [6] and the full derivation is repeated here. It should be noted that using the method below, the exact same results as are given in the paper are not obtained, but verification with different finite element models during this thesis project resulted in comparable results between the analytical and numerical solution.

The first step is to set up a unit cell of the grid stiffened panel, by introducing a vector S describing the appearance of each stiffener, from which the complete panel geometry can be found. The vector S describes the appearance of the 6 different stiffeners as shown in figure D.1. If there are no diagonal stiffeners, the first and second entry of the vector S are zero. It should also be noted that the boundary stiffeners 5 and 6 are normally counted as half the thickness of the cross stiffeners 3 and 4. When one unit cell is then placed next to the other unit cell, the stiffeners 5 and 6 are not counted twice for the whole panel. For this reason, one stiffener is chosen as a reference value of 1 in the unit cell vector S and the others are described as percentages of this reference stiffener by taking the complete panel into account. For the diagonal stiffeners, an angle theta could also be applied, where an angle of 60 degrees and removing the transverse stiffeners results in equilateral triangular skin pockets. This particular structure is also called an isogrid, which is not further analysed during this project.

$$S = \begin{bmatrix} s_1 \\ s_2 \\ s_3 \\ s_4 \\ s_5 \\ s_6 \end{bmatrix} \tag{D.1}$$

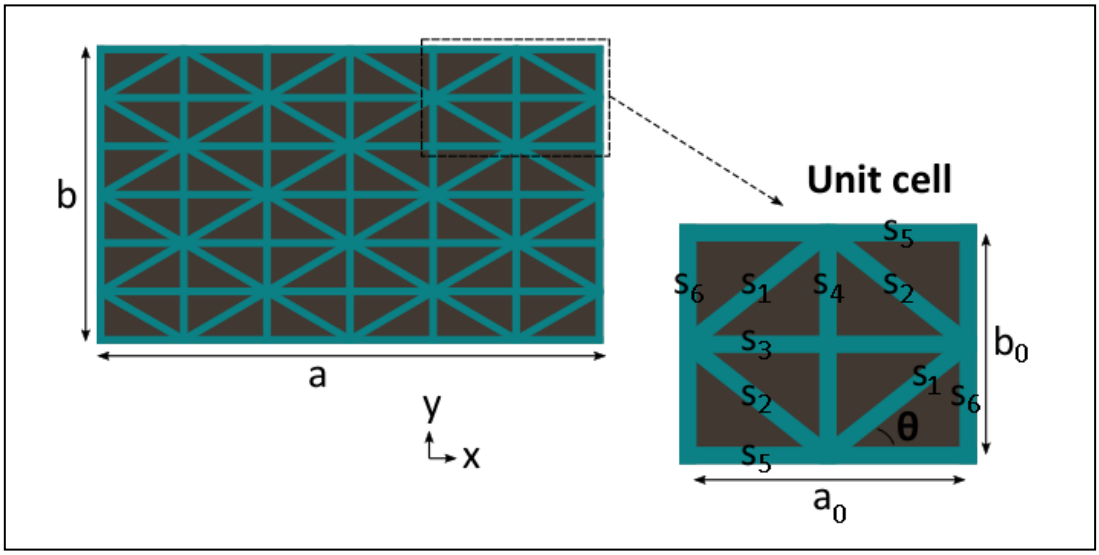

Figure D.1: Unit cell of a grid stiffened structure

To determine the global buckling load, the equivalent stiffness of the panel is described by a superposition of the separate stiffener and skin stiffness contribution, given by equation D.2.

$$\begin{bmatrix} N \\ M \end{bmatrix} = \begin{bmatrix} A_{sk} + A_{st} & B_{sk} + B_{st} \\ B_{sk} + B_{st} & D_{sk} + D_{st} \end{bmatrix} \begin{bmatrix} \varepsilon_0 \\ \kappa \end{bmatrix} \tag{D.2}$$

To determine the stiffener contribution, the portion of the skin at which the stiffener is connected is taken into account. The situation is shown in figure D.2, where the stiffener and the skin section marked with a dark colour will be analysed. If a pure bending moment is assumed, the integral of the normal stress over the area is equal to zero:

$$\iint \sigma_l dA = \int_{-h_0}^{-h_o+t_{sk}} t_{st} E_{sk} \kappa_l z dz + \int_{-h_o+t_{sk}}^{-h_o+t_{sk}+h_{st}} t_{st} E_{st} \kappa_l z dz = 0 \tag{D.3}$$

Evaluating the integrals results in:

$$h_0 = \frac{E_{sk} t_{sk}^2 + E_{st}(h_{st}^2 + 2 t_{sk} h_{st})}{2(E_{sk} t_{sk} + E_{st} h_{st})} \tag{D.4}$$

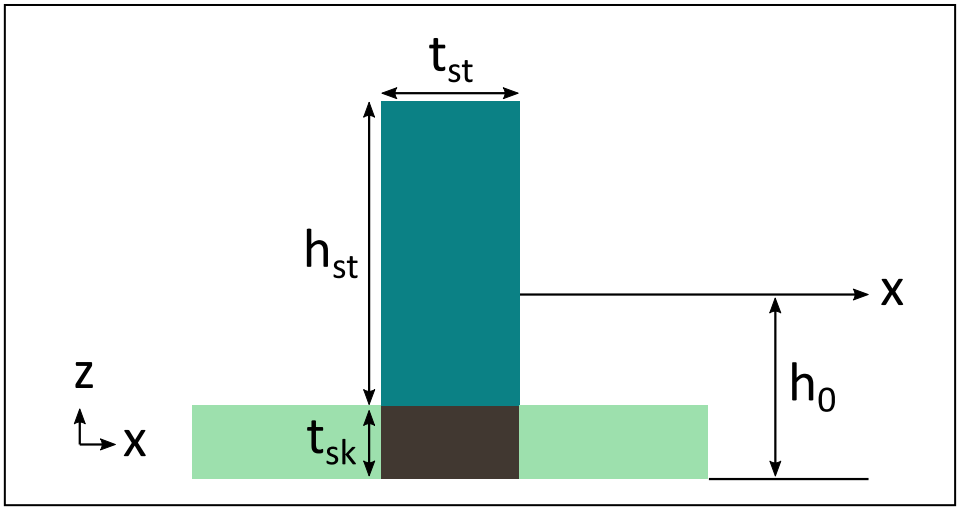

Figure D.2: Cross-section of a random stiffener and its adjacent skin

The stiffener modulus is obtained from classical laminate theory:

$$E_{st} = \frac{1}{t_{st}} \left(A_{11,st} - \frac{A_{12,st}^2}{A_{22,st}} \right) \tag{D.5}$$

Since the stiffness of the skin could change in direction, the neutral surface gives a different value in different directions. An average neutral surface is therefore introduced, given as follows:

$$h_{0av} = \sum v_i h_0(\theta_i) \tag{D.6}$$

Where:

$$v_i = \frac{volume\ of\ particular\ stiffener\ within\ the\ unit\ cell}{total\ volume\ of\ stiffeners\ in\ the\ unit\ cell} \tag{D.7}$$

The skin modulus present in equation (D.4) is dependent on θ as mentioned before and is derived from:

$$\begin{bmatrix}\sigma_l\\ \sigma_n\\ \sigma_{ln}\end{bmatrix}=\begin{bmatrix}c^2 & s^2 & 2sc\\ s^2 & c^2 & -2sc\\ -sc & sc & c^2-s^2\end{bmatrix}\begin{bmatrix}Q_{11} & Q_{12} & 0\\ Q_{12} & Q_{22} & 0\\ 0 & 0 & Q_{66}\end{bmatrix}\begin{bmatrix}c^2 & s^2 & -sc\\ s^2 & c^2 & sc\\ 2sc & -2sc & c^2-s^2\end{bmatrix}*\begin{bmatrix}\varepsilon_l\\ \varepsilon_n\\ \gamma_{ln}\end{bmatrix} \quad (D.8)$$

From the fact that the shear and transverse strain are assumed to be zero in case of uniaxial tension, the above equation results in:

$$E_{sk}=\frac{\sigma_l}{\varepsilon_l}=[c^2 \quad s^2 \quad 2sc]\begin{bmatrix}Q_{11} & Q_{12} & 0\\ Q_{12} & Q_{22} & 0\\ 0 & 0 & Q_{66}\end{bmatrix}\begin{bmatrix}c^2\\ s^2\\ 2sc\end{bmatrix} \quad (D.9)$$

Resulting in:

$$E_{sk}=\ Q_{11}\cos^4\theta+2Q_{12}\cos^2\theta\sin^2\theta+Q_{22}\sin^4\theta+4Q_{66}\cos^2\theta\sin^2\theta \quad (D.10)$$

By using the following relation:

$$\sin^2\theta=1-\cos^2 \quad (D.11)$$

Equation (D.10) can be written as:

$$E_{sk}=\ (Q_{11}-2Q_{12}+Q_{22}-4Q_{66})\cos^4\theta+2(Q_{12}-Q_{22}+2Q_{66})\cos^2\theta+Q_{22} \quad (D.12)$$

In which:

$$Q_{11}=\frac{A_{11,sk}}{t_{sk}} \qquad Q_{12}=\frac{A_{12,sk}}{t_{sk}} \qquad Q_{22}=\frac{A_{22,sk}}{t_{sk}} \qquad Q_{66}=\frac{A_{66,sk}}{t_{sk}} \quad (D.13)$$

The stiffener contribution to the equivalent stiffness matrix can now be found by setting up the force and moment equations given by equation (D.2). This is done by evaluating the following conditions:

1. Reaction moment under pure bending
2. Reaction moment under pure tension or compression
3. Reaction force to the stiffener

The reaction moment M_b from the stiffeners is found by integrating the stress over the cross-sectional area of the stiffener:

$$M_b=\iint\sigma_{st}z\,dA=\iint E_{st}\kappa_l z^2\,dx\,dz=\int_{t_{sk}-h_0}^{h_{st}+t_{sk}-h_0}E_{st}t_{st}\kappa_l z^2\,dz \quad (D.14)$$

Evaluation of the integral results in:

$$M_b=\frac{1}{3}E_{st}t_{st}\kappa_l z^3\Big|_{t_{sk}-h_0}^{h_{st}+t_{sk}-h_0}=\frac{1}{3}E_{st}t_{st}\kappa_l[(h_{st}+t_{sk}-h_0)^3-(t_{sk}-h_0)^3] \quad (D.15)$$

Rewriting the equation to:

$$M_b=\frac{1}{3}E_{st}t_{st}\kappa_l\left[h_{st}^3+3h_{st}^2t_{sk}+3h_{st}t_{sk}^2-3h_{st}^2h_0+3h_{st}h_0^2-6h_{st}t_{sk}h_0\right] \quad (D.16)$$

The above can be rewritten by adding zero in the form of:

$$\frac{1}{4}E_{st}t_{st}\kappa_l h_{st}^3 - \frac{1}{4}E_{st}t_{st}\kappa_l h_{st}^3 \tag{D.17}$$

Resulting in:

$$\begin{aligned} M_b = {} & \frac{1}{12}E_{st}t_{st}\kappa_l h_{st}^3 \\ & + \frac{1}{3}E_{st}t_{st}\kappa_l \left[3h_{st}^2 t_{sk} + 3h_{st}t_{sk}^2 - 3h_{st}^2 h_0 + 3h_{st}h_0^2 \right. \\ & \left. - 6h_{st}t_{sk}h_0 - \frac{3}{4}h_{st}^3\right] \end{aligned} \tag{D.18}$$

Substituting the following relations:

$$I_{z,st} = \frac{t_{st}h_{st}^3}{12} \qquad and \qquad A_{st} = h_{st}t_{st} \tag{D.19}$$

Results in:

$$M_b = E_{st}I_{z,st}\kappa_l + E_{st}A_{st}\kappa_l \left[h_{st}t_{sk} + t_{sk}^2 - h_{st}h_0 + h_0^2 - 2t_{sk}h_0 - \frac{1}{4}h_{st}^2\right] \tag{D.20}$$

Which can be simplified to:

$$M_b = E_{st}I_{z,st}\kappa_l + E_{st}A_{st}\left[\frac{h_{st}}{2} + t_{sk} - h_0\right]^2 \kappa_l \tag{D.21}$$

The curvature of the neutral surface in l direction is dependent on θ and can be found by:

$$\kappa_l = \kappa_x \cos^2\theta + \kappa_{xy}\sin\theta\cos\theta + \kappa_y \sin^2\theta \tag{D.22}$$

The reaction moment under pure tension or compression should be analysed now. As a result from the shift of the neutral axis from the skin/stiffener interaction, the resulting bending moment caused by pure tension or compression is given by:

$$M_p = \iint \sigma_{st} z dA = \int_{t_{sk}-h_0}^{h_{st}+t_{sk}-h_0} E_{st}t_{st}\varepsilon_l^0 z dz \tag{D.23}$$

Evaluating the integral results in:

$$M_p = \frac{1}{2}E_{st}t_{st}\varepsilon_l^0 z^2\Big|_{t_{sk}-h_0}^{h_{st}+t_{sk}-h_0} = \frac{1}{2}E_{st}t_{st}\varepsilon_l^0[(h_{st}+t_{sk}-h_0)^2 - (t_{sk}-h_0)^2] \tag{D.24}$$

$$M_p = \frac{1}{2}E_{st}t_{st}(h_{st}^2 + 2h_{st}t_{sk} - 2h_{st}h_0)\varepsilon_l^0 \tag{D.25}$$

The strain in θ direction can be obtained by following the same transformation as for the curvature and is given by:

$$\varepsilon_l^0 = \varepsilon_x^0 \cos^2\theta + \gamma_{xy}^0 \sin\theta\cos\theta + \varepsilon_y^0 \sin^2\theta \tag{D.26}$$

Finally, the reaction force of the stiffener should be determined. Applying the following rule to the force resultant of the stiffener:

$$\varepsilon_l = \varepsilon_l^0 + z\kappa_l \tag{D.27}$$

The integral over the cross-sectional area of the stiffener for the reaction force is given by:

$$\begin{aligned} F &= \iint \sigma_{st} dA = \int_{t_{sk}-h_0}^{h_{st}+t_{sk}-h_0} E_{st} t_{st} \varepsilon_l dz \\ &= \int_{t_{sk}-h_0}^{h_{st}+t_{sk}-h_0} E_{st} t_{st} \varepsilon_l^0 dz + \int_{t_{sk}-h_0}^{h_{st}+t_{sk}-h_0} E_{st} t_{st} z \kappa_l dz \end{aligned} \tag{D.28}$$

$$F = E_{st} t_{st} \varepsilon_l^0 z\Big|_{t_{sk}-h_0}^{h_{st}+t_{sk}-h_0} + \frac{1}{2} E_{st} t_{st} z^2 \kappa_l \Big|_{t_{sk}-h_0}^{h_{st}+t_{sk}-h_0} \tag{D.29}$$

$$F = E_{st} t_{st} h_{st} \varepsilon_l^0 + \frac{1}{2} E_{st} t_{st} [(h_{st} + t_{sk} - h_0)^2 - (t_{sk} - h_0)^2] \kappa_l \tag{D.30}$$

Giving the final relation by working out the squared terms:

$$F = E_{st} t_{st} h_{st} \varepsilon_l^0 + \frac{1}{2} E_{st} t_{st} (h_{st}^2 + 2 h_{st} t_{sk} - 2 h_{st} h_0) \kappa_l \tag{D.31}$$

The force and moment resultants are now known. The total reaction moment is given by the combination of the two evaluated reaction moments described by equations (D.21) and (D.25) as:

$$M = M_p + M_b \tag{D.32}$$

Using equations (D.21), (D.25), (D.31) and (D.32), the forces and moments in each stiffener of the unit cell can be described as follows:

$$F_1 = s_1 F(\theta) = s_1 E_{st} A_1 \varepsilon_l^0(\theta) + s_1 E_{st} A_2 \kappa_l(\theta) \tag{D.33}$$

$$F_2 = s_2 F(-\theta) = s_2 E_{st} A_1 \varepsilon_l^0(-\theta) + s_2 E_{st} A_2 \kappa_l(-\theta) \tag{D.34}$$

$$F_3 = s_3 F(0) = s_3 E_{st} A_1 \varepsilon_l^0(0) + s_3 E_{st} A_2 \kappa_l(0) \tag{D.35}$$

$$F_4 = s_4 F\left(\frac{\pi}{2}\right) = s_4 E_{st} A_1 \varepsilon_l^0\left(\frac{\pi}{2}\right) + s_4 E_{st} A_2 \kappa_l\left(\frac{\pi}{2}\right) \tag{D.36}$$

$$F_5 = s_5 F(0) = s_5 E_{st} A_1 \varepsilon_l^0(0) + s_5 E_{st} A_2 \kappa_l(0) \tag{D.37}$$

$$F_6 = s_4 F\left(\frac{\pi}{2}\right) = s_6 E_{st} A_1 \varepsilon_l^0\left(\frac{\pi}{2}\right) + s_6 E_{st} A_2 \kappa_l\left(\frac{\pi}{2}\right) \tag{D.38}$$

$$M_1 = s_1 M(\theta) = s_1 E_{st} A_2 \varepsilon_l^0(\theta) + s_1 E_{st} A_3 \kappa_l(\theta) \tag{D.39}$$

$$M_2 = s_2 M(-\theta) = s_2 E_{st} A_2 \varepsilon_l^0(-\theta) + s_2 E_{st} A_3 \kappa_l(-\theta) \quad (D.40)$$

$$M_3 = s_3 M(0) = s_3 E_{st} A_2 \varepsilon_l^0(0) + s_3 E_{st} A_3 \kappa_l(0) \quad (D.41)$$

$$M_4 = s_4 M\left(\frac{\pi}{2}\right) = s_4 E_{st} A_2 \varepsilon_l^0\left(\frac{\pi}{2}\right) + s_4 E_{st} A_3 \kappa_l\left(\frac{\pi}{2}\right) \quad (D.42)$$

$$M_5 = s_5 M(0) = s_5 E_{st} A_2 \varepsilon_l^0(0) + s_5 E_{st} A_3 \kappa_l(0) \quad (D.43)$$

$$M_6 = s_4 M\left(\frac{\pi}{2}\right) = s_6 E_{st} A_2 \varepsilon_l^0\left(\frac{\pi}{2}\right) + s_6 E_{st} A_3 \kappa_l\left(\frac{\pi}{2}\right) \quad (D.44)$$

Where:

$$s_1, s_2, s_3, s_4, s_5 \text{ and } s_6 : parameters\ of\ unit\ cell\ vector\ S \quad (D.45)$$

$$A_1 = t_{st} * h_{st} \quad (D.46)$$

$$A_2 = \frac{t_{st}(h_{st}^2 + 2h_{st}t_{sk} - 2h_{st}h_0)}{2} \quad (D.47)$$

$$A_3 = I_{z,st} + A_{st}\left(\frac{h_{st}}{2} + t_{sk} - h_0\right)^2 \quad (D.48)$$

Equations (D.33) up to and including (D.44) are now used to connect forces, moment and strains via the well known ABD matrix:

$$\begin{bmatrix} N_{x,st} \\ N_{y,st} \\ N_{xy,st} \\ M_{x,st} \\ M_{y,st} \\ M_{xy,st} \end{bmatrix} = \begin{bmatrix} A_{11} & A_{12} & A_{16} & B_{11} & B_{12} & B_{16} \\ A_{21} & A_{22} & A_{26} & B_{21} & B_{22} & B_{26} \\ A_{61} & A_{62} & A_{66} & B_{61} & B_{62} & B_{66} \\ B_{11} & B_{12} & B_{16} & D_{11} & D_{12} & D_{16} \\ B_{21} & B_{22} & B_{26} & D_{21} & D_{22} & D_{26} \\ B_{61} & B_{62} & B_{66} & D_{61} & D_{62} & D_{66} \end{bmatrix} * \begin{bmatrix} \varepsilon_x^0 \\ \varepsilon_y^0 \\ \gamma_{xy}^0 \\ \kappa_x \\ \kappa_y \\ \kappa_{xy} \end{bmatrix} \quad (D.49)$$

Where each A, B and D term is described by:

$$A_{11} = \frac{E_{st} A_1 (s_1 c^3 + s_2 c^3 + s_3 + 2s_5)}{b_0} \quad (D.50)$$

$$A_{12} = A_{21} = \frac{E_{st} A_1 (s_1 c s^2 + s_2 c s^2)}{b_0} = \frac{E_{st} A_1 (s_1 c^2 s + s_2 c^2 s)}{a_0} \quad (D.51)$$

$$A_{16} = A_{26} = 0 \quad (D.52)$$

$$A_{22} = \frac{E_{st} A_1 (s_1 s^3 + s_2 s^3 + s_4 + 2s_6)}{a_0} \quad (D.53)$$

$$A_{66} = \frac{E_{st}A_1(s_1cs^2 + s_2cs^2)}{b_0} \tag{D.54}$$

$$B_{11} = \frac{E_{st}A_2(s_1c^3 + s_2c^3 + s_3 + 2s_5)}{b_0} \tag{D.55}$$

$$B_{12} = B_{21} = \frac{E_{st}A_2(s_1cs^2 + s_2cs^2)}{b_0} = \frac{E_{st}A_2(s_1c^2s + s_2c^2s)}{a_0} \tag{D.56}$$

$$B_{16} = B_{26} = 0 \tag{D.57}$$

$$B_{22} = \frac{E_{st}A_2(s_1s^3 + s_2s^3 + s_4 + 2s_6)}{a_0} \tag{D.58}$$

$$B_{66} = \frac{E_{st}A_2(s_1cs^2 + s_2cs^2)}{b_0} \tag{D.59}$$

$$D_{11} = \frac{E_{st}A_3(s_1c^3 + s_2c^3 + s_3 + 2s_5)}{b_0} \tag{D.60}$$

$$D_{12} = D_{21} = \frac{E_{st}A_3(s_1cs^2 + s_2cs^2)}{b_0} = \frac{E_{st}A_3(s_1c^2s + s_2c^2s)}{a_0} \tag{D.61}$$

$$D_{16} = D_{26} = 0 \tag{D.62}$$

$$D_{22} = \frac{E_{st}A_3(s_1s^3 + s_2s^3 + s_4 + 2s_6)}{a_0} \tag{D.63}$$

$$D_{66} = \frac{E_{st}A_3(s_1cs^2 + s_2cs^2)}{b_0} \tag{D.64}$$

The contribution from the stiffener to the equivalent stiffness matrix is now known. The contribution of the skin to the equivalent stiffness will be determined by finding its neutral surface first. This is done by smearing the stiffeners to obtain a plate of uniform thickness with its neutral surface at the midplane of the stiffener. Figure D.3 shows the situation of the skin and the smeared stiffener. Note that the neutral surface is now taken as a distance from half the skin thickness instead of the bottom of the skin. Again, assuming a pure bending deformation, the following integral can be evaluated to find the neutral surface:

$$\iint \sigma_y dA = \int_{-h_{z0}+d-\frac{t_{smst}}{2}}^{-h_{z0}+d+\frac{t_{smst}}{2}} E_{smst}a_0\kappa_y z dz + \int_{-h_{z0}-\frac{t_{sk}}{2}}^{-h_{z0}+\frac{t_{sk}}{2}} E_{sk}a_0\kappa_y z dz = 0 \tag{D.65}$$

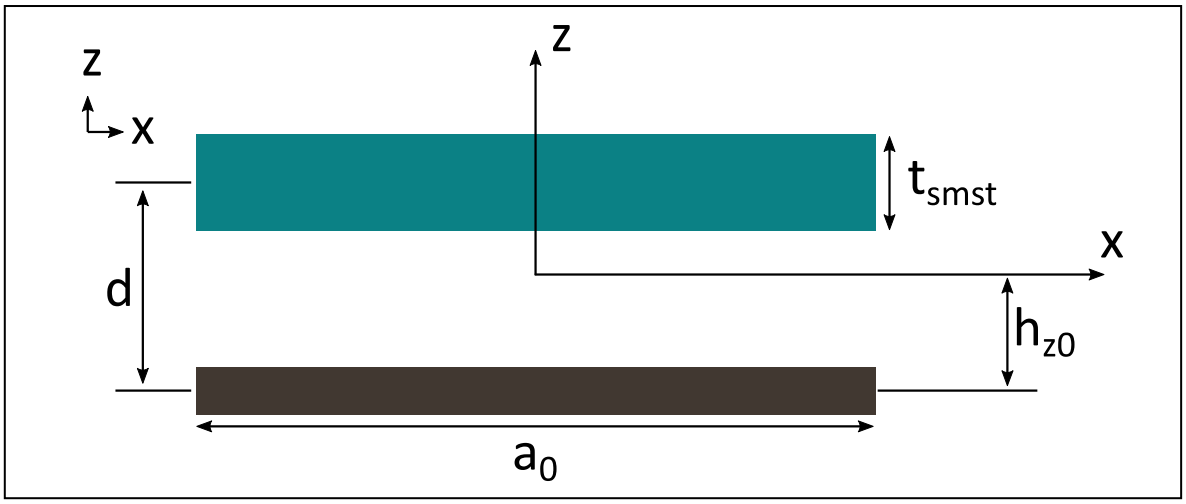

Figure D.3: Cross-section of smeared stiffener and unit cell skin

Evaluation of the integral results in:

$$\frac{1}{2}E_{smst}a_0\kappa_y\left[\left(-h_{z0}+d+\frac{t_{smst}}{2}\right)^2-\left(-h_{z0}+d-\frac{t_{smst}}{2}\right)^2\right] + \frac{1}{2}E_{sk}a_0\kappa_y\left[\left(-h_{z0}+\frac{t_{sk}}{2}\right)^2-\left(-h_{z0}-\frac{t_{sk}}{2}\right)^2\right]=0 \tag{D.66}$$

The above can be simplified to:

$$E_{smst}a_0\kappa_y(dt_{smst}-h_{z0}t_{smst})-E_{sk}a_0\kappa_y(h_{z0}t_{sk})=0 \tag{D.67}$$

$$E_{smst}A_{smst}\kappa_y(d-h_{z0})-E_{sk}A_{sk}\kappa_y h_{z0}=0 \tag{D.68}$$

Solving for the neutral surface location results in:

$$h_{z0}=\frac{d}{1+\frac{E_{sk}A_{sk}}{E_{smst}A_{smst}}} \tag{D.69}$$

Where d is the distance between the midplanes of the skin and smeared stiffeners:

$$d=\frac{t_{sk}}{2}+\frac{h_{st}}{2} \tag{D.70}$$

The area of the skin and smeared stiffener is shown in the view of figure D.3. The smeared stiffener modulus is found by using equation (D.12) and using the A values from the ABD matrix obtained earlier in equation (D.49). The skin modulus is thereby also found by using equation (D.12).
Since the position of the neutral surface will also change here with respect to angle θ, the average neutral surface position is calculated by:

$$h_{z0av}=\sum c_i h_{z0}(\theta_i) \tag{D.71}$$

Where i is connected to each stiffener from the unit cell vector S given in equation (D.1) and c_i is given by:

$$c_i=\frac{E_{sk}(\theta_i)A_{sk}(\theta_i)+E_{smst}(\theta_i)A_{smst}(\theta_i)}{\sum(E_{sk}(\theta_i)A_{sk}(\theta_i)+E_{smst}(\theta_i)A_{smst}(\theta_i))} \tag{D.72}$$

It should be noted that the area of the skin and stiffener is also dependent on the angle, because length a_0 and width b_0 could be different.
In the analysis of equation (D.72), only the angles of the stiffener orientations are evaluated. This means that for an orthogrid type of structure, only the 0 and 90 degree are evaluated to find the averaged neutral axis of the skin and the smeared stiffeners.
Using the neutral surface position, the ABD matrix of the skin can be found by classical laminate theory, where the relation between forces, moments, strains and curvatures are given by:

$$\begin{bmatrix} N_x \\ N_y \\ N_{xy} \end{bmatrix} = \sum_{k=1}^{n} \int_{z_{k-1}}^{z_k} \begin{bmatrix} \sigma_x \\ \sigma_y \\ \tau_s \end{bmatrix}_k dz \tag{D.73}$$

$$\begin{bmatrix} M_x \\ M_y \\ M_{xy} \end{bmatrix} = \sum_{k=1}^{n} \int_{z_{k-1}}^{z_k} \begin{bmatrix} \sigma_x \\ \sigma_y \\ \tau_s \end{bmatrix}_k z dz \tag{D.74}$$

Substituting the stress-strain relation results in:

$$\begin{bmatrix} N_x \\ N_y \\ N_{xy} \end{bmatrix} = \sum_{k=1}^{n} \left\{ \begin{bmatrix} Q_{xx} & Q_{xy} & Q_{xs} \\ Q_{yx} & Q_{yy} & Q_{ys} \\ Q_{sx} & Q_{sy} & Q_{ss} \end{bmatrix}_k \begin{bmatrix} \varepsilon_x^0 \\ \varepsilon_y^0 \\ \gamma_s^0 \end{bmatrix} \int_{z_{k-1}}^{z_k} dz + \begin{bmatrix} Q_{xx} & Q_{xy} & Q_{xs} \\ Q_{yx} & Q_{yy} & Q_{ys} \\ Q_{sx} & Q_{sy} & Q_{ss} \end{bmatrix}_k \begin{bmatrix} \kappa_x \\ \kappa_y \\ \kappa_s \end{bmatrix} \int_{z_{k-1}}^{z_k} z dz \right\} \tag{D.75}$$

$$\begin{bmatrix} M_x \\ M_y \\ M_{xy} \end{bmatrix} = \sum_{k=1}^{n} \left\{ \begin{bmatrix} Q_{xx} & Q_{xy} & Q_{xs} \\ Q_{yx} & Q_{yy} & Q_{ys} \\ Q_{sx} & Q_{sy} & Q_{ss} \end{bmatrix}_k \begin{bmatrix} \varepsilon_x^0 \\ \varepsilon_y^0 \\ \gamma_s^0 \end{bmatrix} \int_{z_{k-1}}^{z_k} z dz + \begin{bmatrix} Q_{xx} & Q_{xy} & Q_{xs} \\ Q_{yx} & Q_{yy} & Q_{ys} \\ Q_{sx} & Q_{sy} & Q_{ss} \end{bmatrix}_k \begin{bmatrix} \kappa_x \\ \kappa_y \\ \kappa_s \end{bmatrix} \int_{z_{k-1}}^{z_k} z^2 dz \right\} \tag{D.76}$$

In which the values of z depends on the location with respect to the weighted average neutral surface found before in (D.72).
When the equivalent stiffness matrix is known, an energy method will be used to obtain the buckling load of the structure. The total potential energy is the sum of the bending strain energy and the work done:

$$\Pi = U + W \tag{D.77}$$

Where the bending strain energy is given by:

$$U = \frac{1}{2} \iint \left\{ D_{11} \left(\frac{\partial^2 w}{\partial x^2} \right)^2 + 2D_{12} \frac{\partial^2 w}{\partial x^2} \frac{\partial^2 w}{\partial y^2} + 4D_{16} \frac{\partial^2 w}{\partial x^2} \frac{\partial^2 w}{\partial x \partial y} + D_{22} \left(\frac{\partial^2 w}{\partial y^2} \right)^2 + 4D_{26} \frac{\partial^2 w}{\partial y^2} \frac{\partial^2 w}{\partial x \partial y} + 4D_{66} \left(\frac{\partial^2 w}{\partial x \partial y} \right)^2 \right\} dxdy \tag{D.78}$$

And the work done is given by:

$$W = -\frac{1}{2} \iint \left\{ N_x \left(\frac{\partial w}{\partial x} \right)^2 + N_y \left(\frac{\partial w}{\partial y} \right)^2 + 2N_{xy} \left(\frac{\partial w}{\partial x} \right) \left(\frac{\partial w}{\partial y} \right) \right\} dxdy \tag{D.79}$$

Minimizing the potential energy by setting its derivative equal to zero and using a Ritz approximation, results in the solution of the buckling load. In order to satisfy simply supported boundary conditions, the following out-of-plane displacement function is chosen:

$$w(x,y) = \sum_{m=1}^{M}\sum_{n=1}^{N} C_{mn} \sin\left(\frac{m\pi x}{a}\right)\sin\left(\frac{n\pi y}{b}\right) \tag{D.80}$$

The derivatives of w found in the equations of the bending strain energy and the work done are given as follows:

$$\frac{\partial w}{\partial x} = \sum_{m=1}^{M}\sum_{n=1}^{N} C_{mn}\left(\frac{m\pi}{a}\right)\cos\left(\frac{m\pi x}{a}\right)\sin\left(\frac{n\pi y}{b}\right) \tag{D.81}$$

$$\frac{\partial w}{\partial y} = \sum_{m=1}^{M}\sum_{n=1}^{N} C_{mn}\left(\frac{n\pi}{b}\right)\sin\left(\frac{m\pi x}{a}\right)\cos\left(\frac{n\pi y}{b}\right) \tag{D.82}$$

$$\frac{\partial^2 w}{\partial x^2} = -\sum_{m=1}^{M}\sum_{n=1}^{N} C_{mn}\left(\frac{m\pi}{a}\right)^2\sin\left(\frac{m\pi x}{a}\right)\sin\left(\frac{n\pi y}{b}\right) \tag{D.83}$$

$$\frac{\partial^2 w}{\partial y^2} = -\sum_{m=1}^{M}\sum_{n=1}^{N} C_{mn}\left(\frac{n\pi}{b}\right)^2\sin\left(\frac{m\pi x}{a}\right)\sin\left(\frac{n\pi y}{b}\right) \tag{D.84}$$

$$\frac{\partial^2 w}{\partial x \partial y} = \sum_{m=1}^{M}\sum_{n=1}^{N} C_{mn}\left(\frac{m\pi}{a}\right)\left(\frac{n\pi}{b}\right)\cos\left(\frac{m\pi x}{a}\right)\cos\left(\frac{n\pi y}{b}\right) \tag{D.85}$$

Before differentiating the total potential energy with respect to the coefficients C_{mn}, the six integrals in the bending strain energy and the three integrals in the work done can be evaluated.
The first integral of the bending strain energy is given by:

$$\begin{aligned}&\frac{1}{2}\iint\left\{D_{11}\left(\frac{\partial^2 w}{\partial x^2}\right)^2\right\}dxdy\\ &= \frac{1}{2}\iint\left\{D_{11}\left(\sum_{m=1}^{M}\sum_{n=1}^{N} C_{mn}^2\left(\frac{m\pi}{a}\right)^4\sin\left(\frac{m\pi x}{a}\right)\sin\left(\frac{n\pi y}{b}\right)\sin\left(\frac{i\pi x}{a}\right)\sin\left(\frac{j\pi y}{b}\right)\right)\right\}dxdy\end{aligned} \tag{D.86}$$

Using the following integration rule:

$$\int_0^a \sin\left(\frac{m\pi x}{a}\right)\sin\left(\frac{i\pi x}{a}\right)dx = \frac{a}{2} \tag{D.87}$$

Evaluation results in:

$$\frac{1}{2}D_{11}\sum_{m=1}^{M}\sum_{n=1}^{N} C_{mn}^2\left(\frac{m\pi}{a}\right)^4\left(\frac{a}{2}\right)\left(\frac{b}{2}\right) \tag{D.88}$$

The second integral of the bending strain energy is given by:

$$\begin{aligned}&\frac{1}{2}\iint\left\{2D_{12}\frac{\partial^2 w}{\partial x^2}\frac{\partial^2 w}{\partial y^2}\right\}dxdy\\ &= \iint\left\{D_{12}\sum_{m=1}^{M}\sum_{n=1}^{N} C_{mn}^2\left(\frac{m\pi}{a}\right)^2\left(\frac{n\pi}{b}\right)^2\sin\left(\frac{m\pi x}{a}\right)\sin\left(\frac{n\pi y}{b}\right)\sin\left(\frac{i\pi x}{a}\right)\sin\left(\frac{j\pi y}{b}\right)\right\}dxdy\end{aligned} \tag{D.89}$$

And evaluation results in:

$$D_{12}\sum_{m=1}^{M}\sum_{n=1}^{N}C_{mn}^{2}\left(\frac{m\pi}{a}\right)^{2}\left(\frac{n\pi}{b}\right)^{2}\left(\frac{a}{2}\right)\left(\frac{b}{2}\right) \tag{D.90}$$

The third integral of the bending strain energy is given by:

$$\frac{1}{2}\iint\left\{4D_{16}\frac{\partial^{2}w}{\partial x^{2}}\frac{\partial^{2}w}{\partial x\partial y}\right\}dxdy$$
$$=\iint\left\{-2D_{16}\sum_{m=1}^{M}\sum_{n=1}^{N}C_{mn}^{2}\left(\frac{m\pi}{a}\right)^{3}\left(\frac{n\pi}{b}\right)\sin\left(\frac{i\pi x}{a}\right)\sin\left(\frac{j\pi y}{b}\right)\cos\left(\frac{m\pi x}{a}\right)\cos\left(\frac{n\pi y}{b}\right)\right\}dxdy \tag{D.91}$$

Using the trigonometric identities:

$$\sin(\alpha)\cos(\beta)=\frac{1}{2}(\sin(\alpha-\beta)+\sin(\alpha+\beta)) \tag{D.92}$$

$$\cos(\alpha+\beta)=\cos(\alpha)\cos(\beta)-\sin(\alpha)\sin(\beta) \tag{D.93}$$

$$\cos(\alpha-\beta)=\cos(\alpha)\cos(\beta)+\sin(\alpha)\sin(\beta) \tag{D.94}$$

The integration is simplified and results in:

$$-2D_{16}\sum_{m=1}^{M}\sum_{n=1}^{N}C_{ij}^{2}\left(\frac{m\pi}{a}\right)^{3}\left(\frac{n\pi}{b}\right)\left[\frac{4ab}{\pi^{2}}\left(\frac{ij}{(m^{2}-i^{2})(n^{2}-j^{2})}\right)\right] \tag{D.95}$$

Only if:

$$m\pm i=odd\quad AND\quad n\pm j=odd$$

Else the result is zero.
The fourth integral of the bending strain energy is given by:

$$\frac{1}{2}\iint\left\{D_{22}\left(\frac{\partial^{2}w}{\partial y^{2}}\right)^{2}\right\}dxdy$$
$$=\frac{1}{2}\iint\left\{D_{22}\sum_{m=1}^{M}\sum_{n=1}^{N}C_{mn}^{2}\left(\frac{n\pi}{b}\right)^{4}\sin\left(\frac{m\pi x}{a}\right)\sin\left(\frac{n\pi y}{b}\right)\sin\left(\frac{i\pi x}{a}\right)\sin\left(\frac{j\pi y}{b}\right)\right\}dxdy \tag{D.96}$$

Evaluating the integral results in:

$$D_{22}\sum_{m=1}^{M}\sum_{n=1}^{N}C_{mn}^{2}\left(\frac{n\pi}{b}\right)^{4}\left(\frac{a}{2}\right)\left(\frac{b}{2}\right) \tag{D.97}$$

The fifth integral of the bending strain energy is given by:

$$\frac{1}{2}\iint\left\{4D_{26}\frac{\partial^{2}w}{\partial y^{2}}\frac{\partial^{2}w}{\partial x\partial y}\right\}dxdy=$$
$$=\iint\left\{-2D_{26}\sum_{m=1}^{M}\sum_{n=1}^{N}C_{mn}^{2}\left(\frac{m\pi}{a}\right)\left(\frac{n\pi}{b}\right)^{3}\sin\left(\frac{i\pi x}{a}\right)\sin\left(\frac{j\pi y}{b}\right)\cos\left(\frac{m\pi x}{a}\right)\cos\left(\frac{n\pi y}{b}\right)\right\}dxdy \tag{D.98}$$

Performing the same evaluation steps as for D_{16}, results in:

$$-2D_{26}\sum_{m=1}^{M}\sum_{n=1}^{N}C_{ij}^{2}\left(\frac{m\pi}{a}\right)\left(\frac{n\pi}{b}\right)^{3}\left[\frac{4ab}{\pi^{2}}\left(\frac{ij}{(m^{2}-i^{2})(n^{2}-j^{2})}\right)\right] \quad (D.99)$$

Only if:

$$m \pm i = odd \quad AND \quad n \pm j = odd$$

Else the result is zero.

The sixth integral of the bending strain energy is given by:

$$\frac{1}{2}\iint\left\{4D_{66}\left(\frac{\partial^{2}w}{\partial x\partial y}\right)^{2}\right\}dxdy$$
$$=\iint\left\{2D_{66}\sum_{m=1}^{M}\sum_{n=1}^{N}C_{mn}^{2}\left(\frac{m\pi}{a}\right)^{2}\left(\frac{n\pi}{b}\right)^{2}\cos\left(\frac{m\pi x}{a}\right)\cos\left(\frac{n\pi y}{b}\right)\cos\left(\frac{i\pi x}{a}\right)\cos\left(\frac{j\pi y}{b}\right)\right\}dxdy \quad (D.100)$$

Evaluation of this integral results in:

$$2D_{66}\sum_{m=1}^{M}\sum_{n=1}^{N}C_{mn}^{2}\left(\frac{m\pi}{a}\right)^{2}\left(\frac{n\pi}{b}\right)^{2}\left(\frac{a}{2}\right)\left(\frac{b}{2}\right) \quad (D.101)$$

Now, the integrals of the work done can be performed. The first integral is given by:

$$-\frac{1}{2}\iint\left\{N_{x}\left(\frac{\partial w}{\partial x}\right)^{2}\right\}dxdy$$
$$=-\frac{1}{2}\iint\left\{N_{x}\sum_{m=1}^{M}\sum_{n=1}^{N}C_{mn}^{2}\left(\frac{m\pi}{a}\right)^{2}\cos\left(\frac{m\pi x}{a}\right)\sin\left(\frac{n\pi y}{b}\right)\cos\left(\frac{i\pi x}{a}\right)\sin\left(\frac{j\pi y}{b}\right)\right\}dxdy \quad (D.102)$$

Evaluation results in:

$$-\frac{1}{2}N_{x}\sum_{m=1}^{M}\sum_{n=1}^{N}C_{mn}^{2}\left(\frac{m\pi}{a}\right)^{2}\left(\frac{a}{2}\right)\left(\frac{b}{2}\right) \quad (D.103)$$

The second integral of the work done is given by:

$$-\frac{1}{2}\iint\left\{N_{y}\left(\frac{\partial w}{\partial y}\right)^{2}\right\}dxdy$$
$$=-\frac{1}{2}\iint\left\{N_{y}\sum_{m=1}^{M}\sum_{n=1}^{N}C_{mn}^{2}\left(\frac{n\pi}{b}\right)^{2}\sin\left(\frac{m\pi x}{a}\right)\cos\left(\frac{n\pi y}{b}\right)\sin\left(\frac{i\pi x}{a}\right)\cos\left(\frac{j\pi y}{b}\right)\right\}dxdy \quad (D.104)$$

Evaluation results in:

$$-\frac{1}{2}N_{y}\sum_{m=1}^{M}\sum_{n=1}^{N}C_{mn}^{2}\left(\frac{n\pi}{b}\right)^{2}\left(\frac{a}{2}\right)\left(\frac{b}{2}\right) \quad (D.105)$$

The third and last integral is given by:

$$-\frac{1}{2}\iint\left\{2N_{xy}\left(\frac{\partial w}{\partial x}\right)\left(\frac{\partial w}{\partial y}\right)\right\}dxdy$$
$$=-\iint\left\{N_{xy}\sum_{m=1}^{M}\sum_{n=1}^{N}C_{mn}^{2}\left(\frac{m\pi}{a}\right)\left(\frac{n\pi}{b}\right)\cos\left(\frac{m\pi x}{a}\right)\sin\left(\frac{j\pi y}{b}\right)\sin\left(\frac{i\pi x}{a}\right)\cos\left(\frac{n\pi y}{b}\right)\right\}dxdy \quad (D.106)$$

Using the same trigonometric identities as for D_{16}, the integration is simplified and results in:

$$-N_{xy}\sum_{m=1}^{M}\sum_{n=1}^{N}C_{ij}^{2}\left(\frac{m\pi}{a}\right)\left(\frac{n\pi}{b}\right)\left[\frac{4ab}{\pi^{2}}\left(\frac{ij}{(m^{2}-i^{2})(n^{2}-j^{2})}\right)\right] \qquad (D.107)$$

Only if:

$$m \pm i = odd \quad AND \quad n \pm j = odd$$

Else the result is zero.
Combining all the equations and taking the derivative of the total potential energy with respect to its coefficients C_{mn} results in:

$$\begin{aligned}\frac{\partial \Pi}{\partial \mathrm{C_{mn}}} = {} & D_{11}C_{mn}\left(\frac{m\pi}{a}\right)^{4}\left(\frac{a}{2}\right)\left(\frac{b}{2}\right)+2D_{12}C_{mn}\left(\frac{m\pi}{a}\right)^{2}\left(\frac{n\pi}{b}\right)^{2}\left(\frac{a}{2}\right)\left(\frac{b}{2}\right)\\ & +2D_{22}C_{mn}\left(\frac{n\pi}{b}\right)^{4}\left(\frac{a}{2}\right)\left(\frac{b}{2}\right)+4D_{66}C_{mn}\left(\frac{m\pi}{a}\right)^{2}\left(\frac{n\pi}{b}\right)^{2}\left(\frac{a}{2}\right)\left(\frac{b}{2}\right)\\ & -N_{x}C_{mn}\left(\frac{m\pi}{a}\right)^{2}\left(\frac{a}{2}\right)\left(\frac{b}{2}\right)-N_{y}C_{mn}\left(\frac{n\pi}{b}\right)^{2}\left(\frac{a}{2}\right)\left(\frac{b}{2}\right)\\ & -\sum_{m=1}^{M}\sum_{n=1}^{N}4D_{16}C_{ij}\left(\frac{m\pi}{a}\right)^{3}\left(\frac{n\pi}{b}\right)\left[\frac{4ab}{\pi^{2}}\left(\frac{ij}{(m^{2}-i^{2})(n^{2}-j^{2})}\right)\right]\\ & -\sum_{m=1}^{M}\sum_{n=1}^{N}4D_{26}C_{ij}\left(\frac{m\pi}{a}\right)\left(\frac{n\pi}{b}\right)^{3}\left[\frac{4ab}{\pi^{2}}\left(\frac{ij}{(m^{2}-i^{2})(n^{2}-j^{2})}\right)\right]\\ & -\sum_{m=1}^{M}\sum_{n=1}^{N}2N_{xy}C_{ij}\left(\frac{m\pi}{a}\right)\left(\frac{n\pi}{b}\right)\left[\frac{4ab}{\pi^{2}}\left(\frac{ij}{(m^{2}-i^{2})(n^{2}-j^{2})}\right)\right]\\ & =0\end{aligned} \qquad (D.108)$$

Simplified to:

$$\begin{aligned}\frac{\partial \Pi}{\partial \mathrm{C_{mn}}} = {} & C_{mn}\left[\frac{m^{4}\pi^{4}b}{4a^{3}}D_{11}+\frac{m^{2}n^{2}\pi^{4}}{2ab}D_{12}+\frac{n^{4}\pi^{4}a}{2b^{3}}D_{22}+\frac{m^{2}n^{2}\pi^{4}}{ab}D_{66}\right.\\ & \left.-\frac{m^{2}\pi^{2}b}{4a}N_{x}-\frac{n^{2}\pi^{2}a}{4b}N_{y}\right]\\ & -C_{ij}\left[\sum_{i=1}^{M}\sum_{j=1}^{N}\left(\frac{16m^{2}\pi^{2}}{a^{2}}D_{16}+\frac{16n^{2}\pi^{2}}{b^{2}}D_{26}\right.\right.\\ & \left.\left.+8N_{xy}\right)\left(\frac{mnij}{(m^{2}-i^{2})(n^{2}-j^{2})}\right)\right]=0\end{aligned} \qquad (D.109)$$

Or by multiplying each term with:

$$\frac{4a^{3}}{b\pi^{4}} \qquad (D.110)$$

The equation can be given as follows:

$$\frac{\partial \Pi}{\partial \mathrm{C_{mn}}} = C_{mn}\left[m^4 D_{11} + \frac{2m^2n^2a^2}{b^2}D_{12} + \frac{n^4a^4}{b^4}D_{22} + \frac{4m^2n^2a^2}{b^2}D_{66} - \frac{m^2a^2}{\pi^2}N_x - \frac{n^2a^4}{\pi^2b^2}N_y\right] - C_{ij}\left[\sum_{i=1}^{M}\sum_{j=1}^{N}\left(\frac{64m^2a}{\pi^2b}D_{16} + \frac{64n^2a^3}{\pi^2b^3}D_{26} + \frac{32a^3}{\pi^4b}N_{xy}\right)\left(\frac{mnij}{(m^2-i^2)(n^2-j^2)}\right)\right] = 0 \quad \textit{(D.111)}$$

From which the term with the summation signs, only give a non-zero contribution when:

$$m \pm i = odd \quad AND \quad n \pm j = odd$$

The above results in a generalized eigenvalue problem, when D_{16}, D_{26} and/or N_{xy} are non-zero. When those three terms are zero, the problem can be solved relatively easy in an analytical way.
The above equations form a matrix, where there are two independent sets of equations:

$$m + n = odd$$

$$m + n = even$$

From the complete matrix, the odd set of homogeneous equations are obtained by deleting all odd rows and columns. The even set of equations are obtained by deleting all even rows and columns from the complete matrix. As an example, the following matrix will give more insight:

$$\begin{array}{cccccccccc} e & o & e & o & e & o & e & o & e & \\ \hline \begin{bmatrix} X & 0 & 0 & 0 & Y & 0 & 0 & 0 & 0 \\ 0 & X & 0 & Y & 0 & Y & 0 & 0 & 0 \\ 0 & 0 & X & 0 & Y & 0 & 0 & 0 & 0 \\ 0 & Y & 0 & X & 0 & 0 & 0 & Y & 0 \\ Y & 0 & Y & 0 & X & 0 & Y & 0 & Y \\ 0 & Y & 0 & 0 & 0 & X & 0 & Y & 0 \\ 0 & 0 & 0 & 0 & Y & 0 & X & 0 & 0 \\ 0 & 0 & 0 & Y & 0 & Y & 0 & X & 0 \\ 0 & 0 & 0 & 0 & Y & 0 & 0 & 0 & X \end{bmatrix} & * & \begin{bmatrix} C_{11} \\ C_{12} \\ C_{13} \\ C_{21} \\ C_{22} \\ C_{23} \\ C_{31} \\ C_{32} \\ C_{33} \end{bmatrix} & = & \begin{bmatrix} 0 \\ 0 \\ 0 \\ 0 \\ 0 \\ 0 \\ 0 \\ 0 \\ 0 \end{bmatrix} & \begin{matrix} m+n=even \\ m+n=odd \\ even \\ odd \\ even \\ odd \\ even \\ odd \\ even \end{matrix} \end{array} \quad \textit{(D.112)}$$

Where e = even, o = odd, X = values from the first term in equation (D.111) and Y = values obtained from the second term of equation (D.111).
In order to solve the generalized eigenvalue problem, the following relation is always obtained:

$$\Big[[E] - N_{x,y,xy}[H]\Big]\{C_{mn}\} = \{0\}$$

Where:

$$[E]: matrix\ with\ all\ terms\ obtained\ from\ the\ equivalent\ D-terms$$

$$[H]: matrix\ containing\ all\ values\ related\ to\ the\ applied\ forces\ N_x, N_y\ and\ N_{xy}$$

$$\{C_{mn}\}: will\ be\ equal\ to\ the\ eigenvector\ after\ evaluation$$

$$N_{x,y,xy}: eigenvalue$$

A non-trivial solution ($C_{mn} \neq 0$) for the above can be found by evaluating:

$$det\left[[E] - N_{x,y,xy}[H]\right] = 0$$

The lowest eigenvalue $N_{x,y,xy}$ in absolute terms is considered to be the buckling load. The corresponding eigenvector determines the buckling mode and is equal to the vector of the C_{mn} terms.

Appendix E

DERIVATION OF THE EXACT SOLUTION OF STIFFENER CRIPPLING

The stiffener is modelled by assuming three simply supported edges and one edge free. Using the principle of minimum potential energy, the potential energy should first be obtained by the strain energy and the work done.

$$\Pi = U + W \tag{E.1}$$

Since all the fibres in the stiffener are unidirectional, bending stiffness terms D_{16} and D_{26} are assumed to be zero and the strain energy is therefore given by:

$$U = \frac{1}{2}\iint \left\{ D_{11}\left(\frac{\partial^2 w}{\partial x^2}\right)^2 + 2D_{12}\frac{\partial^2 w}{\partial x^2}\frac{\partial^2 w}{\partial y^2} + D_{22}\left(\frac{\partial^2 w}{\partial y^2}\right)^2 + 4D_{66}\left(\frac{\partial^2 w}{\partial x \partial y}\right)^2 \right\} dxdy \tag{E.2}$$

The work done is obtained by loading along the stiffener direction and is given by:

$$W = -\frac{1}{2}\iint \left\{ N_{x,sc}\left(\frac{\partial w}{\partial x}\right)^2 \right\} dxdy \tag{E.3}$$

To satisfy the boundary conditions, equation (E.4) is used as an approximating function [13], which was obtained from comparison with experimental work. Applying this function, the stiffener is allowed to buckle in multiple half waves along the stiffener length and only one half wave along the height.

$$w = \sum_{m=1}^{M} C_m \sin\left(\frac{m\pi x}{a}\right)\left(20b^4 y + \frac{10b^2}{3}y^3 - \frac{10b}{3}y^4 + y^5\right) \tag{E.4}$$

The derivatives found in the integrals of the strain energy and the work done are given by:

$$\frac{dw}{dx} = \sum_{m=1}^{M} C_m \left(\frac{m\pi}{a}\right)\cos\left(\frac{m\pi x}{a}\right)\left(20b^4 y + \frac{10b^2}{3}y^3 - \frac{10b}{3}y^4 + y^5\right) \tag{E.5}$$

$$\frac{d^2 w}{dx^2} = \sum_{m=1}^{M} C_m \left(\frac{m\pi}{a}\right)^2 \sin\left(\frac{m\pi x}{a}\right)\left(20b^4 y + \frac{10b^2}{3}y^3 - \frac{10b}{3}y^4 + y^5\right) \tag{E.6}$$

$$\frac{\partial^2 w}{\partial x \partial y} = \sum_{m=1}^{M} C_m \left(\frac{m\pi}{a}\right)\cos\left(\frac{m\pi x}{a}\right)\left(20b^4 + 10b^2 y^2 - \frac{40b}{3}y^3 + 5y^4\right) \tag{E.7}$$

$$\frac{\partial^2 w}{\partial y^2} = \sum_{m=1}^{M} C_m \sin\left(\frac{m\pi x}{a}\right)(20b^2 y - 40by^2 + 20y^3) \tag{E.8}$$

Substituting the above derivatives leads to four integrals for the strain energy equation and one integral for the work done. The first integral to evaluate for the strain energy is given by:

$$\begin{aligned}&\frac{1}{2}\iint\left\{D_{11}\left(\frac{\partial^2 w}{\partial x^2}\right)^2\right\}dxdy\\&=\frac{1}{2}\iint\left\{D_{11}\sum_{m=1}^{M}C_m^2\left(\frac{m\pi}{a}\right)^4\sin\left(\frac{m\pi x}{a}\right)\sin\left(\frac{i\pi x}{a}\right)\left(400b^8y^2\right.\right.\\&+\frac{400b^6}{3}y^4-\frac{400b^5}{3}y^5+\frac{460b^4}{9}y^6-\frac{200b^3}{9}y^7+\frac{160b^2}{9}y^8\\&\left.\left.-\frac{20b}{3}y^9+y^{10}\right)\right\}dxdy\end{aligned}\qquad (E.9)$$

Using the following integration rule:

$$\int_0^a\sin\left(\frac{m\pi x}{a}\right)\sin\left(\frac{i\pi x}{a}\right)dx=\frac{a}{2}\qquad (E.10)$$

Evaluation results in:

$$\begin{aligned}&\frac{1}{2}D_{11}\sum_{m=1}^{M}C_m^2\left(\frac{m\pi}{a}\right)^4\left(\frac{a}{2}\right)\left(\frac{400}{3}+\frac{400}{15}-\frac{400}{18}+\frac{460}{63}-\frac{200}{72}+\frac{160}{81}-\frac{20}{30}\right.\\&\left.+\frac{1}{11}\right)b^{11}\end{aligned}\qquad (E.11)$$

Where:

$$\left(\frac{400}{3}+\frac{400}{15}-\frac{400}{18}+\frac{460}{63}-\frac{200}{72}+\frac{160}{81}-\frac{20}{30}+\frac{1}{11}\right)\approx 143.701\qquad (E.12)$$

The second integral of the strain energy is given by:

$$\begin{aligned}&\iint\left\{D_{12}\frac{\partial^2 w}{\partial x^2}\frac{\partial^2 w}{\partial y^2}\right\}dxdy\\&=\iint\left\{D_{12}\sum_{m=1}^{M}C_m^2\left(\frac{m\pi}{a}\right)^2\sin\left(\frac{m\pi x}{a}\right)\sin\left(\frac{i\pi x}{a}\right)\left(400b^6y^2\right.\right.\\&-800b^5y^3+\frac{1400b^4}{3}y^4-\frac{600b^3}{3}y^5+\frac{660b^2}{3}y^6-\frac{320b}{3}y^7\\&\left.\left.+20y^8\right)\right\}dxdy\end{aligned}\qquad (E.13)$$

Evaluation results in:

$$D_{12}\sum_{m=1}^{M}C_m^2\left(\frac{m\pi}{a}\right)^2\left(\frac{a}{2}\right)\left(\frac{400}{3}-\frac{800}{4}+\frac{1400}{15}-\frac{600}{18}+\frac{660}{21}-\frac{320}{24}+\frac{20}{9}\right)b^9\qquad (E.14)$$

Where:

$$\left(\frac{400}{3}-\frac{800}{4}+\frac{1400}{15}-\frac{600}{18}+\frac{660}{21}-\frac{320}{24}+\frac{20}{9}\right)\approx 13.651\qquad (E.15)$$

The third integral of the strain energy is given by:

$$\begin{aligned}&\frac{1}{2}\iint\left\{D_{22}\left(\frac{\partial^2 w}{\partial y^2}\right)^2\right\}dxdy\\&=\frac{1}{2}\iint\left\{D_{22}\sum_{m=1}^{M}C_m^2\sin\left(\frac{m\pi x}{a}\right)\sin\left(\frac{i\pi x}{a}\right)(400b^4y^2\right.\\&\left.-1600b^3y^3+2400b^2y^4-1600by^5+400y^6)\right\}dxdy\end{aligned}\tag{E.16}$$

Evaluation results in:

$$\frac{1}{2}D_{22}\sum_{m=1}^{M}C_m^2\left(\frac{a}{2}\right)\left(\frac{400}{3}-\frac{1600}{4}+\frac{2400}{5}-\frac{1600}{6}+\frac{400}{7}\right)b^7\tag{E.17}$$

Where:

$$\left(\frac{400}{3}-\frac{1600}{4}+\frac{2400}{5}-\frac{1600}{6}+\frac{400}{7}\right)\approx 3.810\tag{E.18}$$

The fourth integral for the strain energy is given by:

$$\begin{aligned}&\iint\left\{2D_{66}\left(\frac{\partial^2 w}{\partial x\partial y}\right)^2\right\}dxdy\\&=\iint\left\{2D_{66}\sum_{m=1}^{M}C_m^2\left(\frac{m\pi}{a}\right)^2\cos\left(\frac{m\pi x}{a}\right)\cos\left(\frac{i\pi x}{a}\right)\left(400b^8\right.\right.\\&+400b^6y^2-\frac{1600b^5}{3}y^3+300b^4y^4-\frac{800b^3}{3}y^5\\&\left.\left.+\frac{2500b^2}{9}y^6-\frac{400b}{3}y^7+25y^8\right)\right\}dxdy\end{aligned}\tag{E.19}$$

Evaluation results in:

$$\begin{aligned}&2D_{66}\sum_{m=1}^{M}C_m^2\left(\frac{m\pi}{a}\right)^2\left(\frac{a}{2}\right)\left(400+\frac{400}{3}-\frac{1600}{12}+\frac{300}{5}-\frac{800}{18}+\frac{2500}{63}-\frac{400}{24}\right.\\&\left.+\frac{25}{9}\right)b^9\end{aligned}\tag{E.20}$$

Where:

$$\left(400+\frac{400}{3}-\frac{1600}{12}+\frac{300}{5}-\frac{800}{18}+\frac{2500}{63}-\frac{400}{24}+\frac{25}{9}\right)\approx 441.349\tag{E.21}$$

The integral of the work done is given by:

$$-\frac{1}{2}\iint\left\{N_{x,sc}\left(\frac{\partial w}{\partial x}\right)^2\right\}dxdy$$
$$=-\frac{1}{2}\iint\left\{N_{x,sc}\sum_{m=1}^{M}C_m^2\left(\frac{m\pi}{a}\right)^2\cos\left(\frac{m\pi x}{a}\right)\cos\left(\frac{i\pi x}{a}\right)\left(400b^8y^2+\frac{400b^6}{3}y^4\right.\right. \quad (E.22)$$
$$\left.\left.-\frac{400b^5}{3}y^5+\frac{460b^4}{9}y^6-\frac{200b^3}{9}y^7+\frac{160b^2}{9}y^8-\frac{20b}{3}y^9+y^{10}\right)\right\}dxdy$$

Evaluating the integral results in:

$$-\frac{1}{2}N_{x,sc}\sum_{m=1}^{M}C_m^2\left(\frac{m\pi}{a}\right)^2\frac{a}{2}\left(\frac{400}{3}+\frac{400}{15}-\frac{400}{18}+\frac{460}{63}-\frac{200}{72}+\frac{160}{81}-\frac{20}{30}\right. \quad (E.23)$$
$$\left.+\frac{1}{11}\right)b^{11}$$

Where:

$$\left(\frac{400}{3}+\frac{400}{15}-\frac{400}{18}+\frac{460}{63}-\frac{200}{72}+\frac{160}{81}-\frac{20}{30}+\frac{1}{11}\right)\approx 143.701 \quad (E.24)$$

Substituting the evaluated integrals in the potential energy equation:

$$\Pi=\frac{1}{2}D_{11}\sum_{m=1}^{M}C_m^2\left(\frac{m\pi}{a}\right)^4\left(\frac{a}{2}\right)(143.701)b^{11}$$
$$+D_{12}\sum_{m=1}^{M}C_m^2\left(\frac{m\pi}{a}\right)^2\left(\frac{a}{2}\right)(13.651)b^9$$
$$+\frac{1}{2}D_{22}\sum_{m=1}^{M}C_m^2\left(\frac{a}{2}\right)(3.810)b^7 \quad (E.25)$$
$$+2D_{66}\sum_{m=1}^{M}C_m^2\left(\frac{m\pi}{a}\right)^2\left(\frac{a}{2}\right)(441.349)b^9$$
$$-\frac{1}{2}N_{x,sc}\sum_{m=1}^{M}C_m^2\left(\frac{m\pi}{a}\right)^2\frac{a}{2}(143.701)\,b^{11}$$

Differentiating the total potential energy and setting it equal to zero, results in:

$$\frac{\partial\Pi}{\partial C_m}=D_{11}C_m\left(\frac{m^4\pi^4}{2a^3}\right)(143.701)b^{11}+D_{12}C_m\frac{m^2\pi^2}{a}(13.651)b^9$$
$$+D_{22}C_m\left(\frac{a}{2}\right)(3.810)b^7+D_{66}C_m\frac{2m^2\pi^2}{a}(441.349)b^9 \quad (E.26)$$
$$-N_{x,sc}C_m\frac{m^2\pi^2}{2a}(143.701)b^{11}=0$$

Rearranging and dividing by b^{11} terms results in:

$$D_{11}C_m\left(\frac{m^4\pi^4}{2a^3}\right)(143.701) + D_{12}C_m\frac{m^2\pi^2}{ab^2}(13.651) + D_{22}C_m\left(\frac{a}{2b^4}\right)(3.810) + D_{66}C_m\frac{2m^2\pi^2}{ab^2}(441.349) = N_{x,sc}C_m\frac{m^2\pi^2}{2a}(143.701) \quad (E.27)$$

Solving for N_x results in:

$$N_{x,sc} = D_{11}\left(\frac{m^2\pi^2}{a^2}\right) + D_{12}\left(\frac{0.190}{b^2}\right) + D_{22}\left(\frac{0.0265a^2}{m^2\pi^2b^4}\right) + D_{66}\left(\frac{12.285}{b^2}\right) \quad (E.28)$$

Substituting the design variables used to describe an orthogrid structure:

$$a = dx_{st} \quad (E.29)$$

$$b = h_{st} \quad (E.30)$$

Results in the final equation for the stiffener crippling load:

$$N_{x,sc} = D_{11}\left(\frac{m^2\pi^2}{{dx_{st}}^2}\right) + D_{12}\left(\frac{0.190}{{h_{st}}^2}\right) + D_{22}\left(\frac{0.0265{dx_{st}}^2}{m^2\pi^2{h_{st}}^4}\right) + D_{66}\left(\frac{12.285}{{h_{st}}^2}\right) \quad (E.31)$$

Appendix F

DERIVATION OF INTRACELLULAR BUCKLING LOAD UNDER CLAMPED CONDITIONS

The method of minimum potential energy in combination with a Ritz approximation is used to obtain the buckling load of the skin between the stiffeners of a grid stiffened panel. The potential energy is given by the sum of the strain energy and the work done, as shown in equation (F.1).

$$\Pi = U + W \tag{F.1}$$

Where the strain energy U is given by equation (F.2).

$$U = \frac{1}{2}\iint \left\{ D_{11}\left(\frac{\partial^2 w}{\partial x^2}\right)^2 + 2D_{12}\frac{\partial^2 w}{\partial x^2}\frac{\partial^2 w}{\partial y^2} + D_{22}\left(\frac{\partial^2 w}{\partial y^2}\right)^2 + 4D_{66}\left(\frac{\partial^2 w}{\partial x \partial y}\right)^2 \right\} dxdy \tag{F.2}$$

And the work done W by equation (F.3).

$$W = -\frac{1}{2}\iint \left\{ N_{x,ic,cc}\left(\frac{\partial w}{\partial x}\right)^2 \right\} dxdy \tag{F.3}$$

Clamped condition at the edges are described by zero displacement and zero slope at the edges of the panel, which can be written as follows:

$$w(x,y) = 0 \quad at\ x = 0, a$$

$$w(x,y) = 0 \quad at\ y = 0, b$$

$$\frac{\partial w}{\partial x} = 0 \quad at\ x = 0, a$$

$$\frac{\partial w}{\partial y} = 0 \quad at\ y = 0, b$$

The displacement function which satisfies these boundary conditions is given by equation (F.4).

$$w(x,y) = \sum_{m=1}^{M}\sum_{n=1}^{N} C_{mn}\left(1 - \cos\frac{2m\pi x}{a}\right)\left(1 - \cos\frac{2n\pi y}{b}\right) \tag{F.4}$$

To substitute this displacement function in equations (F.2) and (F.3), the relevant derivatives are given by equations (F.5) till (F.8).

$$\frac{\partial w}{\partial x} = \sum_{m=1}^{M}\sum_{n=1}^{N} C_{mn}\frac{2m\pi}{a}\sin\frac{2m\pi x}{a}\left(1 - \cos\frac{2n\pi y}{b}\right) \tag{F.5}$$

$$\frac{\partial^2 w}{\partial x^2} = \sum_{m=1}^{M}\sum_{n=1}^{N} C_{mn}\left(\frac{2m\pi}{a}\right)^2 \cos\frac{2m\pi x}{a}\left(1-\cos\frac{2n\pi y}{b}\right) \tag{F.6}$$

$$\frac{\partial^2 w}{\partial y^2} = \sum_{m=1}^{M}\sum_{n=1}^{N} C_{mn}\left(\frac{2n\pi}{b}\right)^2 \left(1-\cos\frac{2m\pi x}{a}\right)\cos\frac{2n\pi y}{b} \tag{F.7}$$

$$\frac{\partial^2 w}{\partial x \partial y} = \sum_{m=1}^{M}\sum_{n=1}^{N} C_{mn}\left(\frac{2m\pi}{a}\right)\left(\frac{2n\pi}{b}\right)\sin\frac{2m\pi x}{a}\sin\frac{2n\pi y}{b} \tag{F.8}$$

The strain energy is described by four integrals, from which the first is evaluated as follows:

$$\begin{aligned}&\frac{1}{2}\iint D_{11}\left(\frac{\partial^2 w}{\partial x^2}\right)^2 dxdy\\ &= \frac{1}{2}\iint D_{11}\sum_{m=1}^{M}\sum_{n=1}^{N} C_{mn}^2\left(\frac{2m\pi}{a}\right)^4 \cos\frac{2m\pi x}{a}\cos\frac{2i\pi x}{a}\Big(1\\ &-\cos\frac{2n\pi y}{b}-\cos\frac{2j\pi y}{b}+\cos\frac{2n\pi y}{b}\cos\frac{2j\pi y}{b}\Big)\,dxdy\end{aligned} \tag{F.9}$$

Performing the integration with respect to x and y results in equation (F.10).

$$\begin{aligned}&\frac{1}{2}\iint D_{11}\left(\frac{\partial^2 w}{\partial x^2}\right)^2 dxdy\\ &= \frac{1}{2}D_{11}\sum_{m=1}^{M}\sum_{n=1}^{N} C_{mn}^2\left(\frac{2m\pi}{a}\right)^4 \frac{a}{2}\Big(y-\frac{b}{2n\pi}\sin\frac{2n\pi y}{b}\\ &-\frac{b}{2j\pi}\sin\frac{2j\pi y}{b}+\frac{b}{2}\Big)\end{aligned} \tag{F.10}$$

Evaluating the integral along x from 0 to a and along y from 0 to be results in:

$$\frac{1}{2}\iint D_{11}\left(\frac{\partial^2 w}{\partial x^2}\right)^2 dxdy = \frac{1}{2}D_{11}\sum_{m=1}^{M}\sum_{n=1}^{N} C_{mn}^2\left(\frac{2m\pi}{a}\right)^4\left(\frac{ab}{2}+\frac{ab}{4}\right) \tag{F.11}$$

The second integral for the strain energy is given by:

$$\begin{aligned}&\iint D_{12}\frac{\partial^2 w}{\partial x^2}\frac{\partial^2 w}{\partial y^2}\,dxdy\\ &= \iint D_{12}\sum_{m=1}^{M}\sum_{n=1}^{N} C_{mn}^2\left(\frac{2m\pi}{a}\right)^2\left(\frac{2n\pi}{b}\right)^2\Big(\cos\frac{2m\pi x}{a}\cos\frac{2m\pi y}{b}\\ &-\cos\frac{2m\pi x}{a}\cos\frac{2i\pi x}{a}\cos\frac{2n\pi y}{b}\\ &-\cos\frac{2m\pi x}{a}\cos\frac{2n\pi y}{b}\cos\frac{2j\pi y}{b}\\ &+\cos\frac{2m\pi x}{a}\cos\frac{2i\pi x}{a}\cos\frac{2n\pi y}{b}\cos\frac{2j\pi y}{b}\Big)\,dxdy\end{aligned} \tag{F.12}$$

Performing the integration with respect to x and y results in:

$$\iint D_{12}\frac{\partial^2 w}{\partial x^2}\frac{\partial^2 w}{\partial y^2}dxdy = D_{12}\sum_{m=1}^{M}\sum_{n=1}^{N}C_{mn}^2\left(\frac{2m\pi}{a}\right)^2\left(\frac{2n\pi}{b}\right)^2\left(\frac{ab}{4mn\pi^2}\sin\frac{2m\pi x}{a}\sin\frac{2n\pi y}{b} - \frac{ab}{4n\pi}\sin\frac{2n\pi y}{b} - \frac{ab}{4m\pi}\sin\frac{2m\pi x}{a} + \frac{ab}{4}\right) \quad (F.13)$$

Evaluating along the edges results in:

$$\iint D_{12}\frac{\partial^2 w}{\partial x^2}\frac{\partial^2 w}{\partial y^2}dxdy = D_{12}\sum_{m=1}^{M}\sum_{n=1}^{N}C_{mn}^2\left(\frac{2m\pi}{a}\right)^2\left(\frac{2n\pi}{b}\right)^2\left(\frac{ab}{4}\right) \quad (F.14)$$

The third integral is given by:

$$\begin{aligned}&\frac{1}{2}\iint D_{22}\left(\frac{\partial^2 w}{\partial y^2}\right)^2 dxdy \\ &= \frac{1}{2}\iint D_{22}\sum_{m=1}^{M}\sum_{n=1}^{N}C_{mn}^2\left(\frac{2n\pi}{b}\right)^4\left(\cos\frac{2n\pi y}{b}\cos\frac{2j\pi y}{b}\right. \\ &- \cos\frac{2m\pi x}{a}\cos\frac{2n\pi y}{b}\cos\frac{2j\pi y}{b} \\ &- \cos\frac{2m\pi x}{a}\cos\frac{2n\pi y}{b}\cos\frac{2j\pi y}{b} \\ &\left.+ \cos\frac{2m\pi x}{a}\cos\frac{2i\pi x}{a}\cos\frac{2n\pi y}{b}\cos\frac{2j\pi y}{b}\right)dxdy\end{aligned} \quad (F.15)$$

Integrating with respect to x and y results in equation (F.16).

$$\begin{aligned}&\frac{1}{2}\iint D_{22}\left(\frac{\partial^2 w}{\partial y^2}\right)^2 dxdy \\ &= \frac{1}{2}\iint D_{22}\sum_{m=1}^{M}\sum_{n=1}^{N}C_{mn}^2\left(\frac{2n\pi}{b}\right)^4\left(\frac{b}{2}x - \frac{a}{2m\pi}\frac{b}{2}\sin\frac{2m\pi x}{a}\right. \\ &\left.- \frac{a}{2m\pi}\frac{b}{2}\sin\frac{2m\pi x}{a} + \frac{ab}{4}\right)dxdy\end{aligned} \quad (F.16)$$

Evaluating the integral along the edges of the panel:

$$\frac{1}{2}\iint D_{22}\left(\frac{\partial^2 w}{\partial y^2}\right)^2 dxdy = \frac{1}{2}D_{22}\sum_{m=1}^{M}\sum_{n=1}^{N}C_{mn}^2\left(\frac{2n\pi}{b}\right)^4\left(\frac{ab}{2} + \frac{ab}{4}\right) \quad (F.17)$$

The last and fourth integral for the strain energy is given by:

$$\begin{aligned}&\iint 2D_{66}\left(\frac{\partial^2 w}{\partial x\partial y}\right)^2 dxdy \\ &= \iint 2D_{66}\sum_{m=1}^{M}\sum_{n=1}^{N}C_{mn}^2\left(\frac{2m\pi}{a}\right)^2\left(\frac{2n\pi}{b}\right)^2\sin\frac{2m\pi x}{a}\sin\frac{2i\pi x}{a}\sin\frac{2n\pi y}{b}\sin\frac{2j\pi y}{b}dxdy\end{aligned} \quad (F.18)$$

Evaluating the integral results in:

$$\iint 2D_{66}\left(\frac{\partial^2 w}{\partial x \partial y}\right)^2 dxdy = 2D_{66}\sum_{m=1}^{M}\sum_{n=1}^{N} C_{mn}^2\left(\frac{2m\pi}{a}\right)^2\left(\frac{2n\pi}{b}\right)^2\frac{ab}{4} \tag{F.19}$$

The work done is integrated as follows:

$$\begin{aligned}-\frac{1}{2}\iint\left\{N_{x,ic,cc}\left(\frac{\partial w}{\partial x}\right)^2\right\}dxdy \\ = -\frac{1}{2}\iint\left\{N_{x,ic,cc}\sum_{m=1}^{M}\sum_{n=1}^{N} C_{mn}^2\left(\frac{2m\pi}{a}\right)^2\left(\sin\frac{2m\pi x}{a}\sin\frac{2i\pi x}{a}\right.\right. \\ -\sin\frac{2m\pi x}{a}\sin\frac{2i\pi x}{a}\cos\frac{2n\pi y}{b} - \sin\frac{2m\pi x}{a}\sin\frac{2i\pi x}{a}\cos\frac{2n\pi y}{b} \\ \left.\left.+\sin\frac{2m\pi x}{a}\sin\frac{2i\pi x}{a}\cos\frac{2n\pi y}{b}\cos\frac{2j\pi y}{b}\right)\right\}dxdy\end{aligned} \tag{F.20}$$

Evaluation of the integral results in:

$$\begin{aligned}-\frac{1}{2}\iint\left\{N_{x,ic,cc}\left(\frac{\partial w}{\partial x}\right)^2\right\}dxdy \\ = -\frac{1}{2}\iint\left\{N_{x,ic,cc}\sum_{m=1}^{M}\sum_{n=1}^{N} C_{mn}^2\left(\frac{2m\pi}{a}\right)^2\left(\frac{a}{2}y - \frac{ab}{4n\pi}\sin\frac{2n\pi y}{b}\right.\right. \\ \left.\left.-\frac{ab}{4n\pi}\sin\frac{2n\pi y}{b}+\frac{ab}{4}\right)\right\}dxdy\end{aligned} \tag{F.21}$$

Integration along the edges of the plate:

$$-\frac{1}{2}\iint\left\{N_{x,ic,cc}\left(\frac{\partial w}{\partial x}\right)^2\right\}dxdy = -\frac{1}{2}N_{x,ic,cc}\sum_{m=1}^{M}\sum_{n=1}^{N} C_{mn}^2\left(\frac{2m\pi}{a}\right)^2\left(\frac{ab}{2}+\frac{ab}{4}\right) \tag{F.22}$$

The total potential energy is now given by:

$$\begin{aligned}\Pi = \frac{1}{2}D_{11}\sum_{m=1}^{M}\sum_{n=1}^{N} C_{mn}^2\left(\frac{2m\pi}{a}\right)^4\left(\frac{3ab}{4}\right) \\ + D_{12}\sum_{m=1}^{M}\sum_{n=1}^{N} C_{mn}^2\left(\frac{2m\pi}{a}\right)^2\left(\frac{2n\pi}{b}\right)^2\left(\frac{ab}{4}\right) \\ + \frac{1}{2}D_{22}\sum_{m=1}^{M}\sum_{n=1}^{N} C_{mn}^2\left(\frac{2n\pi}{b}\right)^4\left(\frac{3ab}{4}\right) \\ + 2D_{66}\sum_{m=1}^{M}\sum_{n=1}^{N} C_{mn}^2\left(\frac{2m\pi}{a}\right)^2\left(\frac{2n\pi}{b}\right)^2\frac{ab}{4} \\ -\frac{1}{2}N_{x,ic,cc}\sum_{m=1}^{M}\sum_{n=1}^{N} C_{mn}^2\left(\frac{2m\pi}{a}\right)^2\left(\frac{ab}{2}+\frac{ab}{4}\right)\end{aligned} \tag{F.23}$$

Differentiating and setting the result equal to zero gives the following relation:

$$\frac{\partial \Pi}{\partial \mathrm{C_{mn}}} = D_{11}C_{mn}\left(\frac{12m^4\pi^4 b}{a^3}\right) + D_{12}C_{mn}\left(\frac{8m^2n^2\pi^4}{ab}\right) + D_{22}C_{mn}\left(\frac{12n^4\pi^4 a}{b^3}\right) + D_{66}C_{mn}\left(\frac{16m^2n^2\pi^4}{ab}\right) - N_{x,ic,cc}C_{mn}\left(\frac{3m^2\pi^2 b}{a}\right) = 0 \quad \textit{(F.24)}$$

Solving equation (F.24) for the applied load $N_{x,ic,cc}$ results in:

$$N_{x,ic,cc}\left(\frac{3m^2\pi^2 b}{a}\right) = D_{11}\left(\frac{12m^4\pi^4 b}{a^3}\right) + D_{12}\left(\frac{8m^2n^2\pi^4}{ab}\right) + D_{22}\left(\frac{12n^4\pi^4 a}{b^3}\right) + 4D_{66}\left(\frac{4m^2n^2\pi^4}{ab}\right) \quad \textit{(F.25)}$$

or:

$$N_{x,ic,cc} = D_{11}\left(\frac{4m^2\pi^2}{a^2}\right) + D_{12}\left(\frac{8n^2\pi^2}{3b^2}\right) + D_{22}\left(\frac{4n^4\pi^2 a^2}{m^2 b^4}\right) + D_{66}\left(\frac{16n^2\pi^2}{3b^2}\right) \quad \textit{(F.26)}$$

It can easily be seen that the buckling load is minimized for n = 1:

$$N_{x,ic,cc} = D_{11}\left(\frac{4m^2\pi^2}{a^2}\right) + D_{12}\left(\frac{8\pi^2}{3b^2}\right) + D_{22}\left(\frac{4\pi^2 a^2}{m^2 b^4}\right) + D_{66}\left(\frac{16\pi^2}{3b^2}\right) \quad \textit{(F.27)}$$

Intracellular buckling of the unit cells under clamped conditions can be stated by substituting the following design variables for length a and width b:

$$a = dx_{st} \quad \textit{(F.28)}$$

$$b = dy_{st} \quad \textit{(F.29)}$$

Resulting in:

$$N_{x,ic,cc} = D_{11}\left(\frac{4m^2\pi^2}{{dx_{st}}^2}\right) + D_{12}\left(\frac{8\pi^2}{3{dy_{st}}^2}\right) + D_{22}\left(\frac{4\pi^2 {dx_{st}}^2}{m^2 {dy_{st}}^4}\right) + D_{66}\left(\frac{16\pi^2}{3{dy_{st}}^2}\right) \quad \textit{(F.30)}$$

Appendix G

DATA-POINTS FOR NUMERICAL CONVERGENCE STUDY ON THE ORTHOGRID PANELS

The values of the data-points, which are graphically presented in subsection 3.2.3 are given in this appendix. There are a total of 12 tables presented, two for each of the example designs. Each table shows the number of elements in the first column and the approximate element size between brackets. The second column shows the applied load to the panel, before the buckling analysis is performed. The applied load changes with number of elements, because each node is given a unit compressive load. In the third column, the lowest found eigenvalue related to the mode of failure is given. The fourth column shows the predicted failure load, which is the multiplication of the applied load and the eigenvalue. The mode of buckling is shown in the fifth column, where "combined" relates to a combination of stiffener crippling and intracellular buckling.

Table G.1 and table G.2 show the data of the convergence graphs of the first example panel, predicting intracellular buckling.
Table G.3 and table G.4 show the data of the convergence graphs of the second example panel, predicting intracellular buckling.
Table G.5 and table G.6 show the data of the convergence graphs of the first example panel, predicting stiffener crippling.
Table G.7 and table G.8 show the data of the convergence graphs of the second example panel, predicting stiffener crippling.
Table G.9 and table G.10 show the data of the convergence graphs of the first example panel, predicting global buckling.
Table G.11 and table G.12 show the data of the convergence graphs of the second example panel, predicting global buckling.

Table G.1: Numerical convergence of intracellular buckling on orthogrid panel, example panel 1

# of elements (element size)	Applied load [N]	Lowest eigenvalue	Buckling load [N]	Buckling mode
260 (50 mm)	-	-	-	-
860 (25 mm)	-42	3720	-156240	Combined
6120 (10 mm)	-147	642.6	-94462	Combined
27500 (5 mm)	-606	149.5	-90597	Combined
75808 (3 mm)	-1485	60.42	-89724	Combined
171744 (2 mm)	-3237	27.63	-89438	Combined

Table G.2: Numerical convergence of global buckling on orthogrid panel, example panel 1

# of elements (element size)	Applied load [N]	Lowest eigenvalue	Buckling load [N]	Buckling mode
260 (50 mm)	-18	14630	-263340	Global buckling
860 (25 mm)	-42	5810	-244020	Global buckling
6120 (10 mm)	-147	1626	-239022	Global buckling
27500 (5 mm)	-	-	-	-
75808 (3 mm)	-	-	-	-
171744 (2 mm)	-	-	-	-

Table G.3: Numerical convergence of intracellular buckling on orthogrid panel, example panel 2

# of elements (element size)	Applied load [N]	Lowest eigenvalue	Buckling load [N]	Buckling mode
2131 (17 mm)	-	-	-	-
3526 (15 mm)	-	-	-	-
4921 (11 mm)	-	-	-	-
7772 (10 mm)	-	-	-	-
11314 (9 mm)	-138	1461	-201618	Combined
14104 (8 mm)	-183	1091	-199653	Combined
18396 (7 mm)	-244	820.2	-200129	Combined
27549 (6 mm)	-304	497.9	-151361	Combined
38172 (5 mm)	-455	333.2	-151606	Combined
65000 (4 mm)	-726	190.9	-138593	Combined
130737 (3 mm)	-1328	93.1	-123637	Combined
177326 (2.5 mm)	-1764	68.27	-120428	Combined
278400 (2 mm)	-2651	44.18	-117121	Combined

Table G.4: Numerical convergence of global buckling on orthogrid panel, example panel 2

# of elements (element size)	Applied load [N]	Lowest eigenvalue	Buckling load [N]	Buckling mode
2131 (17 mm)	-32	5458	-174656	Global buckling
3526 (15 mm)	-62	2637	-163494	Global buckling
4921 (11 mm)	-92	1770	-162840	Global buckling
7772 (10 mm)	-138	1168	-161184	Global buckling
11314 (9 mm)	-138	1162	-160356	Global buckling
14104 (8 mm)	-183	874.2	-159979	Global buckling
18396 (7 mm)	-244	654.0	-159576	Global buckling
27549 (6 mm)	-304	523.9	-159266	Global buckling
38172 (5 mm)	-455	349.5	-159022	Global buckling
65000 (4 mm)	-	-	-	-
130737 (3 mm)	-	-	-	-
177326 (2.5 mm)	-	-	-	-
278400 (2 mm)	-	-	-	-

Table G.5: Numerical convergence of stiffener crippling on orthogrid panel, example panel 3

# of elements (element size)	Applied load [N]	Lowest eigenvalue	Buckling load [N]	Buckling mode
82 (80 mm)	-	-	-	-
212 (50 mm)	-18	6486	-116748	Stiffener crippling
616 (30 mm)	-34	1584	-53856	Stiffener crippling
1386 (20 mm)	-50	747.5	-37375	Stiffener crippling
2222 (15 mm)	-66	531.0	-35046	Stiffener crippling
5544 (10 mm)	-147	237.2	-34868	Stiffener crippling
24500 (5 mm)	-606	55.39	-33566	Stiffener crippling
67936 (3 mm)	-1485	22.43	-33309	Stiffener crippling

Table G.6: Numerical convergence of global buckling on orthogrid panel, example panel 3

# of elements (element size)	Applied load [N]	Lowest eigenvalue	Buckling load [N]	Buckling mode
82 (80 mm)	-10	17090	-170900	Global buckling
212 (50 mm)	-18	7426	-133668	Global buckling
616 (30 mm)	-34	3625	-123250	Global buckling
1386 (20 mm)	-	-	-	-
2222 (15 mm)	-	-	-	-
5544 (10 mm)	-	-	-	-
24500 (5 mm)	-	-	-	-
67936 (3 mm)	-	-	-	-

Table G.7: Numerical convergence of stiffener crippling on orthogrid panel, example panel 4

# of elements (element size)	Applied load [N]	Lowest eigenvalue	Buckling load [N]	Buckling mode
1046 (20 mm)	-	-	-	-
2764 (15 mm)	-58	5661	-328338	Stiffener crippling
7284 (10 mm)	-129	1858	-239682	Stiffener crippling
41314 (5 mm)	-594	332.9	-197743	Stiffener crippling
109712 (3 mm)	-1395	138.2	-192789	Stiffener crippling
251976 (2 mm)	-3107	61.69	-191671	Stiffener crippling

Table G.8: Numerical convergence of global buckllling on orthogrid panel, example panel 4

# of elements (element size)	Applied load [N]	Lowest eigenvalue	Buckling load [N]	Buckling mode
1046 (20 mm)	-30	14010	-420300	Global buckling
2764 (15 mm)	-58	6721	-389818	Global buckling
7284 (10 mm)	-129	2784	-359136	Global buckling
41314 (5 mm)	-594	592.7	-352064	Global buckling
109712 (3 mm)	-	-	-	-
251976 (2 mm)	-	-	-	-

Table G.9: Numerical convergence of local failure on orthogrid panel, example 5

# of elements (element size)	Applied load [N]	Lowest eigenvalue	Buckling load [N]	Buckling mode
196 (50 mm)	-	-	-	-
512 (30 mm)	-	-	-	-
1504 (20 mm)	-50	1849	-92450	Combined
2180 (15 mm)	-62	1389	-86118	Combined
4928 (10 mm)	-98	732.9	-71824	Combined
23058 (5 mm)	-388	177.3	-68792	Combined
64070 (3 mm)	-978	69.41	-67883	Combined

Table G.10: Numerical convergence of global buckling on orthogrid panel, example 5

# of elements (element size)	Applied load [N]	Lowest eigenvalue	Buckling load [N]	Buckling mode
196 (50 mm)	-14	3851	-53914	Global buckling
512 (30 mm)	-26	1795	-46670	Global buckling
1504 (20 mm)	-50	913.5	-45675	Global buckling
2180 (15 mm)	-62	734.6	-45545	Global buckling
4928 (10 mm)	-98	463.7	-45442	Global buckling
23058 (5 mm)	-388	117.0	-45396	Global buckling
64070 (3 mm)	-978	47.29	-46250	Global buckling

Table G.11: Numerical convergence of local failure on orthogrid panel, example 6

# of elements (element size)	Applied load [N]	Lowest eigenvalue	Buckling load [N]	Buckling mode
1046 (20 mm)	-	-	-	-
2764 (15 mm)	-	-	-	-
5154 (10 mm)	-86	2426	-208636	Combined
31374 (5 mm)	-396	440.5	-174438	Combined
85202 (3 mm)	-930	181.7	-168981	Combined

Table G.12: Numerical convergence of global buckling on orthogrid panel, example 6

# of elements (element size)	Applied load [N]	Lowest eigenvalue	Buckling load [N]	Buckling mode
1046 (20 mm)	-30	3106	-93180	Global buckling
2764 (15 mm)	-58	1486	-86188	Global buckling
5154 (10 mm)	-86	996.9	-85733	Global buckling
31374 (5 mm)	-396	213.4	-84506	Global buckling
85202 (3 mm)	-930	90.87	-84509	Global buckling

Appendix H

DATA-POINTS OF THE NUMERICAL ANALYSIS PERFORMED FOR THE PARAMETRIC STUDY

The values of the data-points shown in this appendix are related to the parametric study performed in subsection 3.2.4. All numerical results presented here are modelled with an approximate element size of 2 mm. In each of the tables, the first column shows the value of the design variable which is changed. The second and third column present the applied load and the found eigenvalue from the buckling analysis of Marc Mentat respectively. The multiplication of the two is the resulting critical load and is given in the fourth column. The last column indicates the mode of failure related to the found critical buckling load.

The numerical analysis on the influence of the skin thickness on the local and global modes of failure are given in table H.1 and table H.2 respectively.

The numerical analysis on the influence of the stiffener thickness on the local and global modes of failure are given in table H.3 and table H.4 respectively.

The numerical analysis on the influence of the stiffener height on the local and global modes of failure are given in table H.5 and table H.6 respectively.

The numerical analysis on the influence of the number of longitudinal stiffeners on the local and global modes of failure are given in table H.7 and table H.8 respectively.

The numerical analysis on the influence of the number of transverse stiffeners on the local and global modes of failure are given in table H.9 and table H.10 respectively.

Table H.1: Numerically predicted local failure load by varying the skin thickness

Skin thickness [+/-45]-plies	Applied load [N]	Lowest eigenvalue	Buckling load [N]	Buckling mode
1	-2684	20.02	-53733	IC buckling
2	-2684	98.48	-264320	IC buckling
3	-2684	228.4	-613065	Combined
4	-2684	351.0	-942084	Combined
5	-2684	400.5	-1074942	Combined
6	-2684	443.7	-1190891	Combined
7	-2684	480.5	-1289662	Combined
8	-2684	511.9	-1373940	Combined
9	-2684	539.7	-1448555	Combined
10	-2684	564.5	-1515118	Combined

Table H.2: Numerically predicted global buckling load by the varying skin thickness

Skin thickness [+/-45]-plies	Applied load [N]	Lowest eigenvalue	Buckling load [N]	Buckling mode
1	-	-	-	-
2	-2684	98.85	-265313	Global buckling
3	-2684	111.0	-297924	Global buckling
4	-2684	119.5	-320738	Global buckling
5	-2684	126.6	-339794	Global buckling
6	-2684	132.9	-356704	Global buckling

7	-2684	139.2	-373613	Global buckling
8	-2684	145.7	-391059	Global buckling
9	-2684	152.7	-409847	Global buckling
10	-2684	164.9	-442592	Global buckling

Table H.3: Numerically predicted local failure load by varying the stiffener thickness

Stiffener thickness [0]-plies	Applied load [N]	Lowest eigenvalue	Buckling load [N]	Buckling mode
2	-2684	12.08	-32422	Stiffener crippling
4	-2684	76.5	-205326	Stiffener crippling
6	-2684	194.1	-520964	Combined
8	-2684	351.0	-942084	Combined
10	-2684	481.1	-1291272	Combined
12	-2684	561.2	-1506261	IC buckling
14	-2684	623.4	-1673206	IC buckling
16	-2684	690.9	-1854376	IC buckling
18	-2684	757.3	-2032593	IC buckling
20	-2684	822.9	-2208664	IC buckling

Table H.4: Numerically predicted global buckling load by the varying stiffener thickness

Stiffener thickness [0]-plies	Applied load [N]	Lowest eigenvalue	Buckling load [N]	Buckling mode
2	-	-	-	-
4	-2684	68.08	-182727	Global buckling
6	-2684	94.82	-254497	Global buckling
8	-2684	119.5	-320738	Global buckling
10	-2684	142.8	-383275	Global buckling
12	-2684	164.9	-442592	Global buckling
14	-2684	186.2	-499761	Global buckling
16	-2684	206.7	-554783	Global buckling
18	-2684	226.7	-608463	Global buckling
20	-2684	246.2	-660801	Global buckling

Table H.5: Numerically predicted local failure load by varying the stiffener height

Stiffener height [mm]	Applied load [N]	Lowest eigenvalue	Buckling load [N]	Buckling mode
2	-	-	-	-
4	-	-	-	-
6	-	-	-	-
8	-	-	-	-
10	-	-	-	-
12	-	-	-	-
14	-	-	-	-
16	-	-	-	-

18	-2440	384.5	-938180	Combined
20	-2684	351.0	-942084	Combined
22	-2928	324.4	-949843	Combined
24	-3172	303.2	-961750	Combined
26	-3416	286.3	-978001	Combined
28	-3660	272.7	-998082	Combined
30	-3904	261.7	-1021676	Combined
32	-4148	252.7	-1048200	Combined
34	-4392	245.2	-1076918	Combined
36	-4636	239.1	-1108468	Combined
38	-4880	233.9	-1141432	Combined
40	-5124	229.5	-1175958	Combined

Table H.6: Numerically predicted global buckling load by the varying stiffener height

Stiffener height [mm]	Applied load [N]	Lowest eigenvalue	Buckling load [N]	Buckling mode
2	-488	9.025	-4404	Global buckling
4	-732	10.74	-7862	Global buckling
6	-976	16.32	-15928	Global buckling
8	-1220	24.89	-30365	Global buckling
10	-1464	36.01	-52719	Global buckling
12	-1708	49.33	-84256	Global buckling
14	-1952	64.56	-126021	Global buckling
16	-2196	81.48	-178930	Global buckling
18	-2440	99.86	-243658	Global buckling
20	-2684	119.5	-320738	Global buckling
22	-2928	140.3	-410798	Global buckling
24	-3172	162.1	-514181	Global buckling
26	-3416	184.7	-630935	Global buckling
28	-3660	208.0	-761280	Global buckling
30	-3904	231.9	-905338	Global buckling
32	-4148	256.2	-1062718	Global buckling
34	-4392	280.8	-1233274	Global buckling
36	-	-	-	-
38	-	-	-	-
40	-	-	-	-

Table H.7: Numerically predicted local failure load by varying the number of longitudinal stiffeners

Longitudinal stiffeners	Applied load [N]	Lowest eigenvalue	Buckling load [N]	Buckling mode
2	-	-	-	-
4	-2750	57.93	-159308	Combined
6	-2761	128.3	-354236	Combined
8	-2706	243.2	-658099	Combined
10	-2684	351.0	-942084	Combined
12	-2673	426.3	-1139500	Combined
14	-2728	494.2	-1348178	Combined
16	-2651	591.7	-1568597	Combined
18	-2629	684.7	-1800076	Combined

20	-2728	748.0	-2040544	Combined
22	-2552	879.3	-2243974	Combined
24	-2541	955.7	-2428433	Combined
26	-2761	946.3	-2612734	Combined
28	-2684	1042	-2796728	Combined
30	-	-	-	-

Table H.8: Numerically predicted global buckling load by varying the number of longitudinal stiffeners

Longitudinal stiffeners	Applied load [N]	Lowest eigenvalue	Buckling load [N]	Buckling mode
2	-2761	12.61	-34816	Global buckling
4	-	-	-	-
6	-2761	88.28	-243741	Global buckling
8	-2706	105.6	-285754	Global buckling
10	-2684	119.5	-320738	Global buckling
12	-2673	131.2	-350698	Global buckling
14	-2728	138.0	-376464	Global buckling
16	-2651	150.5	-398976	Global buckling
18	-2629	159.5	-419325	Global buckling
20	-2728	160.5	-437844	Global buckling
22	-2552	178.3	-455022	Global buckling
24	-2541	185.4	-471101	Global buckling
26	-2761	176.1	-486212	Global buckling
28	-2684	186.6	-500834	Global buckling
30	-2563	200.8	-514650	Global buckling

Table H.9: Numerically predicted local failure load by varying the number of transverse stiffeners

Transverse stiffeners	Applied load [N]	Lowest eigenvalue	Buckling load [N]	Buckling mode
3	-2684	176.1	-472652	Combined
5	-2684	184.1	-494124	Combined
7	-2684	216.8	-581891	Combined
9	-2684	254.0	-681736	Combined
11	-2684	292.2	-784265	Combined
13	-2684	319.1	-856464	Combined
15	-2684	351.0	-942084	Combined
17	-2684	383.8	-1030119	Combined
19	-2684	415.4	-1114934	Combined
21	-2684	444.5	-1193038	Combined
23	-2684	471.2	-1264701	Combined
25	-2684	495.8	-1330727	Combined
27	-2684	519.4	-1394070	Combined
29	-2684	541.9	-1454460	Combined
31	-	-	-	-
33	-	-	-	-
35	-	-	-	-
37	-	-	-	-

39	-	-	-	-
41	-	-	-	-

Table H.10: Numerically predicted global buckling failure load by varying the number of transverse stiffeners

Transverse stiffeners	Applied load [N]	Lowest eigenvalue	Buckling load [N]	Buckling mode
3	-2684	53.16	-142681	Global buckling
5	-2684	72.34	-194161	Global buckling
7	-2684	86.66	-232595	Global buckling
9	-2684	97.75	-262361	Global buckling
11	-2684	106.4	-285578	Global buckling
13	-2684	113.5	-304634	Global buckling
15	-2684	119.5	-320738	Global buckling
17	-2684	124.8	-334963	Global buckling
19	-2684	129.6	-347846	Global buckling
21	-2684	133.9	-359388	Global buckling
23	-2684	138.0	-370392	Global buckling
25	-2684	141.8	-380591	Global buckling
27	-2684	145.4	-390254	Global buckling
29	-2684	148.8	-399379	Global buckling
31	-2684	152.0	-407968	Global buckling
33	-2684	155.2	-416557	Global buckling
35	-2684	158.2	-424609	Global buckling
37	-2684	161.1	-432392	Global buckling
39	-2684	164.0	-440176	Global buckling
41	-2684	166.8	-447691	Global buckling

Appendix I

RESULTS FOR THE THEORETICAL LOW-WEIGHT ORTHOGRID DESIGNS

The determined failure loads by the analytical and numerical models for the preliminary designs related to the theoretical low-weight designs are outlined in table I.1 and table I.2 respectively. The locations of the assumed critical location for first ply failure is indicated between brackets in the most right column of table I.1.The critical locations are indicated in figure 4.3.

Table I.1: Analytical solutions for preliminary orthogrid designs (theoretical)

Loadcase [kN]	Global buckling [N]	Stiffener crippling [N]	Intracellular buckling (ss) [N]	Intracellular buckling (cc) [N]	First ply failure [N], [critical location]
50	57009	81812	35515	100081	173543 [6]
100	113411	165892	68043	198371	244290 [6]
150	177423	241827	168116	467260	403474 [6]
200	228010	324381	227114	662651	324219 [6]
250	281097	408091	175085	497671	399683 [6]
300	336624	499162	254782	839538	315967 [6]
350	404232	578270	328514	1041067	387019 [6]
400	448226	646432	488392	1427408	505560 [6]
450	507040	748310	527832	1570942	526781 [6]
500	579201	806814	369623	1060578	603198 [6]
550	625282	890617	354104	1163005	428220 [6]
600	678031	1005482	456579	1316102	696259 [6]
650	753917	1079370	476542	1382540	722698 [6]
700	791732	1154810	440495	1498582	458731 [6]
750	841088	1272446	516581	1529285	749255 [6]
800	907799	1316913	533846	1773935	503770 [6]

Table I.2: Numerical solution of the preliminary orthogrid designs (theoretical)

Loadcase [kN]	Numerical solution x_1 [N], (applied load *eigenvalue)	Failure mode	Numerical solution x_2 [N], (applied load *eigenvalue)	Failure mode
50	61407 (1928*31.85)	Global buckling	75423 (1928*39.12)	Combined
100	120826 (24800*4.872)	Global buckling	153388 (24800*6.185)	Combined
150	181653 (2684*67.68)	Global buckling	263649 (2684*98.23)	Combined
200	229223 (2629*87.19)	Global buckling	251569 (2629*95.69)	Combined
250	277313 (2892*95.89)	Global buckling	347040 (2892*120.0)	Combined
300	316746 (3133*101.1)	Combined	327085 (3133*104.4)	Global buckling
350	390550 (3107*125.7)	Global buckling	399560 (3107*128.6)	Combined
400	433199 (3055*141.8)	Global buckling	520878 (3055*170.5)	Combined
450	487907 (3290*148.3)	Global buckling	583975 (3290*177.5)	Combined
500	559409 (3374*165.8)	Global buckling	693694 (3374*205.6)	Combined
550	529996 (3735*141.9)	Combined	583034 (3735*156.1)	Global buckling
600	646724 (3615*178.9)	Global buckling	852779 (3615*235.9)	Combined

650	712155 (3615*197.0)	Global buckling	906281 (3615*250.7)	Combined
700	637838 (3984*160.1)	Combined	721901 (3984*181.2)	Global buckling
750	792794 (3856*205.6)	Global buckling	1022226 (3856*265.1)	Combined
800	767917 (3904*196.7)	Combined	832723 (3904*213.3)	Global buckling

The analytical and numerical determined critical loads for the improved designs are shown in table I.3 and table I.4 respectively.

Table I.3: Analytical solutions for improved low-weight orthogrid designs (theoretical)

Loadcase [kN]	Global buckling [N]	Stiffener crippling [N]	Intracellular buckling (ss) [N]	Intracellular buckling (cc) [N]	First ply failure [N], [critical location]
50	50970	53080	35143	98593	174720 [6]
100	100138	108828	151899	443614	333154 [6]
150	155457	150224	96515	268467	329706 [6]
200	211751	183814	130933	363815	401442 [6]
250	256706	217868	236288	666299	507952 [6]
300	305080	295083	261398	728457	562317 [6]
350	399238	409174	382660	1078020	461317 [6]
400	467600	455313	452385	1269153	527463 [6]
450	481436	520926	522209	1465042	543046 [6]
500	547483	515153	685675	1905234	631670 [6]
550	575768	616998	777630	2161190	681790 [6]
600	635003	630626	798708	2219770	708560 [6]
650	712427	697755	924529	2568810	753552 [6]
700	779790	743394	518395	1440594	774911 [6]
750	811967	822406	605502	1682404	850888 [6]
800	835971	959711	701957	1950384	876209 [6]

Table I.4: Numerical solutions for improved low-weight orthogrid designs (theoretical)

Loadcase [kN]	Numerical solution x_1 [N], (applied load *eigenvalue)	Failure mode	Numerical solution x_2 [N], (applied load *eigenvalue)	Failure mode
50	53598 (1928*27.80)	Combined	55758 (1928*28.92)	Global buckling
100	103445 (2115*48.91)	Global buckling	130982 (2115*61.93)	Combined
150	158028 (2673*59.12)	Global buckling	160540 (2673*60.06)	Combined
200	205477 (2892*71.05)	Combined	213111 (2892*73.69)	Global buckling
250	259385 (2796*92.77)	Global buckling	270429 (2796*96.72)	Combined
300	305561 (3133*97.53)	Global buckling	352776 (3133*112.6)	Combined
350	364140 (3107*117.2)	Combined	395210 (3107*127.2)	Global buckling
400	416185 (3290*126.5)	Combined	451717 (3290*137.3)	Global buckling
450	469762 (3472*135.3)	Global buckling	476011 (3472*137.1)	Combined
500	516757 (3248*159.1)	Combined	532347 (3248*163.9)	Global buckling
550	555887 (3402*163.4)	Global buckling	606236 (3402*178.2)	Combined
600	609809 (3645*167.3)	Global buckling	625847 (3645*171.7)	Combined
650	684684 (3564*197.6)	Global buckling	706167 (3465*203.8)	Combined
700	744150 (3824*194.6)	Global buckling	752946 (3824*196.9)	Combined
750	770424 (3760*204.9)	Global buckling	840360 (3760*223.5)	Combined
800	803520 (3968*202.5)	Global buckling	966604 (3968*243.6)	Combined

Appendix J

RESULTS FOR THE PRACTICAL LOW-WEIGHT ORTHOGRID DESIGNS

The determined failure loads by the analytical and numerical models for the preliminary designs related to the more practical designs are outlined in table J.1 and table J.2 respectively. The locations of the assumed critical location for first ply failure is indicated between brackets in the most right column of table J.1.The critical locations are indicated in figure 4.3.

Table J.1: Analytical solutions for preliminary orthogrid designs (practical)

Loadcase [kN]	Global buckling [N]	Stiffener crippling [N]	Intracellular buckling (ss) [N]	Intracellular buckling (cc) [N]	First ply failure [N], [critical location]
50	56509	662093	36739	102152	507094 [6]
100	114405	440444	73839	205772	428927 [6]
150	172991	383006	110066	305916	534318 [6]
200	229057	393321	153297	430067	650852 [6]
250	290963	417461	200258	557269	705204 [6]
300	342975	500929	257812	723285	801470 [6]
350	391865	610292	255613	717113	635537 [6]
400	491549	675549	290718	815593	791818 [6]
450	519668	772332	320811	900020	944085 [6]
500	583657	897571	356206	992666	1152831 [6]
550	615534	925925	432391	1204972	729565 [6]
600	689290	1009547	440553	1224274	757621 [6]
650	728180	1112003	506583	1436906	882826 [6]
700	786841	1128538	524915	1458541	1043915 [6]
750	841469	1267942	603107	1754347	1049213 [6]
800	909994	1291987	570229	1599760	750550 [6]

Table J.2: Numerical solution of the preliminary orthogrid designs (practical)

Loadcase [kN]	Numerical solution x_1 [N], (applied load *eigenvalue)	Failure mode	Numerical solution x_2 [N], (applied load *eigenvalue)	Failure mode
50	52731 (1928*27.35)	Global buckling	61137 (1928*31.71)	IC buckling
100	116183 (2490*46.66)	Global buckling	123753 (2490*49.70)	IC buckling
150	136079 (2684*50.70)	Combined	142735 (2684*53.18)	Global buckling
200	194274 (3012*64.50)	Combined	204665 (3012*67.95)	Global buckling
250	265531 (2916*91.06)	Combined	268943 (2916*92.23)	Global buckling
300	318988 (2892*110.3)	Global buckling	402566 (2892*139.2)	Combined
350	373874 (3237*115.5)	Global buckling	433434 (3237*133.9)	Combined
400	445859 (3486*127.9)	Global buckling	455969 (3486*130.8)	Combined
450	379625 (3486*108.9)	Combined	406119 (3486*116.5)	Global buckling
500	342985 (3735*91.83)	Combined	560250 (3735*150.0)	Global buckling
550	577350 (3514*164.3)	Global buckling	819816 (3514*233.3)	Combined
600	647279 (3514*184.2)	Global buckling	885879 (3514*252.1)	Combined

650	675391 (3514*192.2)	Global buckling	958971 (3514*272.9)	Combined
700	635664 (3936*161.5)	Combined	662035 (3936*168.2)	Global buckling
750	771449 (3765*204.9)	Global buckling	983795 (3765*261.3)	IC buckling
800	820580 (3735*219.7)	Global buckling	1011811 (3735*270.9)	Combined

The analytical and numerical determined critical loads for the improved practical designs are shown in table J.3 and table J.4 respectively.

Table J.3: Analytical solutions for improved low-weight orthogrid designs (practical)

Loadcase [kN]	Global buckling [N]	Stiffener crippling [N]	Intracellular buckling (ss) [N]	Intracellular buckling (cc) [N]	First ply failure [N], [critical location]
50	56509	662093	36740	102152	507094 [6]
100	107291	443305	74993	210388	436057 [6]
150	176628	423877	108812	305269	494102 [6]
200	220212	429353	145289	403970	612113 [6]
250	265620	459103	195139	544623	671185 [6]
300	321638	471873	206220	581114	696498 [6]
350	392661	512951	262296	735856	672067 [6]
400	456636	531038	263076	730991	693174 [6]
450	509626	726402	284333	790057	787701 [6]
500	564927	733322	299649	858386	615419 [6]
550	602906	642469	485833	1353903	896980 [6]
600	652704	777006	462332	1311387	759892 [6]
650	720816	759675	506211	1420161	922853 [6]
700	783225	801629	590410	1680484	759605 [6]
750	834347	937971	553681	1539482	1095444 [6]
800	879860	734336	1012202	2814373	995892 [6]

Table J.4: Numerical solutions for improved low-weight orthogrid designs (practical)

Loadcase [kN]	Numerical solution x_1 [N], (applied load *eigenvalue)	Failure mode	Numerical solution x_2 [N], (applied load *eigenvalue)	Failure mode
50	61407 (1928*31.85)	Global buckling	75423 (1928*39.12)	Combined
100	102215 (2490*41.05)	Global buckling	114266 (2490*45.89)	Combined
150	174702 (2684*65.09)	Global buckling	180553 (2684*67.27)	Combined
200	206274 (2761*74.71)	Global buckling	233028 (2761*84.40)	Combined
250	259582 (2916*89.02)	Global buckling	310262 (2916*106.4)	Combined
300	308512 (2916*105.8)	Global buckling	335923 (2916*115.2)	Combined
350	360602 (3237*111.4)	Combined	365457 (3237*112.9)	Global buckling
400	414834 (3486*119.0)	Combined	433658 (3486*124.4)	Global buckling
450	477931 (3486*137.1)	Global buckling	489783 (3486*140.5)	Combined
500	505214 (3458*146.1)	Combined	519737 (3458*150.3)	Global buckling
550	554509 (3514*157.8)	Global buckling	609328 (3514*173.4)	Combined
600	609328 (3514*173.4)	Global buckling	731966 (3514*208.3)	Combined
650	662263 (3765*175.9)	Global buckling	756389 (3765*200.9)	Combined
700	727952 (3735*194.9)	Global buckling	733928 (3735*196.5)	Combined
750	763542 (3765*202.8)	Global buckling	916401 (3765*243.4)	Combined
800	800389 (4016*199.3)	Combined	816051 (4016*203.2)	Global buckling

Appendix K

QUALITY ANALYSIS MEASUREMENTS OF SAMPLE ORTHOGRID PANEL 1 AND PANEL 2

The measurements performed on the plug, the mould and the two sample orthogrid panels are outlined in this appendix. The measurements on the plug were performed on the points indicated in figure K.1. The numbers indicate the locations in the xy-plane of the panel and act as a reference for the measurement indicated in table K.1 and table K.2.
In the tables, the z locations refer to skin (z = 0), stiffener at the bottom (z = 1), middle (z = 2) and top (z = 3).
For all the measurements, the average and standard deviations are calculated and written down in the tables as well.

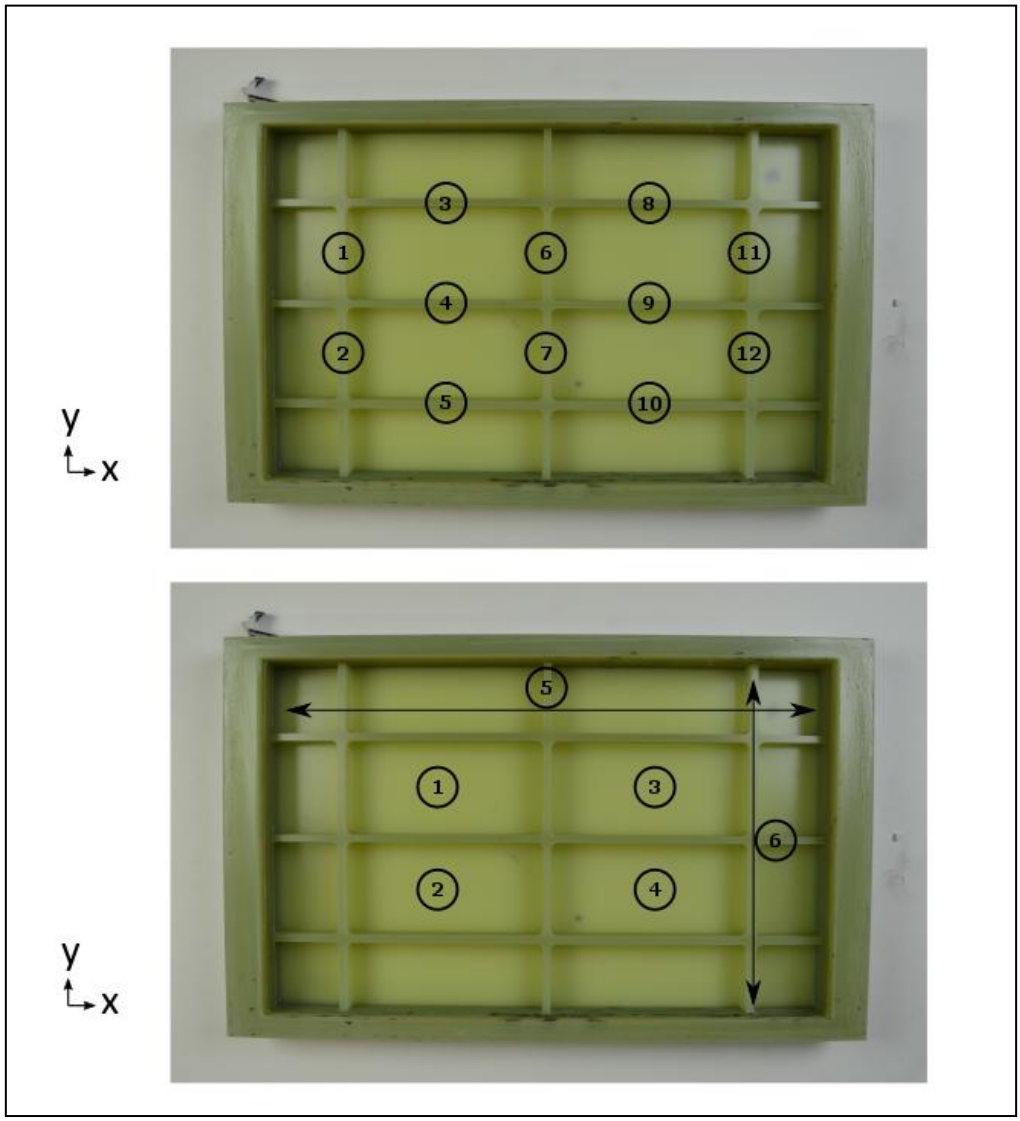

Figure K.1: Measurement locations on the sample orthogrid plug

Table K.1: Stiffener measurements plug

Location	t_{st} (z = 1) [mm]	t_{st} (z = 2) [mm]	t_{st} (z = 3) [mm]	h_{st} [mm]
1	5.19	5.17	5.15	19.66
2	5.19	5.19	5.26	19.61
3	5.28	5.17	5.27	19.69
4	5.30	5.31	5.27	19.56
5	5.31	5.28	5.30	19.26
6	5.29	5.31	5.34	19.74
7	5.24	5.29	5.23	19.52
8	5.20	5.20	5.23	19.70
9	5.25	5.18	5.17	19.52
10	5.26	5.32	5.25	19.37
11	5.21	5.21	5.25	19.68
12	5.20	5.21	5.20	19.56
Average	5.24	5.24	5.24	19.57
Standard deviation	0.0429	0.0573	0.0505	0.1364

Table K.2: Cell measurements plug

Location	Stiffener spacing (dx_{st} - t_{st}) [mm]				Stiffener spacing (dy_{st} - t_{st}) [mm]			
	1	2	3	Average	1	2	3	Average
1	141.77	141.76	141.73	141.75	67.04	67.09	67.06	67.06
2	141.71	141.66	141.70	141.69	67.04	67.00	67.03	67.02
3	141.72	141.67	141.70	141.70	67.01	67.06	67.09	67.05
4	141.74	141.73	141.75	141.74	67.06	67.07	67.06	67.06
Total average				141.72				67.05
Standard deviation				0.0324				0.0269

	Length and width of the plug (inside measure) [mm]				
	1	2	3	Average	Standard deviation
5	400.0	400.0	400.0	400.0	0.0
6	250.0	250.0	250.0	250.0	0.0

The measurements on the mould were performed on the points indicated in figure K.2. The numbers indicate the locations in the xy-plane of the panel and act as a reference for the measurement indicated in table K.3 and table K.4.
In the tables the z locations refer to skin (z = 0), stiffener at the bottom (z = 1), middle (z = 2) and top (z = 3). For the mould, only the (z = 1) location could be measured, since the flexibility of the mould did not allow accurate measurements on the other locations.
The numbers indicated in figure K.2 can also be compared to the same numbers indicated for the plug or the product in figure K.3.
Averages and standard deviations as a result of the measurements are also presented in the tables.

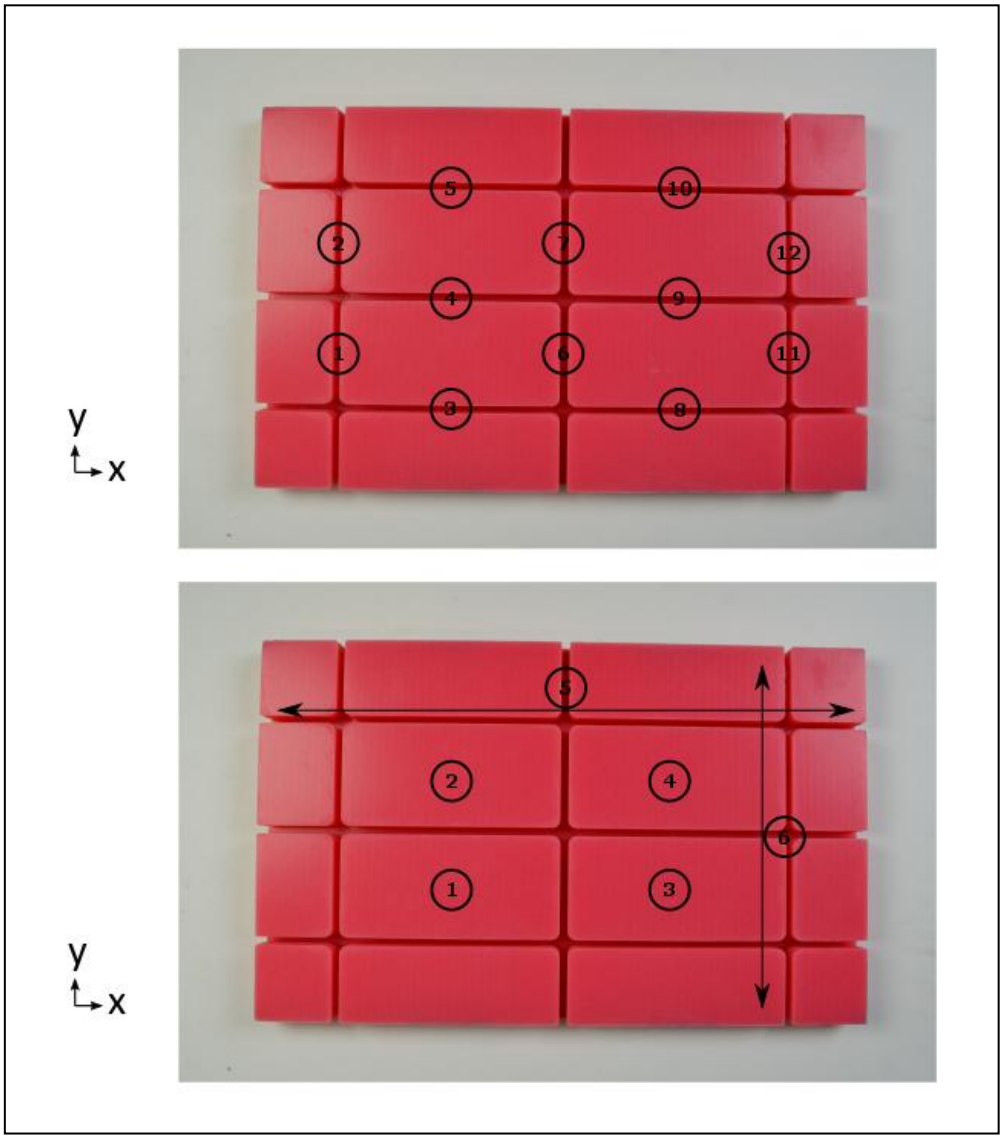

Figure K.2: Measurement locations on the sample orthogrid mould

Table K.3: Stiffener measurements mould

Location	t_{st} (z = 1) [mm]	h_{st} [mm]
1	4.93	19.81
2	4.94	19.24
3	4.85	19.85
4	4.92	19.21
5	4.96	19.29
6	5.05	19.80
7	5.07	19.48
8	4.90	19.65
9	5.07	19.32
10	5.01	18.98
11	4.97	19.36
12	5.05	19.24
Average	4.98	19.44
Standard deviation	0.0697	0.2689

Table K.4: Cell measurements mould

Location (xy)	Stiffener spacing (dx_{st} - t_{st}) [mm]				Stiffener spacing (dy_{st} - t_{st}) [mm]			
	1	2	3	Average	1	2	3	Average
1	141.66	141.73	141.71	141.70	67.23	67.13	67.27	67.21
2	141.70	141.69	141.77	141.72	67.21	67.28	67.12	67.20
3	141.75	141.69	141.89	141.78	67.34	67.27	67.21	67.27
4	141.87	141.84	141.76	141.82	67.26	67.10	67.15	67.17
Total average				141.76				67.21
Standard deviation				0.0719				0.0718

	Length and width of the mould (inside measure) [mm]				
	1	2	3	Average	Standard deviation
5	401.0	400.5	400.2	400.6	0.3300
6	251.0	250.5	250.0	250.5	0.4082

The measurement locations of the first sample orthogrid panel are indicated in figure K.3. The blue line indicates the position of the resin runner during the vacuum infusion, which is placed all around the panel. The arrow indicates the inlet position and the directions of the resin flow.
The numbers indicate the locations in the xy-plane of the panel and act as a reference for the measurement indicated in table K.5 and table K.6.
In the table the z locations refer to skin (z = 0), stiffener at the bottom (z = 1), middle (z = 2) and top (z = 3).

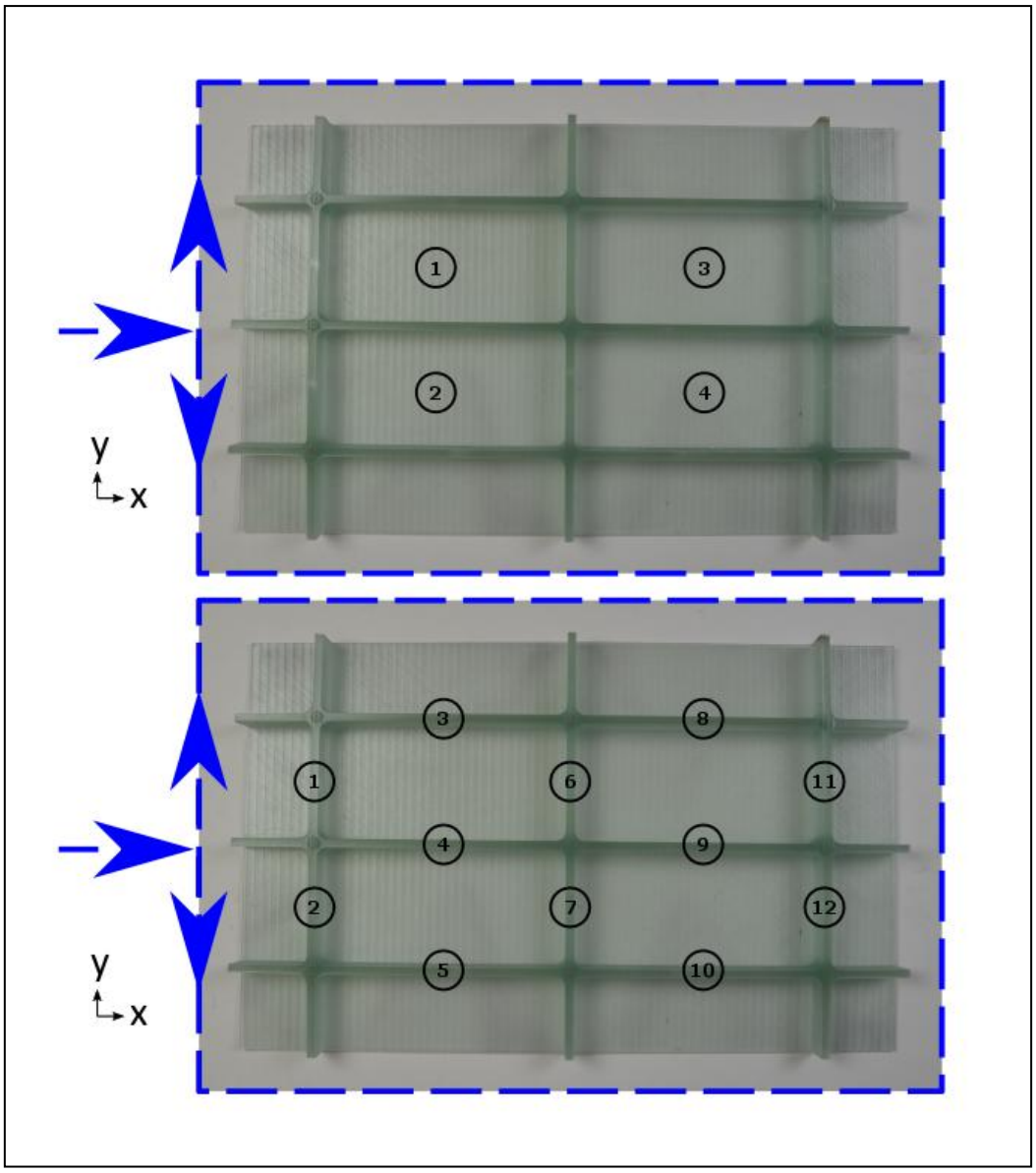

Figure K.3: Measurement locations on the sample orthogrid panel

Table K.5: Cell measurements sample orthogrid panel 1

Location	t_{sk} (z = 0) [mm]	Stiffener spacing (dx_{st} - t_{st}) [mm]	Stiffener spacing (dy_{st} - t_{st}) [mm]	Voids
1	1.71	142.07	67.48	None
2	1.80	142.06	67.46	None
3	1.70	142.08	67.48	None
4	1.75	142.10	67.47	None
Average	1.74	142.08	67.47	
Standard deviation	0.0394	0.0148	0.0083	

Table K.6: Stiffener measurements sample orthogrid panel 1

Location	t_{st} (z = 1) [mm]	t_{st} (z = 2) [mm]	t_{st} (z = 3) [mm]	h_{st} [mm]	Voids
1	4.49	4.36	4.79	19.05	z = 2, 3
2	4.44	4.50	4.92	18.96	z = 2, 3
3	4.22	4.19	4.86	19.07	z = 2
4	4.43	4.33	4.87	19.06	z = 2
5	4.18	4.16	4.85	18.80	z = 2
6	4.80	4.66	4.93	19.19	None
7	4.83	4.72	4.95	19.02	z = 2, 3
8	4.42	4.16	4.83	19.09	z = 2
9	4.32	4.54	4.88	18.93	z = 2
10	4.10	4.16	4.81	18.74	z = 2
11	4.44	4.56	4.83	19.06	z = 2
12	4.38	4.45	4.75	18.95	z = 2, 3
Average	4.42	4.40	4.86	18.99	
Standard deviation	0.2101	0.1939	0.0565	0.1208	

The same measurement locations for the second sample orthogrid panel are used. The related measurements are outlined in table K.7 and table K.8.

Table K.7: Cell measurements sample orthogrid panel 2

Location	t_{sk} (z = 0) [mm]	Stiffener spacing (dx_{st} - t_{st}) [mm]	Stiffener spacing (dy_{st} - t_{st}) [mm]	Voids
1	1.75	142.04	67.58	None
2	1.80	141.98	67.49	None
3	1.70	142.10	67.63	None
4	1.70	142.14	67.59	None
Average	1.74	142.07	67.57	
Standard deviation	0.0415	0.0606	0.0512	

Table K.8: Stiffener measurements sample orthogrid panel 2

Location	t_{st} (z = 1) [mm]	t_{st} (z = 2) [mm]	t_{st} (z = 3) [mm]	h_{st} [mm]	Voids
1	4.20	4.17	4.63	19.08	z = 2
2	4.32	4.42	4.72	19.37	z = 2
3	3.98	4.17	4.72	19.18	z = 2
4	4.31	4.30	4.77	19.49	None
5	3.73	4.09	4.70	19.64	z = 2
6	4.30	4.26	4.73	19.43	None
7	4.43	4.28	4.77	19.60	None
8	3.78	3.85	4.66	19.01	z = 2
9	4.01	4.10	4.73	19.32	None
10	3.86	3.90	4.79	19.54	None
11	4.20	4.22	4.75	19.03	z = 2
12	4.08	3.97	4.68	19.15	None
Average	4.10	4.14	4.72	19.32	
Standard deviation	0.2201	0.1635	0.0454	0.2158	

All the measurements performed on the sample orthogrid panels are compared by their found values and plotting their normal distributions, obtained from the measurements.
The comparison of the skin thickness is shown in table K.9, where it is shown that the thickness is found to be lower than initially designed.

Table K.9: Comparison of skin thickness

	Design value	Panel 1	Panel 2
Total thickness [mm]	2.025	1.74	1.74

The measurements on the stiffener height are presented as normal distributions in figure K.3. From the graphs, it can be seen that the manufactured plug already has a lower stiffener height than the design value of 20 mm.
The mould also introduces a small change of the average stiffener height. However, the mould measurements tend to be inaccurate, because of the flexibility of the silicon. The silicon can be easily indented, which also explains the larger variation of the normal distribution.
Sample orthogrid panel 1 shows another decrease of the stiffener height, which could be explained by the applied vacuum during the infusion. The pressure applied, compresses the mould and therefore reduces the stiffener height.
This reduction of the stiffener height is less apparent for the second sample orthogrid panel. The difference of 0.33 mm on the average between both panels, could possibly be addressed to tolerances in manufacturing. However, more panels should be manufactured and measured in order to validate this statement.

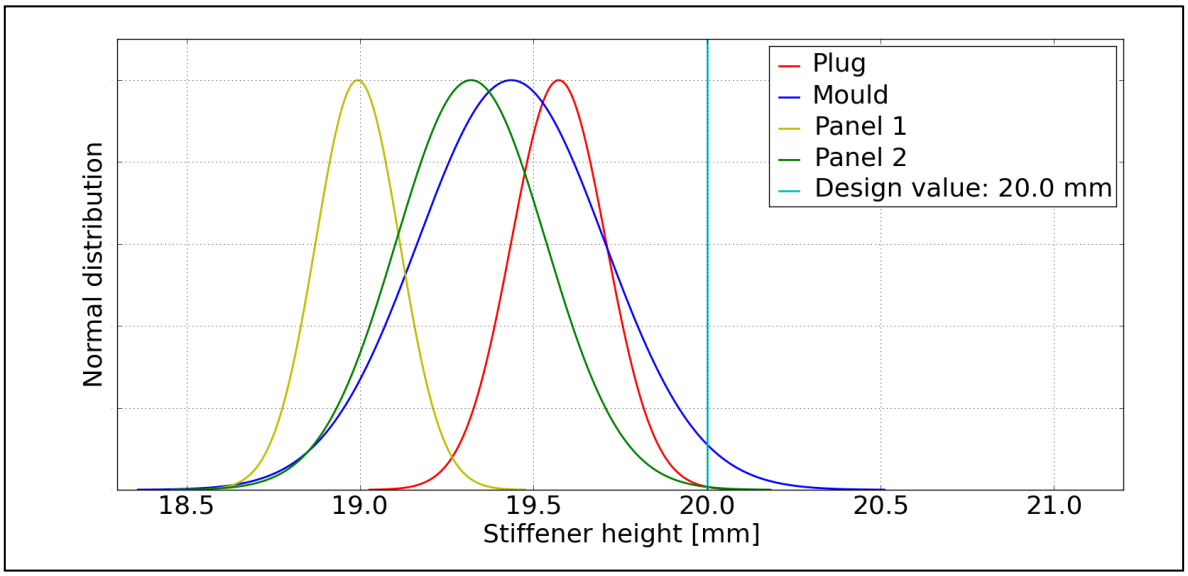

Figure K.4: Normal distributions of stiffener height measurements

The thickness of the stiffener is measured on different locations along the height of the stiffener. The normal distributions of the performed measurements are shown in figure K.5, figure K.6 and figure K.7. The locations along the height are indicated by z = 1, z = 2 and z = 3, which can be related to the bottom, middle and top of the stiffener respectively. For the design value, the thickness was unintentionally set at 5.40 mm, where a thickness of 5.04 mm was initially designed.
After milling the plug and pouring the mould, the stiffener thickness was reduced by approximately 0.5 mm with low variations on the measurements. The measurements on the mould could only be performed at the z = 1 locations, since measuring inside the channels would result in inaccurate measurements.

After the vacuum infusion process, the stiffener thickness was reduced significantly on locations z = 1 and z = 2, which is explained by the deformation of the silicon mould at the top of the silicon mould channels. At location z = 3, the silicon is relatively stable due to the thick layer of silicon on the bottom, which prevents the mould from compressing the stiffener. Less variation in the measurements are also found at the top of the grid.

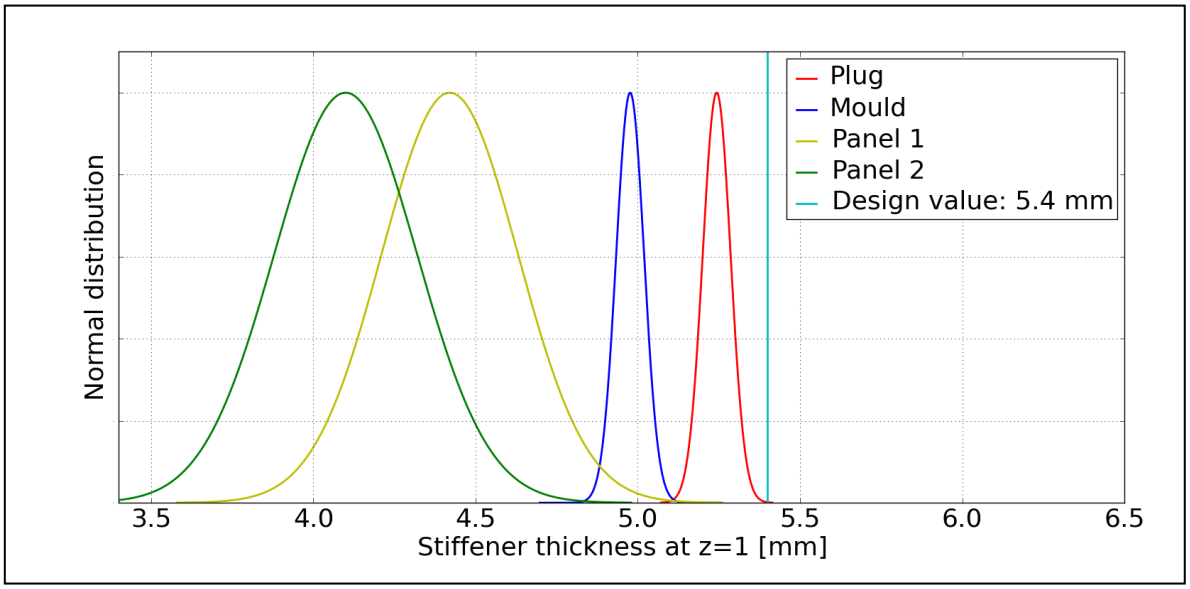

Figure K.5: Normal distributions of stiffener thickness at z=1

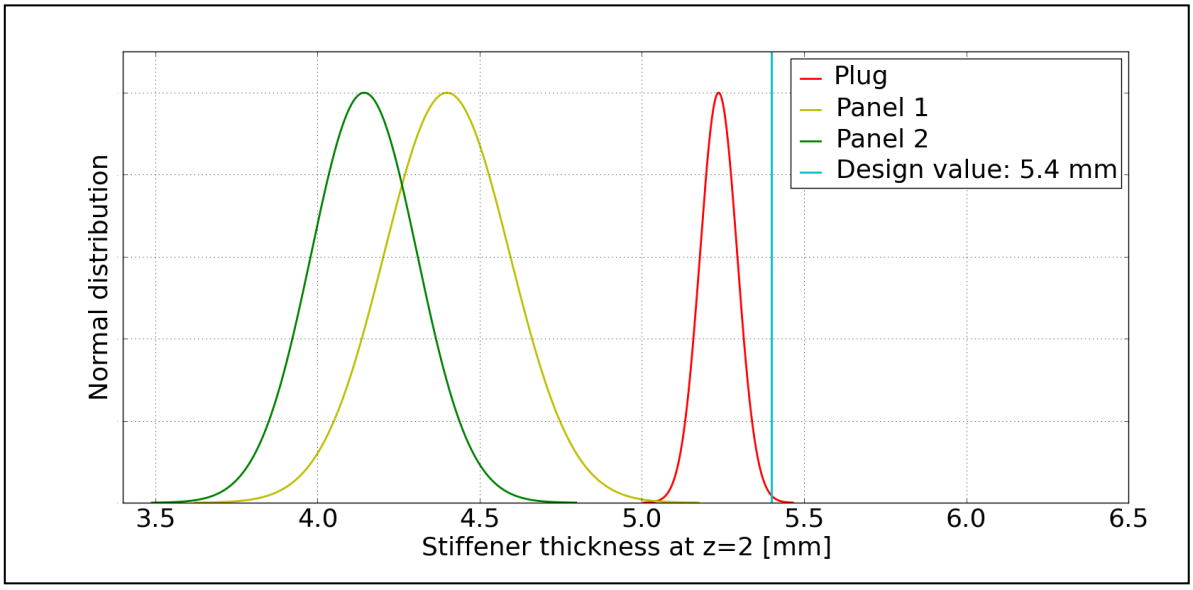

Figure K.6: Normal distributions of stiffener thickness at z=2

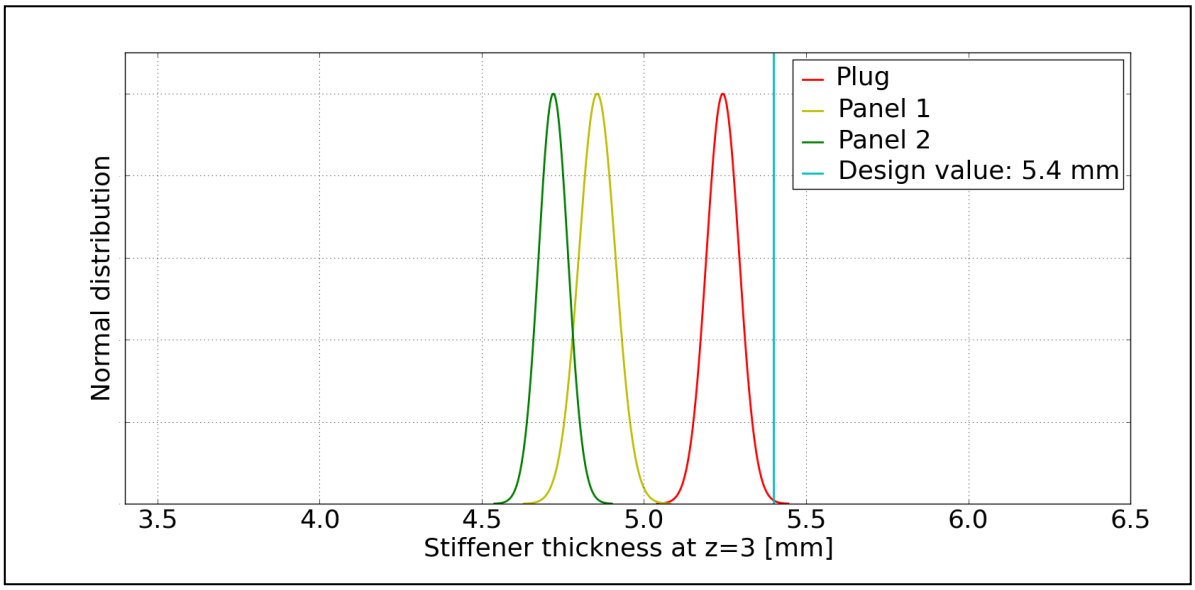

Figure K.7: Normal distributions of stiffener thickness at z=3

The results of the measurements on the stiffener spacing are drawn in figure K.8 and K.9. The figures show the normal distributions of the spacing along the x-axis and along the y-axis respectively.
The plug and silicon mould show an increase of the spacing between the stiffeners, which is a result of the milling machines tolerances. This increase is also in agreement with the lower thickness of the stiffeners.
Orthogrid sample panels 1 and 2 also show another increase of the stiffener spacing, which could be a result of the applied pressure from the vacuum. The increase of the stiffener spacing is however approximately 0.4 mm in both x and y direction. From this same value in both directions, it could be considered that not the full silicon block deforms under the applied pressure, because the block has a length to width ratio of 2.
The change could also be addressed to expansion of the silicon mould caused by an increase of temperature. However, the temperature rise as a result of the exothermal reaction could be considered small, because the used hardener for the epoxy maintains the temperature at approximately 30 degrees Celsius for at least three hours according to the data sheet.

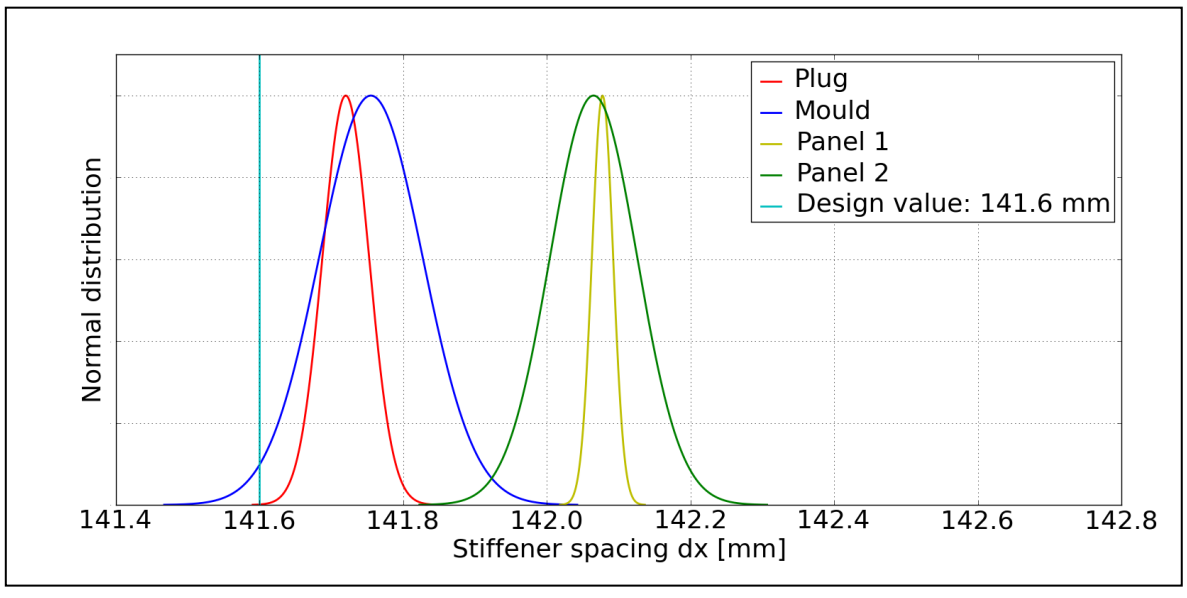

Figure K.8: Normal distributions of stiffener spacing dx

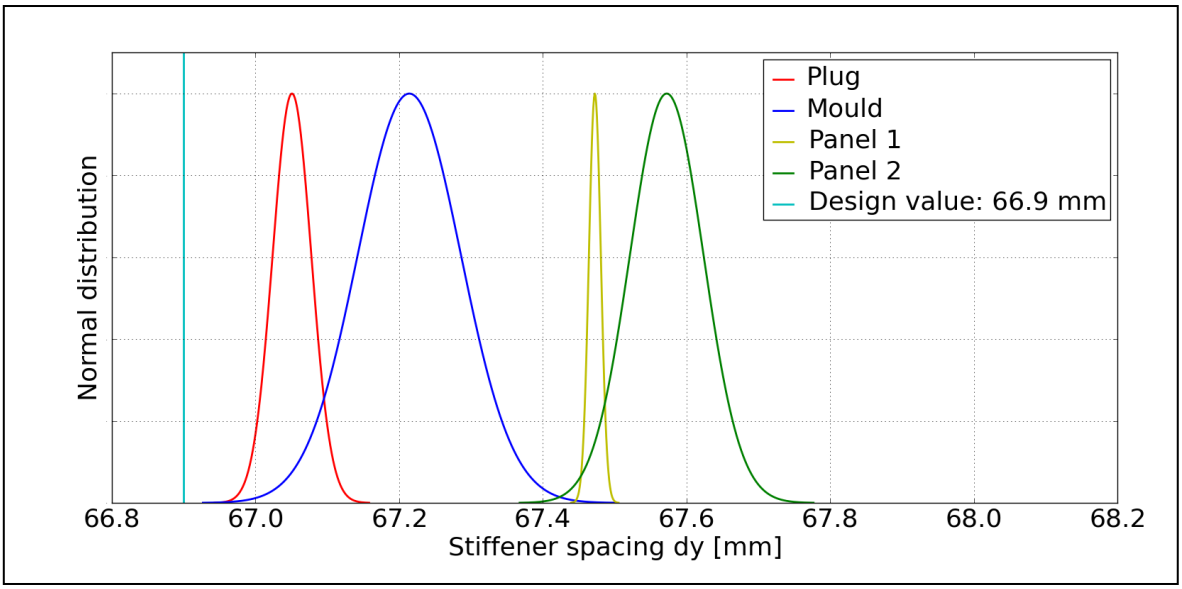

Figure K.9: Normal distributions of stiffener spacing dy

Appendix L

QUALITY ANALYSIS MEASUREMENTS OF THE SANDWICH PANEL

Figure L.1 shows the measurements locations on the sandwich panel. The blue line indicates the position of the resin runner, which is placed on one side of the panel. The arrow indicates the inlet position and the initial direction of the resin flow during the vacuum infusion process. The numbers indicate the locations in the xy-plane of the panel and act as a reference for the measurements outlined in table L.1 and table L.2.
The foam core measurements in table L.2 are obtained by measuring the dry foam core, before the vacuum infusion was performed.

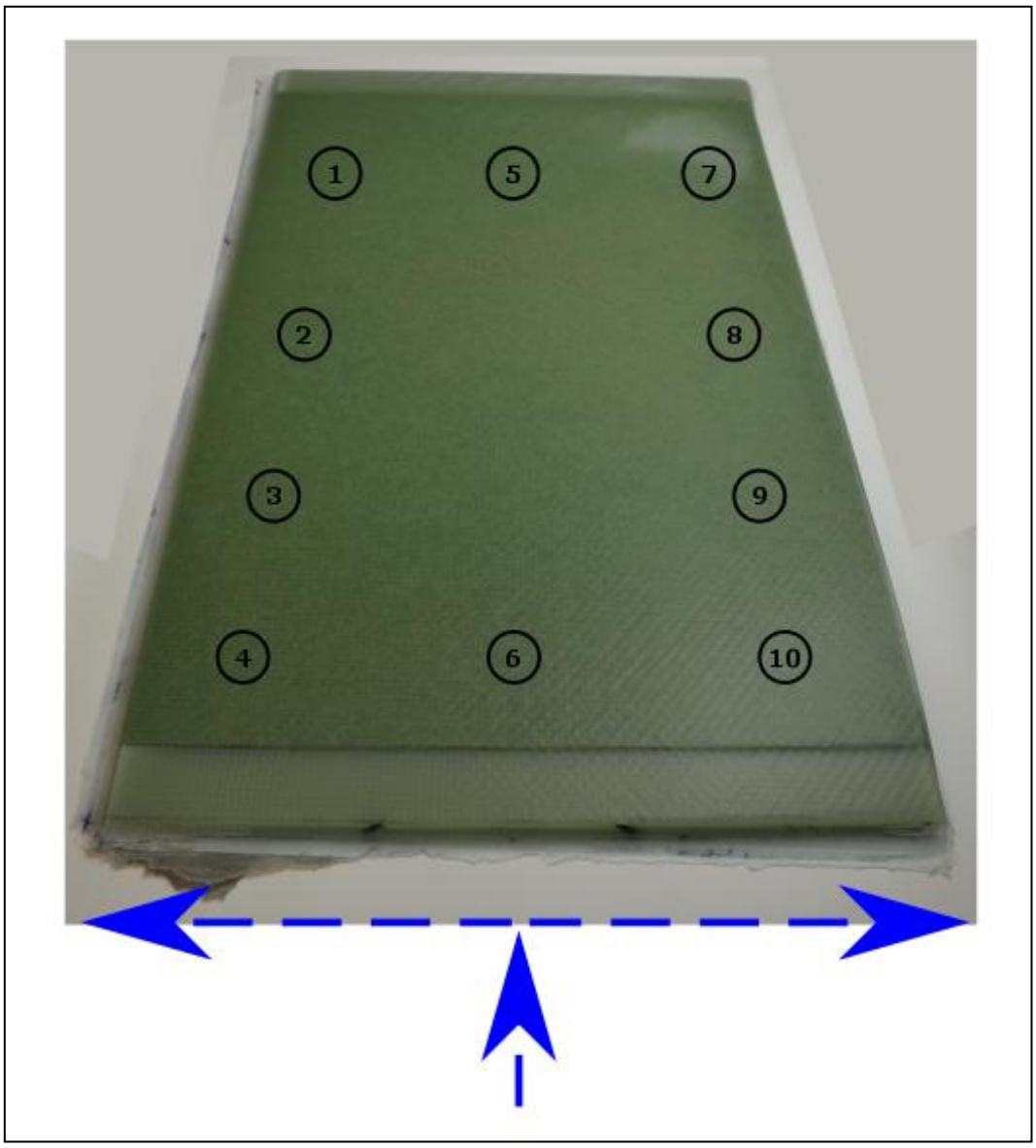

Figure L.1: Measurement locations on the sandwich panel

Table L.1: Sandwich panel measurements

Location	($t_f + t_c$) [mm]	Design thickness [mm]	Voids
1	14.40	14.70	None
2	14.42		None
3	14.45		None
4	14.42		None
5	14.49		None
6	14.50		None
7	14.50		Yes
8	14.55		None
9	14.50		None
10	14.50		None
Average	14.473		
Standard deviation	0.045398		

Table L.2: Foam core measurements

Location	t_c [mm]	Design thickness [mm]
1	12.17	12.0
2	12.20	
3	12.19	
4	12.18	
5	12.18	
6	12.24	
7	12.09	
8	12.09	
9	12.13	
10	12.08	
Average	12.155	
Standard deviation	0.0516236	

The total thickness was measured on several locations of the panel, from which the normal distribution is plotted in figure L.2. The initial design predicted a thickness of 14.7 mm, where the average from the measurements is found 0.227 mm thinner on 14.473 mm.

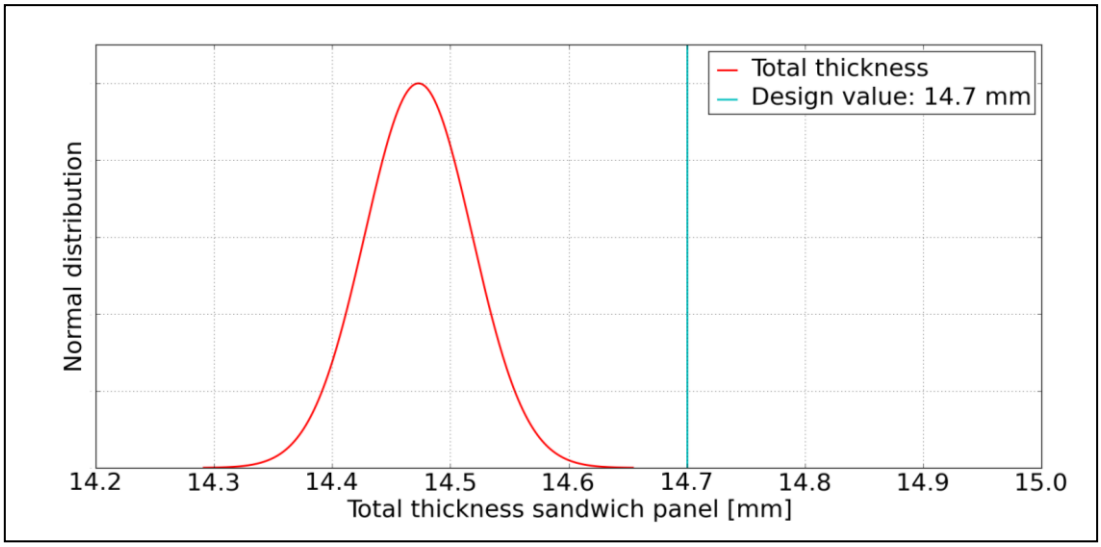

Figure L.2: Normal distributions of sandwich panel total thickness

The foam core thickness was measured prior to manufacturing and the normal distribution about the average of 12.155 is drawn in figure L.3. This value is higher than the design value of 12 mm, but could be addressed to manufacturing tolerances of the foam core material.

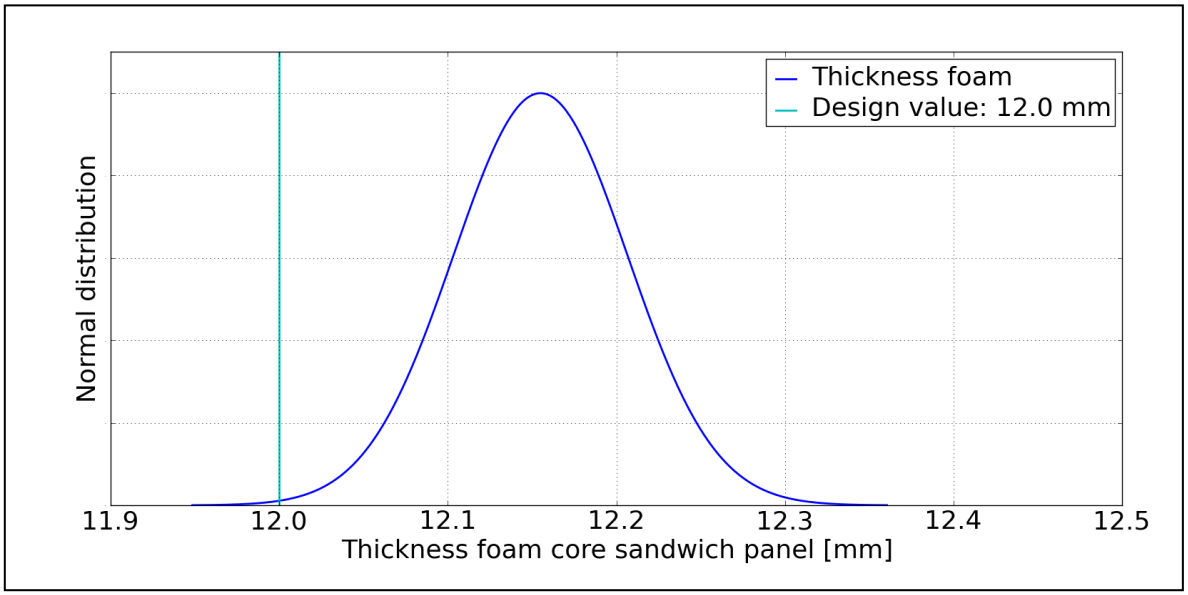

Figure L.3: Normal distributions of foam core thickness

The thickness of the face sheets are determined by subtracting the foam core thickness from the total average thickness. This results in a value of 2.318 mm of both face sheets. Since one face sheet is a stacking of 2 layers of biaxial glass-fibre, 1 ply is giving a thickness of 0.580 mm. This is different from the thickness used for design, where 1 ply was considered 0.675 mm.

Appendix M

QUALITY ANALYSIS MEASUREMENTS OF THE ORTHOGRID PANEL

This appendix shows all the performed measurements on the plug, the mould and the final orthogrid panel. The plug was 3D printed and the measurement locations are indicated in figure M.1. Each location indicates an area of a 3D printed part. The values obtained from the measurements are outlined in table M.1 and table M.2.
At each indicated location 3 measurements are performed, indicated by m1, m2 and m3 in the table M.1. For the cell measurements in table M.2, 5 different measurements are performed on each location, indicated by m1, m2, m3, m4 and m5.

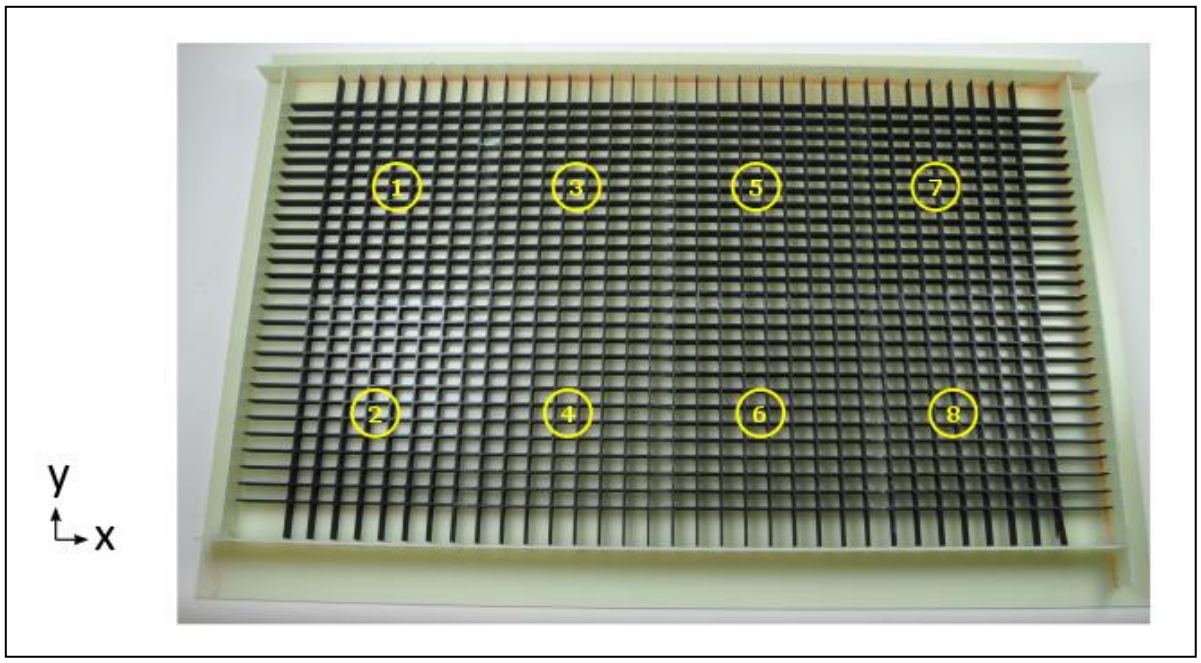

Figure M.1: Measurement locations on the plug of the orthogrid panel

Table M.1: Stiffener measurements 3D printed plug

Location	t_{st} (z = 1) [mm]			t_{st} (z = 2) [mm]			t_{st} (z = 3) [mm]			h_{st} [mm]		
	m1	m2	m3	m1	m2	m3	m1	m2	m3	m1	m2	m3
	average			average			average			average		
1	2.39	2.35	2.30	2.27	2.27	2.22	2.20	2.21	2.24	17.47	17.40	17.40
1 average		2.35			2.25			2.22			17.42	
2	2.45	2.43	2.31	2.28	2.51	2.27	2.49	2.39	2.56	17.00	17.07	17.37
2 average		2.40			2.32			2.48			17.06	
3	2.29	2.19	2.27	2.06	2.19	2.16	2.29	2.28	2.26	17.17	17.27	17.31
3 average		2.25			2.14			2.28			17.25	
4	2.35	2.29	2.25	2.13	2.07	2.04	2.14	2.14	2.16	17.10	17.01	17.20
4 average		2.30			2.08			2.15			17.10	

5	2.24	2.28	2.34	2.30	2.31	2.36	2.59	2.69	2.72	16.98	16.93	16.88
5 average		2.29			2.32			2.67			16.93	
6	2.37	2.30	2.32	2.03	2.18	2.23	2.18	2.24	2.26	16.98	17.03	16.99
6 average		2.33			2.15			2.23			17.00	
7	2.30	2.14	2.14	2.19	2.25	2.03	2.38	2.27	2.29	17.16	17.31	17.22
7 average		2.19			2.16			2.31			17.23	
8	2.24	2.37	2.21	2.13	2.15	2.04	2.25	2.12	2.25	17.34	17.27	17.16
8 average		2.27			2.11			2.21			17.26	
Average		2.30			2.19			2.32			17.16	
Standard deviation		0.0602			0.0872			0.1616			0.1511	

Table M.2: Cell measurements 3D printed plug

Location	Stiffener spacing (dx_{st} - t_{st}) [mm]					Stiffener spacing (dy_{st} - t_{st}) [mm]				
	m1	m2	m3	m4	m5	m1	m2	m3	m4	m5
			Average					Average		
1	24.72	24.66	24.66	24.67	24.67	16.92	16.87	16.91	16.95	16.98
1 average			24.68					16.93		
2	24.27	24.26	24.11	24.38	24.32	16.61	16.42	16.76	16.63	16.60
2 average			24.27					16.60		
3	24.61	24.66	24.69	24.77	24.76	16.99	16.96	16.79	16.78	16.90
3 average			24.70					16.88		
4	24.86	24.86	24.91	24.86	24.85	17.13	17.17	17.20	16.95	17.06
4 average			24.87					17.10		
5	24.22	24.22	24.17	24.23	24.18	16.47	16.56	16.48	16.43	16.33
5 average			24.20					16.45		
6	24.63	24.65	24.74	24.56	24.62	16.95	16.97	17.00	16.89	16.87
6 average			24.64					16.94		
7	24.54	24.79	24.45	24.52	24.55	16.51	16.82	16.87	17.01	16.96
7 average			24.57					16.83		
8	24.43	24.43	24.38	24.22	24.49	16.90	16.93	16.86	16.87	16.89
8 average			24.39					16.89		
Average			24.54					16.83		
Standard deviation			0.2168					0.1931		

The measurement locations of the silicon mould are indicated in figure M.2. The numbers indicate the locations in the xy-plane of the panel and act as a reference for the measurements indicated in table M.3 and table M.4.
In the tables the z locations refer to skin (z = 0), stiffener at the bottom (z = 1), middle (z = 2) and top (z = 3). For the silicon mould, measurements are only performed at (z = 1), because the flexibility of the silicon does not allow accurate measurements in the channels of the mould.
The numbers indicated in the figure can be related to the same numbers in figure M.1 and figure M.3.

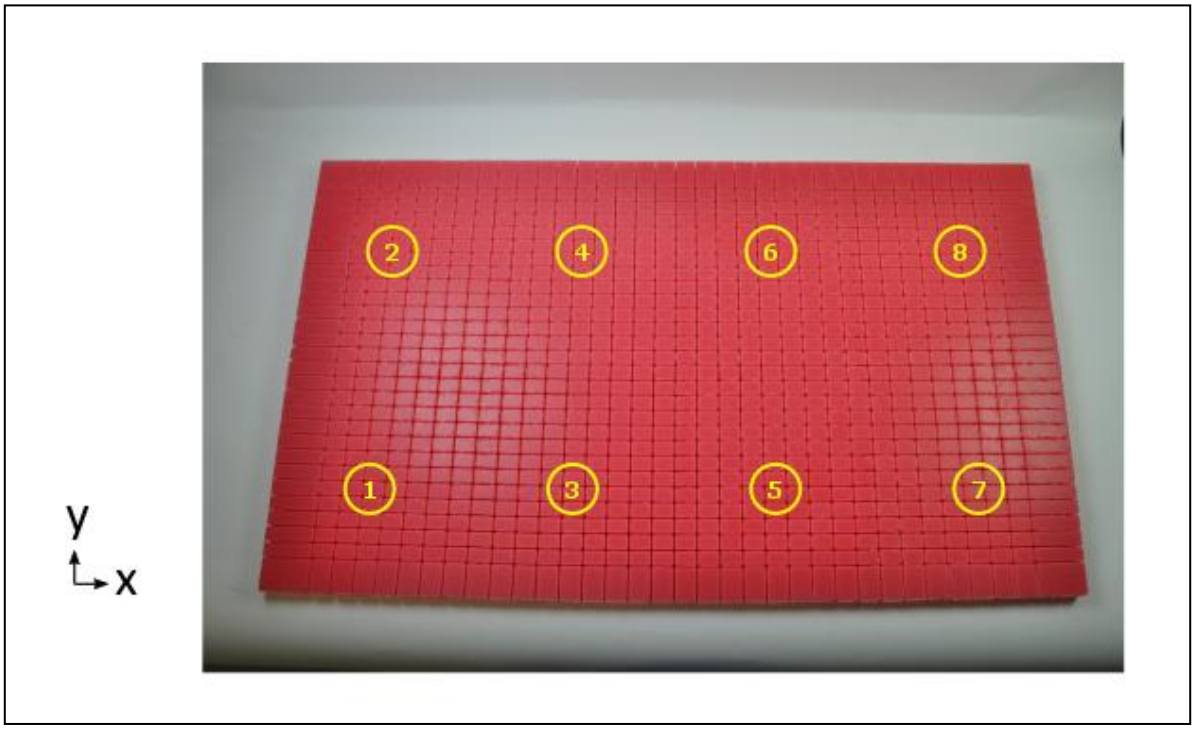

Figure M.2: Measurement locations on the mould of the orthogrid panel

Table M.3: Stiffener measurements orthogrid mould

Location	t_{st} (z = 1) [mm]			h_{st} [mm]		
	m1	m2	m3	m1	m2	m3
		average			average	
1	2.54	2.22	2.09	17.11	17.31	17.02
1 average		2.28			17.15	
2	1.97	1.92	2.15	17.27	17.18	17.28
2 average		2.01			17.24	
3	2.26	2.42	2.41	17.02	17.10	17.08
3 average		2.36			17.07	
4	2.24	2.27	2.27	17.22	17.07	16.92
4 average		2.26			17.07	
5	2.06	2.10	2.27	16.93	17.35	17.13
5 average		2.14			17.14	
6	2.17	1.91	1.97	17.24	17.17	17.35
6 average		2.02			17.25	
7	2.20	2.21	2.32	17.05	17.11	17.20
7 average		2.24			17.12	

8	2.31	2.33	1.84	17.39	17.52	17.32
8 average		2.16			17.41	
Average		2.18			17.18	
Standard deviation		0.1166			0.1071	

Table M.4: Cell measurements orthogrid mould

Location	Stiffener spacing (dx_{st} - t_{st}) [mm]					Stiffener spacing (dy_{st} - t_{st}) [mm]				
	m1	m2	m3	m4	m5	m1	m2	m3	m4	m5
			Average					Average		
1	24.72	24.60	24.93	24.59	24.80	17.04	17.06	17.01	17.15	16.98
1 average			24.73					17.05		
2	24.87	25.28	25.35	25.23	24.98	17.38	17.37	17.36	17.25	17.16
2 average			25.34					17.30		
3	24.49	24.70	24.68	24.80	24.41	16.56	16.88	16.67	16.68	16.83
3 average			24.62					16.72		
4	25.14	25.24	24.93	25.11	25.03	16.85	17.07	17.40	17.38	17.19
4 average			25.09					17.18		
5	25.27	25.07	25.14	25.25	24.89	17.41	17.48	17.54	17.31	17.30
5 average			25.12					17.41		
6	25.08	24.90	25.28	24.95	25.14	17.21	17.26	17.35	17.17	17.31
6 average			25.07					17.26		
7	24.84	25.16	24.81	24.94	24.80	17.34	17.27	17.03	17.25	17.26
7 average			24.91					17.23		
8	24.88	24.72	24.95	24.84	24.93	16.82	17.08	16.81	16.90	17.18
8 average			24.86					16.96		
Average			24.97					17.14		
Standard deviation			0.2178					0.2060		

The measurement locations for the orthogrid panel are indicated in figure M.3. The yellow arrow shows the inlet position at the left side of the panel. The yellow line indicates the resin runner, which was positioned all around the panel during the vacuum infusion.
The numbers indicate the locations in the xy-plane of the panel and act as a reference for the measurement indicated in table M.5, table M.6 and table M.7.
In the tables, the z locations refer to skin (z = 0), stiffener at the bottom (z = 1), middle (z = 2) and top (z = 3). The skin thickness will be calculated by subtracting the total thickness and the stiffener height, since the cells were too small to make proper skin thickness measurements.
Multiple measurements are performed at each location, indicated by m1, m2, m3, m4 and m5 in the tables.

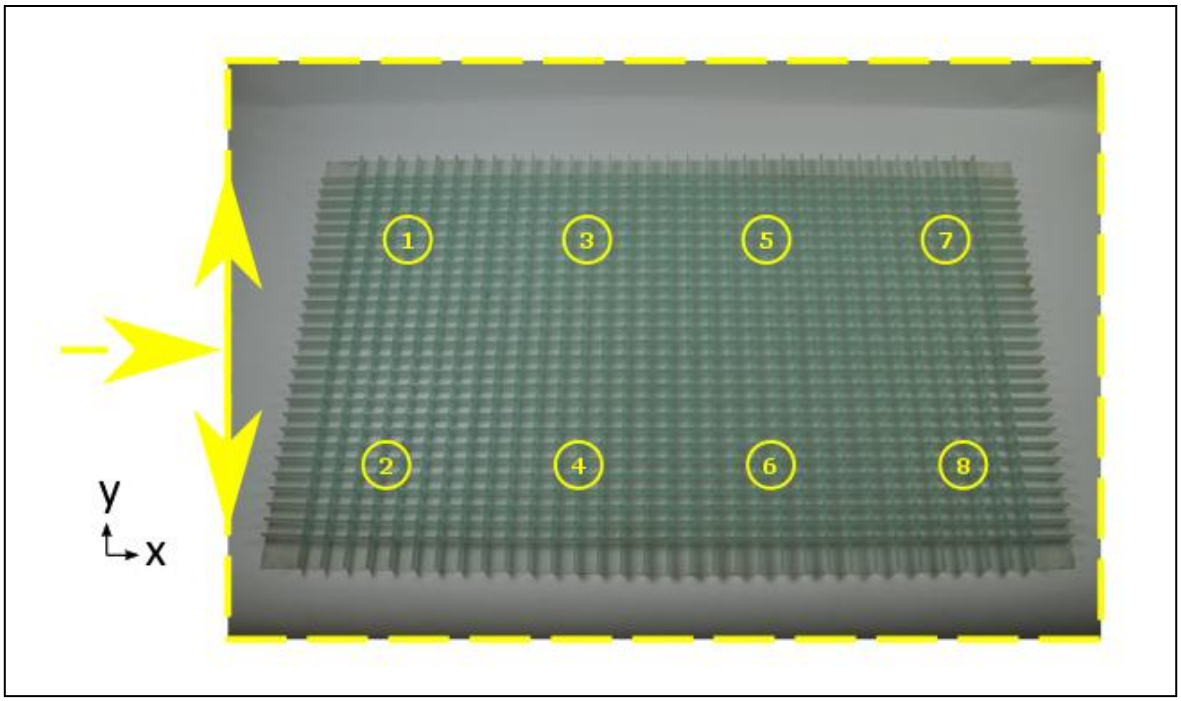

Figure M.3: Measurement locations on the orthogrid panel

Table M.5: Stiffener measurements orthogrid panel

Location	t_{st} (z = 1) [mm]			t_{st} (z = 2) [mm]			t_{st} (z = 3) [mm]			h_{st} [mm]		
	m1	m2	m3	m1	m2	m3	m1	m2	m3	m1	m2	m3
		average			average			average			average	
1	2.11	2.18	2.34	2.52	2.37	2.45	2.20	2.27	2.13	16.95	17.21	17.04
1 average		2.21			2.45			2.20			17.07	
2	2.23	1.92	2.18	2.83	2.49	2.62	2.49	2.60	2.37	16.70	16.98	16.94
2 average		2.11			2.65			2.49			16.87	
3	2.18	2.17	2.13	2.24	2.52	2.25	2.27	2.27	2.18	16.93	17.36	17.08
3 average		2.16			2.34			2.24			17.12	
4	2.33	2.17	2.42	2.11	2.06	2.39	2.12	2.10	2.21	16.88	16.85	16.86
4 average		2.31			2.19			2.14			16.86	
5	2.22	2.14	2.18	2.42	2.33	2.34	2.63	2.60	2.59	16.71	16.88	16.67
5 average		2.18			2.36			2.61			16.75	
6	2.42	2.30	2.48	2.31	2.25	2.20	2.30	2.16	2.43	16.63	16.84	16.63
6 average		2.40			2.25			2.30			16.70	
7	2.14	2.21	2.18	2.45	2.25	2.32	2.25	2.36	2.19	16.90	17.11	16.83
7 average		2.18			2.34			2.27			16.95	
8	2.27	2.46	2.32	2.28	2.17	2.28	2.26	2.11	2.19	16.94	17.07	16.90
8 average		2.35			2.24			2.19			16.97	
Average		2.24			2.35			2.31			16.91	
Standard deviation		0.0961			0.1360			0.1517			0.1363	

Table M.6: Total thickness measurements orthogrid panel

Location	(t_{sk} +h_{st}) [mm]		
	m1	m2	m3
		average	
1	17.80	17.65	17.60
1 average		17.68	
2	17.60	17.50	17.40
2 average		17.50	
3	17.75	17.70	17.80
3 average		17.75	
4	17.35	17.30	17.25
4 average		17.30	
5	17.20	17.10	17.30
5 average		17.20	
6	17.30	17.20	17.20
6 average		17.23	
7	17.35	17.45	17.40
7 average		17.40	
8	17.50	17.50	17.40
8 average		17.47	
Average		17.44	
Standard deviation		0.1874	

Table M.7: Cell measurements orthogrid panel

Location	Stiffener spacing (dx_{st} - t_{st}) [mm]					Stiffener spacing (dy_{st} - t_{st}) [mm]				
	m1	m2	m3	m4	m5	m1	m2	m3	m4	m5
			Average					Average		
1	24.86	24.53	24.79	24.81	24.72	16.99	17.05	17.11	17.00	16.86
1 average			24.74					17.00		
2	24.36	24.32	24.58	24.40	24.57	16.84	16.66	16.82	16.45	16.84
2 average			24.45					16.72		
3	24.85	24.69	24.77	24.57	24.91	17.16	17.08	16.93	16.98	16.88
3 average			24.76					17.01		
4	24.88	24.91	24.85	24.90	24.87	17.13	17.26	17.23	17.18	17.28
4 average			24.88					17.22		
5	24.34	24.29	24.25	24.30	24.40	16.51	16.62	16.61	16.65	16.64
5 average			24.32					16.61		
6	24.80	24.83	24.64	24.65	24.72	17.09	17.06	16.92	17.00	16.97
6 average			24.73					17.01		
7	24.65	25.12	24.56	24.63	24.89	17.05	16.93	17.03	17.13	17.05
7 average			24.77					17.04		
8	24.55	24.65	24.76	24.51	24.56	16.83	17.15	16.97	16.93	16.94
8 average			24.61					16.96		
Average			24.66					16.95		
Standard deviation			0.1746					0.1800		

The performed measurements are outlined and graphically presented by plotting the normal distribution related to the averages and standard deviations.
The total thickness of the panel is measured at 24 locations of the panel. The average of the measurements was found to be 17.44 mm, where the designed value was given by 17.675 mm as is shown in table M.8. The explanation could be found after measuring the average stiffener height.

Table M.8: Comparison of total thickness orthogrid panel

	Theoretical value [mm]	Orthogrid panel [mm]
Total thickness [mm]	17.675	17.44

The stiffener spacing of the orthogrid panel has been measured for the plug, the silicon mould and the orthogrid panel and are compared in figure M.4 and figure M.5. For both directions of stiffener spacing, a total of 40 measurements were performed.

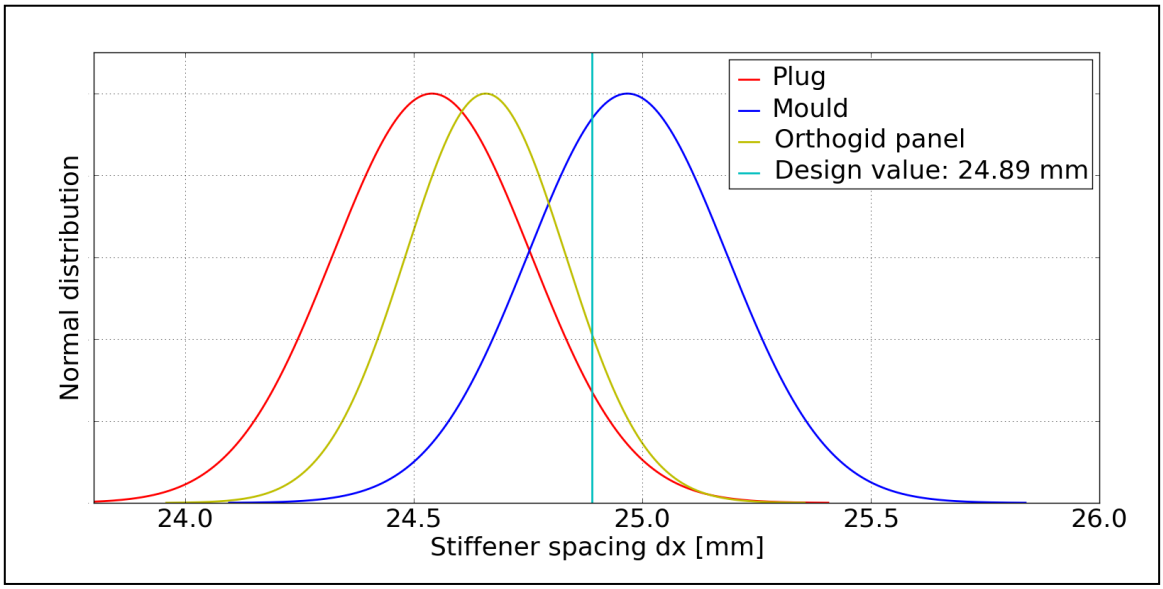

Figure M.4: Normal distributions of stiffener spacing dx of the orthogrid panel

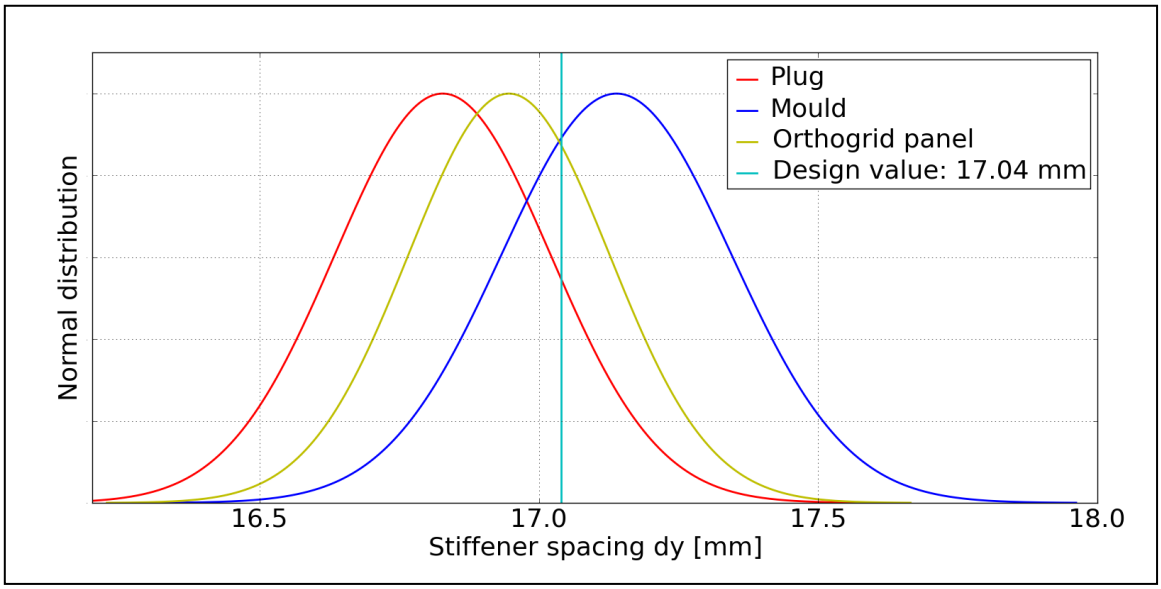

Figure M.5: Normal distributions of stiffener spacing dy of the orthogrid panel

The stiffener spacing for the plug was smaller than the initial design, which is a result of the increase in stiffener thickness of the 3D printed grid. The mould has a higher average stiffener spacing, where the final orthogrid panel is comparable with the plug. The relatively large standard deviation will have an impact on the standard deviation of the stiffener thickness as well, which was already designed very thin.
The measurements on the stiffener height are graphically presented as normal distributions in figure M.6. The plug and mould were measured with an average between 17.1 mm and 17.2 mm. After the vacuum infusion process, the average height of the orthogrid panel was measured on 16.91 mm, which is a 0.09 mm difference with the design value.

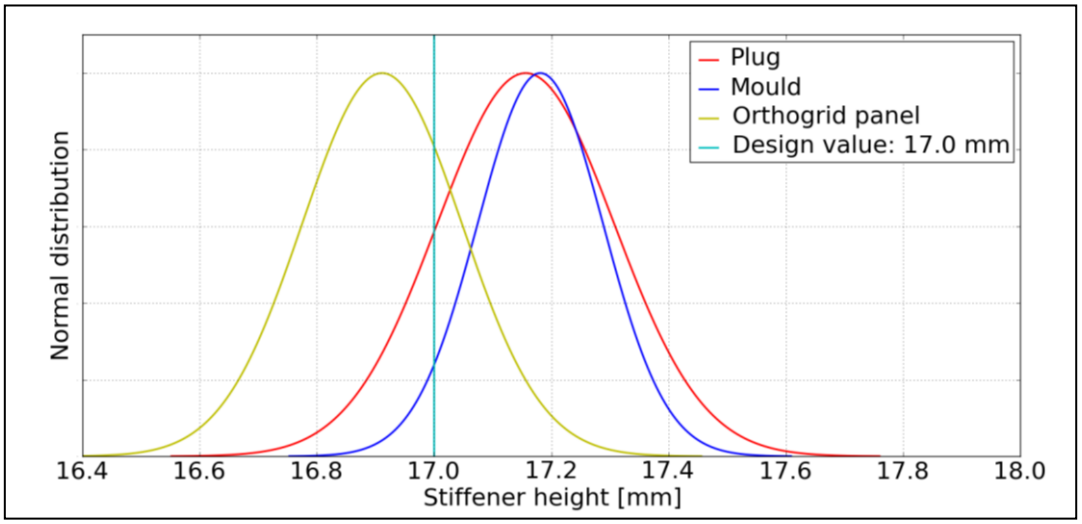

Figure M.6: Normal distributions of the stiffener height of the orthogrid panel

Due to the small cells, accurate measurements of the skin thickness were hard to perform. The skin thickness is therefore calculated by subtracting the average stiffener height from the average total thickness. This results in a skin thickness of 0.53 mm, which is lower than the design value of 0.675 mm. This value is much lower than expected, which could be a result of the larger scatter in the results of the total thickness measurements. Therefore, measurements on the skin thickness were performed after cutting pieces from the orthogrid panel after the test. From a total of 8 measurements, an average skin thickness of 0.676 mm was found with a standard deviation of 0.0173 mm. This is in good agreement with the expected thickness of the skin.

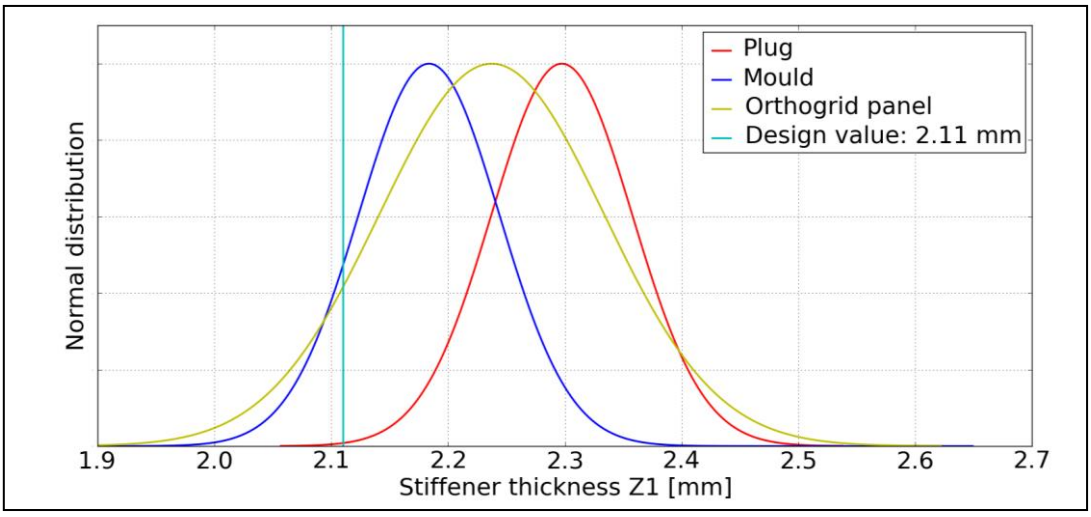

Figure M.7: Stiffener thickness Z1 normal distributions large orthogrid panel

The thickness of the grid was measured on three height locations; bottom, middle an top, of which the normal distributions of the measurements are shown in figure M.7, figure M.8 and figure M.9 respectively. An unexpected result is that the stiffener thickness is not decreased during the vacuum infusion process. The standard deviation seems to be relatively large and since not the exact same locations were measured for the plug, mould and panel, the comparison is harder to make. The orthogrid panel, indicated by the yellow lines does show a constant average thickness along the height.
The silicon mould measurements were not performed on (z = 2) and (z = 3), because the specific area was hard to reach with a calliper and would therefore results in inaccurate measurements.

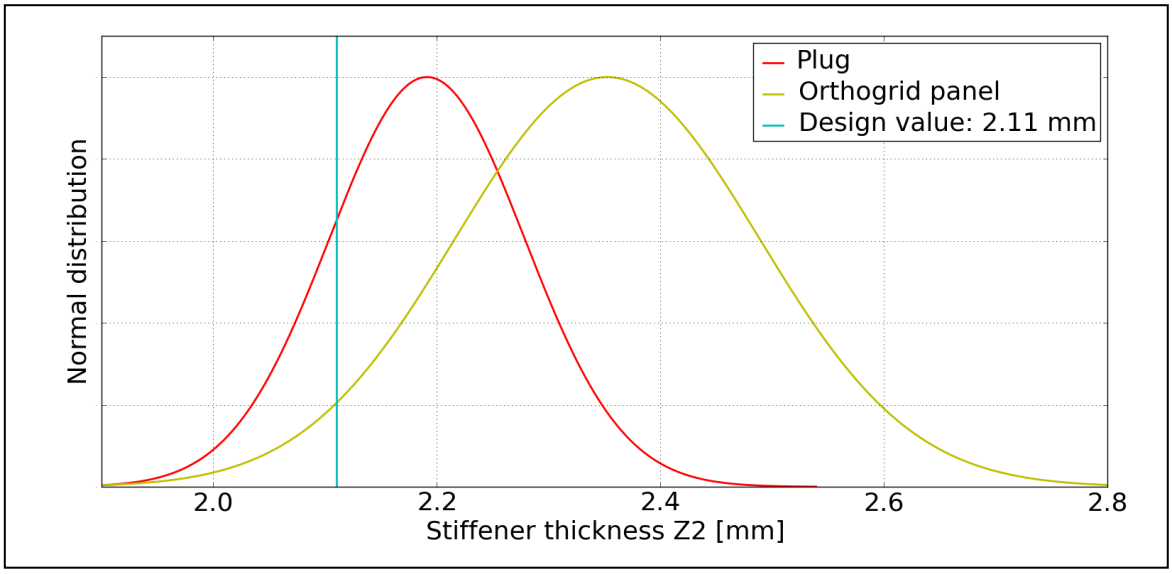

Figure M.8: Stiffener thickness Z2 normal distributions large orthogrid panel

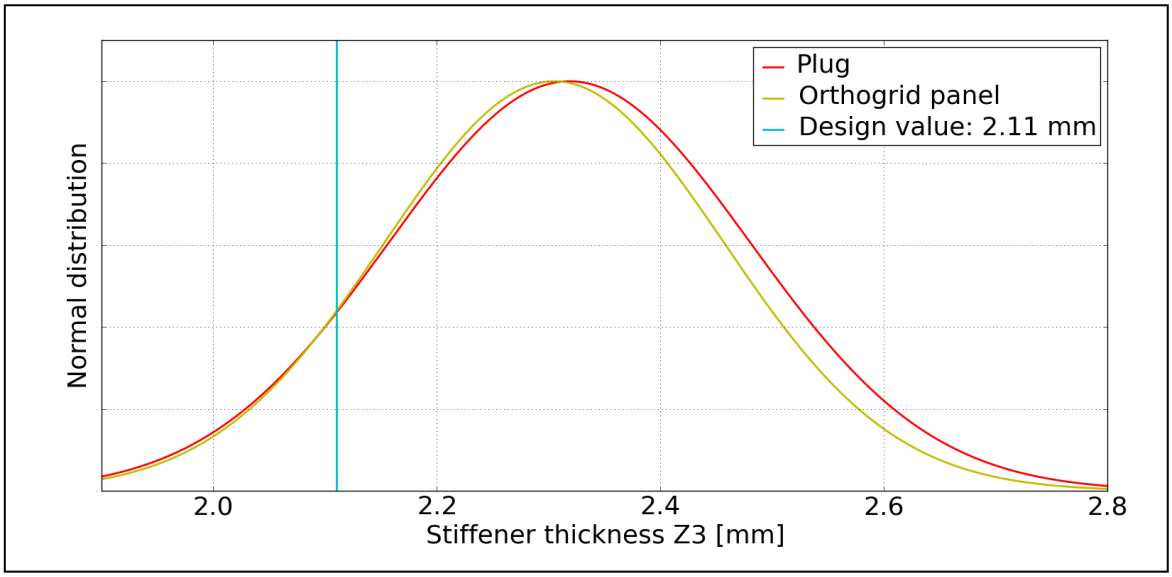

Figure M.9: Stiffener thickness Z3 normal distributions large orthogrid panel

Appendix N

EXPLANATION OF NON-LINEAR NUMERICAL MODELS

This appendix gives information on the different boundary conditions and model choices made with respect to the numerical models presented in chapter 7. The aim is to give a more clear understanding by showing prints screens of the applied load, boundary conditions and other constraints. This should help in reproducing the results for future researchers. The information is based on an example orthogrid panel, but the same set-up could be introduced on other configurations.

Materials of the numerical model

The test panels which were manufactured and tested during this study, had been slightly modified by adding tab material and slightly increasing the length and width. These changes have been taken into account in the numerical model, which is shown in figure N.1.

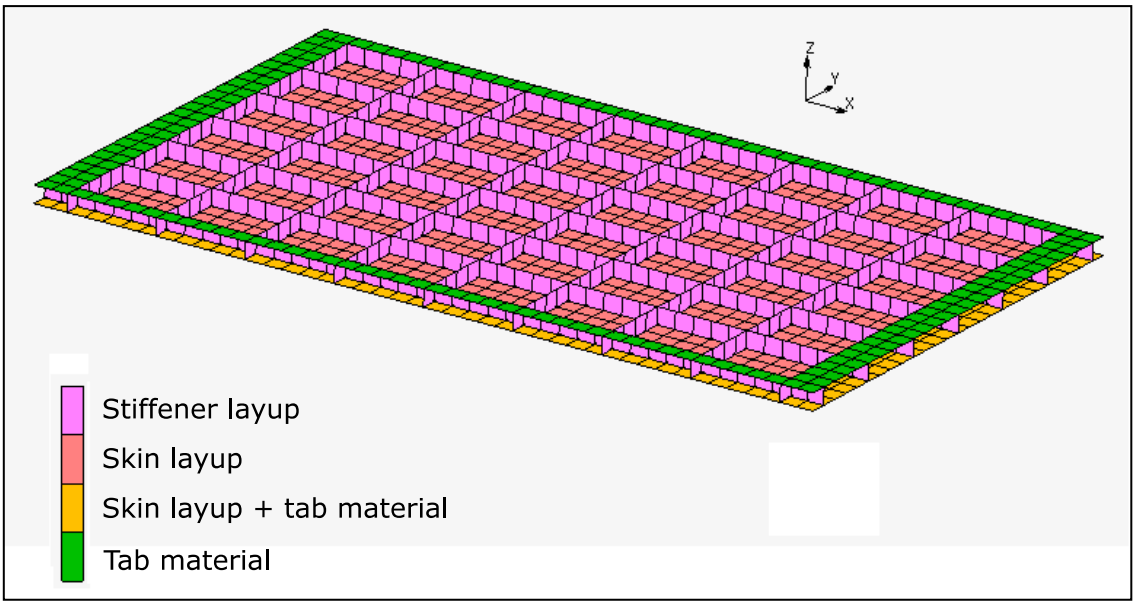

Figure N.1: Numerical model of an example orthogrid panel, showing the element set-up and the related material lay-ups

Boundary conditions

The boundary conditions of the numerical model were not changed with respect to the initial models used in chapter 3 and chapter 4. A print screen of the applied boundary conditions is shown in figure N2.

Links

In chapter 3 and 4, no links were introduced to the model. However, the links introduce more realistic behaviour with respect to the experiment and were therefore introduced to the non-linear models in chapter 7. At the edge where only a fixed displacement in x and y is present, the panel is allowed to rotate around the y axis. The links will introduce a uniform displacement in x at this edge of the panel, which is also occurring in the compression test. A print screen of the situation is given in figure N.3.

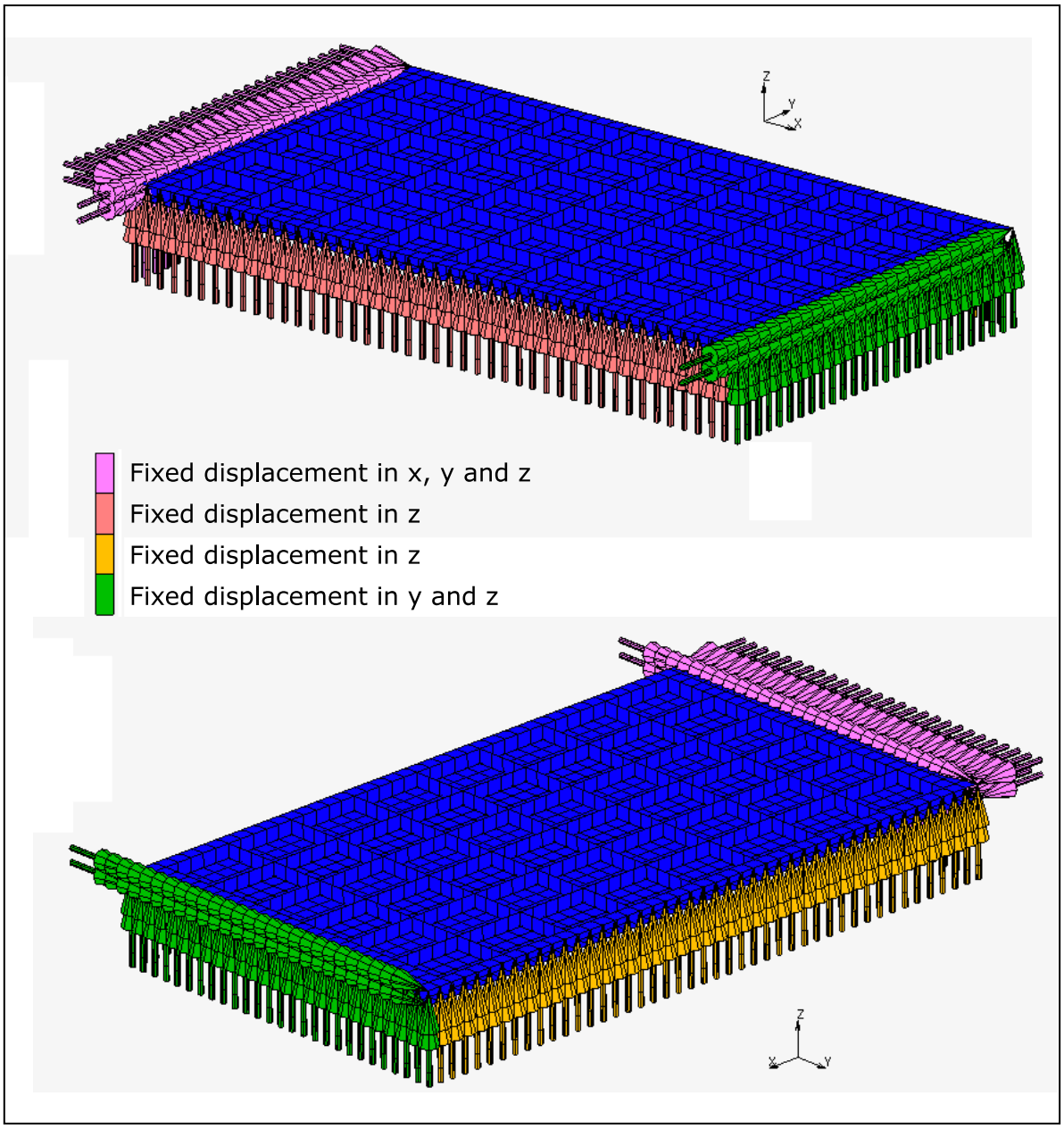

Figure N.2: Boundary conditions on the numerical models used in this study

Applied load (eigenvalue analysis)

For the eigenvalue analysis, a unit-load is introduced at every node on one side of the panel, which is shows in figure N.4.

Applied load (non-linear analysis)

For the non-linear analysis, the full applied load is introduced at the node which is connected to all the nodes at the edge via the links. The situation is shown in figure N.5.

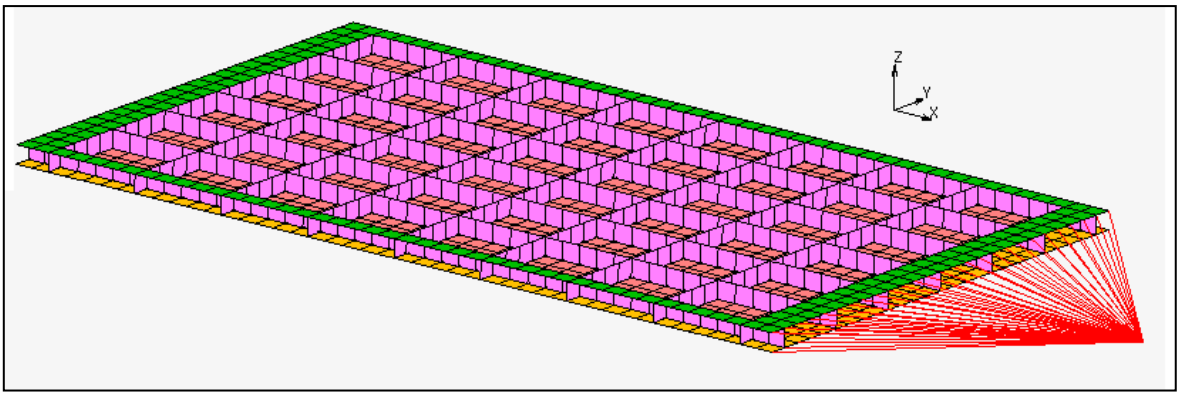

Figure N.3: Nodal ties appended to create a uniform displacement at the related edge

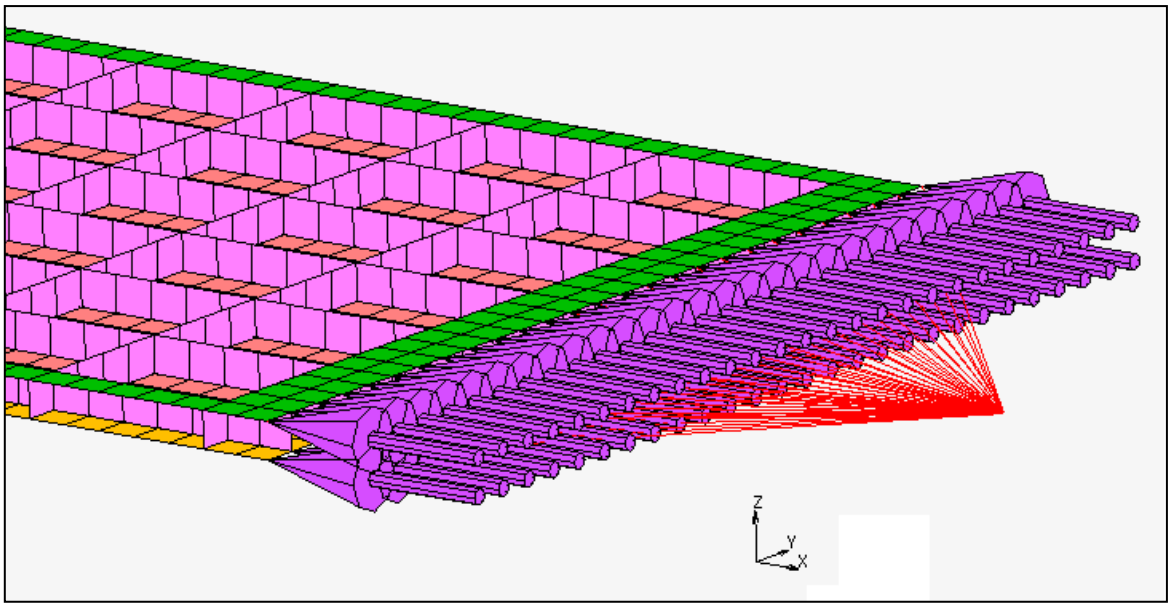

Figure N.4: Applied unit loads when performing the eigenvalue analysis

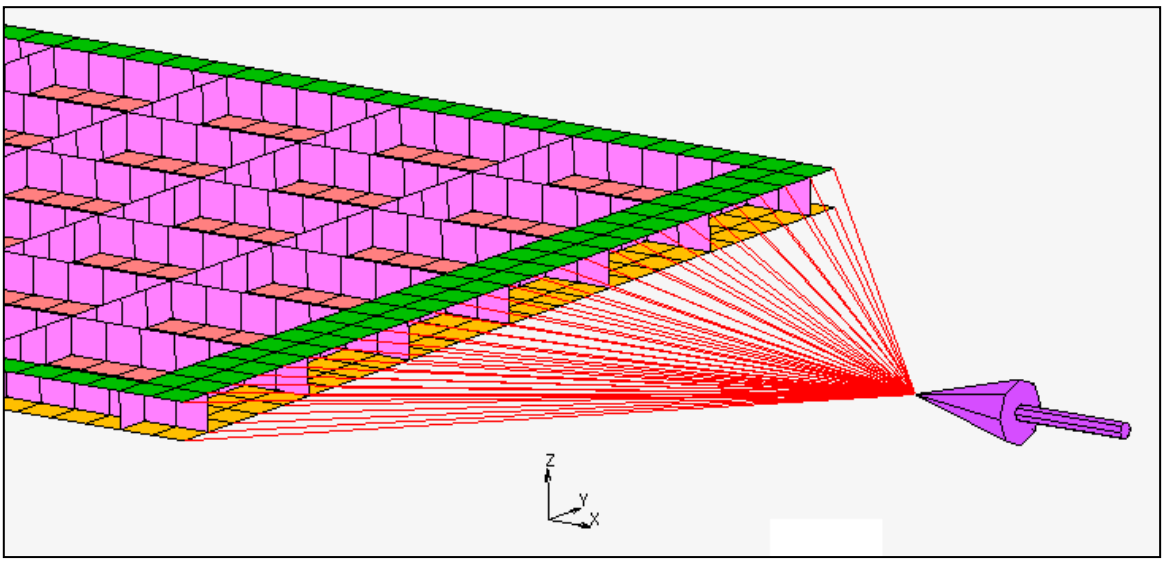

Figure N.5: Applied full load, introduced with the non-linear analysis

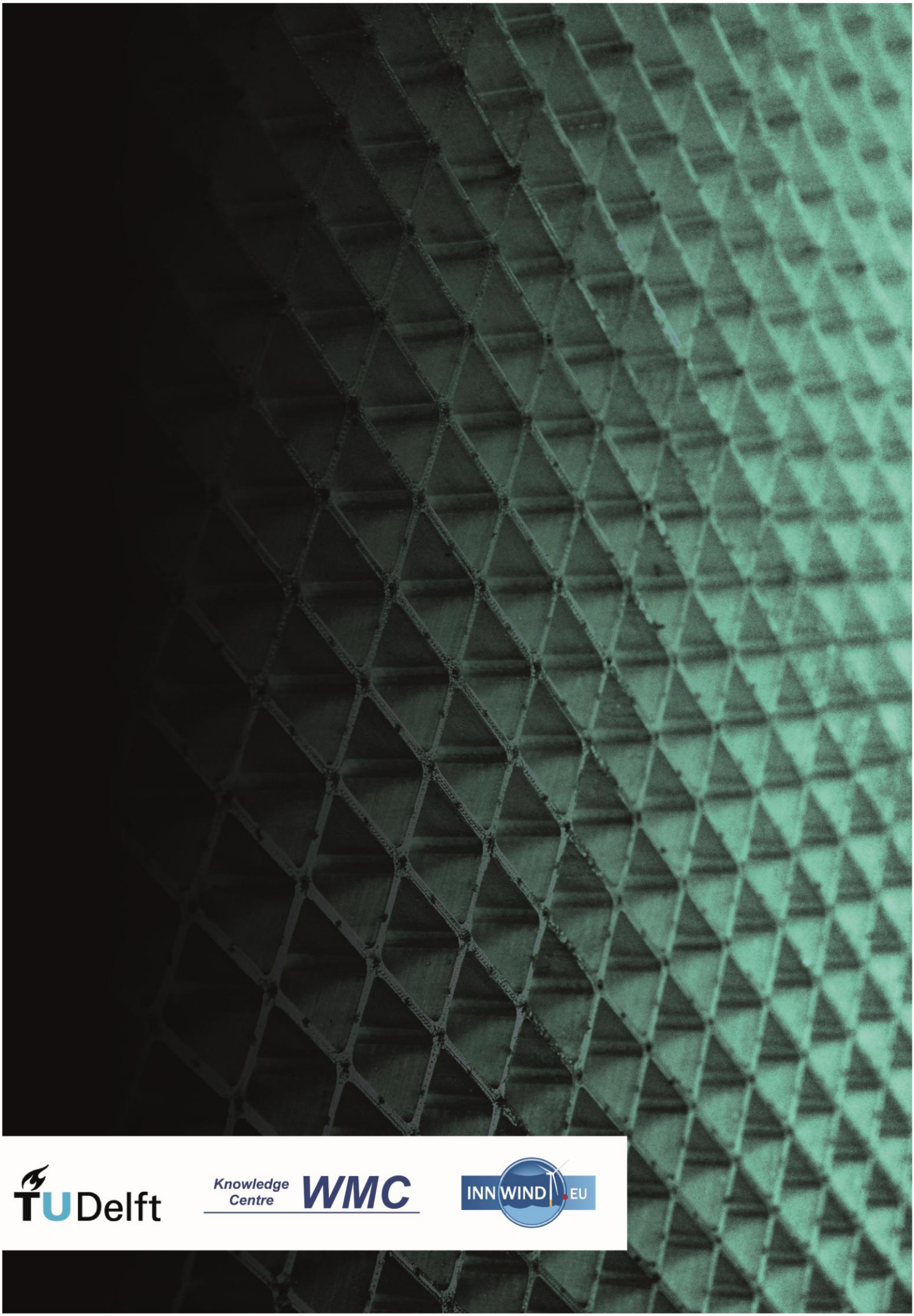
TU Delft
Knowledge Centre WMC
INNWIND.EU